INFRARED THERMOGRAPHY AS A POTENTIAL INSPECTION METHOD FOR THE CF-188 INNER WING STEPPED-LAP JOINT

LA THERMOGRAPHIE INFRAROUGE COMME MÉTHODE D'INSPECTION POTENTIELLE POUR LE JOINT À RECOUVREMENT ÉTAGÉ DE L'AILE INTÉRIEURE DU CF-188

A Thesis Submitted
To the Division of Graduate Studies of the Royal Military College of Canada

by

Keith George, rmc, BSc
Captain

In Partial Fulfillment of the Requirements for the Degree of
Master of Science in Physics.

August 2022

ROYAL MILITARY COLLEGE OF CANADA
COLLEGE MIITAIRE ROYAL DU CANADA

DIVISION OF GRADUATE STUDIES AND RESEARCH
DIVISION DES ÉTUDES SUPÉRIEURES ET DE LA RECHERCHE

This is to certify that the thesis prepared by / Ceci certifie que le thèse redigée par
K.K. George
entitled / intitulée
Infrared Thermography as a Potential Inspection Method for the CF-188 Inner Wing Stepped-Lap Joint
La Thermographie Infrarouge comme Méthode D'inspection Potentielle pour le Joint à Recouvrement Étagé de L'aile Intérieure du CF-188
Complies with the Royal Military College of Canada regulations and that it meets the accepted standards of the Graduate School with respect to quality, and, in the case of a doctoral thesis, originality, / satisfait aux règlements du Collège Militaire Royal du Canada et qu'elle respecte les norms acceptées par la Faculté des études supérierues quant à la qualité et, dans le cas d'une thèse de doctorat, l'originalité,

for the degree of / pour le diplôme de
Master of Science / Maîtrise en Science
Signed by the final examining committee: /
Signé par les members du comité examinateur de la soutenance de these

________________________, Chair / President
________________________, External Examiner / Examinateur externe
________________________, Main Supervisor / Directeur de thèse principal
____
____

Approved by the Head of Department: /
Approuvé par le Directeur du Département: ____________________ Date : ___________

To the Librarian: This thesis is not to be regarded as classified. /
Au Bibliothécaire: Cette thèse n'est pas considerée comme a publication restreinte.

____
Main Supervisor / Directeur de thèse principal

ABSTRACT

The CF-188 Inner Wing Stepped-Lap Joint (IWSLJ) is a titanium (Ti-6Al-4V) and Carbon Fibre Reinforced Polymer (CFRP) bonded joint that serves as the principle structural member, transferring loads between the fuselage and wing. Research over the last two decades by allied nations has highlighted the IWSLJ's vulnerability to disbond areas. This vulnerability can be linked to prolonged exposure to high temperatures, moisture ingress, and fatigue. Of specific concern is a special type of disbond area called a "kissing bond" which is generally caused by surface contamination during the manufacturing process rather than in-service exposure factors. A kissing bond is difficult to detect by conventional methods such as ultrasonic testing. Large disbond areas under operational loads have the potential to initiate a wing-fuselage structural failure and separation, with the consequent loss of a wing.

Presently a Quality Engineering and Test Establishment (QETE) ultrasonic Non-Destructive Testing (NDT) technique, serves as the latest IWSLJ inspection method, and has proven to be highly successful in detecting disbond areas. However, since infrared thermography has emerged as a relatively rapid and inexpensive means of inspecting for disbond and delaminated areas, it may be the ideal method for this situation. Hence, this thesis presents an experimental investigation to evaluate both flash and induction thermography as potential means to rapidly inspect the IWSLP for disbond areas. The results are compared to those of the current ultrasonic inspection technique for the IWSLJ by QETE.

The following four studies were conducted: Study 1, A parametric study to determine the optimal parameters for induction thermography; Study 2, the detection and dimensioning of artificial disbond areas; Study 3, the detection depth of each methods; and Study 4, the sensitivity of detection. It was determined that flash thermography had a greater rate of detection and defect detail in comparison to induction thermography. Although induction thermography was not able to detect the artificial kissing bonds, it was the fastest method of inspection. Furthermore, induction thermography provided higher accuracy in terms of defect dimensions, and both thermography methods were only able to penetrate to the fourth step of the nine step IWSLJ. Ultimately, ultrasonic testing remained the superior inspection method by out-performing thermography in terms of detection and dimensioning for the studies perform in this thesis. However, ultrasonic testing had a longer setup and scan time. Also, very few people nationwide are authorized to carry out the technique. Although thermography is not ideal for this application, it could still be a complementary inspection method.

RÉSUMÉ

Le CF-188 joint à recouvrement étagé de l'aile intérieure est un joint collé en titane (Ti-6Al-4V) et de polymère renforcé de fibre de carbone (CFRP) qui sert de principal élément structurel, transférant les charges entre le fuselage et l'aile. Les recherches menées au cours des deux dernières décennies par les nations alliées ont mis en évidence la vulnérabilité du joint à recouvrement étagé de l'aile intérieure aux zones de dislocation. Cette vulnérabilité peut être liée à une exposition prolongée à des températures élevées, à la pénétration d'humidité et à la fatigue. Une préoccupation particulière est un type spécial de zone de décollement appelée « liaison de baiser » qui est généralement causée par une contamination de surface pendant le processus de fabrication plutôt que par des facteurs d'exposition en service. Un lien de baiser est difficile à détecter par des méthodes conventionnelles telles que les tests par ultrasons. De grandes zones de décollement sous des charges opérationnelles ont le potentiel d'initier une défaillance structurelle et une séparation aile-fuselage, avec la perte conséquente d'une aile.

Actuellement, une technique d'essais non destructifs par ultrasons d'un établissement d'ingénierie et d'essais de qualité sert de dernière méthode d'inspection du joint à recouvrement étagé de l'aile intérieure et s'est avérée très efficace pour détecter les zones de décollement. Cependant, étant donné que la thermographie infrarouge est devenue un moyen relativement rapide et peu coûteux d'inspecter les zones décollées et décollées, elle peut être la méthode idéale pour cette situation. Par conséquent, cette thèse présente une enquête expérimentale pour évaluer à la fois la thermographie flash et par induction comme moyen potentiel d'inspecter rapidement l'IWSLP pour les zones de décollement. Les résultats sont comparés à ceux de la technique actuelle d'inspection par ultrasons pour la joint à recouvrement étagé de l'aile intérieure.

Les quatre études suivantes ont été menées: Etude 1, Une étude paramétrique pour déterminer les paramètres optimaux pour la thermographie par induction; Etude 2, la détection et le dimensionnement des zones artificielles de décollement; Etude 3, la profondeur de détection de chaque méthode; et l'étude 4, la sensibilité de détection. Il a été déterminé que la thermographie flash avait un taux de détection et de détail des défauts supérieur à celui de la thermographie à induction. Bien que la thermographie par induction n'ait pas été en mesure de détecter les liens de baiser artificiels, c'était la méthode d'inspection la plus rapide. De plus, la thermographie par induction a fourni une plus grande précision en termes de dimensions des défauts, et les deux méthodes de thermographie n'ont pu pénétrer que jusqu'à la quatrième étape des neuf étapes du joint à recouvrement étagé de l'aile intérieure. En fin de compte, le contrôle par ultrasons est resté la méthode d'inspection supérieure en surpassant la thermographie en

termes de détection et de dimensionnement pour les études menées dans cette thèse. Cependant, les tests par ultrasons avaient une configuration et un temps de balayage plus longs. De plus, très peu de personnes dans tout le pays sont autorisées à pratiquer la technique. Bien que la thermographie ne soit pas idéale pour cette application, elle pourrait tout de même être une méthode d'inspection complémentaire.

ACKNOWLEDGEMENTS

I wish to declare my sincerest gratitude to my thesis advisors, Dr. Thomas Walter Krause and Dr. Diane Wowk, for their wisdom and guidance throughout the course of this academic endeavor. Their perpetual support made light of the unprecedented academic adversities encountered within the COVID-19 global pandemic. Additionally, I wish to thank Mr. Steve Savage (QETE) for contributing his expertise and deep understanding on ultrasonic testing. Mr. Savage's professionalism, enthusiasm, and energy for the Non-Destructive Testing field is simply empowering.

I am indebted to Mr. Tanner Rellinger (RMC) for imparting his research and extensive knowledge of Flash Thermography onto me. My research would not have been possible without Mr. Rellinger's contribution. In addition, I would like to thank Mr. Brendan Freeman, Mr. Charles Sadiq and Mr. Cory Sharpe (RMC Mech/Aero Dept) for their manufacturing support and technical expertise. Furthermore, I wish to express my appreciation to Dr. Ross Underhill (RMC) for his technical support in the Non-Destructive Testing laboratory. I would also like to thank Ambrell Corporation and Marc Genest (NRC) for allowing me access to their specialized laboratory equipment. Moreover, I am grateful for the Non-Destructive Testing group at RMC for their academic support and encouragement; special thanks to Ms. Laura Burchell (Queen's) for her friendship outside of working hours.

I am forever grateful to the Government of Canada and the Canadian Armed Forces for the opportunity to honourably serve my country and my family. In the same breath, I would like to thank our First Responders, Medical Professionals, Canadian Armed Forces personnel, Department of National Defence personnel, and all others charged with the responsibility of safeguarding for our country and countrymen during the COVID-19 pandemic. Their sacrifices have truly made them a rarer gift than gold.

Most importantly, my wife Katherine, whom without life would be impossible. I wish to thank Katherine for her limitless love and support. There are no pleasantries or words of praise to express my gratitude to Katherine. To Katherine, let the words of Elizabeth Barrett Browning direct my thoughts - *I love thee with the breath, smiles, tears, of all my life; and, if God choose, I shall but love thee better after death*. Katherine, along with close friends and family, sustained my motivation and determination throughout this academic venture.

TABLE OF CONTENTS

LIST OF APPENDICES

LIST OF FIGURES

LIST OF TABLES

LIST OF ABBREVIATIONS, ACRONYMS, AND DEFINITIONS

AGC	Automatic Gain Control
APE	Advanced Plateau Equalization
ARMANDA	Automated Robotic Manipulator Arm for Non-Destructive Assessment
A-Scan	Ultrasonic waveform energy display as a function of time
ATESS	Aerospace and Telecommunications Engineering Support Squadron
B-Scan	2D Cross-sectional view of ultrasonic waveform energy data
CAF	Canadian Armed Forces
CF/E	Carbon Fibre/Epoxy
CFRP	Carbon Fibre Reinforced Polymer
CGSB	Canadian General Standards Board
C-Scan	2D planar view of ultrasonic waveform energy data
DTAES	Directorate of Technical Airworthiness and Engineering Support
ET	Eddy Current Testing
FBH	Flat Bottom Hole
HTCL	Hybrid Titanium Composite Laminate
IML	Inner Mould Line
IWSLJ	Inner Wing Stepped-Lap Joint
MCI	Metal Composite Interface
MT	Magnetic Particle Testing
NDE	Non-Destructive Evaluation
NDI	Non-Destructive Investigation
NDT	Non-Destructive Testing
NRC	National Research Council
OML	Outer Mould Line
PT	Liquid Penetrant Testing
PZT	Lead Zirconate Titanate
QETE	Quality Engineering and Test Establishment
RT	Radiography Testing
RAAF	Royal Australian Air Force
RCAF	Royal Canadian Air Force
RMC	Royal Military College of Canada
TT	Tap Testing
Ti	Titanium
USN	United States Navy
UT	Ultrasonic Testing
VI	Visual Inspection

LIST OF SYMBOLS

e	Thermal Effusivity
f	Frequency in Hertz
i	Instantaneous change in current
m	Mass
n	Normal Vector
q	Heat Flux by Conduction
t	Time
v	Voltage of Self Inductance
z	Depth of Discontinuity
z	Impedance
$\boldsymbol{A}$	Arbitrary Vector
$\boldsymbol{B}$	Magnetic Field
C	Contrast
$\boldsymbol{E}$	Electric Field Strength
H	Henry
$\boldsymbol{H}$	Magnetic Field Intensity
I	Current
$\boldsymbol{J}$	Current Density
L	Self Inductance of the Element
M	Mutual Induction
N	Number of Turns
Q	Heat Transfer Rate
Q	Pulse Heat
R	Electrical Resistance
T	Temperature
α	Thermal Diffusivity
δ	Skin Effect or Skin Depth
ϵ_o	Permittivity of Free Space
κ	Thermal Conductivity
λ	Magnetic Flux Linkage
μ	Isotropic Permeability
μ_o	Permeability of Free Space
ρ	Density (Mass Per Unit Volume) or Charge Density
σ	Electrical Conductivity
σ_{SB}	Stefan Boltzmann Constant
Φ	Magnetic Flux
ω	Angular Frequency of the Current
∇	Del operator
∂	Partial Differential
Cp	Specific Heat Capacity
I_{peak}	Sinusoidal Peak Amplitude of the Current
$\tilde{\boldsymbol{J}}_s$	Surface Current Density
$\tilde{\boldsymbol{J}}_x$	Current Density in x direction
q_r	Heat Flux by Radiation
q_v	Rate of Energy Generation per Unit Volume
$\mathbf{u}_{trans}$	Velocity Vector of Translational Motion
V_C	Capacitive Voltage
V_L	Inductive Voltage
V_p	Peak Voltage
V_R	Resistive Voltage
X_C	Capacitive Reactance
X_L	Inductive Reactance

CHAPTER 1 – INTRODUCTION

1.1 General Introduction

Non-Destructive Evaluation (NDE) is an all-encompassing field of study with the objective of quantitatively characterizing the properties of materials through the technological advancement of non-invasive measurement and analytical methods [1]. NDE encompasses the interchangeable terms of Non-Destructive Inspection (NDI) and Non-Destructive Testing (NDT), which is the practice of NDE. NDT is the preferred term by the Canadian Armed Forces (CAF) and is predominant in this thesis [2]. Note that NDT refers to the five certified techniques mentioned below and does not presently consider thermography. The primary advantage of NDE over destructive testing is the ability to evaluate a test piece without permanently altering the structure or structural properties – saving both time and money. However, a distinct disadvantage of NDE is the inability to test the limitations of materials (i.e. assessing how and when a material will fail).

For an excess of fifty years, the CAF have used NDE techniques to support the health monitoring and maintenance of their air, land, and marine weapon systems (i.e. fighter jets, artillery guns, and warships). Traditionally, NDT technicians are certified in the five primary inspection techniques: Liquid Penetrant Testing (PT); Magnetic Particle Testing (MT); Eddy Current Testing (ET); Ultrasonic Testing (UT); and Radiographic Testing (RT)[1]. However, the CAF has access to advanced techniques through their facilities at the Quality Engineering and Test Establishment (QETE). These advanced techniques include computed radiography, thermography, optics, and enhanced ultrasonics (through-transmission and phased array). Additionally, the CAF also relies on the National Research Council Canada (NRC) and the Royal Military College of Canada (RMC) for the development and implementation of innovative NDE practices. This thesis will focus on thermographic and ultrasonic NDE methods.

Technological advancements in Infrared (IR) thermography and IR camera capabilities have rendered the method as reliable, fast, efficient, and cost effective, significantly so, with complex high-performance advanced materials [3]. Thermography has a reputation of being a qualitative assessment tool due to a lack of specific information that may be acquired such as a specific defect location and dimensions of the damaged area. However, technological

[1] These techniques will be discussed further in Section 2.5 of the literature review and Appendix A.

advancements and research have allowed thermography to fully characterize defects (describing the distinctive dimensions or features of the defects). Hence, these advancements have demonstrated their effectiveness in fully quantifying defects. Given advancements in IR thermography, the Canadian General Standards Board (CGSB) is establishing the method for Canada through standards and requirements for certification. With the industrial focus on cost savings, quality, and mass production, IR thermography is capable of being automated, affecting a greater inspection area in minimal time, and producing high quality defect characterization or dimensioning [3] [4]. Additionally, induction thermography can be applied to ferrous and non-ferrous material, detect sub-surface hidden defects, reliably discriminate between true and false defects, and remains relatively less expensive than ultrasonic and radiographic testing.

1.2 Motivation

The motivation for this research thesis was derived from a Directorate of Technical Airworthiness and Engineering Support (DTAES) project to develop an IR thermography non-destructive testing (NDT) method for the CF-188 Inner Wing Stepped-Lap Joint (IWSLJ) as shown in Figures 1 and 2. It was also an opportunity to explore and evaluate infrared thermography as a potential inspection method. The intent is to rapidly inspect the CF-188 IWSLJ for all potential disbond areas between the Carbon Fibre Reinforced Polymer (CFRP) wing skin and titanium interface or Outer Mould Line (OML) as shown in Figure 3. Note that the IWSLJ is a composite structure consisting of Ti-6Al-4V and CFRP (bonded together) that is commonly referred to as Carbon Fibre/Epoxy – Titanium (CF/E-Ti). Additionally, the IWSLJ design was selected for the relatively even adhesive shear stress distribution properties it provides [5]. Research over the last two decades by the Royal Canadian Air Force (RCAF), the Royal Australian Air Force (RAAF), and the United States Navy (USN) has highlighted the IWSLJ's vulnerability to disbond areas. The IWSLJ, being the primary structural member transferring loads between the wing and fuselage, disbond areas have the potential to lead to a wing-fuselage separation. Although there has never been an occurrence of a wing-fuselage separation, this problem is still of significant concern because of the vast number of F/A-18s in service worldwide and the discovery of significant disbond areas in several operational F/A-18s.

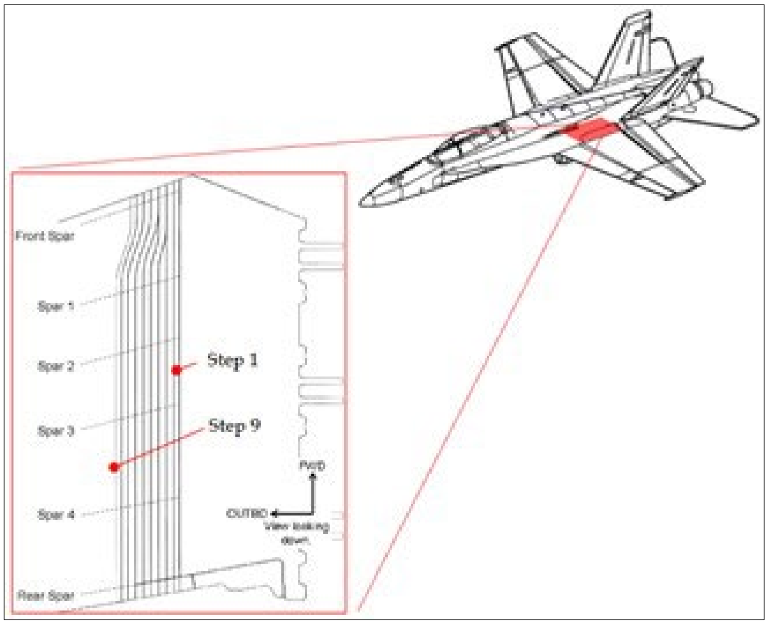

Figure 1: A diagram of the CF-188 IWSLJ with the nine cascading steps of the IWSLJ adapted from [5][6].

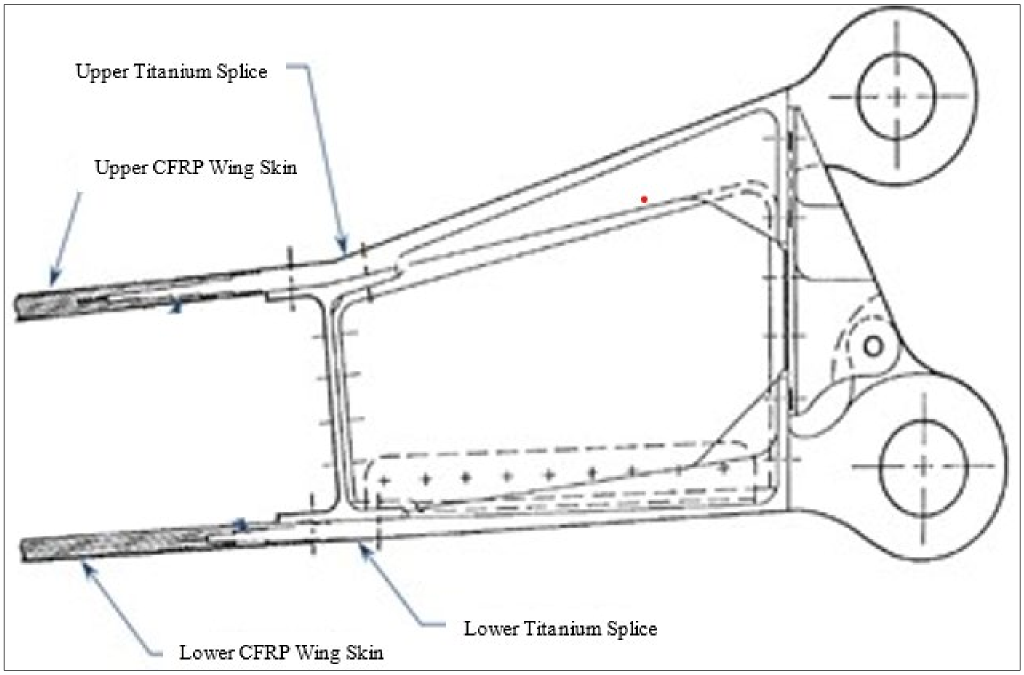

Figure 2: The Upper and Lower IWSLJ cross-sectional view adapted from [5][6].

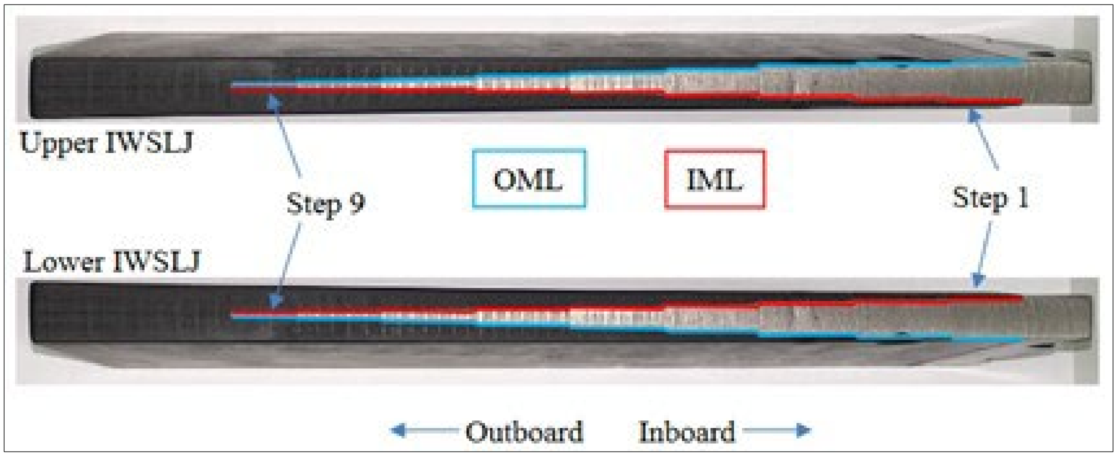

Figure 3: Upper and Lower IWSLJ cross-sectional view with the locations of the Outer and Inner Mould Line (OML/IML) [6].

1.3 Statement of Deficiency – Defining the Problem

The CFRP and Ti-6Al-4V based IWSLJ are vulnerable at the Metal Composite Interface (MCI). This vulnerability can be linked to prolonged exposure to high temperatures, moisture ingress, and fatigue. Depending on the failure initiation mechanism, the adhesive may experience internal failure, or the adhesive and surrounding material may experience an adherent failure. The MCI or Outer and Inner Mould Line (OML/IML) is the interface of the metal and composite, and disbond areas are generated as the primary failure mode[2]. The CF-188 IWSLJ RCAF NDE technique developed by QETE is the latest IWSLJ inspection method and has proven to be highly successful in detecting disbond areas [6]. However, infrared thermography may be the ideal method for this situation because it is traditionally successful in locating disbond areas and it is a relatively fast inspection method. Nevertheless, it is critical to understand the failure criterion leading to disbond areas in order to properly apply an adequate NDE inspection method.

[2] Other potential defects are discussed in the background section.

1.4 Objective

The objective of this thesis is to compare and evaluate the capabilities of pulsed (flash) and induction thermography for detecting disbond area defects in Ti-6Al-4V and CFRP bonded joints through an experimental investigation on the subject NDT methods. Specifically, the following will be accomplished:

- In order to help define experimental test parameters for induction heating in Study 1, finite element analysis using the *COMSOL Multiphysics®* software will be used to observe trends in induction heating through an established temperature distribution prediction method. Experimental results will be used to validate the model;
- Study 1 – A parametric study will be performed to determine the optimal parameters for induction heating of a Ti-6Al-4V and CFRP bonded joint. Namely, the following parameters will be examined: frequency; number of turns of a coil (N-turns); uniform heating; current; separation distance from the surface of the specimen to the bottom plane of the coil (lift-off); heating time; and scanning speed;
- Study 2 – A detection and dimension study will be conducted to locate disbond areas within the Ti-6Al-4V and CFRP specimens with flash and induction thermography. Explicitly, the x and y planar dimension of the disbond areas will be determined. Note that the reference plane is from the top view perspective and parallel to the specimen (the x direction being left to right and the y direction being up and down);
- Study 3 – A penetration depth study will be performed to identify the penetration limit of flash and induction thermography with respect to the IWSLJ. Penetration limit is the maximum depth at which the Ti-6Al-4V is still visible on a thermographic image through the CFRP;
- Study 4 – A detection sensitivity study will be conducted to assess the level of discriminating detail obtained through each inspection method. Varying artificial disbond defects will be embedded within a specimen and each method will be used to obtain details on the defects; and
- All infrared thermography results will be compared against the results of ultrasonic testing (UT) with a TecScan© Automated Robotic Manipulator Arm for Non-Destructive Assessment (ARMANDA) system.

1.4 Statement of Originality

Note that the use of induction thermography as a potential inspection method for the IWSLJ and the in-depth comparison with all inspection methods within this thesis are novel. The literature review in Chapter 2 focuses on the research and published journal papers with regards to thermography. During the research project for the literature review, there were no examples of an in-depth comparison of pulse (flash) thermography, induction thermography, and ultrasonic testing.

CHAPTER 2 – LITERATURE REVIEW

2.1 Literature Review

Published literature was reviewed to explore existing work on the properties of CF/E-Ti bonded joints and IR thermography versus other NDT techniques. The literature review is composed of an overview including thermography history, infrared technology and thermography types, infrared thermography applications, and other potential NDT techniques for the IWSLJ. The following literature review highlights applicable information and forms a basis of understanding of the research enclosed in this thesis.

2.2 Thermography History and Infrared Technology

Infrared technology began with the observation of the infrared radiation spectrum by William Hershel (1738-1822) in the 1800s [7]. Herschel separated light with the use of a prism and used a thermometer to measure the temperature of the light. In his experiment, he noted that the maximum temperature elevation occurred beyond the visible spectrum. Furthermore, Herschel's finding is the sum of three distinct ideas: Herschel grappled with the similarity between *heat* and *light*. He referred to his discovery, the infrared radiation spectrum, as "invisible rays" that carry heat. *Heat* (infrared radiation) and *light* (visible radiation) are now recognized as belonging to the electromagnetic radiation spectrum at their respective wavelength and frequency; Herschel's experiment proved that quantitative measurement of the infrared radiation spectrum is possible; and Herschel also demonstrated that "invisible rays" (infrared radiation) behave the same as visible rays with respect to transmission and reflection. Additionally, the "invisible rays" transmission is affected by material properties (same as light).

After Herschel, there were other significant development in infrared technologies. In 1829, Leopold Nobili (1784-1835), created the first thermocouple [7]. In 1833, Macedonia Melloni (1798-1854), invented the first thermopile. In 1840, John Herschel (1792-1871), used an evaporograph to generate the first infrared image [7]. In 1880, Samuel Pierpont Langley (1834-1906), was able to sense the heat of a cow from 400 m away with a bolometer he created [7]. In the 1940s, Robert McMaster and colleagues fostered a significant increase in infrared and thermal methods of non-destructive testing. Their research covered bar testing, measuring strain in opaque glass, weld testing, sheet testing, pipe thickness testing, and radiant heat detection. World War II ushered in heightened progress in infrared technologies – namely in the detection of adversary soldiers, machinery, ships and icebergs [7]. After World War II, infrared technology and non-destructive testing flourished for both military and commercial applications [7].

2.3 Infrared Thermography

Infrared thermography (IRT or IR Thermography) is a non-contact, non-destructive evaluation method derived from the use of temperature differences and infrared technology. IRT is a rapidly advancing method due to technological progression in detector sensitivity, spatial resolution, and computational power. The most significant advantage IRT has over other methods is the rapid contactless inspection over a large area and the ease of processing optical data. IRT can be classified into two groups – Passive and Active thermography as shown in Figure 4. The Passive IRT approach exploits the inherent infrared radiation of an object, which differs from the ambient or natural background temperature or radiation; there is no external/internal source of excitation to the object's thermal gradient. The Active IRT approach uses external or internal thermal excitation to create a material temperature gradient within the material structure. Table 1 highlights the application of passive and active thermography for process control, discontinuity detection and material characterization. It also defines terms shown in Figure 4.

Table 1: Application of Infrared Thermographic Techniques adapted from [7].

Technique	**Process Control**	**Discontinuity Detection**	**Material Characterization**
Passive Thermography	Carton sealing line inspection, automobile brake system efficiency, heat dissipation of electronic modules, recycling process identification, printed circuit boards, glass industry (bottles, bulbs), welding process, metal (steel) casting	Walls, moisture evaluation, roofs, assemblies Liquid levels in tanks	Glaze thickness on ceramics, crush test investigations
Lockin Thermography (active)	Aircraft structural component inspection, loose bolts detection Plastic pipe inspection Radar absorbing structure investigation	Crack identification, disbonding, impact damage in carbon fiber reinforced plastics	Adhesion strength, anisotropic material characterization, coating thickness in ceramics, moisture evaluation Depth profile of thermal conductivity or diffusivity
Pulsed Thermography (active)	Aircraft structural component inspection, solder quality for electronic components, spot welding inspection Water entrapment in buildings and fresco delamination	Metal corrosion, crack detection, disbonding, impact damages in carbon fiber reinforced plastics, turbine blades, subsurface defect characterization (depth, size, properties) in composites, wood, metal, plastics	Thermophysical properties (diffusivity etc.), underalloyed and over alloyed phases in coatings on steel, moisture, anisotropic material characterization
Step Heating Thermography (active)	Degradation of erasable programmable read-only memory chips Thesis structure (cockling)	Defects in adhesive and spot-welded lap joint	Thermal conductivity measurement in carbon fiber reinforced plastics Coating thickness measurements
Vibrothermography (active)	Failure analysis	Coating wear, fatigue test, closed crack detection	Variations in viscoelasticity and emissivity
Induction Thermography (active)	Conductive (metallic) aircraft structure component inspection and welding inspection Water entrapment in honeycomb structures	Metal corrosion, surface and near surface cracks, disbond areas in conductive materials (turbine blades and wheel hubs), and impact damage in carbon fiber reinforced plastics.	Surface and subsurface defect characterization (depth, size, properties) in conductive metals and composites. Moisture evaluation. Depth profile of thermal conductivity or diffusivity

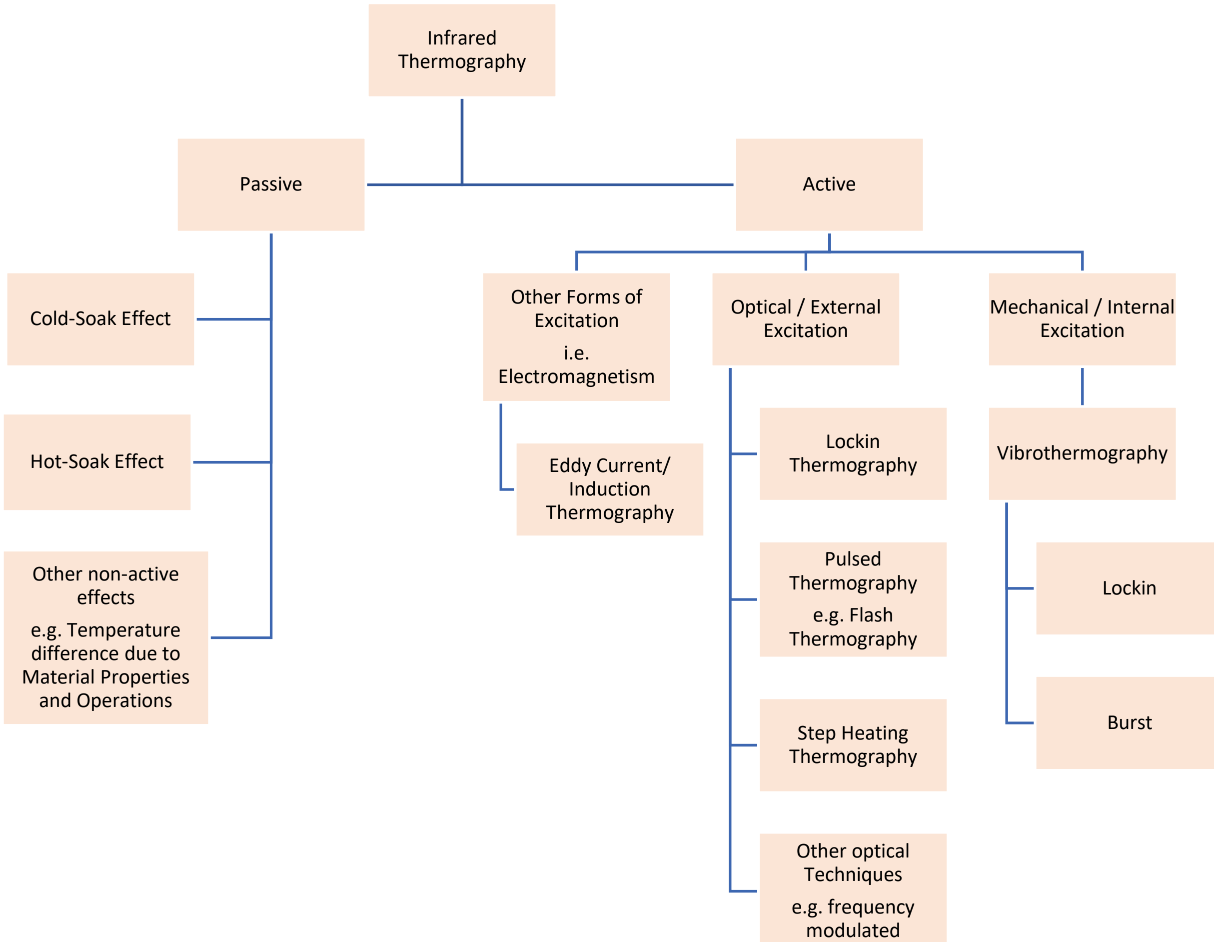

Figure 4: A classification hierarchy of infrared thermography methods in NDT adapted from [7].

In aviation, passive IRT can include the natural cold and hot-soak effects from aircraft operating within temperature extremes. An aircraft is considered to be "cold-soaked" when the aircraft internal structure or fluids (fuel, moisture, etc.) are significantly colder than the external ambient temperature. This effect commonly occurs as an aircraft transits from a very cold high altitude to a warmer airdrome elevation upon landing. Likewise, the effect can also occur if relatively cold fuel is used to refuel the aircraft. Typically, moisture trapped within the aircraft structure turns to ice and has a colder temperature gradient than the encapsulating structure. Hence, Passive IRT can be used to detect water ingress in the aircraft structure. Additionally, it can be used to detect aircraft fluid leaks. *Edwards* [2] reported that the CAF was able to successfully use passive thermography to detect water in the vertical stabilizer rudder of the CF-188. Hot-soak effects adopt the opposite notion to cold-soak effects. Additionally, passive thermography can be used to monitor aircraft operation in real-time. For example, abnormal hot spots detected during engine operation can be an indication of insufficient cooling or lubrication or a breach of the thermally insulating structure, which are premises for additional investigation.

Active IRT can be further classified into three sub-groups: optical/external excitation; mechanical/internal excitation; and other forms of excitation (i.e. electromagnetism). In Figure 28, the sub-groups branch out to methods such as Lockin, Pulsed, Step Heating, Induction, and vibrothermography. Pulsed and Induction IR thermography will be discussed in the next sections. However, the following is an explanation for the other forms of excitation:

Lockin Thermography or photothermic radiometry is predicated on the periodic (sinusoidal) application of input energy wave or signal (i.e. thermal lamp, hot air jet, cold air jet, thermal emitter, ultrasound, microwave, eddy current) on the surface of the specimen and examining the subsequent temperature differential on the surface of the specimen [7]. Specifically, the input energy signal undergoes a phase shift as it propagates through the specimen and partially reflects as it interacts with a discontinuity. The reflections then meet another input signal at the surface, which creates a thermal interference pattern with a distinct temperature variation from the unaffected or homogeneous surroundings on the surface of the specimen [7].

Step Heating Thermography is similar in methodology to pulsed thermography (defined in Chapter 4). Step heating thermography differs from pulsed thermography in that step heating has a longer pulse of heat emitted from a lamp or another thermal excitation device such as hot air jets. *Kaminska et al.* [8] considered 10, 12, and 16 seconds as a long pulse time. In this thesis, a relatively lower energy density than pulsed thermography is used; however, an increased in surface temperature can be expected with the longer pulse. A discontinuity within a specimen would cause a concentration of thermal energy at the boundaries and resulting energy intensity would translate to a higher temperature profile. Step heating thermography has many applications including evaluating multilayer coating thickness, assessing multilayered composite structures, and evaluating coating-to-substrate bond [7].

Vibrothermography uses external mechanical vibrations (20 to 50 Hz) to generate thermal energy through friction between the discontinuity and the surrounding material [7]. This technique allows for the precise detection of discontinuities, such as closed cracks and delamination. Vibrothermography is also used in fatigue testing and to detect coating wear.

Passive and active thermographic techniques have their respective advantages and disadvantages based on their application and the discontinuity of interest. For example, passive thermography is a quick and effective technique for water ingress in comparison to vibrothermography, which is best suited for closed cracks. Note that vibrothermography may be worth exploring for the detection of kissing bonds as a kissing bond is similar to a closed crack. Table 2 summarizes the advantages and disadvantages of infrared thermographic techniques.

Table 2: Advantages and Limitation of Infrared Thermographic Techniques adapted from [7].

Technique	**Advantages**	**Disadvantages**
All Thermographic Techniques	Fast surface inspection Ease of deployment Deployment on one side only Safety (no harmful radiation) Ease of numerical thermal modeling Ease of interpretation of thermograms Great versatility of applications A unique tool (i.e. finding corrosion around rivets)	Variable emissivity Cooling losses (convection/radiation causing perturbing contrasts) Absorption of infrared signals by the atmosphere (especially for distances greater than a few meters [about 10 feet]) Difficulty to get uniform heating (active procedures) Transitory nature of thermal contrasts requiring fast recording infrared cameras Need of straight viewing corridor between infrared camera and target (although it could be folded through first surface mirrors) Limited contrasts and limited signal-to-noise ratio causing false alarms – measurement of a few degrees above background at around 300 K (27°C = ~80°F) Observable defects are generally shallow (near surface only)
Passive Thermography	No interaction with specimen No physical contact	Works only if thermal contrast is naturally present
Lockin Thermography (active)	No physical contact Large inspected surface – several m^2 simultaneously Phase and modulation images available Modulated ultrasonic heating (for some applications, might require physical contact or bath immersion)	Requires modulated thermal perturbation Requires observation for at least one modulation cycle (longer observation with respect to pulsed thermography) Thickness of inspected layer under the surface related to the modulation frequency (unknown defect depth might require multiple investigations at different frequencies)
Pulsed Thermography (active)	No physical contact Quick (pulsed thermal stimulation: cooling or heating) Phase and modulation images available with frequency processing (as in pulsed phase thermography)	Requires apparatus to induce the pulsed thermal perturbation Computation of thermal contrasts requires a prior knowledge of defect free zone in field of view Inspection surface limited (~0.25 m^2 maximum)
Step Heating Thermography (active)	- No physical contact	- Requires apparatus to induce the thermal perturbation - Risk of overheating the specimen
Vibrothermography (active)	- Reveal close cracks	- Difficulty to generate mechanical loading - Thermal patterns appear only at specific frequencies - Physical contact required to induce thermal stimulation
Induction Thermography (active)	- No physical contact - Covers a large surface area - Effective with a wide range of material and geometries - Efficient Heating	- Difficulties with uniform heating - Difficulty in discriminating between multiple defects - Material surface finish may cause unwanted reflections - Precise dimensioning of defects is challenging

Whether passive or active IRT, the infrared radiation signature (thermal pattern) of the material is imaged by an infrared camera. Specifically, the infrared camera senses the object's radiation and converts it into an electronic signal that can be recorded. Afterwards, the signal data is processed, and then analyzed to study internal discontinuities (defects) and material characteristics. IRT experimentation can be conducted in two different ways – transmission or reflection as shown in Figure 5. In transmission, the thermal excitation source and the infrared camera are located on opposite sides of the test sample being investigated. Contrariwise, in reflection, the thermal excitation source and the infrared camera are located on the same side of the test sample being investigated. This thesis focuses on IR thermography, specifically pulsed (flash) and induction IR thermography. Furthermore, only the reflection method of IRT experimentation was used. Additionally, pulsed and induction IR thermography were specifically explored, because they are both ideal for detecting disbond areas and delamination in fibre metal bonded structures.

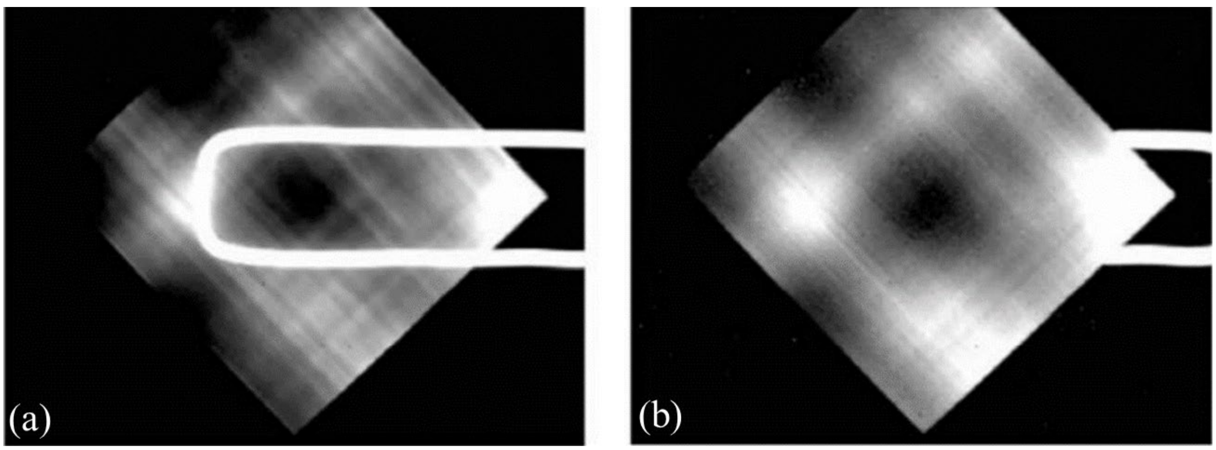

Figure 5: (a) Reflection Mode and (b) Transmission Mode [9].

2.4 Research Accomplished with Induction Thermography

Induction thermography has been used extensively over a wide range of conductive materials with many different model simulations. *Netzelmann et al.* [4] identifies induction thermography as being applicable to a wide range of materials that exhibit at least some electrical conductivity. Namely, those materials are ferromagnetic metals (nickel and iron), non-magnetic metals (silver, zinc, aluminum and copper), metallic alloys with low conductivity (stainless steel, Inconel and titanium), and composites (CFRP, Ceramics, etc.). Its ability to detect both surface cracks and hidden cracks close to the surface is incredibly attractive, in particular for inspection of ferritic steel. *Netzelmann et al.* [4] research is beneficial because it compares induction thermography to magnetic particle testing and with a wide range of materials. *Netzelmann et al.* [4] findings agreed with *Genest et al.* [10] [11] in that thermography is great for open and closed cracks in metals and is effective over a wide range of conductive material.

Specifically, for CFRP, *Yarlagadda et al.* [12] examines three possible heating mechanisms: Fibre (joule losses) and fibre cross over junctions (dielectric hysteresis and contact resistance). The three heating mechanisms are represented as an electrical circuit and correlate well with models in the literature. It is important to note that the excitation current flows along the fibres and in the fibre direction. Hence, the results of induction heating will vary based on the lay-up pattern. Junction heating effects dominate compared with fibre heating, except for small values of resistance not generally observed in carbon fibre systems. Conductive fibre architecture (with the ability to transfer electrical and thermal energy) is critical to determine the dominant heating mechanism. Temperature and fibre architecture may reduce contact resistance and force the dominant mechanism to be fibre heating. The research of *Yarlagadda et al.* [12] is beneficial to my thesis because it captures the theory of CFRP heating mechanisms. Similarly, *Bayerl et al.* [13] summarizes the principal of induction heating with respect to polymer composite processing. This paper identifies eddy currents and magnetic (dielectric) hysteresis as induction heating mechanisms. Additionally, this thesis identifies properties and effects of heating with regards to general susceptor influences. It states that induction heating efficiency is affected by the following parameters: coil geometry; magnetic flux concentrators; coupling distance; frequency; and inductor current [13]. Furthermore, the undesirable effects occurring during magnetic induction heating are identified as skin effect, proximity effect, ring effect, and edge effects. This paper is beneficial because it covers the general application of induction thermography. Furthermore, there is a comparison in 3D induction heating simulators and advanced materials are identified as a future development prospect.

Many different analytical and numerical simulations were developed over the years for induction heating. *Vrana et al.* [14] presents an analytical model for the calculation of current density including backflow current (from back electromotive force) along with finite element calculations. *Vrana's* [14] research thesis and models allow for general understanding of current flow and defect detection from an analytical perspective. *Abidin et al.* [3] used three dimensional numerical simulations to support their experimental investigation. *Abidin et al.* [3] explores the advantages and applications of eddy current thermography testing for comprehensive and reliable defect assessment. Other published articles support the complex reality of induction heating and the need for robust numerical simulations in the future [15] [16].

Throughout this review, it is clear that induction thermography has a very narrow capability; it is ideal for surface and subsurface defects (cracks, delaminations, disbonds, etc.) of conductive materials. Induction thermography is best for open and closed cracks in metals (i.e. rail tracks and wheels, forged parts, aircraft engine parts, etc.), and disbond and delaminated areas in composite material (all defects at relatively shallow depths). Additionally, there are no examples of an in-depth comparison of pulse (flash) thermography, induction thermography, and ultrasonic testing supported by numerical simulations. Lastly, induction thermography is still advancing and needs to be more quantitative to be an accepted as a technique world wide.

2.5 Potential NDT Inspection Method for IWSLJ

As mentioned in the introduction, CAF NDT technicians primarily use Liquid Penetrant Testing (PT), Magnetic Particle Testing (MT), Eddy Current Testing (ET), Ultrasonic Testing (UT), and Radiographic Testing (RT). However, there are many methods used to inspect fibre metal bonded joints for disbond areas – namely Thermography, Ultrasonic Testing (UT), Radiography Testing (RT), Eddy Current Testing (ET), Visual Inspection (VI), Tap Testing (TT), etc. For the purpose of this thesis, only thermography and ultrasonics are discussed in detail, because these methods are the most effective means for examining disbond areas. Explanations and arguments against the use of other NDE methods can be found in Appendix A.

CHAPTER 3 – BACKGROUND

The background is an overview of the properties of the IWSLJ. It is composed of titanium properties, CFRP properties, the manufacturing process, and failure mechanisms for the IWSLJ. The following background highlights information required to best understand the research enclosed in this thesis. Note that the word "titanium" used throughout this thesis refers to Ti-6Al-4V or Grade 5 titanium when not otherwise explicitly indicated.

3.1 IWSLJ as a Bonded Joint

The CF-188 Hornet or CF-18, Canada's sole multi-role fighter jet, first entered service at 410 (Operational Training Unit) Squadron in Canadian Forces Base Cold Lake on 25 October 1982 [17]. The CF-188 was derived from the F/A-18 Hornet and manufactured by McDonnell Douglas (now a Boeing acquisition) and Northrop (now a Northrop Grumman acquisition) [17]. The CF-188 Hornet was designed to reduce maintenance and be technologically advanced with exceptional aerodynamic performance [17]. In order to achieve an enhanced aerodynamic performance, the CF-18 was made to be lighter than other dated fighters (F-14 Tomcat and A-6 Intruder) through the use of structures such as composite honeycomb sandwich panels and Carbon Fibre/Epoxy – Titanium (CF/E-Ti) bonded joints. Approximately 10% of the F/A-18 models A - D (Hornets) structural weight is composite. Similarly, 19% of the F/A-18 models E - F (Super Hornets) structural weight is composite [18]. Furthermore, composites can be used in isolation as a laminate sheet or part of a composite structure such as a bonded joint or honeycomb sandwich panel.

The wing skin is constructed from AS4/3501-6350 cure carbon/epoxy composite. The top and bottom wing skins are bonded to a titanium (Ti-6Al-4V) splice fitting (a double-stepped-lap joint) with FM-300 adhesive. This bonded structure or joint is attached to the center fuselage bulkheads using three sets of lugs on the inboard end of the bonded structure. The double-overlap configuration of the joint has the ability to carry significant compressive loads in comparison to the single-overlap configuration [18]. These double-stepped-lap bonded joints are designed to withstand substantial loads and complex stress distributions [18]. Furthermore, FM-300 film adhesive can endure significant shear strains. Overall, the IWSLJ is instrumental in evenly distributing the high shear stress and accommodating the low interlaminar shear strength of composites [18]. The FM-300 adhesive is also exceptional for moisture and fatigue resistance with no significant reduction in mechanical properties [18].

Across the aviation, marine, and automotive industry, Ti-6Al-4V and CFRP structural components are gaining more attention in comparison to traditional structural materials due to their complimentary mechanical properties. For instance, Boeing and Airbus heavily use Ti-6Al-4V and CFRP structures in their latest generation of airplanes (Airbus XWB 350 and Boeing 787 Dreamliner) [19]. CFRP and Ti-6Al-4V combined, offers enhanced strength and durability to aircraft components [19].

3.2 Properties of Titanium and Carbon Fibre Reinforced Polymer

Ti-6Al-4V is the most widely used titanium alloy in the alpha + beta ($\alpha + \beta$) class, where the $\alpha + \beta$ class is a titanium alloy with aluminium and vanadium β phase stabilizers as alloying materials [21]. Ti-6Al-4V is a versatile material offering a high strength-to-weight ratio, high fatigue resistance, good biocompatibility and osseoconductivity [21]. Similarly, CFRP has a superior strength-to-weight ratio, good fatigue & corrosion resistance, and high stiffness in comparison to traditional aerospace materials such as aluminum or steel. Furthermore, titanium is a great candidate for CFRP because (unlike aluminum) titanium does not galvanically corrode when in contact with CFRP and has a low coefficient of thermal expansion [18]. Lastly, titanium is significantly lighter than steel for the same value of strength. These mechanical properties foster increased performance, durability and long fatigue life in comparison to other bonded structures and materials. This section investigates the physical, chemical, and mechanical properties of Ti-6Al-4V and CFRP laminate, as well as applications in industry.

3.2.1 Titanium – Physical and Chemical Properties

Pure titanium and titanium alloys are silver in colour, low density, high strength, and bonds well with other materials. Additionally, they are highly corrosion resistant over a range of temperatures. Titanium and its alloys are responsible for the rapid advancement of aircraft structures. Commercial titanium (unalloyed or pure) is soft and ductile with a hexagonal crystal structure as shown in Figure 6.

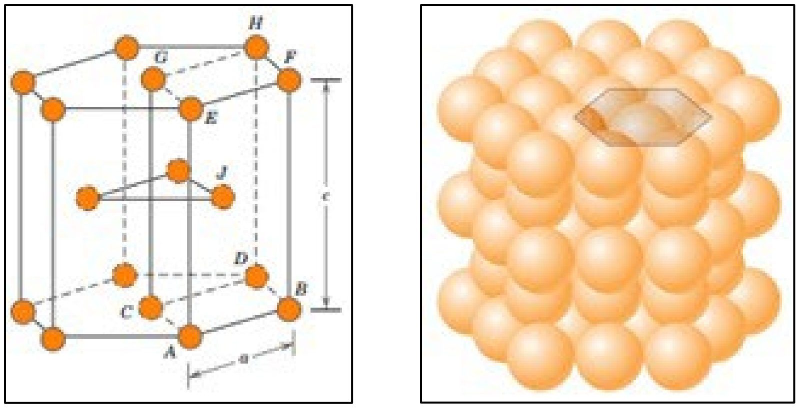

Figure 6: Hexagonal Crystal Structure of Titanium [22].

Pure titanium is typically alloyed with aluminium, iron, niobium, molybdenum, tin, vanadium and other elements to form alloys. Typical applications of pure titanium includes jet engine shrouds, airframe skins, and corrosion-resistant marine equipment [22]. Pure titanium and the corresponding alloying elements have the atomic characteristics detailed in Table 3. These alloying elements heavily influence the transition temperature (883˚C) of the titanium as the (α phase) hexagonal close-packed crystal transitions to a body-centered cubic (or β phase) [22]. Furthermore, the alloys influence electromagnetic and thermal properties such as conductivity.

Table 3: Chemical properties of titanium and common alloying elements [23].

Element	***Symbol***	***Atomic Number***	***Atomic Weight (amu)***	***Density of Solid, 20˚C***	***Crystal Structure. 20˚C***	***Atomic Radius (nm)***	***Ionic Radius (nm)***	***Most Common Valence***	***Melting Point (˚C)***
Titanium	Ti	22	47.87	4.51	HCP	0.145	0.068	4+	1668
Aluminum	Al	13	26.98	2.71	FCC	0.143	0.053	3+	660.4
Iron	Fe	26	55.85	7.87	BCC	0.124	0.077	2+	1538
Molybdenum	Mo	42	95.94	10.22	BCC	0.136	0.070	4+	2617
Niobium	Nb	41	92.91	8.57	BCC	0.143	0.069	5+	2468
Tin	Sn	50	118.71	7.27	Tetra	0.151	0.071	4+	232
Vanadium	V	23	50.94	6.1	BCC	0.132	0.059	5+	1890

Titanium alloys are classified into four distinct phases: alpha (α), near-alpha, alpha + beta (α + β), and beta (β). These distinctions are important because there is a specific set of mechanical properties and associated microstructure with each class. Figure 7 offers a visual representation of the different phases.

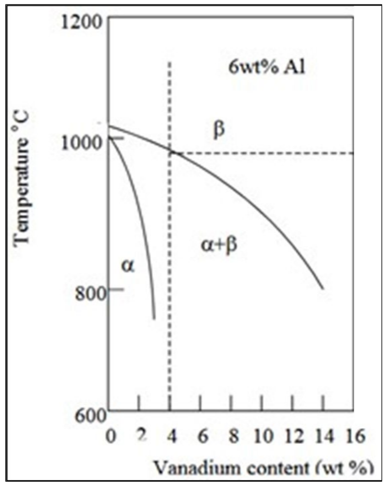

Figure 7: A phase diagram illustrating the microstructures associated with Ti-6Al-4V at varying temperatures [24].

Alpha + beta (α + β) alloys are the most widely used titanium alloys across the aerospace-marine-automotive industry. These alloys are stable in both constituent phases with the influence of the respective alloying elements. Ti-6Al-4V with 6% aluminum and 4% vanadium is the most common alpha + beta alloy. Alpha + beta alloys are poor heat conductors and generally not weldable [25]. However, their ductility allows for excellent forming characteristics. Applications of alpha + beta titanium includes rocket engine case airframes, high-strength prosthetic implants and CF-188 IWSLJ [22]. Applications are limited due to cost and weight in comparison to materials such as aluminium and composites.

3.2.1.1 Titanium – Manufacturing Process

Ti-6Al-4V and other titanium alloys are manufactured through a process called Carbo-Chlorination. Referencing the Britannica encyclopedia [26], titanium ore (TiO_2) reacts with chlorine (Cl) to produce gaseous $TiCl_4$ in liquidized petroleum coke (at 850-1000˚C). The $TiCl_4$ is cleaned of impurities through a series of refining processes [26]. The purified $TiCl_4$ is reduced with either sodium (Na) or magnesium (Mg) via the respective Hunter or Kroll process (at 800-1000˚C) [26]. The titanium (Ti) extracted from the reduction is an extremely porous substance called sponge [26]. The sponge and alloying elements are mechanically pressed into a cylindrical bar and melted for bonding of alloying elements. Finally, the molten titanium alloy solidifies into ingots, and are thereafter, milled or machined for industrial consumption [26]. Of note, grain size is significant to both the mechanical and electromagnetic properties of titanium. Smaller grains result in an increase in grain boundaries and electrical impedance.

3.2.1.2 Titanium – Surface Treatment Options

Prior to lamination, the surface of the Ti-6Al-4V sheet is prepared or treated in order to foster strong bonds with the adhesive and CFRP layers. Furthermore, strong bonding leads to excellent durability and interlaminar fracture toughness (upwards of 1222% with anodization versus untreated titanium) [27]. Interlaminar fracture toughness is a standardized test to evaluate the bond's ability to withstand being pulled apart. Although the exact surface treatment for the CF-18 IWSLJ titanium alloy is unknown, a surface treatment can be accomplished through one or more of the following common processes: liquid honing, chemical etching, sandblasting, anodizing, annealing, and/or the application of adhesive primer [20].

- *Liquid honing*: Liquid honing, or vapour blasting, is an abrasive machining process where a mixture of a liquid (often water) and a compound is used to create a uniform high quality finish texture on the micro surface [28]. This process has the added advantage of removing micro surface defects (burrs, organic material, etc.) and leaving the titanium with a clean polished texture.
- *Chemical etching*: Chemical etching is the process of using acids or bases, often under high pressures and temperatures, to permanently remove fine layer(s) of surface material. The process concludes when the desired surface finish is achieved.
- *Sandblasting*: Sandblasting, grit blasting or abrasive blasting is the process of smoothing and or removing surface contaminants by means of blasting with a high velocity propellant.
- *Anodizing*: Anodizing is an electrolytic process used to create an oxidized layer on the surface of metals – rendering the surface corrosion resistant and ready for bonding. The degree of anodization depends on the anodizing voltage, temperature, and time.
- *Annealing*: Annealing is using heat treatment to remove residual stresses caused by other processes (machining, milling, liquid honing, sandblasting, etc.). Additionally, annealing promotes better bonding by transforming surface titanium oxide (TiO) to titanium dioxide (TiO_2) [20].

- *Adhesive Primer*: Adhesive primer can be applied to the metallic surface prior to adding the adhesive for enhanced bonding, durability, and resistance to harsh environments [29].

Other treatment processes include plasma treatment, micro arc oxidation, and ozone formation. After the Ti-6Al-4V sheet is machined to specifications and receives a surface treatment, it is ready for the adhesive and CFRP layers.

3.2.2 CFRP – Physical and Chemical Properties

Carbon Fibre Reinforced Polymer (CFRP) composite or graphite/epoxy composite consists of continuous carbon fibres and a polymer epoxy resin matrix. They are used extensively in sports and recreational equipment (fishing rods, golf clubs), filament-wound rocket motor cases, pressure vessels, and aircraft structural components—both military and commercial, fixed-wing and helicopters (e.g., as wing, body, stabilizer, and rudder components) [22].

Carbon, including polymorphs of carbon, are recognized for high strength, but there are other desirable properties such as good chemical stability at elevated temperatures and in nonoxidizing atmospheres, high thermal conductivity, low coefficient of thermal expansion and high resistance to thermal shock, high adsorption of gases, and good machinability [22]. The term *carbon fibre* does not refer necessarily to the element carbon; Carbon fibre refers to a hexagonal carbon molecular network of both graphitic and non-crystalline regions that is typical of graphite (as shown in Figure 8) [22].

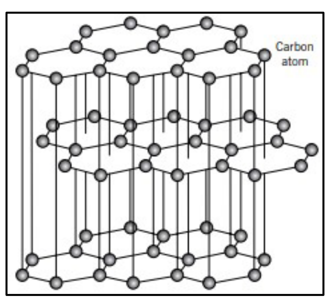

Figure 8: The structural arrangement of graphite.

Furthermore, carbon fibres are grey in colour, align either parallel or perpendicular to each other, and are approximately 4 - 10 micrometers in diameter [22]. Carbon fibres can adopt a variety of physical and mechanical characteristics to achieve a specific engineered property. Namely, high-performance carbon fibres are often in a woven or unidirectional structure (Figure 9).

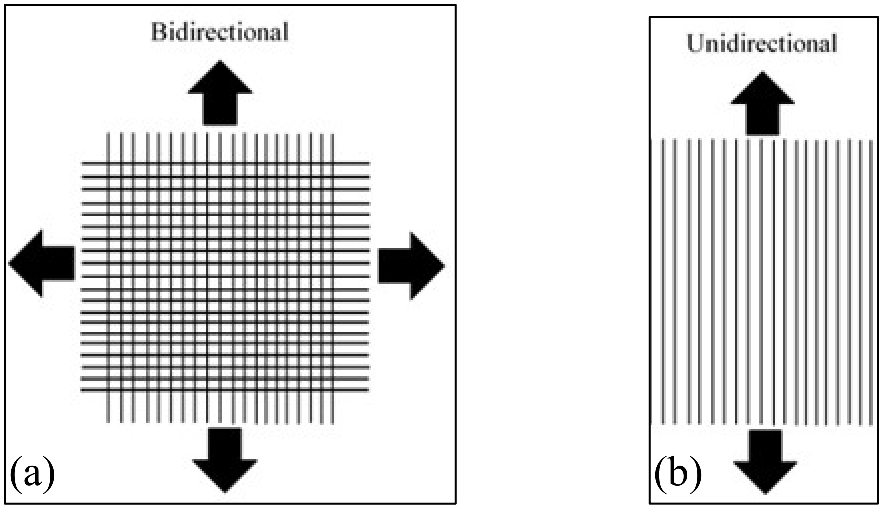

Figure 9: (a) Woven and (b) unidirectional carbon fibre structures.

CFRP has carbon fibres embedded within a polymer resin matrix. The resin matrix is a reinforcing plastic of a high-molecular-weight [22]. Additionally, the matrix bonds the carbon fibres together and acts as a medium for the transfer of loads. Furthermore, the matrix provides a means of protection against the surrounding environment. Finally, the matrix separates individual carbon fibres, which prevents crack propagation from fibre to fibre. For CFRP, epoxy ($C_{21}H_{25}ClO_5$) is the resin matrix; it has improved mechanical properties and moisture resistance compared to esters or vinyl resin [22].

3.2.2.1 CFRP – Manufacturing Process

Prepreg is the principal method for the CFRP used in the manufacturing of the IWSLJ. Prepreg refers to a continuous-fibre reinforcement pre-impregnated with partially cured polymer resin [22]. The consumer simply has to mould the prepreg into a desired application and completely cure the resin. Figure 10 illustrates the prepreg process. Continuous carbon fibres from supplier spools are sandwiched between resin rich release thesis and carrier thesis. The carbon fibres are saturated with resin from the release thesis as the fibre and resin pass through the heated calendaring rollers. The carrier thesis carries the final prepreg product to a cardboard cored spool to be wound and packaged.

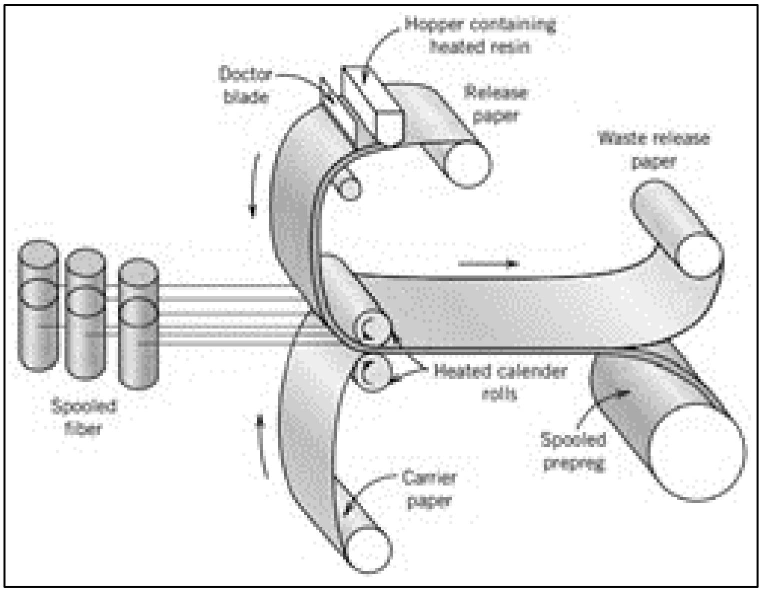

Figure 10: Diagram illustrating the prepreg process adapted from [22].

3.2.2.2 CFRP – Layup Treatment

In Figure 11, the CFRP layup is typically composed of two-dimensional unidirectional sheets stacked in a 0˚/90˚ or a combination of 0˚/±45˚/90˚ orientation [30]. The 0˚/±45˚/90˚ stacking sequence is typical of a "quasi-isotropic" layup where it will behave similarly to an isotropic material [30]. It offers the same stiffness in all in-plane directions and is used extensively in the aerospace industry. The stacking sequence or ply layup is dictated by the required directional strength of a component. The stacking of the sheets is typically symmetrical between the top half of the stack and the bottom half of the stack. This is a typical means of balancing out internal stresses during the curing process. It also ensures that there is no interaction between the extensional and bending stiffness; there is no twisting when the material is in tension. For the purposes of this thesis, the CFRP sheets are stacked in a 0˚/90˚ orientation for the test specimens. The 0˚/±45˚/90˚ stacking sequence is used for the IWSLJ. However, given the structural requirements, a variety of stacking levels and directional combinations are possible.

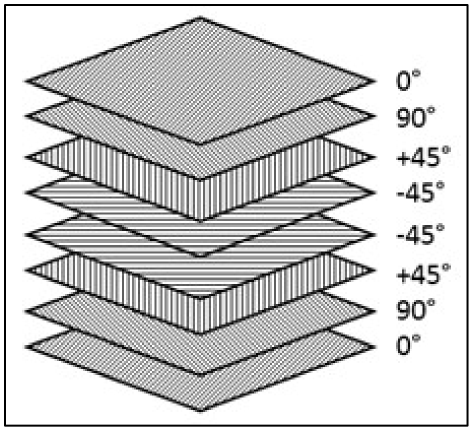

Figure 11: Typical stacking of carbon fibre reinforced polymer sheets. Image used with authorization by originator [30].

3.2.3 Titanium and CFRP Assembly

After the manufacturing process for the titanium alloy and CFRP, the assembly and lamination process can occur as shown in Figure 12. The Ti-6Al-4V and CFRP laminate assembly consists of three main components: a Ti-6Al-4V sheet or desired Ti-6Al-4V structure, CFRP (made of multiple unidirectional plies), and an adhesive at the metal composite interface (MCI). Occasionally, the assembly has a primer as an additional component. For example, the adhesive primer used for the CF-188, a FM 300 variant, has the option of a corrosion inhibiting primer called BR® 127. The plies of unidirectional CFRP are stacked together and cemented to the Ti-6Al-4V plate through the use of the film adhesive. Afterwards, the layup of Ti-6Al-4V, adhesive, and CFRP can be bonded together by the following common bonding process: Autoclave, Vacuum-Bag, or Press. In the case of the CF-188, the exact bonding process is unknown.

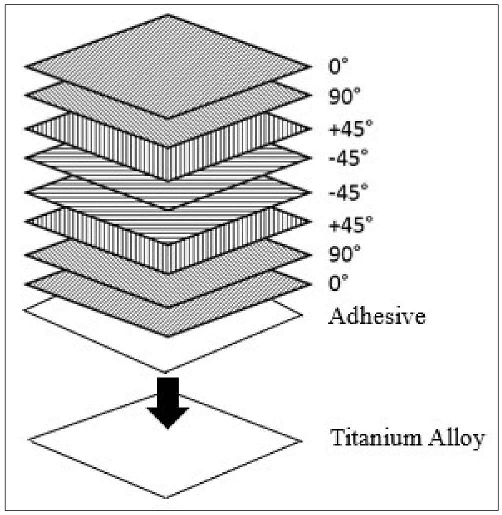

Figure 12: Illustrates a common assembly stack of CFRP, the adhesive film, and the titanium alloy. Image adapted from [31].

3.2.3.1 Bonding Process Options

The autoclave bonding or moulding process is the principal means of bonding CFRP and titanium utilized by leading manufacturers (Boeing, Lockheed, ATK, Northrop, etc.). Autoclave bonding is the use of a pressure vessel and the controlled application of evenly distributed temperature and pressure to both bond and cure laminated structure. This is illustrated in Figure 13. The entire lay-up assembly can be loaded into the autoclave for ease of processing. Therefore, components that require secondary bonding can be co-cured in a single operation. Other bonding processes include vacuum bag bonding, press bonding, Vacuum-Assisted Resin Infusion (VARI) and Vacuum-Assisted Resin Transfer Moulding (VARTM).

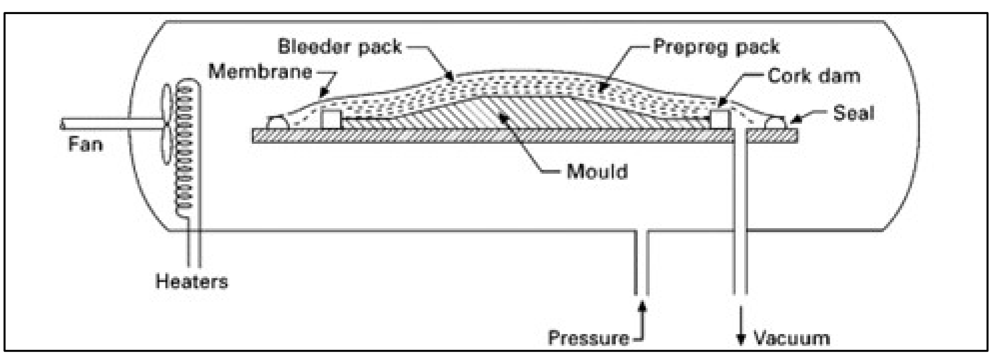

Figure 13: Schematic diagram showing the autoclave bonding process adapted from [32].

3.2.4 Mechanical Properties of the IWSLJ

As indicated in the introduction, CFRP and Ti-6Al-4V bonded structures were specifically engineered for the following mechanical properties: superior strength, high stiffness (Young's modulus/Modulus of Elasticity), low weight, high durability (fatigue life) and damage tolerance. These desired mechanical properties were requirements for fighter planes (USN F/A-18) under high operational speed and temperatures [20]. Table 4 highlights the mechanical property data of Ti-6Al-4V, CFRP, and FM300K adhesive (commonly used for adhering the CFRP to the Ti-6Al-4V on the CF-188). CFRP and Ti-6Al-4V are the ideal selection of materials because they achieve the engineering requirements, while having similar mechanical properties. Referencing Table 4, CFRP and Ti-6Al-4V have similar strength, elasticity, and Poisson's ratio – allowing for superb combined material performance. Stronger metals such as steel was simply too heavy for this aerospace application.

Table 4: Mechanical Properties of Ti-6Al-4V, CFRP, and FM 300K [29] [33] [34].

Mechanical Properties of Ti-6Al-4V, CFRP, and FM300K					
Ti-6Al-4V		CFRP (Standard Unidirectional)		Film Adhesive, FM300K	
Density	4.43 g/cm^3	Density	1.6 g/cm^3	Weight	390 gsm
Hardness, Vickers	349	Young's Modulus 0°	135 Gpa	Thickness	0.32 mm
Tensile Strength, Ultimate	950 MPa	Young's Modulus 90°	10 Gpa	Modulus of Elasticity	2.35 GPa
Tensile Strength, Yield	880 MPa	In-plane Shear Modulus	5 Gpa	Poisson's Ratio	0.3
Elongation at Break	14 %	Major Poisson's Ratio	0.3	Shear Modulus	0.907 GPa
Modulus of Elasticity	113.8 GPa	Ult. Tensile Strength 0°	1500 MPa	Tensile Shear	29.8 MPa
Poisson's Ratio	0.342	Ult. Comp. Strength 0°	1200 MPa	Plasticity Data	
Fracture Toughness	75 MPa-m½	Ult. Tensile Strength 90°	50 MPa	Shear Stress, Linear Limit	14.2 MPa
Shear Modulus	44 GPa	Ult. Comp. Strength 90°	250 MPa	Shear Strain, Linear Limit	0.0156
Shear Strength	550 MPa	Ult. In-plane Shear Stren.	70 MPa	Shear Stress, Knee	42.1 MPa
		Ult. Tensile Strain 0°	1.05%	Shear Strain, Knee	0.0932
		Ult. Comp. Strain 0°	0.85%	Shear Stress, Ultimate Failure	49.8 MPa
		Ult. Tensile Strain 90°	0.50%	Shear Strain, Ultimate Failure	0.5446
		Ult. Comp. Strain 90°	2.50%		
		Ult. In-plane shear strain	1.40%		

In order to truly appreciate the properties of Ti-6Al-4V and CFRP, a direct comparison with other materials is appropriate. Holistically, Ti-6Al-4V and CFRP offers relatively superior stiffness, strength, and fracture resistance in comparison to many metals, ceramics, polymers, and composites. In fact, both Ti-6Al-4V and CFRP are generally ~50% lighter than stainless steel with a strength and fracture toughness equivalent to iron and steel alloys. Finally, the distinguishing factor between the CF/E-Ti bonded structure is the superior performance at high-temperatures, fatigue life, and damage tolerance – namely high velocity impact damage [35]. Hence, CF/E-Ti bonded structures are ideal for fighter planes under high speed and temperature.

3.2.5 Failure Mechanisms of Bonded Joints

As previously mentioned, the most common defect has been disbond areas at the MCI, which compromises the load carrying ability of the bonded joint. Furthermore, there are two general mechanisms by which disbond areas can occur – Manufacturing or In-service (or a combination of both). During the manufacturing process, disbond areas and other defects can be attributed to the following: defective engineering processes or procedures (i.e. lack of detail for the process or incorrect procedural order); poor quality raw materials; poor control of temperature and humidity; operator error or incompetence; poor machining or inadequate tooling; poor surface preparation; and inadequate technology [36]. Similarly, in-service operation of bonded joints can lead to disbond areas and other defects. Typical causes of in-service operational damage include high and low velocity impact, overload conditions (in terms of excessive tensile, compressive, and shear stress), temperature exposure (both prolonged exposure to high temperatures or exposure to changes in temperature), water ingress and fatigue. Generally, these defects are difficult to detect visually because (1) the defects are sub-surface and (2) there is no discernable evidence of damage at the surface. The CFRP (and titanium laminate) may appear to be undamaged at the surface because the internal residual stress in the CFRP forces the structure back into the original position. The structure returns to the original "un-damaged" position after an overload/impact event [31]. Hence, NDT is required for the non-destructive evaluation of bonded joints.

Research supports the following manufacturing defects and in-service damage with bonded joints. Sections 3.2.5.1 and 3.2.5.2 cover manufacturing defects and operational damage, respectively.

3.2.5.1 Common Manufacturing Defects

Resin starved and resin rich locations are areas of insufficient or excessive resin epoxy (respectively) in the resin layers between plies or the resin within a single layer of a CFRP or composite structure. These defects are the result of a poor manufacturing process. For instance, the autoclave vacuum bag bonding process is a specific manufacturing process that can lead to resin being squeezed or displaced from areas of lower vacuum pressure to areas of high vacuum pressure. Other factors such as the shape complexity of the component can lead to a build up of resin at the corners and edges of the component. An area of resin rich or resin starved epoxy results in a localized region of dissimilar mechanical properties in comparison to the rest of the structure. This can result in dissimilar strength, stiffness, and weight. Furthermore, the entire composite structure is compromised with localized weak spots; a uniform composite structure (without insufficient or excessive resin) would have uniform mechanical properties and little to no localized weak spots. The same principle consideration could be applied to **insufficient or excessive adhesive** at the metal composite interface (Figure 14).

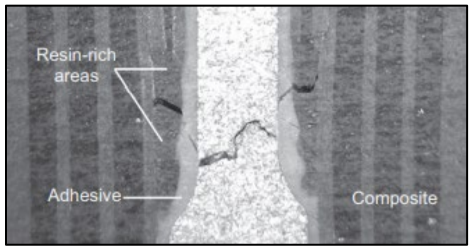

Figure 14: Image of progressive fatigue failure with resin rich and excessive adhesive areas on an IWSLJ coupon [18].

Porosity fraction are all defects stemming from a poor manufacturing process. The size of the pores are generally within the range of 10^6 nm to 10^8 nm in dimension [22]. Porosity is always present and commonly considered a volumetric measurement or ratio of voids to the total volume of the material. Depending of the material application, the acceptable level of porosity in the material may vary. With respect to Carbon Fibre Reinforced Polymer, porosity is pockets of air, unfilled volume of space, or foreign debris trapped between fibres and/or layers [36]. Porosity typically occurs during the bonding or curing process as gasses become trapped within the layers of the composite, or within the matrix of a single ply [36]. Improper manufacturing processes may also lead to porosity; moisture, debris, bodily oils, and other undesirable microscopic materials may get trapped during the preparatory process [36]. Porosity can result in the formation of delamination, disbond areas, compromised mechanical properties (elasticity and strength), which act as a stress riser for cracks.

3.2.5.2 Common In-Service Operational Damage

Disbond areas are defined as a defect or damage in which an area of the bonded joints becomes unbonded or is no longer adhered at the MCI. In this case, a disbond area can occur from a broken bond between the CFRP and film adhesive or between the adhesive film and titanium alloy or within the adhesive leaving adhesive on the titanium and CFRP. Disbond areas are subsurface and cannot be visually detected. Typically for the CF-188 IWSLJ, disbond areas are generated as a result of the titanium elastically buckling and the brittle composite ply fracturing under impact damage, fatigue cracking or an overload event during operation as illustrated in Figure 15 [20]. However, disbond areas can also be generated during the manufacturing process – typically from machining, tooling, resin starved regions, and poor surface preparation. Lastly, disbond areas grow as a result of stress.

Kissing bonds are a special type of disbond area that can be defined as two materials pressed tightly against each other ("kissing") that appear to be bonded, but in fact, they are not bonded and the structure has little to no adherent strength. By this definition, for two surfaces touching with no gap, tensile and shear loads are not able to be passed between the surfaces. Kissing bonds are typically created by poor surface preparation.

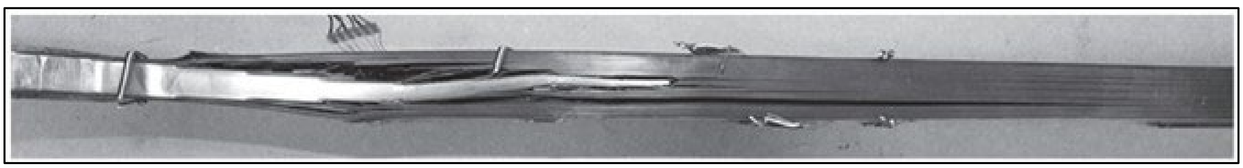

Figure 15: IWSLJ coupon failure due to titanium plastically buckling and brittle plies of CFRP fracturing [18].

Delamination is an area of separation that occurs between the individual layers or plies of carbon fibre reinforced polymer (Figure 16). Similar to disbond areas, delamination cannot be seen via means of a visual inspection. Additionally, a delaminated area within the CFRP can also be caused by impact damage, fatigue cracking or an overload event during operational service. These events can generate a force capable of splitting carbon fibre layers; the forces act on micro-defects/damage (pores, voids, micro-cracks, etc.) in the carbon fibre material. This splitting effect or delamination is increased with compressive forces, which causes the delamination to grow in length.

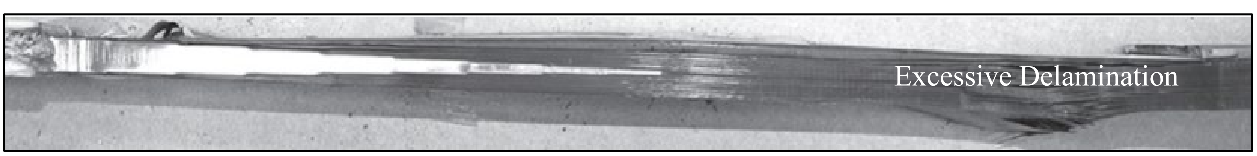

Figure 16: Composite failure on the IWSLJ leading to excessive delamination [18].

CFRP **fracture or cracking** may occur within the carbon fibre structure as the result of operational fatigue, impact damage, or even extreme thermal fluctuations [31]. As mentioned previously, there is a tendency for the titanium alloy to buckle and the composite plies to fracture in an adverse condition (Figure 17). The fracture characteristics (direction, size, shape, formation, etc.) are dependent on the causation event. For example, fatigue damage can cause fractures in the matrix and carbon fibre portion of the structure. Furthermore, impact damage can result in a localized pine tree type fracture pattern across the layers of composite. Similar to disbond areas and delamination, CFRP fracture is also not typically detectable via means of a surface visual inspection. **Micro-fractures/Stress Risers** are the initiators of fractures. Furthermore, these initiators are generally caused by improper manufacturing practices, and can lead to early and unpredictable structural failure under stress.

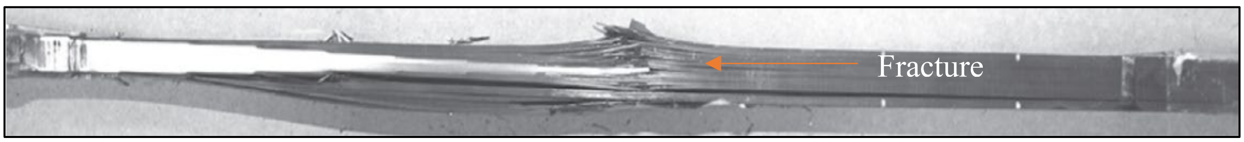

Figure 17: Compressive failure on the IWSLJ leading to matrix fracture, where the stress riser is at the end of the titanium rather than being in the uniform composite [18].

Research supports the following damage mechanisms with respect to bonded structures:

Impact damage is a defect due to a collision between foreign objects and the surface of the bonded joint structure. Impact damage to composite structures is commonplace and can be caused by a variety of means; Impact damage in the case of the CF-188 IWSLJ can be caused by extreme weather (wind, hail or ice precipitation, etc.), environmental conditions (airfield debris, bird strikes, etc.), aircraft maintenance support equipment (cranes, lifts, tow truck, tools, etc.), and human error. Impacts can be classified into two distinct categories, high velocity and low velocity [38]. There are many ways to discriminate between a high velocity impact and a low velocity impact. Cantwell and Morton [38] define a high velocity impact as being over 10 m/s, whereas Adbrate [38] coins a high velocity impact as being over 100 m/s. Others use the type of damage as a guideline to discriminate between high and low velocity impact. For instance, damage due to penetration through composite layer(s), which fractures the carbon fibres, is the result of a high velocity impact. A low velocity impact can result in disbond areas, delamination, and matrix fracture or cracking. For the purpose of this thesis, the definition of low and high velocity impact is irrelevant because the focus lies on the impact damage defect – namely disbond areas.

Temperature and Moisture. Although titanium based bonded joints were specifically designed for relatively high temperatures, and generally, titanium based bonded joints have a protective coating against moisture, they are not impervious to the degrading effects of temperature and moisture. Temperature damage is degradation due to prolonged exposure to relatively high temperature. Water damage is degradation due to water ingress in the structure and plasticization – water molecules occupying microscopic voids in the polymer or adhesive [21]. Temperature and moisture have the potential to result in a shortened fatigue life or early laminate failure. Galvez et al [21], noted the effects of temperature (80˚C vs room temperature) on epoxy single lap adhesive joints and noted that there was a 32% reduction in the strength – due to the adhesive being compromised. Additionally, prolonged exposure to high temperatures resulted in increased polymer chain mobility, while decreasing the strength and stiffness. Water that seeps into the structure adds to the overall weight of the structure and degradation of molecular structure. The CF-188 IWSLJ film adhesive, FM300, can absorb a moisture content of upwards of 10% by weight. Moreover, water undergoes expansion at the freezing point; this effect increases the volume of the affected area. For instance, below 4˚C, water expands slightly, and at freezing point, it expands by 9%. Test samples of CF/E-Ti were exposed to both temperature (60˚C) and moisture (99% relative humidity) over a period of 24 hours suffered a 40% decrease in stiffness at the MCI [21]. Ultimately, temperature and moisture damage can lead to disbond areas and complete fibre-metal separation failure (Figure 18).

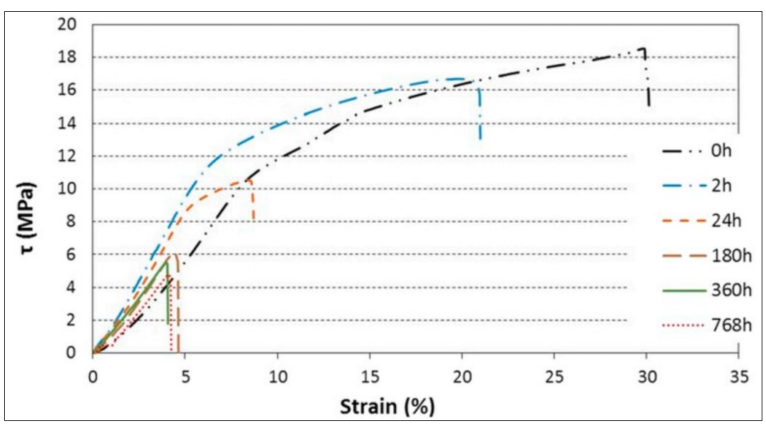

Figure 18: The stress – strain curves of CF/E-Ti samples exposed to temperature and moisture over different periods of time [39]. The degrading effect of temperature and moisture over time.

Fatigue damage, shown in Figure 19, is deformation and cracking due to the destructive effects of cyclic loading or repetitive stressing over a duration of time. The following expands on the modes of failure due to fatigue stresses and the specific vulnerability to disbond areas at the Metal Composite Interface (MCI).

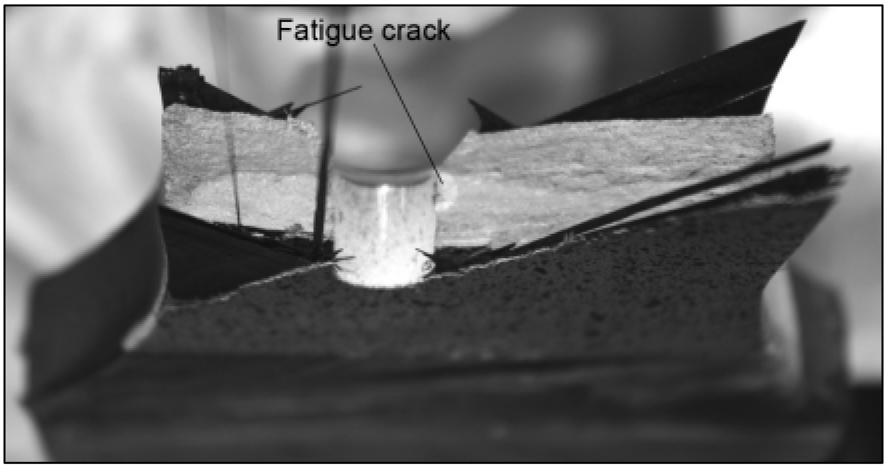

Figure 19: Fatigue damage from a corner crack at a fastener hole [18].

3.2.6 Modes of Failure – Fatigue Stress

In-service failure is categorized into Mode I, II, and III based on the dominant stress state (Figure 20) that is present. Mode I is failure due to tensile stress [40]. Tension or tensile stress is an extension or elongation of a material due to the force of a pulling action or positive linear strain. Mode II is failure due to compressive stress [40]. Compression or compressive stress is the compression of a material due to a pressing action or negative linear strain. Mode III is failure due to shear stress [40]. Shear stress occurs as opposing forces are applied parallel to opposite sides of a material. Rhymer et al. [35] noted that the fatigue life of the bond decreased in a tension-compression test versus a tension-tension test. This is a result of the increased stress range in a tension-compression test. These stresses are common in in-service fatigue failure or failure in general during operation.

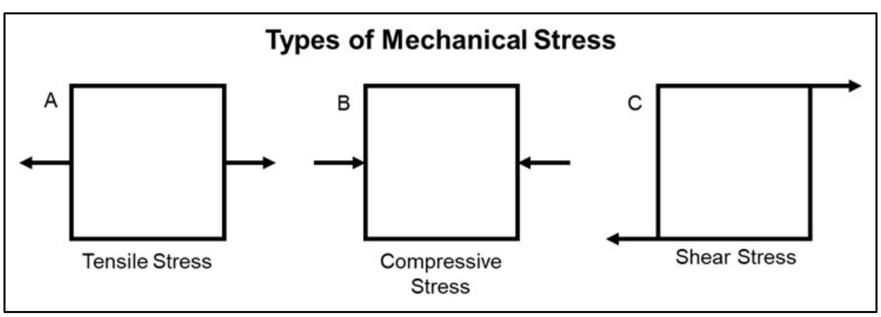

Figure 20: An illustration of mechanical stresses including (A) Tensile Stress, (B) Compressive Stress, and (C) Shear Stress.

3.2.6.1 Vulnerability at the Metal Composite Interface (MCI)

Undoubtedly, Ti-6Al-4V and CFRP form a superior bonded structure with excellent mechanical properties and performance [19]. Nevertheless, the MCI plays a critical role in maintaining the integrity of the bonded joint against destructive events. Li et al. [20] explains that the MCI consumes a small amount of energy during failure, but heavily influences the stiffness and failure modes of the structure. The USN conducted a study on the Ti-6Al-4V CFRP IWSLJ in an effort to evaluate the residual static strength and remaining service life of the joint [18]. The prominent failure characteristics at the MCI were identified as Cohesive, Adhesive, and Substrate failure, which are defined as:

> *Cohesive failure* is defined as the internal failure of an adhesive as a result of being incapable of resisting separation. Cohesive failure is indicated with adhesive present on both mating surfaces upon separation [18].
>
> *Adhesive failure* is defined as a failure at the joint's adhesive-adherend interface. This is the result of insufficient chemical and/or mechanical surface preparation. Adhesive failure is indicated by a sharp reduction of strength in the specimen under peel stresses and adhesive separating from the adherend [18].
>
> *Substrate (adherend) failure* is defined as failure of the adherend as a result of having a lower strength value than the adhesive [18].

The general solution to improving the MCI properties is strengthening through improving the adhesive and/or surface treatment of the titanium. Li et al. [20] noted that Boing's Sol-Gel combined with FM® adhesives led to the best fracture toughness and fatigue crack growth resistance. However, the ultimate compromise with extensive increase in MCI strength is reduced fatigue life [35].

CHAPTER 4 – FUNDAMENTAL THEORY

This chapter covers the principles of infrared thermography theory and highlights the nuances of heat transfer. Additionally, infrared radiation and infrared cameras are both explained and discussed. Furthermore, ultrasonic testing theory is also covered towards the end of the chapter.

4.1 Infrared Radiation

Conduction, convection, and radiation are responsible for producing a surface temperature pattern, which can be observed remotely. All objects in the natural universe or greater than absolute zero (zero Kelvin) emit electromagnetic radiation (infrared radiation included) by means of atomic particle motion. The temperature and surface properties of the object determines the intensity and spectrum of the radiation. Infrared radiation is within the electromagnetic radiation spectrum (shown in Figure 21) between microwaves and visible light at a wavelength between ~780 nm and ~1 mm [41]. Thermal infrared radiation is classified within a wavelength range of 0.75 – 14 µm and further separated into the following ranges: Short-Wave, 0.9 - 1.7 µm; Mid-Wave, 3.0 - 5.0 µm; and Long-Wave, 8 – 14 µm [31]. Wavelength λ is directly proportional to the speed of propagation *c* and inversely proportional to frequency *f*. This relationship is expressed in Equation (1) [41].

$$c = f \cdot \lambda \tag{1}$$

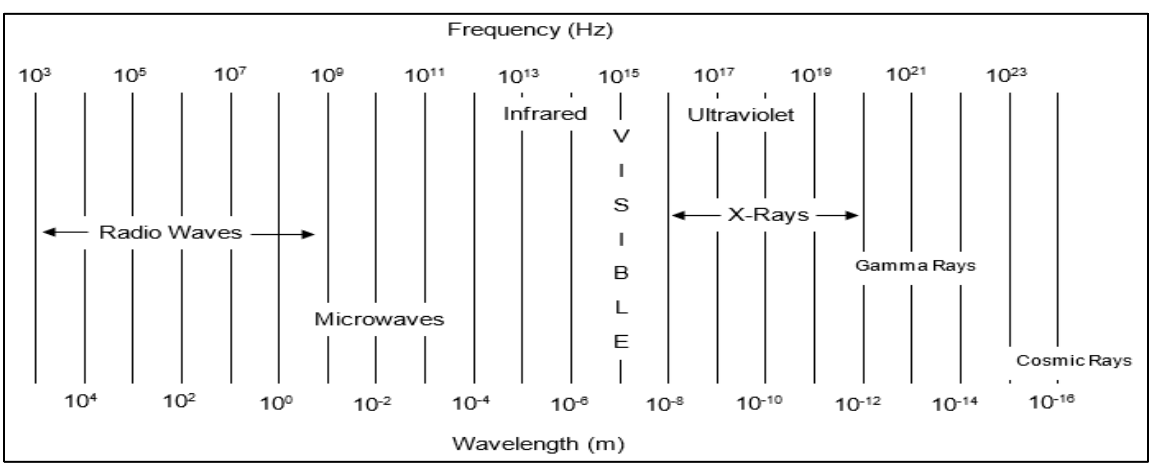

Figure 21: The electromagnetics spectrum [7].

The type of wave form and medium (namely CF/E-Ti) determines the speed of propagation of the wave. There are two types of traveling waves: longitudinal waves, where the wave travels parallel to the direction of propagation; and transverse waves, where the wave travels perpendicular to the direction of propagation [31]. Electromagnetic waves (Figure 24), with respect to thermal infrared radiation, are transverse waves with an energy level proportional to temperature, as shown in the Stefan-Boltzmann Law equation [41]:

$$Q_{rd} = e\sigma_{SB}T^4, \tag{2}$$

where the radiation energy or heat Q_{rd} is the product of the thermal effusivity e, the temperature T in Kelvin units, and the Stefan-Boltzmann constant σ_{SB} Thermal effusivity is discussed further in Section 4.5.

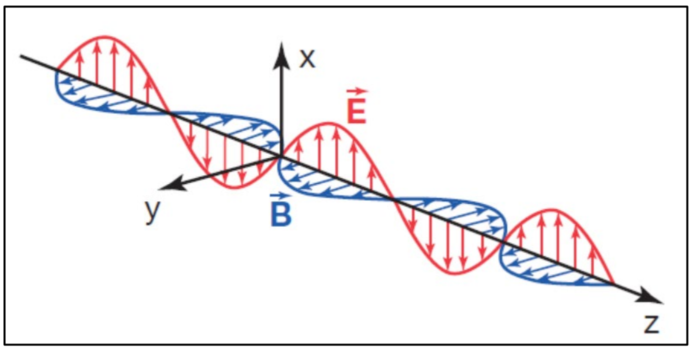

Figure 22: Electromagnetic waves containing an electric field (**E**) and magnetic field (**B**) [31].

Electromagnetic radiation energy can either be reflected or refracted (absorbed) off the surface of a medium and this interaction follows the Law of Reflection [31], as shown in Figure 23.

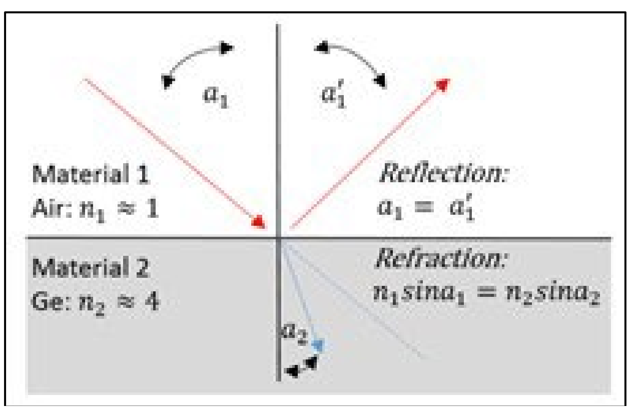

Figure 23: Energy being reflected (red arrows) and refracted (blue arrow) in accordance with the law of reflection. Image used from [31] with the author's permission.

Where α_1 is the angle of incidence, α_1 is the angle of reflection, α_2 is the angle of refraction, n is the index of refraction with respect to the medium, and $n_1 \sin \alpha_1 = n_2 \sin \alpha_2$ (Snell's Law) is the relationship between reflection and refraction. Note that Figure 23 shows a specular reflection off of a smooth surface, however, reflections can also be diffuse depending on the roughness of the surface.

In infrared thermography, the radiation is absorbed by the material and the heat diffusion within the material is captured by an infrared camera. However, the absorption of radiation may be hindered by surface finish reflections and emissivity – a measure of material radiation emission efficiency, where a shiny (totally reflective) object has an emissivity of zero and a blackbody has an emissivity of one. Of note, near or imperfect blackbody radiation (emissivity of 0.90) is called graybody radiation as shown in Figure 24.

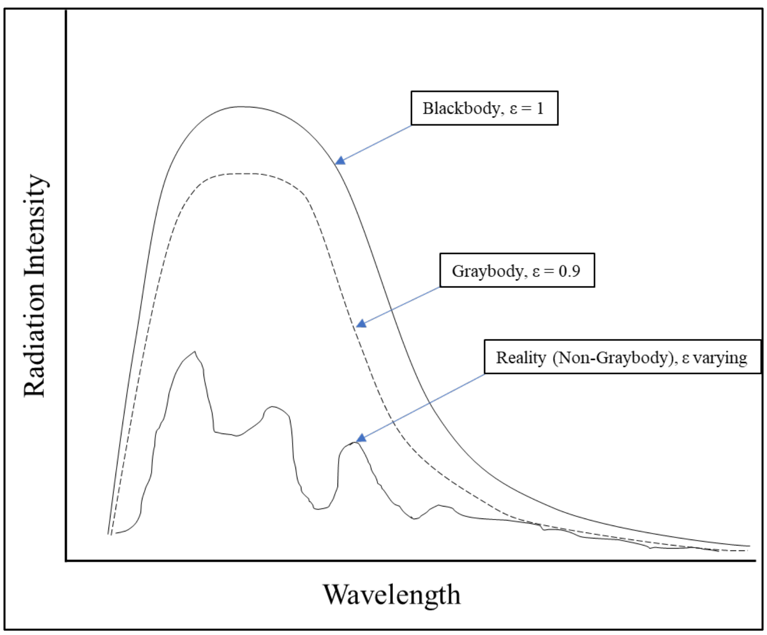

Figure 24: Blackbody, Graybody, and Real (Non-Graybody) emissions [7].

Emissivity, specifically high emissivity, is critical to the success of infrared thermography. Many significant effects are directly attributed to high emissivity. First, as shown in the Stefan-Boltzmann Law Equation (2), high emissivity leads to higher radiation energy intensity for the given temperature, thus leading to a stronger signal for the infrared camera or detector. Second, a high emissivity surface leads to poor reflectors, thus leading to less noise by other radiant sources within the surrounding environment. Hence, there would be less error and higher energy readings by the detector from the actual radiation emission source being examined. Third, high emissivity naturally results in increased absorption – reducing the energy required for infrared thermography and once again providing a stronger signal to the detector.

4.2 Basics of an Infrared Camera

Infrared thermography uses surface temperature measurement from an infrared camera or radiometer. Infrared cameras (shown in Figure 25) use the principles of radiometry, a set of methods used in measuring electromagnetic radiation. Generally, a radiometer collects and focuses infrared radiation on a sensitive detector. The radiation is converted into an electrical signal by the detector, and later, processed into a thermographic image (showing temperature by colour or gray scale). There are many different types of infrared radiometers, including: Frame Grabber, which digitally captures individual still frames; Focal-Plane Array, with an array of electromagnetic detectors in the focal plane of the imaging system; and Stirling Cooling, where the detector is cooled to increase sensitivity to tiny changes in the temperature gradient. Holistically, radiometry methods include: Video radiometry, a standard infrared video camera that records temperature variations and gradient patterns; scanning radiometry, where an optically scanning infrared camera scans an object in a fraction of a second and constructs a thermographic image; and detector arrays, where each element of the detector array can monitor an object's surface gradient for the full period of observation.

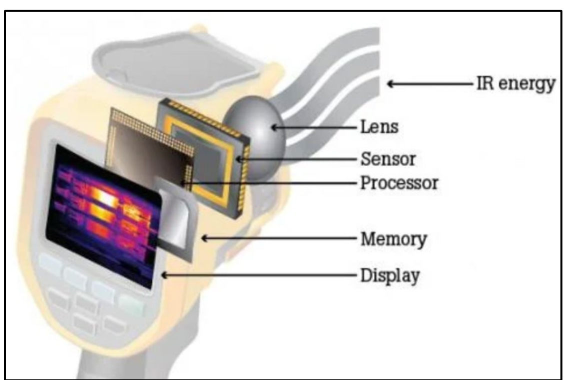

Figure 25: A generic illustration of the components to an IR camera [42].

The infrared camera used is similar to visible light cameras, but uses a focal plane array (FPA) microbolometer, which senses IR sections of the electromagnetic spectrum [31]. The FPA microbolometer sensor chip contains detector plates made from electrically conductive vanadium oxide or silicon [16]. Radiation emitted by the material enters the lens of the IR camera and is directed to the sensor. When the radiation hits the sensor, the electrical resistance of the sensor changes and the change in electrical resistance is converted to a radiographic signal in the camera's processor [31]. The variance in the radiographic signal is visually represented as temperature or radiance on the camera's screen or display [31].

4.3 Fundamentals of Heat Transfer in Thermography

Heat transfer in an object or between objects is described by the Laws of Thermodynamics and occurs by three distinct means: conduction, convection, and radiation (Figures 26 – 28). Conduction occurs as a function of dissimilar temperatures in an object or between two objects in contact; it is the heat flow through motionless matter. In **conduction**, heat propagates from a point of higher temperature to a point of lower temperature in order to achieve thermal equilibrium as shown in Figure 26. Three-dimensional (3D) heat transfer problems are closer to reality, but difficult to solve analytically. Often, 3D heat transfer problems require numerical analysis. Hence, for a simplistic interpretation of conduction, consider the following one-dimensional case (only in the "x-direction") derived from Fourier's law [7]:

$$Q_{cd} = -k\frac{\partial T(x,t)}{\partial x}, \tag{3}$$

where Q_{cd} $(W \cdot m^{-2})$ is conductive heat transfer, k (W/m-K) is thermal conductivity, and T (K) is temperature in the x-direction. Of note, thermal conductivity is a measure of a material's ability to transfer or transport heat. The one-dimensional (1D) equation can be further simplified with the assumptions of a conductor (plate or wire) of thickness or length L and stationary temperatures T_1 and T_2 – where $T_2 > T_1$. The conductive heat transfer would be equal to:

$$Q_{cd} = \frac{T_2 - T_1}{R}, \tag{4}$$

where R (m^2.K/W) is thermal resistance (the opposing effect to thermal conductivity) and is equal to length L divided by thermal conductivity k [7].

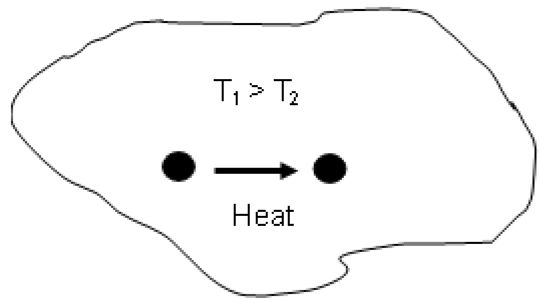

Figure 26: Illustration of Conduction.

Convection is heat transfer through molecular mass movement of fluids over distances; it is the heat flow through fluid movement as shown in Figure 27. Thermal energy can transfer between objects coupled with a fluid through convection [7]; heat from an object thermally excites the fluid molecules, which transfers the thermal energy to another object of lower thermal energy. Convective heat transfer can be described with Newton's law of cooling:

$$Q_{cv} = h_{cv}(T_s - T_f), \tag{5}$$

where Q_{cv} ($\mathrm{W \cdot m^{-2}}$ or J) is convective heat transfer, T_s is the surface temperature of an object, T_f is the temperature of the fluid, and h_{cv} (W/m^{2}K) is the convective heat transfer coefficient.

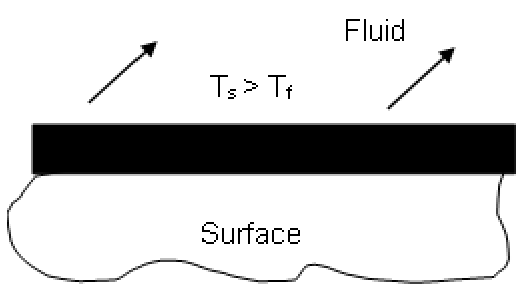

Figure 27: Illustration of Convection.

Radiation heat transfer is discussed further in the next section. Radiation can be defined as heat flow by electromagnetic waves. All objects at temperatures greater than absolute zero emit radiation and radiation energy can be transferred through all mediums – even in a vacuum without conduction or convection (Figure 28). Radiation energy is described by the Stefan-Boltzmann Law Equation (2) [41]:

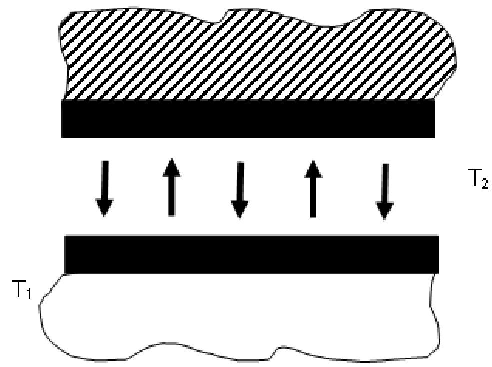

Figure 28: Illustration of Radiation.

4.4 Induction Thermography

Induction Thermography or Eddy Current Thermography (ECT) is the coupling of electromagnetism and thermography as a non-invasive method of inspecting the structural characteristics of conductive materials. Induction thermography is the newest development in active thermography, and with the use of IR cameras, has proven to be a rapid inspection method with improved visual interpretation of flaws in a complex geometry. Induction heat generation in conductive materials occurs due to induced eddy currents and Joule heating effect. Electromagnetic induction heating can be traced back to 1932 [7], and uses an alternating current flowing through an inductor or coil, which generates an alternating magnetic field around the coil [7]. The alternating magnetic field then induces eddy currents in a nearby conductive sample material. Depending on the eddy current density distribution in the sample material, heating occurs as a function of the electrical conductivity of the material. Discontinuities are highlighted given the temperature differential across the sample. Induction Thermography is steadily gaining more interest by the aerospace industry due to its rapid inspection ability [7].

4.4.1 Electromagnetic Induction

This section covers the detailed analysis of the mathematical equations behind the electromagnetic induction phenomena with consideration to a conductive material being excited by an induction coil. Mathematically, electromagnetic induction heating is described by Maxwell's equations. According to Faraday's law, an alternating current flowing through a wire or coil will produce an alternating magnetic field of the same frequency as the source current. According to Ampere's law, the electromagnetic field can in-turn induce an alternating current in a nearby conductive material. The electromagnetic field strength is dependent on the coil current, the coil geometry, and the distance from the coil. Maxwell's equations [43] in a vacuum are given as:

$$\text{Gauss' Law for electricity:} \qquad \nabla \cdot \boldsymbol{E} = \frac{\rho}{\epsilon_o} \tag{6}$$

$$\text{Gauss' Law for magnetism:} \qquad \nabla \cdot \boldsymbol{B} = 0 \tag{7}$$

$$\text{Faraday's Law:} \qquad \nabla \times \boldsymbol{E} = -\frac{\partial \boldsymbol{B}}{\partial t} \tag{8}$$

$$\text{Ampere's Law:} \qquad \nabla \times \boldsymbol{B} = \mu_o \boldsymbol{J} + \mu_o \epsilon_o \frac{\partial \boldsymbol{E}}{\partial t}\,, \tag{9}$$

where $\boldsymbol{E}$ is the electric field, ρ is the charge density, ϵ_o is the permittivity of free space, $\boldsymbol{B}$ is the magnetic field, $\boldsymbol{J}$ is the current density, and μ_o is the permeability of free space. Note that the **bold** font indicates a vector quantity. Also, Equation 9 has Maxwell's correction to Ampere's Law.

4.4.1.1 Electromagnetic Waves in Conductive Material

Within the confines of conducting materials that are linear, homogeneous and isotropic in nature (i.e. permittivity, permeability, and conductivity do not vary throughout the material), Ohm's law can be defined as [43]:

$$\boldsymbol{J} = \sigma \boldsymbol{E}\,, \tag{10}$$

where σ is the electrical conductivity. Additionally, the displacement current $\boldsymbol{D}$ relates to electric field strength by ϵ, permittivity (or dielectric constant), as shown in the following equation:

$$\boldsymbol{D} = \epsilon \boldsymbol{E}\,. \tag{11}$$

Furthermore, the magnetic field $\boldsymbol{B}$ and the magnetic field intensity $\boldsymbol{H}$ share the following relationship [43]:

$$\boldsymbol{B} = \mu \boldsymbol{H}\,, \tag{12}$$

where μ is the isotropic permeability within the linear medium. Equations (10) and (12) can be used to derive solutions to Maxwell's equations. Hence, (10) and (12) can be used to apply Maxwell's equations to linear materials. It is important to understand that in real materials there is a degree of non-linearity in the relationship of $\boldsymbol{B}$ and $\boldsymbol{H}$. However, for the purposes of the thesis $\boldsymbol{B}$ and $\boldsymbol{H}$ are assumed to have a linear relationship. Therefore, Maxwell's equations in a linear and isotropic media are given as [44]:

$$\nabla \cdot \boldsymbol{E} = \frac{\rho_f}{\epsilon} \tag{13}$$

$$\nabla \cdot \boldsymbol{B} = 0 \tag{14}$$

$$\nabla \times \boldsymbol{E} = -\frac{\partial \boldsymbol{B}}{\partial t} \tag{15}$$

$$\nabla \times \boldsymbol{H} = \boldsymbol{J}_f + \frac{\partial \boldsymbol{D}}{\partial t} \; or \; \nabla \times \boldsymbol{H} = \mu\sigma\boldsymbol{E} + \mu\epsilon\frac{\partial \boldsymbol{E}}{\partial t} \;, \tag{16}$$

where ρ_f is the free charge density in the medium and $\boldsymbol{J}_f$ is the free current density.

Maxwell's Equations (13) to (16) represent a theoretical electromagnetic wave propagation and do not directly represent experimental observations in an analysis of eddy current wave generation. Nevertheless, the equations are ideal for formulating an expression to best understand electromagnetic wave propagation and interpret eddy current results, namely the expression for continuity. The continuity equation describes the relationship between current density and charge density through the Law of Conservation of Charge. The Law of Conservation in this case, states that a change in charge over a given volume must correspond with the flow of charge by means of a current. In other words, the divergence of current is equal in rate to the decrease of the free charge density. The continuity equation can be derived from Ampere's Law and Gauss' Law as shown in Equation 17 [43].

$$\nabla \cdot \boldsymbol{J}_f = -\frac{\partial \rho_f}{\partial t} \tag{17}$$

Ohm's Law (Equation 10) and Gauss' Law in a medium (Equation 13) are applied to Equation (17), which describes the behaviour of free charge density and current as a result of electromagnetic wave propagation in a conductive homogeneous linear material.

$$\frac{\partial \rho_f}{\partial t} = -\sigma(\nabla \cdot \boldsymbol{E}) = -\frac{\sigma}{\epsilon}\rho_f \tag{18}$$

Given the first-order partial differential equation (Equation 18) and initial conditions of $t = 0$ as $\rho_f = \rho_f(0)$, the following solution can be derived:

$$\rho_f(t) = -\rho_{f0}e^{-\frac{\sigma}{\epsilon}t}\,. \tag{19}$$

Of which the characteristic relaxation time (or atomic collision time) $\tau = \frac{\epsilon}{\sigma}$ is the time taken for free charge to dissipate by a value of 1/e (36.8%) in a material. For materials with high conductivity such as copper, τ reduces to a negligible value (i.e. Copper, with a conductivity of 5.8 x 10^7 S/m, has a characteristic relaxation time on the order of 10^{-14} s [43] and is therefore, negligible). Using this consideration for good conductors, Equation (13) becomes Equation (38).

$$\nabla \cdot \boldsymbol{E} = 0 \tag{20}$$

4.4.1.2 Diffusion Equations for Good Conductors

In order to model the effects of EM waves within a specimen, first start by manipulating Maxwell's equation (Equation 15), Faraday's Law. Taking the curl of Equation (15) produces the following:

$$\nabla \times (\nabla \times \boldsymbol{E}) = -\nabla \times \frac{\partial \boldsymbol{B}}{\partial t} \tag{21}$$

The Laplacian identity (of a vector) where $\boldsymbol{A}$ is an arbitrary vector, given in [43], states the following:

$$\nabla^2 \boldsymbol{A} = \nabla(\nabla \cdot \boldsymbol{A}) - \nabla \times (\nabla \times \boldsymbol{A}) \tag{22}$$

The Laplacian identity (22) can be substituted in (21) and the resultant would be (23).

$$\nabla(\nabla \cdot \boldsymbol{E}) - \nabla^2 \boldsymbol{E} = -\frac{\partial}{\partial t}(\nabla \times \boldsymbol{B}) \tag{23}$$

In a good conductor where Equation (20) is the case, Equation (23) simplifies to Equation (24).

$$\nabla^2 \boldsymbol{E} = -\frac{\partial}{\partial t} (\nabla \times \boldsymbol{B}) \tag{24}$$

Substituting (13) and (16) with respect to $\boldsymbol{B}$ into (23) will result in:

$$\nabla^2 \boldsymbol{E} = \frac{\partial}{\partial t} \left(\mu\sigma \boldsymbol{E} + \mu\epsilon \frac{\partial \boldsymbol{E}}{\partial t} \right), \tag{25}$$

$$\nabla^2 \boldsymbol{E} = \mu\sigma \frac{\partial \boldsymbol{E}}{\partial t} + \mu\epsilon \frac{\partial^2 \boldsymbol{E}}{\partial t^2}, \tag{26}$$

where (26) can be used to model the behaviour of EM waves within a conductor. Since the $\mu\sigma$ component is much greater than the $\mu\epsilon$ component, for good conductors at frequencies below approximately 10^8 Hz [44], the first term in (26) dominates the second term. Hence the second term (the displacement current term) can be neglected. For example, the $\mu\sigma$ component of copper is on the order of 72.9 [44], whereas the $\omega\mu\epsilon$ component is ω x 1.11 x 10^{-17}(ω being the radial frequency associated with the changing magnetic field). With the second term removed from (26), the EM fields are quasistatic [44] and (26) can be approximated by the following:

$$\nabla^2 \boldsymbol{E} = \mu\sigma \frac{\partial \boldsymbol{E}}{\partial t}. \tag{27}$$

Using Maxwell's Equations 4 and the same derivation process, the equation for magnetic field diffusion on the surface of a good conductor is approximated by the following:

$$\nabla^2 \boldsymbol{B} = \mu\sigma \frac{\partial \boldsymbol{B}}{\partial t}. \tag{28}$$

4.4.1.3 Skin Effect

Skin effect or skin depth δ is the electromagnetic energy penetration depth limitation in a conductive material at a given frequency. The penetration limitation is due to a causative electromagnetic field from an induced magnetic field with opposite direction (Lenz's Law). The ultimate limit is achieved when the current density decreases to 1/e or (36.8%) of the surface value. Skin depth can be approximated by starting with the surface diffusion Equation (27). Then, considering that current varies sinusoidally in time, the skin depth equation (in MKS or SI units) is then [43]:

$$\delta = \sqrt{\frac{2}{\mu\sigma\omega}} = \sqrt{\frac{T}{\pi\mu\sigma}} \;, \tag{29}$$

where ω is the radial frequency and *T* is the period. This equation assumes that the material is an infinitely thick plate and a plane wave electromagnetic field excitation applied parallel to the material surface, is rarely achieved in a practical situation or laboratory. For a conductor or material with infinite dimension in the x and y directions and semi-infinite in the z-direction, Equation (26) and (19) can be used to express the exponential decay of current as shown:

$$\tilde{\boldsymbol{J}}_x(z) = ke^{i\alpha z} \;, \tag{30}$$

where $\tilde{\boldsymbol{J}}$ is the complex expression for the current density, *z* is the depth in the conductor, *k* is a constant, and $\alpha = (1+i)/\delta$.

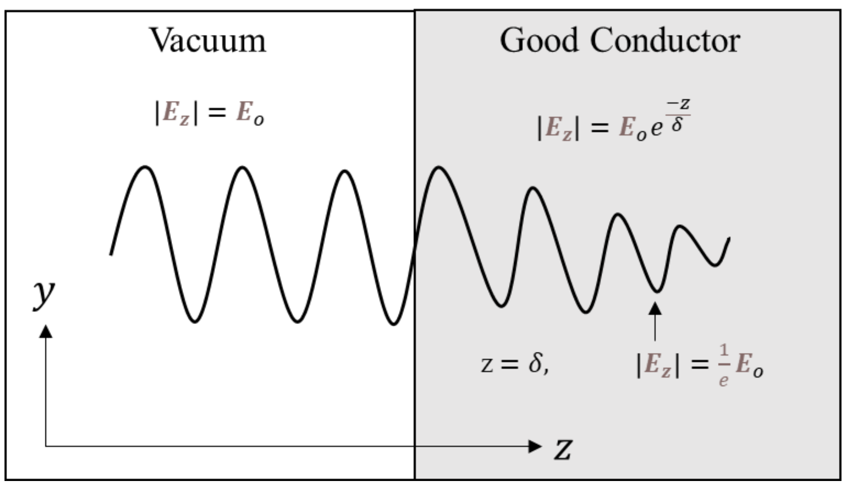

Figure 29: Electric field in vacuum versus the electric field at depth in a conductive material adapted from [45].

Given the complex current density at the surface $\tilde{J}_s$ and α, the exponential current density decay with reference to the surface is

$$\tilde{\boldsymbol{J}}_x(z) = \tilde{\boldsymbol{J}}_s e^{\frac{-z}{\delta}} \;. \tag{31}$$

The electric field that drives the current is accompanied by a larger magnetic field and an expression for the electric field can be obtained with Ohm's Law (Equation (10)):

$$\tilde{\boldsymbol{J}}_x(z) = \sigma\tilde{\boldsymbol{E}}_x(z) = \sigma\tilde{\boldsymbol{E}}_o e^{\frac{-z}{\delta}} \;, or \tag{32}$$

$$\widetilde{\boldsymbol{E}}_x(z) = \widetilde{\boldsymbol{E}}_o e^{\frac{-z}{\delta}} . \tag{33}$$

Lastly, for the particular case of inductive heating (purely with respect to resistive heating), Equation (34) can be derived for the time average power input per unit volume.

$$P_{resistive} = Q_r = \langle \boldsymbol{J} \cdot \boldsymbol{E} \rangle = \frac{1}{2} \sigma \widetilde{\boldsymbol{E}}_o{}^2 e^{\frac{-2z}{\delta}} \tag{34}$$

In the case of a material such as titanium (Ti-6Al-4V) with a conductivity of 5.8×10^5 S/m and a frequency of 1-100 kHz, skin depth can be on the order of 21-2.1 mm. Skin depth is a contributing cause of the volumetric type heating nature of the induction heating process. It allows for minimal energy to be used to have heating occur at a desired depth and volume. Furthermore, it is the reason why induction heating is an efficient heating process compared to other heating process such as flash heating, oven heating, or an open flame.

4.4.2 Conventional Electrical Prospective – Electromagnetic Induction

This part covers the basics of electromagnetic induction from a circuit analysis prospective, specifically concerning self-inductance, mutual inductance, and impedance.

4.4.2.1 Self-Inductance

The early history of electromagnetic induction is directly linked to the effort of Michael Faraday (1791 – 1867), who observed that an alternating magnetic field generates an alternating electric field, which induced both a voltage and current within a conducting loop in the field. The effect was called Faraday's Law of Induction and was derived from experimental investigations by Faraday in 1831. The voltage induced was labelled as electromotive force (emf), and with the concept of magnetic flux linkage, Faraday's Law is

$$emf = -\frac{d\Phi}{dt} . \tag{35}$$

Note that magnetic flux Φ is equal to magnetic field times area (or $\boldsymbol{B} \cdot \boldsymbol{A}$), and in this equation, is linked to the current. Furthermore, the negative sign in Equation (35) denotes that the induced voltage is in the opposing direction to the circuit current; this opposing directional change is known as Lenz's Law. For this reason, emf is often referred to as back emf or inductance reactance.

Additionally, there is an induced current or opposing current flow lagging behind the induced voltage. Faraday's Law, Equation (35), can be rewritten in term of the induced voltage *v*

$$v = -\frac{d\Phi}{dt} \ , \tag{36}$$

where induced voltage is *v*.

Furthermore, changes in current in a conducting loop result in a change in magnetic flux through that loop. Hence, Faraday's law can be re-expressed as shown:

$$v = -\frac{d\Phi}{di}\frac{di}{dt} = -L\frac{di}{dt} \ . \tag{37}$$

In electrical theory, induced voltage *v* is the *voltage of self-inductance*, change in current i, and inductance L is the *self-inductance* of the element (or loop). Specifically, the inductance L within an electrical circuit carrying current can be defined as the ratio or constant of proportionality of the linking magnetic flux to the current producing the magnetic flux. It is in a unit called *henry, H*. In other words, the alternating current produces a magnetic field, which creates a magnetic flux that passes through a conductor. Faraday hypothesized that magnetic fields were coupled with electric fields and an alternating current would be able to produce an alternating magnetic field. However, he was unable to validate his hypothesis, (It was explained with Maxwell's Equation (8) in 1873 and Hertz in 1893).

4.4.2.2 Self-Inductance – Number of Identical Turns

A coil, also know as an inductor, is a conductive material (typically a relatively low resistance metal such as copper) in the shape of a wound loop through which alternating current flows. It is a significant component in the induction heating system because it determines the effectiveness and efficiency of heating the work piece. Coils can range in complexity depending on the desired heating application. The simplest coil would be a helical (or solenoid) coil constructed from a number of windings (turns) of copper tube around a mandrel. If the conductor has a number (N) of turns, the magnetic flux linkage is directly proportional to N identical turns as

$$\lambda = N\Phi \ , \tag{38}$$

where the magnetic flux linkage is λ. Furthermore, for a static (or, at most, low frequency) current I in a coil containing N turns, the magnetic flux linkage can be written as Equation 39 with respect to inductance L.

$$\lambda = LI \ , \tag{39}$$

or with consideration to Equation (38) as

$$L = \frac{N\Phi}{I} \ . \tag{40}$$

The practical application of the number of turns may be limited depending on the power available. Increasing the number of turns increases the impedance and increases the power required. This is discussed more in the Chapter 5.

4.4.2.3 Self-Inductance – Total Impedance

Total impedance is an important factor with respect to the practical application of electromagnetic inductance; many induction heating systems are designed with consideration of the total impedance. Impedance, *z*, is the total opposition to current flow in an alternating current (AC) circuit and is measured in *ohms*. Current with respect to AC circuit impedance is

$$i(t) = I_{peak} \sin(\omega t) \tag{41}$$

where I_{peak} is the sinusoidal peak amplitude of the current, and ω is the angular frequency of the current. Notably, ω is equal to $2\pi f$ where *f* is frequency in Hertz. Ultimately, high impedance can result in a significant reduction in system current, and overall loss in the intended practical application. There are three key components in total impedance: electrical resistance, R (i.e. resistor); inductive reactance (i.e. back emf), X_L; and capacitive reactance, X_C. These components are considered the common elements of a Resistive Inductive Capacitive (RLC) circuit and can be pictorially represented by Figure 30.

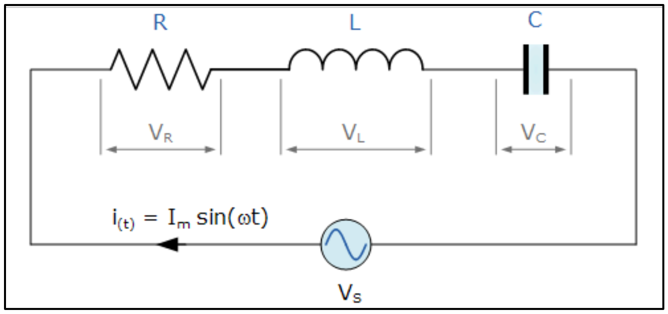

Figure 30: RLC Series circuit adapted from [46].

Inductive and capacitive reactance in an RLC circuit varies as a function of frequency. Additionally, resistive voltage V_R is "in-phase" with current, inductive voltage V_L "leads" the current by 90˚, and capacitive voltage V_C "lags" current by 90˚ [46]. Furthermore, it should be noted that inductive and capacitive voltage are 180˚ "out-of-phase" or in opposition to each other [46].

Electrical resistance R is the intrinsic resistance to electron movement based on the material resistivity. Additionally, a circuit can have an electrical device called a resistor, which also restricts current flow. Inductance reactance X_L is the back emf or induced voltage v previously mentioned in the last section. Inductance can occur naturally within the circuit conductor and/or with an electrical device called an inductor. Using Equation (37) for induced voltage and Equation (41) for current, the following equation for induced voltage with respect to an alternating current can be derived:

$$v(t) = \omega L I_{peak} \cos(\omega t) \tag{42}$$

or

$$v_L(t) = \omega L I_{peak} \sin\left(\omega t + \frac{\pi}{2}\right) \ . \tag{43}$$

Furthermore, at peak amplitude, the induced voltage as expressed by Equation (43) can be simplified to

$$V_p = 2\pi f L I_p \ , \tag{44}$$

where V_p is the peak voltage. Therefore, inductance reactance X_L is expressed as

$$X_L = \frac{V_p}{I_p} = 2\pi f L \quad , \tag{45}$$

In contrast, capacitive reactance is 180° "out-of-phase" or in opposition with inductive reactance X_C; as frequency increases, inductive reactance increases (decreasing current) and capacitive reactance decreases (increasing current). As frequency decreases the opposite reaction is true. Hence, the following equation for capacitive voltage (v_c)

$$v_C(t) = \frac{I_{peak}}{\omega C} \sin\left(\omega t - \frac{\pi}{2}\right) \quad , \tag{46}$$

where C is for capacitance and is quantified in *farads.* Also, capacitive reactance X_C is

$$X_C = \frac{1}{2\pi f C} \quad . \tag{47}$$

Therefore, total impedance z is the proportionality constant of system voltage and current, and is equal to the hypotenuse of the three key vector quantities - resistive, inductive, and capacitive reactance as shown in Figure 31. The equation for impedance is

$$z = \sqrt{R^2 + (X_L - X_C)^2} \ . \tag{48}$$

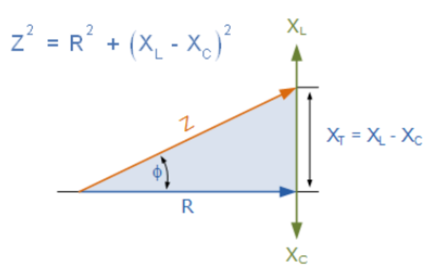

Figure 31: Impedance Triangle for an RLC circuit in series adapted from [46].

Finally, inductive reactance is equal to capacitive reactance at the resonance frequency, and in this situation, impedance is simply equal to resistance. The resonance frequency condition is

$$\omega = \frac{1}{\sqrt{LC}} \ . \tag{49}$$

4.4.2.4 Mutual Inductance

Mutual inductance occurs when the magnetic flux of a coil induces an emf (and "lagging" current) in an adjacent coil or conductive material. In Figure 32, magnetic flux generated by coil 1 couples with Coil 2 of N_2 turns and induces a voltage v_2 of mutual induction in Coil 2. Voltage v_2 is given by

$$v_2 = N_2 \frac{d\Phi_{12}}{dt}, \tag{50}$$

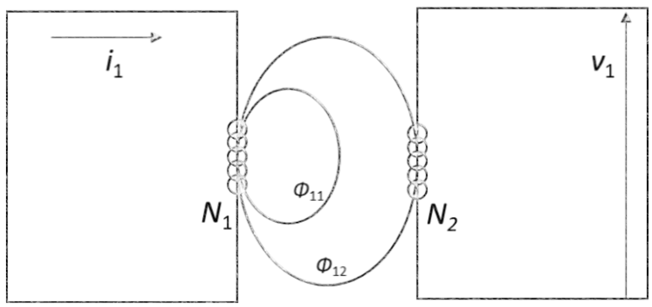

Figure 32: Mutual inductance between two coils.

with the negative sign omitted. Hence, the mutual induction *M* is the proportionality constant of induction *L* between the two coils and is expressed as the following:

$$M_{12} = \frac{N_2 \Phi_{12}}{I_1}, \tag{51}$$

M_{12} being the mutual induction between Coil 1 and Coil 2. Furthermore, changes in current i_1 across Coil 1 results in changes in magnetic flux Φ_{12} within that same element and changes in voltage v_2 of mutual induction in Coil 2. Hence, voltage v_2 becomes

$$v_2 = N_2 \frac{d\Phi_{12}}{di_1} \frac{di_1}{dt} = M_{12} \frac{di_1}{dt} \ . \tag{52}$$

Similar to the concept of back emf or inductive reactance, the induced current in Coil 2 (when excited by Coil 1) generates an opposing magnetic – resulting in a cancellation effect.

Nevertheless, mutual inductance is a proportionality constant between Coils 1 and 2. If the roles were reversed between the coils and Coil 2 was initially energized by current i_2, the following holds true for v_1

$$v_1 = M_{21}\frac{di_2}{dt} \quad . \tag{53}$$

Hence the reciprocating relationship of mutual inductance is $M_{12} = M_{21}$.

4.4.2.4.1 Heat Generation in Titanium

Induction heating in most materials is based on three categories of heating: Resistive Heating (also called Eddy Current Losses or Joule Losses), Dielectric Heating, and Friction Losses (or Magnetic Hysteresis) [13]. Resistive heating or joule losses is the main heating mechanism in induction heating. It is the thermal energy generated by induced currents flowing against inherent impedance of an electrical conductor (joule or ohmic losses ***J·E***) [13]. Dielectric heating occurs when dipolar molecules rotate to align with a time-varying electric field [13]. Lastly, friction losses or magnetic hysteresis is heat generated by atomic dipoles aligning as ferromagnetic material is within a magnetic field [13].

4.4.2.4.2 Heat Generation in CFRP

During induction heating, CFRP has three distinct forms of heat generation: joule losses; dielectric hysteresis; and contact resistance as shown in Figure 33 [12]. Note that current can only be induced back and forth in carbon fibres. In joule losses, conductive fibres can generate heat due to their intrinsic electrical impedance [12]. Fibre-fibre crossover junctions can generate heat through dielectric hysteresis if the fibres are separated by a small polymer gap (the polymer gap can be modelled as a Capacitor) [12]. Contact resistance heating is due to the net sum of impedance as fibres are in direct contact [12]. The net resultant heating is ‘‘volumetric’’ in nature, which is superior to conventional manufacturing processes like conduction, convection, or radiation heat transfer. According to Yarlagadda et al. [12], volumetric heating leads to higher throughput and reduced cycle times; this is particularly advantageous for processing of thick-section composites.

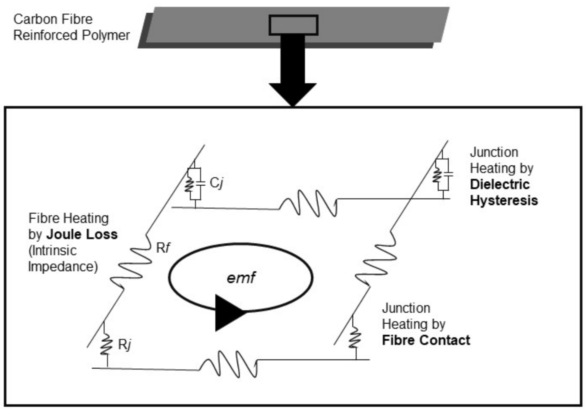

Figure 33: Electrical diagram to model the joule losses, dielectric hysteresis, and contact resistance heating within CFRP adapted from [12].

4.4.2.5 Finite Element Analysis for Induction Heating

The *Heat Transfer* module in *COMSOL Multiphysics®* can simultaneously couple electromagnetic induction and thermal excitation under the *Joule Heating* interface. The FEM model captures the *multiphysics* coupling node as *Electromagnetic Heating*. COMSOL Multiphysics® uses the following governing equation to solve heat transfer problems in a solid [47]:

$$\rho C_p \left(\frac{\partial T}{\partial t} + \mathbf{u}_{\mathrm{trans}} \cdot \nabla T \right) + \nabla \cdot (\mathbf{q} + \mathbf{q}_r) = -\alpha T : \frac{dS}{dt} + \mathbf{Q} \tag{54}$$

- *ρ is the density (SI unit: kg/m^3)*
- *C_p is the specific heat capacity at constant stress (SI unit: J/(kg·K))*
- *T is the absolute temperature (SI unit: K)*
- *$\boldsymbol{u}_{trans}$ is the velocity vector of translational motion (SI unit: m/s)*
- *$\boldsymbol{q}$ is the heat flux by conduction or $\boldsymbol{Q}_{cd}$ in Equations (3) and (4) (SI unit: W/m ^{2})*
- *$\boldsymbol{q}_r$ is the heat flux by radiation or $\boldsymbol{Q}_{rd}$ in Equation (2) (SI unit: W/m^2)*
- *α is the coefficient of thermal expansion (SI unit: 1/K)*
- *S is the second Piola-Kirchhoff stress tensor (SI unit: Pa)*
- *$\boldsymbol{Q}$ contains additional heat sources or $\boldsymbol{Q}_r$ in Equation (34) (SI unit: W/m ^{3})*
- *d/dt* operator is the material derivative

Of note, in steady-state problems, the time derivative terms disappear, and temperature is not a function of time. Also, the colon seen in the first term on the right-hand side denotes that the coefficient of thermal expansion and temperature is a function of the second Piola-Kirchhoff stress tensor. Governing equations offer a multitude of options for boundary conditions and their use depends on the desired numerical effect [47]. For example, the electromagnetic heating *multiphysics* is accounted for with the following equation:

$$\rho C_p \left(\frac{\partial T}{\partial t}\right) - \nabla \cdot (k\nabla T) = \boldsymbol{Q}_e \quad (55)$$

where resistive (ohmic) heating is account for as a function of electrical current [47]. Additionally, $\boldsymbol{Q}_e$, observed as $\boldsymbol{Q}_r$ in Equation (34), represents the resistive heating. Finally, for a specific solution to a specific numerical problem, COMSOL Multiphysics® has many options in terms of boundary conditions, material effects (steady state studies, transient studies, motion studies, deformation studies, etc.) and customizable integration.

4.4.2.6 Considerations with Induction Heating

Induction thermography is limited to the experimental parameters for the desired research. These parameters can cause undesirable electromagnetic phenomena effects. These undesirable effects are an important consideration for the purposes of this research and should be mitigated to yield the desired results. These effects are summarized in the Table 5 [13]. Additionally, it is important to consider the following: a weak current density strength may lead to the thermal signature reading being eclipsed by the ambient surroundings or IR camera noise; and conductive equipment nearby may distort readings. It is important to note these limitations and considerations to render the most definitive induction thermography results.

Table 5: Summary of effects occurring during induction thermography [13].

Name	Characteristics	Schematic
Skin effect	Limitation of the penetration depth of the causative electromagnetic field due to induced magnetic fields with opposite direction (Lenz's Law). This is captured by the skin depth Equation (29):	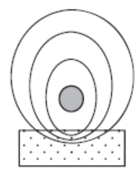 [39]
Proximity effect	Interference with close conducting elements disturbing the electromagnetic field, which results in undesirable heating of neighboring conductive elements and the target work piece.	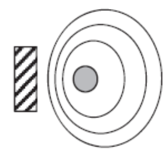 [39]
Ring effect	Concentration of magnetic field lines at the center of a circular coil causes an inhomogeneous field and heating (ring effect).	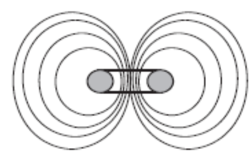 [39]
Edge effects	Change of electrical paths and field lines at the edges of a work piece due to the differences in current density.	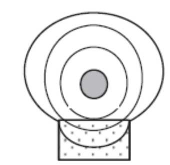 [39]

4.5 Pulsed Thermography

Pulsed thermography is a commonly used thermographic technique because it allows for a relatively simple rapid evaluation of specimens. Note that flash thermography, a subset of pulsed thermography, was used in this thesis and the two nomenclatures may be used interchangeability throughout this narrative. Pulsed IR thermography starts with thermal excitation or heat generation source – lamps or hot/cold air jets. The duration of the thermal excitation can be from 3 ms for a good thermal conductor (i.e. metal components) or 4 s for poor conductors (i.e. plastics or CFRP) [7]. Furthermore, thermal excitation generally only increases the specimen's surface temperature by a few degrees and does not change the material properties of the specimen. In this thesis, halogen bulbs were used as a source of heat generation to rapidly heat a material to a desired temperature gradient with a single pulse. The heat front diffuses through the material. If the material is free of defects and properly bonded, the material thermal properties (conductivity, specific heat capacity, and diffusion) would be uniform as the heat travels through the material. However, if there is an area of delamination, disbond, or inclusion in the material, the thermal energy will concentrate at the boundaries of these areas where thermal energy is impeded or has a slower diffusion rate. Disbond areas, delaminated areas, inclusions or areas containing foreign debris would register as having a greater temperature on an infrared camera. Figure 34 is the setup for pulsed thermography, where two halogen bulbs provide rapid heating of a material and the event is captured by an infrared camera [48].

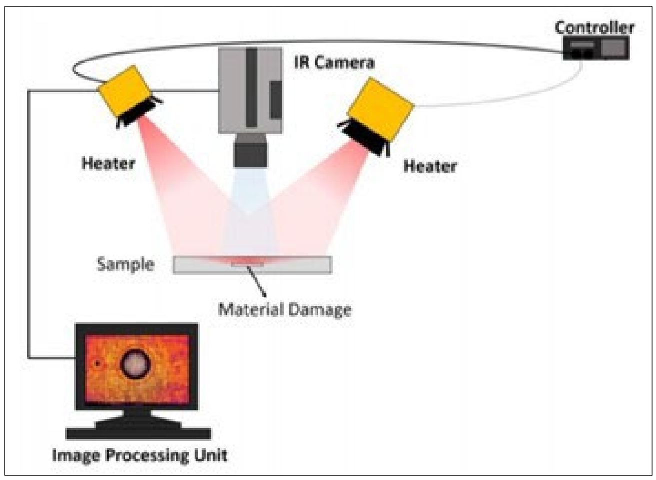

Figure 34: Setup for Pulsed IR Thermography [48].

In pulsed thermography and other types of thermography, the depth of the discontinuity has an effect on the contrast in the thermal image due to the diffusion of heat. Hence, the deeper a discontinuity is in a specimen the later it will be observed and with reduced contrast. This delay and dilution effect is due to the thermal front (after excitation deposits heat at the surface), which diffuses in all directions within the specimen (horizontally as well as laterally). This diffusion in all directions is also known as the spreading effect [7]. Furthermore, the relationship between contrast and depth can be approximated with the following equation [7]:

$$C \cong \frac{1}{z^3} \, , \tag{56}$$

where C is the contrast between the discontinuity and the unaffected surrounding material, and z is the depth of the discontinuity. Additionally, z must be greater than zero. Evidently, the loss of contrast is proportional to the inverse cube of the depth. Additionally, time increases as the square of depth and can be seen in Equation (56) [7]:

$$t \cong \frac{z^2}{\alpha} \quad , \tag{57}$$

where α is the thermal diffusivity of the material.

The theoretical simulation of thermal diffusion in an isotropic solid object is important for prediction analysis in pulsed thermography non-destructive testing and these simulations can be accomplished with the three-dimensional heat equation. Fourier's law states that the rate of heat transfer over a cross-sectional area (or *q=Q/A*) is proportional to the negative gradient of temperature. Consequently, the three-dimensional diffusion heat equation for theoretical simulation is derived from Fourier's law and the conservation of energy equation. The following general differential equation is given as:

$$\frac{\partial}{\partial x}\left(k_x \frac{\partial T}{\partial x}\right) + \frac{\partial}{\partial y}\left(k_y \frac{\partial T}{\partial y}\right) + \frac{\partial}{\partial z}\left(k_z \frac{\partial T}{\partial z}\right) + q_v(x, y, z) = \rho C_p \frac{\partial T}{\partial t} \quad , \tag{58}$$

where q_v is the rate of energy generation per unit volume. Equation (58) accounts for both the isotropic (such as pure metals) and anisotropic material properties (such as composites). If the material is considered to be only isotropic with no internal heat component q_v, and there is a steady state heat flow with no generation, then Equation (58) can be drastically simplified to the Laplace Equation 59:

$$\frac{\partial^2 T}{\partial x^2} + \frac{\partial^2 T}{\partial y^2} + \frac{\partial^2 T}{\partial z^2} = 0 \tag{59}$$

The Laplace equation offers expedient means of simulating the steady state heat flow. However, for more advanced heat transfer problems in pulsed thermography, numerical solvers such as *COMSOL Multiphysics*® can efficiently handle those problems. Equation 58 is the governing heat diffusion equation for simulations in solids given their thermal properties. Table 6 shows the thermal properties of the CF-188 IWSLJ materials.

Table 6: Thermal Properties for CF-188 IWSLJ Materials. Thermal conductivity *k* is equal to the product of density, specific heat capacity, and thermal diffusivity.

Material	Density [kg/m^3]	Thermal Conductivity [W/m-K]	Specific Heat Capacity [J/kg-K]	Thermal Diffusivity [m^2/s]
Titanium (Ti-6Al-4V)[33]	4430	6.70	565	2.677×10^{-6}
CFRP (T700S) [31]	1800	9.34	753	6.891×10^{-6}

Moreover, pulsed IR thermography is a simple method that relies on using Xenon or Halogen bulbs to deposit thermal energy into an object, while observing the object's surface with an IR camera. While other methods of active thermography may incur costly expenses, pulsed IR thermography is ideal in this case because it can accurately detect a range of discontinuities over a vast area and be easily employed at a relatively low cost.

4.6 Ultrasonic Testing

Ultrasonic non-destructive testing uses high frequency sound waves or organized mechanical vibrations to detect defects both on the surface and sub-surface of a material. Ultrasonic testing is used in this thesis to both verify and act as a basis of comparison for the thermography results. The sound wave velocity and direction are specific and predictable as waves propagate as a focused beam in the material [49]. Additionally, the boundaries encountered by the sound waves reflect or transmit the waves given the boundary conditions.

4.6.1 Wave propagation

Ultrasonic wave propagation is a disturbance (either oscillations or vibrations of the particles) that travel in a material carrying an energy. Ultrasonic waves can propagate in solid, liquid, or gas and propagate according to the properties of the material. There are four types of wave propagation modes: longitudinal waves, transverse waves, surface (Rayleigh) waves, and plate (Lamb) waves [49]. Longitudinal or compression waves are the most common waves used for the inspection of material. In longitudinal waves, the particles of the medium travel parallel to the propagation of the wave by means of compression and rarefaction. Transverse or shear waves are waves in which the particles of the medium travel perpendicular to the propagation of the wave. Surface or Rayleigh waves are waves in which the particles of the medium travels in a circular motion to the propagation of the wave. Plate or Lamb waves are exclusive to thin plates (made of composite or metal) and the particle motion is either symmetrical (dilatation) or asymmetrical (bending) as the wave propagates. Although all waves are applicable to NDT, longitudinal and shear waves are predominately used (as shown in Figure 35).

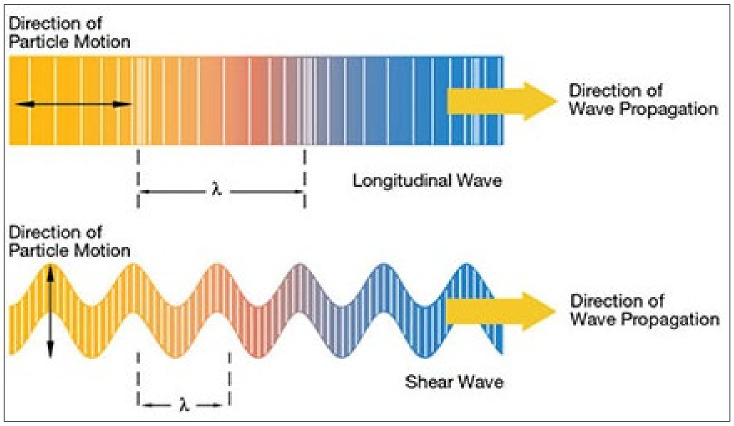

Figure 35: Illustration of longitudinal and shear waves [50].

Additionally, all of these waves are considered pressure waves because of the associated compressional and dilatational forces.

4.6.2 Wave Generation and Types of Ultrasonic Testing

Ultrasonic testing starts with the use of an ultrasonic probe and its piezoelectric transducer. A piezoelectric transducer contains a crystal (such as quartz or Lead Zirconate Titanate, PZT), which converts electrical energy/excitation into mechanical energy/vibrations [49]. The mechanical vibrations from the transducer are transmitted as sound waves in the prospective material and the transducer also receives the sound waves as reflections from the material boundaries. Note that a coupling medium, often water or gel, is used at the interface between the probe transducer and the material being inspected to ensure maximal transmission of sound waves. Additionally, Table 7 shows the acoustic properties such as density, velocity of sound, and acoustic impedance, which determines the wave propagation in the material.

Table 7: Acoustic Properties of Common Materials.

Material	**Density (kg/m^3)**	**Longitudinal Velocity of Sound (m/s)**	**Acoustic Impedance [Z] (kg/m^{2}s)**
Water [51]	1000	1483	1.5 x 10^6
Air (20 C) [51]	1.204	343	413.2
CFRP [51]	1450	2622	11 x 10^6
Titanium	4430	6100 [51]	27 x 10^6

When the sound waves are being received by the transducer, the transducer crystal converts the mechanical vibrations into electrical signals. If a defect is present in the material, it will be represented within the electrical signal as a discontinuity within the otherwise uniform material. These electrical signals are then reassembled, displaying the internal features of the material, and analyzed. The analysis may consist of considering the signals due to the material features or boundaries, amplitude changes in the transmitted and reflected signal, the time-of-flight of the sound wave, and attenuation of the sound wave signal [51]. Ultrasonic testing is generally in two forms: through-transmission and pulse-echo as shown in Figures 36 and 37, respectively.

Through-Transmission Ultrasound Testing uses a transducer for transmitting sound waves, and another transducer for receiving sound waves (Figure 36). The basic principle of through-transmission is that the receiving transducer does not receive acoustic energy that has been attenuated or reflected by a defect in a medium.

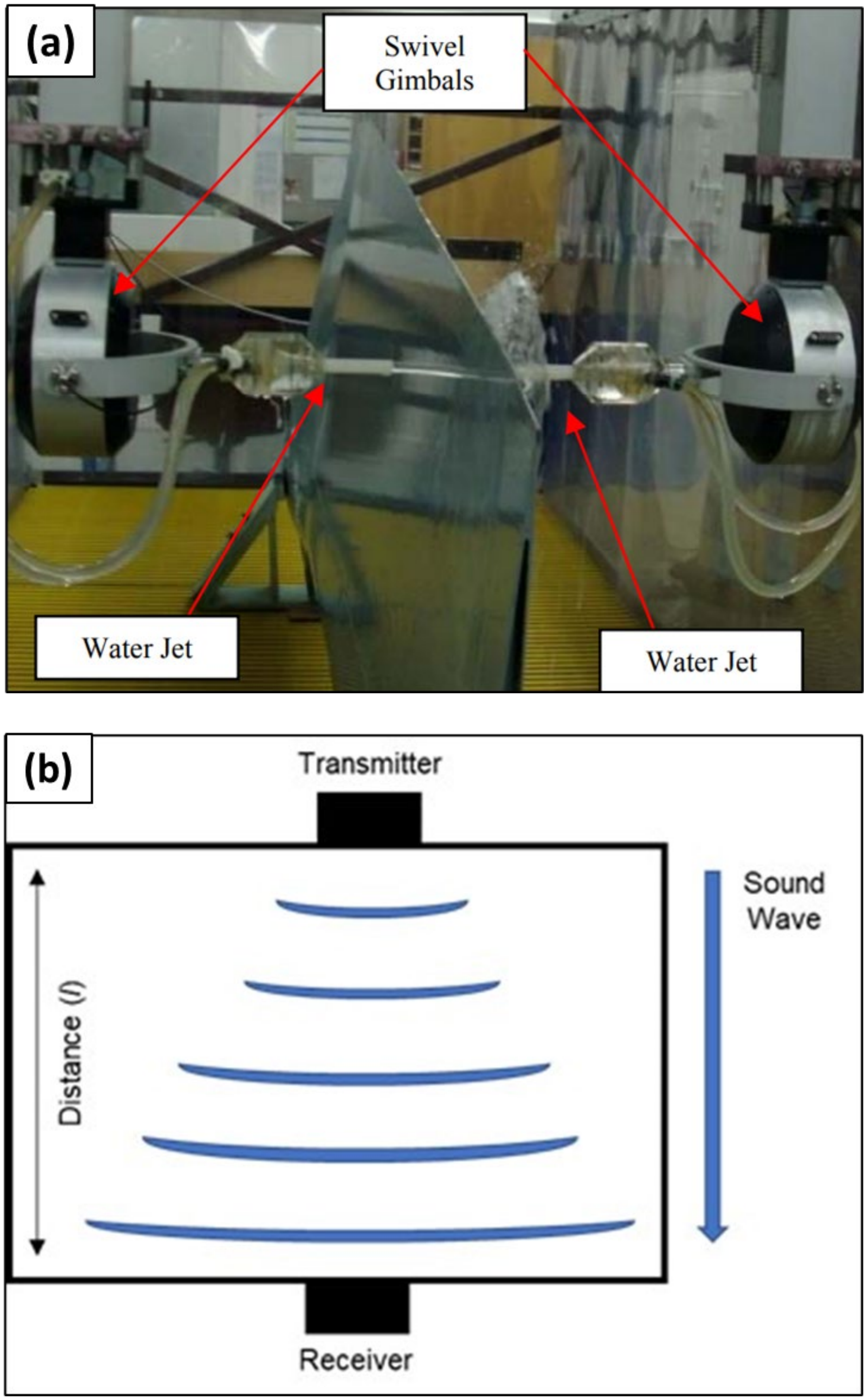

Figure 36: (a) Through-Transmission UT Set-Up for an Aircraft Component at QETE [51]. (b) Fundamentals of through-transmission UT where a transducer is transmitting sound waves and another transducer is receiving sound waves.

The ultrasonic testing preformed by the ARMANDA system employs pulse-echo ultrasonic testing. Pulse-Echo ultrasonic inspection uses pulses of ultrasonic energy through a single probe transducer to both transmit and receive sound waves (Figure 37).

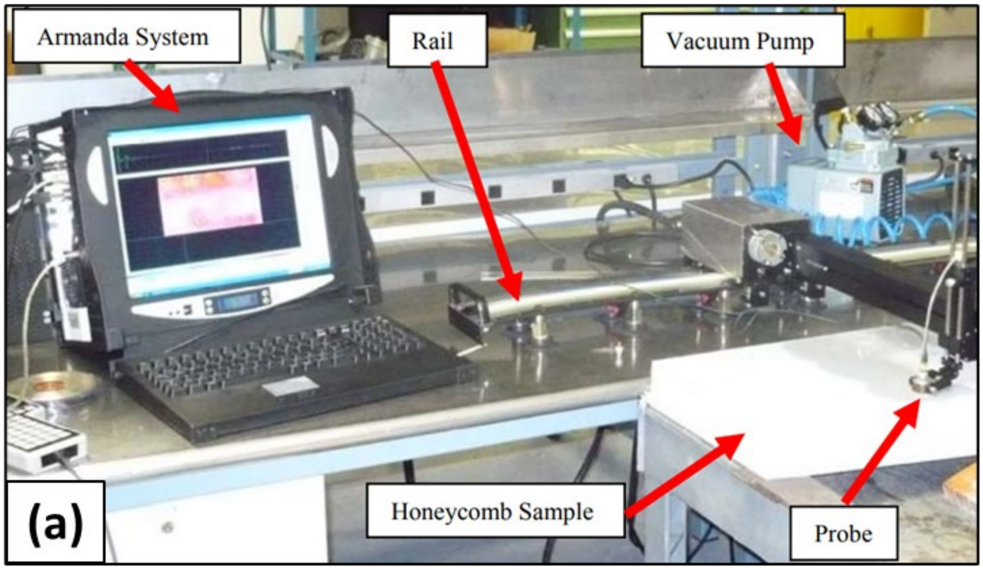

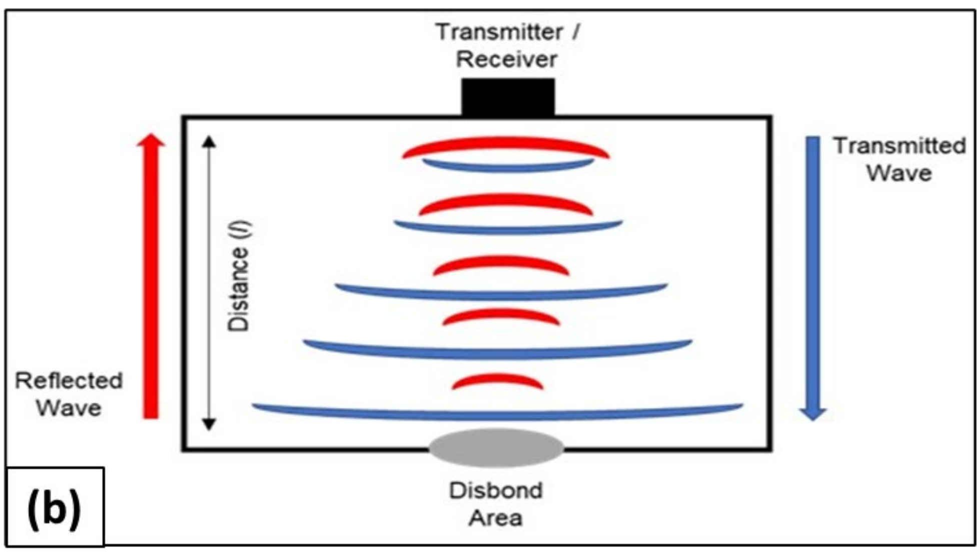

Figure 37: (A)Experimental Set-up of TecScan Armanda System Scanning a Disbond Sample [51]. (B) Principles of Pulse-Echo Ultrasonic Testing where a transducer is both transmitting and receiving sound waves.

4.6.3 Attenuation and Reflection

Attenuation is a reduction in amplitude of the ultrasonic beam as a function of distance through a medium. It is an important factor in ultrasonic testing because the reduction in signal amplitude can reduce the quality of the image and lead to difficulty finding defects. CFRP is relatively high in terms of attenuation, and therefore, inherently difficult to inspect with ultrasonic testing. Attenuation is directly linked to the distance and frequency. The reduction in acoustic pressure of a media will decay as:

$$\boldsymbol{P} = \boldsymbol{P}_o e^{-\alpha L} \,, \tag{60}$$

where $\boldsymbol{P}$ is the acoustic pressure of the second reference location, $\boldsymbol{P}_o$ is the initial acoustic pressure at the source, α is the attenuation coefficient, and L is the distance travelled by pulse from the source to the second reference location. Attenuation is measured in decibels per meter (dB) and can be expressed as:

$$\alpha L = 20 log \frac{\boldsymbol{P}_o}{\boldsymbol{P}} dB \ . \tag{61}$$

In ultrasonic testing, ± 6 dB is an important point of reference because it constitutes an increase or decrease of a factor of two in signal amplitude. In fact, the – 6 dB drop is widely used to approximate the length or width of a discontinuity in a material [49]. A -6 dB drop correspond to half the original amplitude.

Reflection of acoustic waves occurs as waves pass through one medium and enters another medium of a different acoustic impedance. Reflection is the fraction of the acoustic wave that bounces back or does not enter the medium. Reflections is important because it prevents the detection of discontinuities by virtue of not passing an acoustic wave through to the second medium. The percentage or amount of reflection is determined by impedance difference between the two mediums. The impedance, Z (kg/m^{2}s), is expressed as $Z = \rho c$, where ρ is the density of the material, and c (m/s) is the speed of sound through the material. Hence, the Equation (62) defines the percentage of reflection between two mediums.

$$\% \, Reflection = \left[\frac{z_2 - z_1}{z_2 + z_1}\right]^2 . \tag{62}$$

Note that Z_1 is the first medium and Z_2 is the second medium. This ultrasonic testing theory was crucial for understanding the experimental work.

CHAPTER 5 – FINITE ELEMENT METHOD MODELS FOR INDUCTION HEATING

5.1 Introduction

In order to help define or narrow down experimental test parameters for induction heating in Study 1, finite element analysis using the *COMSOL Multiphysics*® software version 5.6 was used to observe trends in induction heating by first establishing a temperature distribution prediction method. The FEM model was validated with experimental results and allowed for trends to be observed using induction heating simulations. As mentioned in Chapter 3, an analytical solution for induction heating is often not possible due to the simultaneous processes of electromagnetic induction and thermal diffusion. Additionally, the boundary conditions and complexity of the geometry are contributing factors. Hence, numerical analysis through a FEM model is required. FEM models are used throughout science and engineering because they can handle complex geometries and boundary conditions, while applying the appropriate physics. FEM solvers employ sophisticated algorithms to simultaneously solve systems of partial differential equations through matrix inversion or recursive minimization.

The study of induction coil parameters was accomplished with a FEM model that predicts temperature distribution from the application of a magnetic field. In the FEM model construction, *COMSOL Multiphysics®* was used to establish the following for the component: definition of environmental or atmospheric condition, geometry, material(s), the physics interface, and the mesh. Then, the results were obtained and compared to the experimental results. Finally, trends were observed from simulations with the FEM model in a parametric investigation.

5.2 Experimental Parameters for Validation

In order to validate the baseline FEM model, a strong agreement with experimental data was required. The experiment setup consisted of a pancake coil and a titanium alloy (Ti-6Al-4V) plate. The pancake coil had five turns of 6.35 mm square copper tube with an inside diameter (ID) of 12.7 mm and an outside diameter (OD) of 88.9 mm. The titanium plate was 152.4 mm x 152.4 mm x 2.54 mm and coated with black paint (approx. 0.97 in emissivity). The experimental procedure consisted of heating the titanium for a period of six seconds and observing the event with a FLIR infrared camera. The maximum temperature at one second intervals on the surface of the titanium plate was observed. The induction system was set to 60 A and the coil was placed at height of 6.35 mm above the surface of the titanium. The resonance frequency during the induction heating process was 348 kHz. Note that power was not controlled and was a function of the input current. Also, the temperature distribution increased over time and the highest temperatures were directly beneath the coil tubing. The experiment was repeated several times for the sake of repeatability. No significant variation was noted. Finally, the data collected was used to validate the baseline FEM model.

5.3 Baseline Model

In order to build a FEM model in *COMSOL Multiphysics®*, the *Model Wizard* interface was used to select the component geometry in the 2D axisymmetric domain, the induction heating physics interface, and the frequency-transient study. The 2D axisymmetric domain was appropriate for the component geometry given that the experimental setup was axisymmetric about the z-axis. The *Model Wizard* is a user interface that is used to select the space dimension, physics interfaces, and the study for the applicable FEM component. The 2D axisymmetric domain allowed construction of 2D FEM models in the $r\ \varphi\ z$ cylindrical coordinate system. The radial distance r is the distance from the z-axis, the azimuthal angle φ is the angle between the reference plane and the final plane, and z is the distance between two points on the z-axis. 2D FEM models have the advantage of simplifying the model through dimensional symmetry and reducing computational time and memory. Hence, this advantage was the premise for building in the 2D axisymmetric domain. *COMSOL Multiphysics®* has a feature for electromagnetic heating simulations called the Induction Heating Physics Interface. This interface couples electromagnetic induction and heating to predict temperature distribution in induction heating problems. Lastly, the frequency-transient study was selected because it computes electromagnetic fields in the frequency domain and temperature in the time domain [47]. This is the proper study for induction heating, microwave heating, inductively coupled plasma and microwave plasma problems [47].

5.3.1 Geometry

The geometries required for the FEM model consisted of a pancake coil and a titanium alloy (Ti-6Al-4V) plate. The pancake coil had five turns of 6.35 mm square copper tube with an inside diameter (ID) of 12.7 mm and an outside diameter (OD) of 88.9 mm. The titanium alloy plate was 76.2 mm in radius with reference to the centre or axis of symmetry. It was also 2.54 mm thick. The CFRP was excluded because experimental data demonstrated that the thermal signature of titanium eclipsed that of the CFRP, meaning that thermograms generally showed the titanium heat signature over the CFRP heat signature. This was due the significantly higher thermal conductivity and electrical of titanium. Chapter 7 (Section 7.1.3.3) contains more details. The coil was 6.35 mm above the titanium plate. Table 8 highlights the parameters used to construct the FEM model.

Table 8: Description of parameters used to build the FEM model in COMSOL Multiphysics®.

Name	**Description**	**Assigned Value [mm]**
Lift_Off	Distance between coil and titanium surface.	6.35
Coil_Dia	Diameter of a solid copper tubing for circular tubing. Also, it is the dimension of the length and width for the square tubing.	6.35
Outer_Sphere	Diameter of the spherical environment or the outer boundary of the modeling domain.	200
Inf_Dom	Thickness of the infinite domain layer.	40
Ti_Thickness	Titanium Thickness.	2.54
Ti_Width	Titanium Width (radius length from the centre line).	152
Coil_Gap	The gap between the coil tubing with each turn of the coil.	3.18

In *COMSOL Multiphysics®*, the geometry tab allowed for the quick construction of the coil and titanium plate from primitive shapes such as circles and squares. To create a realistic environment, *COMSOL Multiphysics®* has a feature or report node called an Infinite Element Domain. An infinite element domain is the application of a real-valued coordinate scaling to a layer of virtual domains surrounding the physical region of interest [47]. Through coordinate stretching, a virtual representation of physical space is simulated. In short, an Infinite Element Domain represent an infinite medium of air with specified atmospheric conditions (i.e. temperature, pressure, mass flow/wind, etc.). In Figure 38, the Infinite Element Domain is the layer of semi-circles surrounding the coil and titanium plate.

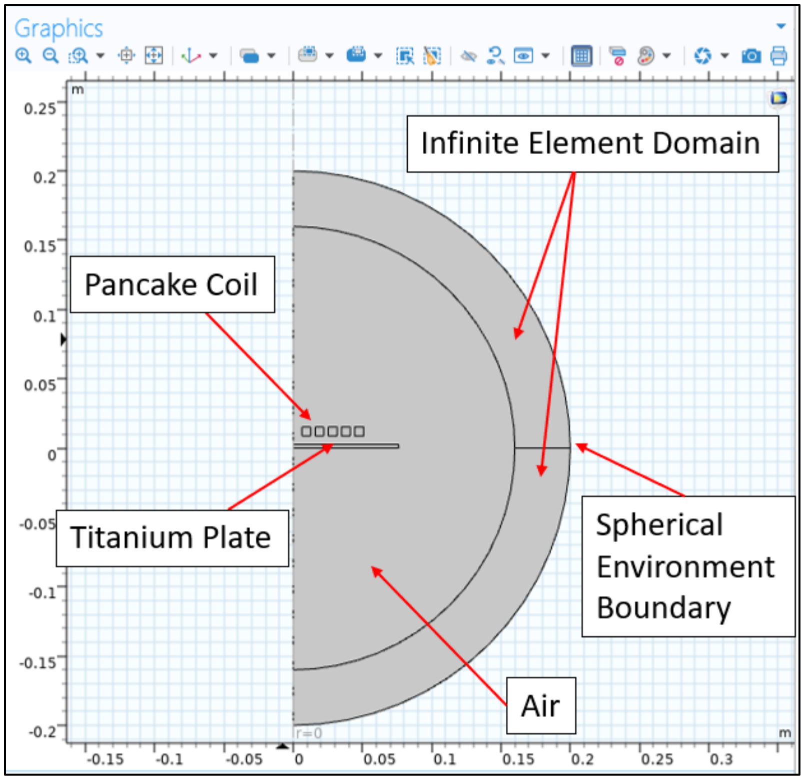

Figure 38: An image of the components of the FEM model.

5.3.2 Material Properties

The FEM model was constructed with three materials: air, copper, and titanium (Ti-6Al-4V). These materials align well with the fact that the experimental coil was copper, the titanium was used for the plate, and everything else was surrounded by air. *COMSOL Multiphysics*® has a library of materials built into the software. Air and Copper were taken from the *COMSOL Multiphysics*® material library, but values for titanium were entered specifically for Ti-6Al-4V. The material properties are shown in Table 9. Furthermore, an emissivity of 0.97 was applied to the surface of the titanium alloy to best simulate a coat of black paint (similar to the experimental coating described in Section 6.2.2).

Table 9: Material properties for the baseline FEM model in COMSOL Multiphysics®. Note that the variables in the table are derived from the simulated atmosphere conditions in COMSOL Multiphysics®.

	Air	**Copper**	**Ti-6Al-4V**
Relative Permeability	1	1	1
Electrical Conductivity [S/m]	0	5.998e7	5.8e5
Heat Capacity [J/kg·K]	Cp(T)	385	565
Relative Permittivity	1	1	1
Density [kg/m^3]	Rho(pA,T)	8960	4430
Thermal Conductivity [W/m-K]	k(T)	400	6.7

5.3.3 Boundary Conditions

There are seven categories of boundary conditions available in the heat transfer module of *COMSOL Multiphysics®*. This FEM work focused on radiation and convection as the boundary conditions of interest. Heat radiating from the Ti-6Al-4V to ambient was applied to the surfaces or boundaries of the Ti-6Al-4V through the *COMSOL Multiphysics® surface-to-ambient radiation* node. In *COMSOL*, the *surface-to-ambient radiation* boundary condition was applied based on the surface emissivity of 0.97 and an ambient temperature of 293.15 K. For the radiation boundary condition, *COMSOL* solves Equation (2) at the interface or boundaries. Note that the copper coil did not receive any boundary conditions because induction heating of the titanium plate is the basis of the FEM simulations. Also, in the experimental investigation, the copper coil was water cooled, and hence, induction heating of the titanium was the only source of heat. There was no radiation from the copper coil. Convection was applied to the boundaries of the Ti-6Al-4V with the *Heat Flux* node. Convection was a factor in the experimental investigation because a fan blowing air was used throughout for rapid cooling, and later, for contrast. For convection, the heat transfer coefficient of air (the basis of the boundary condition in *COMSOL*) was set to 20 W/m^2·K to reflect the use of the fan in the experimental investigation. For the convection boundary condition, *COMSOL* solves Equation (5) at the interface or boundaries. Finally, a default discretization of the second-order (quadratic) for induction heating was used because the partial differential equation (54) had a dominant second derivative term.

5.3.4 Mesh Construction

The *mesh* is the foundation of the FEM model and consists of a network of *finite elements* connected by *nodes* as shown in Figure 39. Note that in Figure 39, the coils are square which accurately matches the experiment pancake coil.

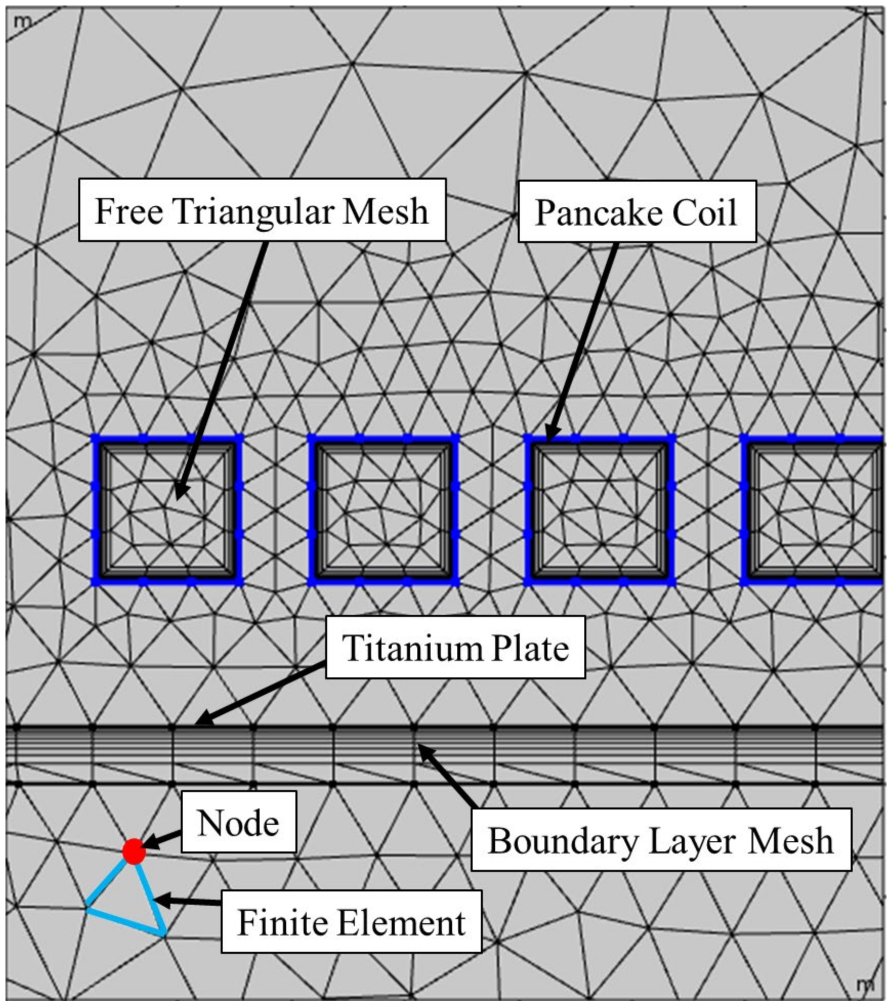

Figure 39: Illustration of FEM model mesh and associated elements.

The partial differential equation is applied to the elements, and the solution is calculated at the nodes. The shape of the mesh is selected based on the geometry. If the mesh is small enough, it will not affect the solution. The solution is only a good solution if it is mesh independent. The FEM model solution is a combination of all nodal results. A fine mesh, or a mesh consisting of high nodal density, is used for complex geometries and can yield accurate numeric results, if applied appropriately. Additionally, a fine mesh is also used in regions where the dependent variable (i.e. temperature) has a high gradient. In other words, where the magnitude of the temperature differs greatly between adjacent elements.

In the coil parameters study conducted, as shown in Figure 39, the following mesh types were established: a Free Triangular mesh was used for regions of lesser importance throughout the geometry; and a Boundary Layer mesh was used with special attention to the penetration depth of electromagnetic skin effect. Given the relative simplicity of the induction heating study and the symmetry of the associated component geometry, accurate numeric trends were achieved with only two-dimensional (2D) FEM models. A three-dimensional (3D) FEM models were not worth the additional computational cost.

5.4 Results

The following are the results from a trend investigation using FEM models.

5.4.1 Trends

COMSOL Multiphysics® allowed for the examination of three different coils: a helical coil perpendicular to the simulated titanium alloy; a helical coil parallel to the simulated titanium alloy; and a pancake coil. Examples of these coils can be observed in Figures 40 and 41.

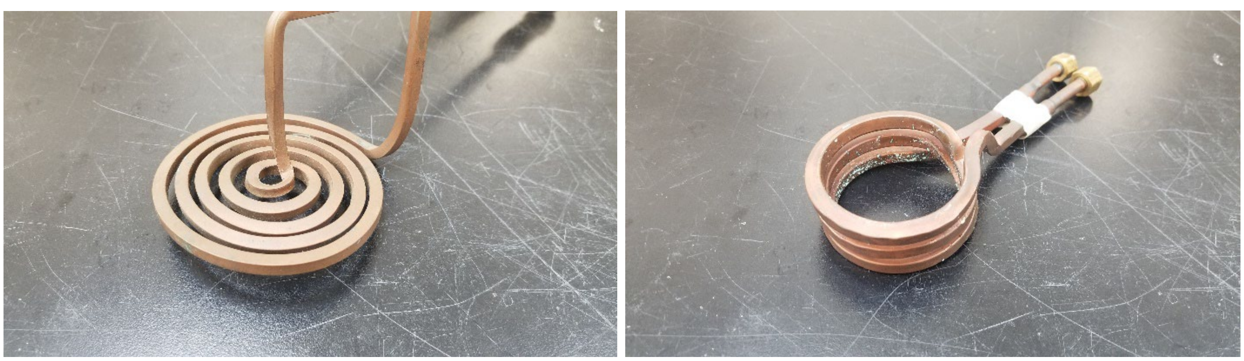

Figure 40: An example of a pancake coil (left) and a helical coil (right).

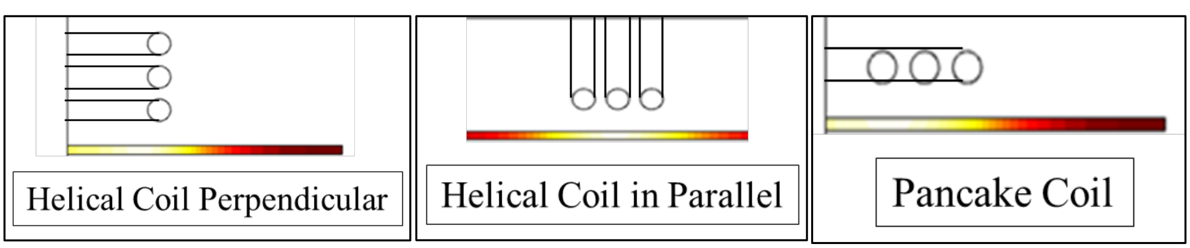

Figure 41: A helical coil perpendicular to the simulated titanium alloy, a helical coil parallel to the simulated titanium alloy, and a pancake coil.

These coils were selected for assessment because of their efficiency in induction heating and design. A numerical analysis was preformed on the coils to gather information on: (1) a reasonable frequency range for efficient induction heating; (2) the number of turns for efficient heating; (3) the coils' heating pattern and potential for even heating; and (4) which coil is most efficient. The following settings remain constant for all coils in the numerical analysis: copper was used for the coil and titanium was used for the plate; the lift-off distance was 6.35 mm; the coil current was 60 A; the mesh was consistent throughout; and the boundary conditions also remained consistent throughout. Figure 42 shows the three coils and the resulting lines of simulated magnetic flux.

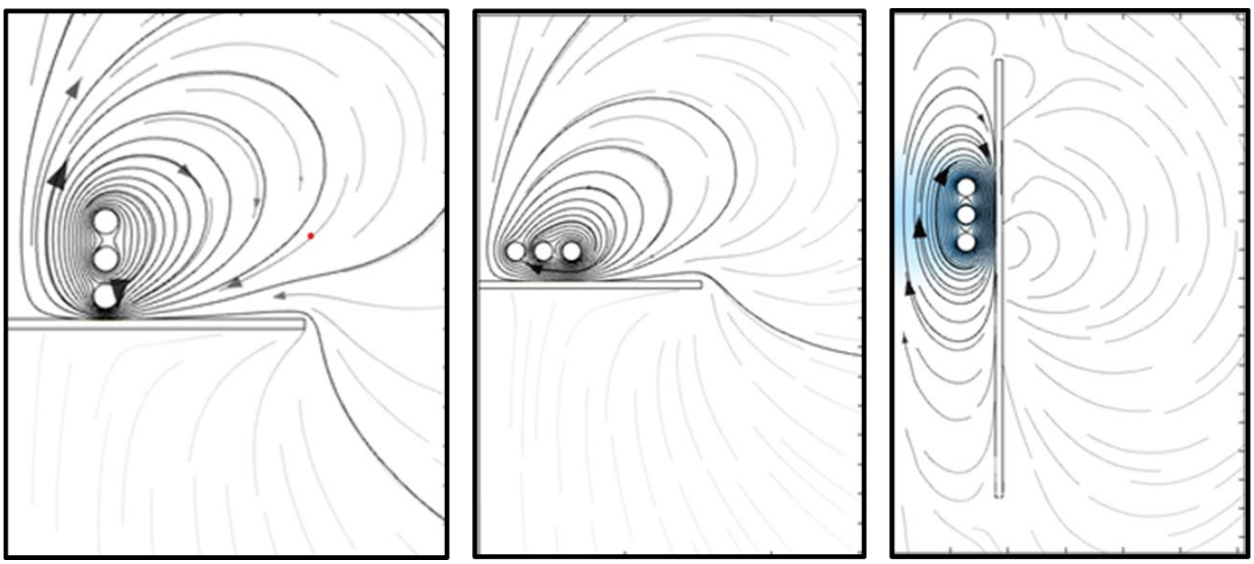

Figure 42: Magnetic flux of a helical coil perpendicular to the simulated titanium alloy, a pancake coil and helical coil parallel to the simulated titanium alloy.

5.4.1.1 Trend – Frequency and Induction Heating

The first part to the analysis examined the effects of frequency on induction heating of the three coils. In Figure 43, the data from the FEM models are shown. Additionally, the coil power and titanium alloy surface current density were plotted for each coil. The ultimate goal was to determine an appropriate frequency for each coil and compare the results. The point on the plot where power and current density intersect was considered to be the point of best coil power input for resultant surface current density. These points corresponded to the following frequencies: 375

kHz for the helical coil in parallel; 280 kHz for the perpendicular helical coil; and 240 kHz for the pancake coil. Beyond these points there is a substantial amount of power required for little surface current density returns. This is because as frequency increases, impedance increases and there are diminishing returns in surface current density for the power input. Also, skin depth decreases, concentrating the current on the surface. I**t was determined that 240 – 375 kHz would be a reasonable frequency range for induction heating**. These results were inline with the resonance frequencies from the experimental result (235 – 351 kHz) in Chapter 7.

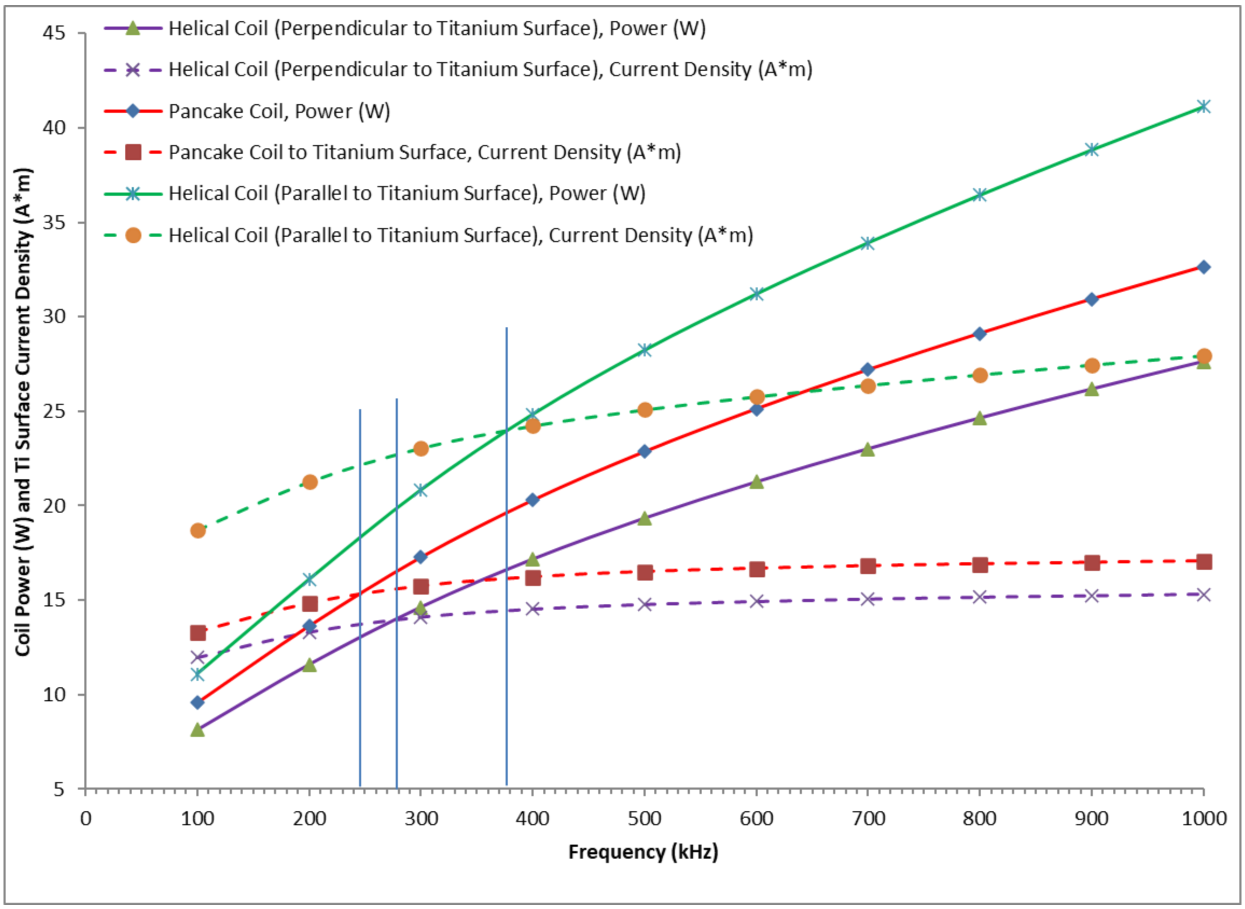

Figure 43: Coil Power and Titanium Surface Current Density with respect to frequency.

The FEM temperature results (on the surface of the titanium) was plotted as a function of frequency in Figure 44. This graph acted as a means of comparing the three coils in terms of temperature and frequency. The **pancake coil generated the highest temperature given the frequency** – followed by the helical coil in parallel and the perpendicular helical coil. The magnetic flux density, and subsequent, volumetric losses density is greatest with the pancake coil because of its geometry and orientation relative to the titanium alloy plate.

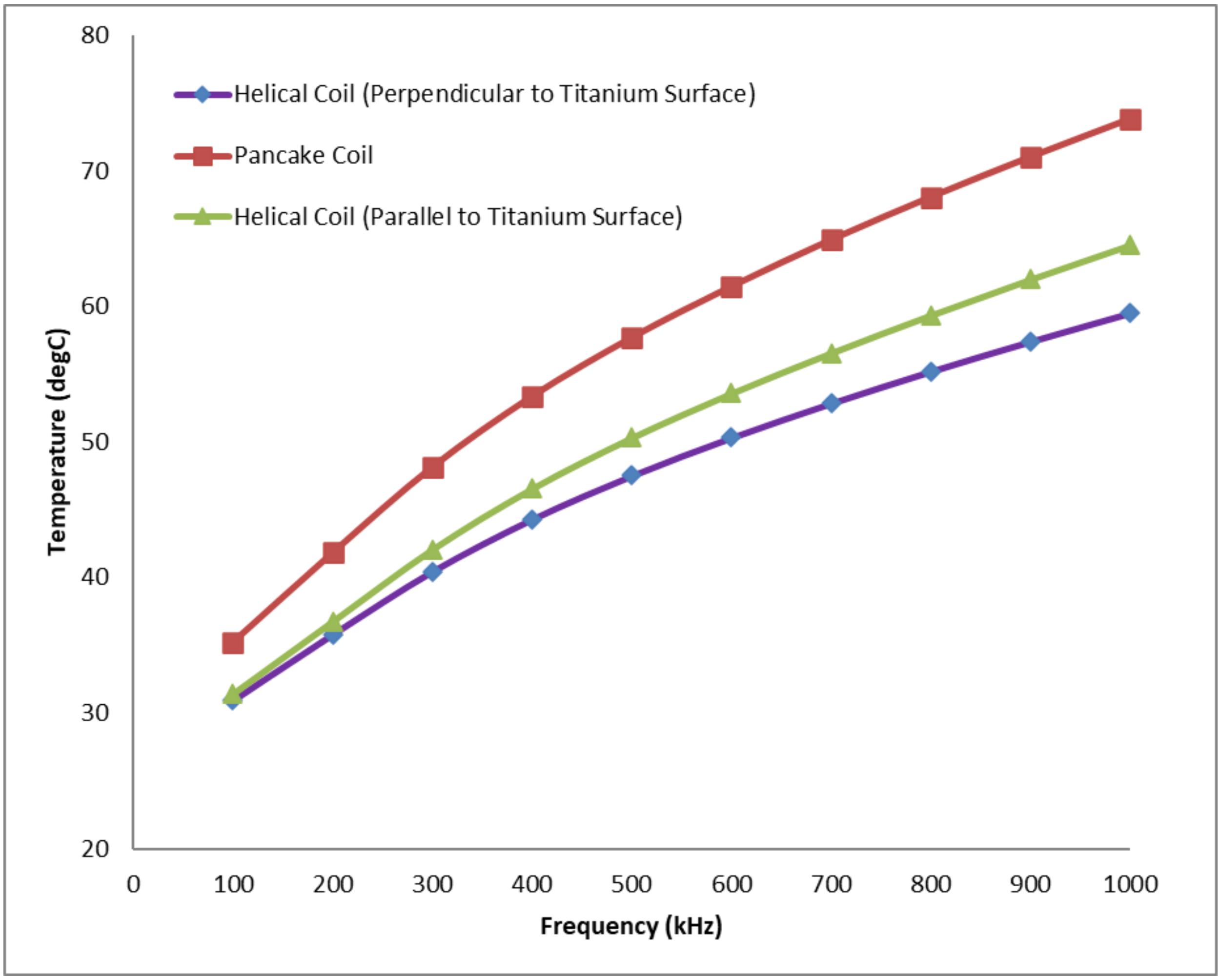

Figure 44: Temperature on the surface of the titanium with respect to frequency.

5.4.1.2 Trend – Number of Turns (N) and Induction Heating

Secondly, the FEM models were used to gather information on the number of turns or windings and input power for efficient heating. This was significant in the coil selection and design process due to the vast number of possible turns. In Figure 45, coil power and titanium surface current density were plotted against the number of turns in each coil. Only the first seven turns of the coil were examined; additional turns of the coil would settle beyond the length of the titanium plate for the pancake coil and parallel helical coil. The frequency was set to 100 kHz. There existed a point in the plot where power and current density intersect. This point is considered the point of best coil power input to resultant surface current density. Beyond these points for the helical coils, more power is required for little surface current density returns for the subsequent turns. However, for the pancake coil the opposite is true. The ideal number of turns was determined to be five turns of the pancake coil, 3-4 turns for the perpendicular helical coil, and beyond seven turns for the helical coil in parallel.

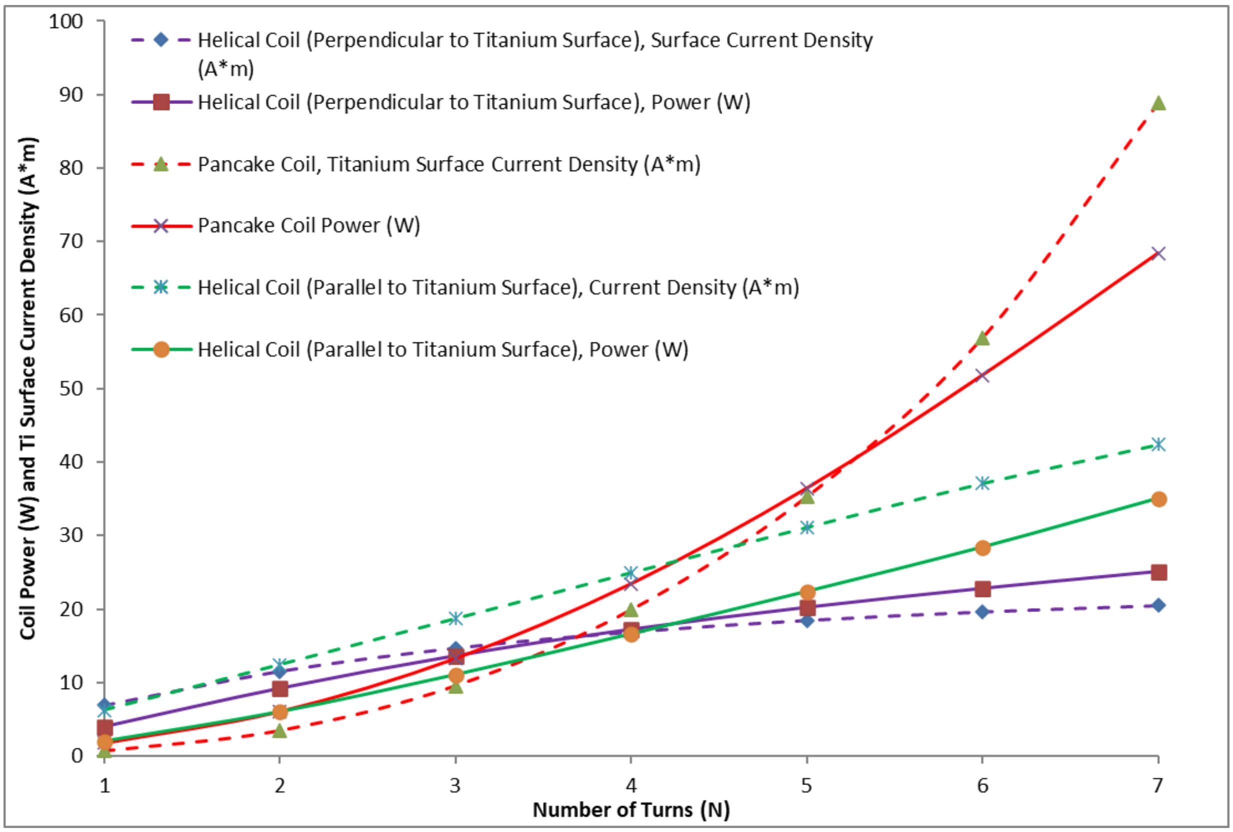

Figure 45: Coil Power and Titanium Surface Current Density with respect to the number of turns.

5.4.1.3 Trend – Uniform Heating and Coil Type

Thirdly, the heating pattern of each coil was examined with *COMSOL* to assess the most even heating. One difficulty of induction heating was establishing uniform heating. Uniform heating is important for eliminating false positives. The **pancake coil was determined to offer the best uniform heating with the lowest power input** as shown in Figure 46. This assessment resulted from observing an even temperature distribution along the length of the titanium alloy plate and the greatest rise in temperature at a given power input. The perpendicular helical coil, in Figure 46(a), had a high heat concentration directly under the coil rather than along the titanium alloy plate. This was not ideal. The helical coil in parallel, Figure 46(c), had an even heat distribution along the length of the titanium alloy plate, but had a lower temperature than the pancake coil. Meaning more power would be required by the helical coil in parallel to achieve the same temperature as the pancake coil.

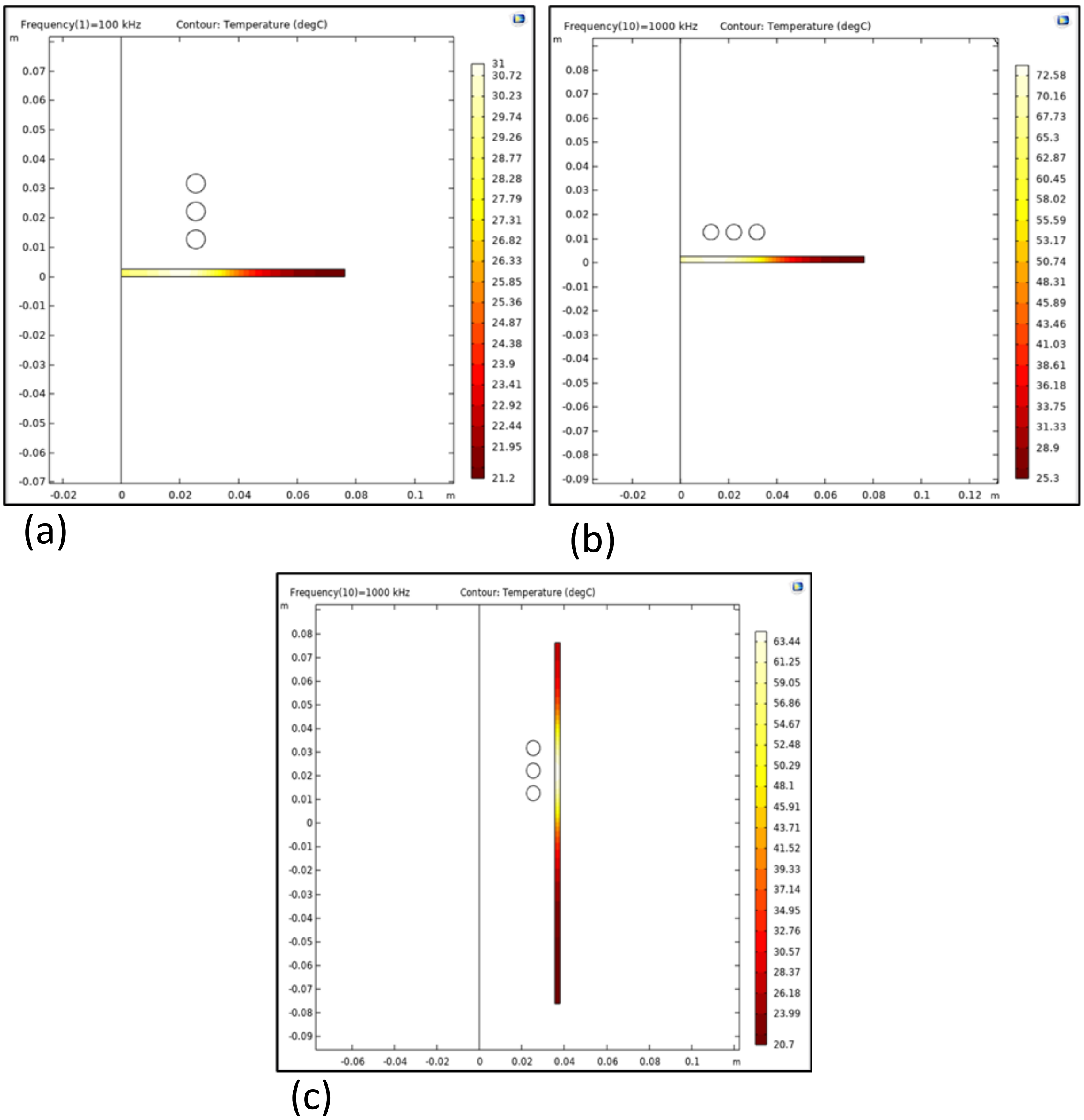

Figure 46: Heating patterns of the three coils of interest: (a) the helical coil perpendicular to the surface; (b) the pancake coil, and (c) the helical coil parallel to the surface.

5.5 Validation Results

In Section 5.2, all experimental parameters for the validation of the *COMSOL Multiphysics®* numerical results were outlined. Note that a mesh convergence study was conducted to further reduce computational time. Also, the boundary conditions highlighted in Section 5.3.3 remained the same for this validation. The FEM model validation is shown in Table 10 with a maximum percent difference of 5.7% between the experimental and FEM model. A pancake coil and a frequency of 348 kHz were used. The slight percent difference can be attributed to the variations between the simulation boundary conditions and the conditions within the experimentation. Nevertheless, the agreement between the FEM model and experimental investigation was adequate for the follow-on trend study.

Table 10: FEM model validation table. The experimental temperature values are the maximum temperatures for the titanium alloy (Ti-6Al-4V) plate measured from the highest temperature value on the surface of the plate.

Time [s]	Experimental [˚C]	COMSOL [˚C]	% Difference
0	25.7	25.7	0.0%
1	25.7	25.7	0.0%
2	25.7	25.7	0.0%
3	26.6	27.9	-4.9%
4	29.8	29.7	0.3%
5	32.7	31.5	3.7%
6	35.2	33.2	5.7%

5.6 Conclusion

In summary, numerical analysis through a Finite Element Method (FEM) was used to simultaneously solve an electromagnetic induction and heat transfer problem. The type of mesh applied to a structure determines the accuracy of the solution and the finite elements required for the validity of the model. At the end of the analysis, it was determined that a frequency range of 240 – 375 kHz would be reasonable. The pancake coil at three turns generated the highest temperature given the frequency and offered the best even uniform heating. Although the helical coils were more power efficient in term of the number of turns, the pancake coil was superior in almost all other aspects such as power-to-surface current density, temperature as a function of frequency, and uniform heating.

CHAPTER 6 – EXPERIMENTAL METHODOLOGY

In the introduction, the objective of this thesis was established as a comparison and evaluation of flash and induction thermography for detecting and dimensioning disbond areas in the IWSLJ (CF/E-Ti laminate). The objective was achieved through experimental testing on a Calibration Block and manufactured CF/E-Ti specimens with artificial disbond areas. Different surface preparation methods were also considered in order to create and compare kissing bonds and traditional disbonds (i.e. Disbond areas created with thermal tape inserts and Flat Bottom Holes). For the purpose of this experimental work, all specimens were composed of Grade-5 titanium Ti-6Al-4V and VTC401 Prepreg unidirectional CFRP. The results were then compared to the standard method of ultrasonic testing (UT) as a verification step. The comparison process of flash and induction thermography consisted of four studies. Namely:

Study 1 – Induction thermography was used on a manufactured panel of CFRP and Ti with artificial defects (Bonded Panel 2). Different coils and coil parameters were used to determine the optimal parameters for induction heating;

Study 2 – Flash and induction thermography was used on different CFRP thicknesses of manufactured CFRP and Ti panels with artificial defects (Bonded Panel 1 - 4). The goal was to detect disbond areas and determine the dimensions (in the x and y direction) of the disbond areas. The results were compared to UT results for verification;

Study 3 – The penetration limit of flash and induction thermography was evaluated using a Calibration Block with all nine steps of the IWSLJ as well as the manufactured panels (identified in Study 2) with varying CFRP thicknesses. The results were once again compared to UT results for verification; and

Study 4 – In order to assess the level of disbond discrimination obtained through each inspection method, Sample No. 1 was inspected with each method. Sample No. 1 was ideal for this testing because it contained many different types of disbond defects from different inserts and surface treatments.

The experimental methodology was specifically designed to achieve the objective of this thesis (Section 1.4) and this chapter outlines all particulars involved in the experimental methodology. Of note, the ARMANDA system ultrasonic method is covered extensively elsewhere (Section 6.5) and this chapter will simply summarize the UT method used.

6.1 Test Specimens

6.1.1 IWSLJ Ultrasonic Testing Calibration Block

As mentioned in the introduction, the CF-188 wings are complete with two lap joints called the Upper and Lower IWSLJ with respect to their positional location. There are two lamination interfaces of the titanium and CFRP on each IWSLJ – labelled the Outer and Inner Mould Line (OML & IML) as shown Figure 3. Note that the IML is enclosed within the wing and cannot be accessed to perform a direct NDE method. For this reason, this thesis only focuses on the OML – with special attention to the first two steps (Steps 1 and 2 on the inboard end of the bonded joint) where disbond areas are most likely to form. The first two steps are also of significance because they have the thinnest layers of CFRP and disbonds can be easily detected with thermography. Although UT can detect disbond areas past the first two steps, it may not be necessary if the disbond area is detected by thermography in the first two steps (Steps 1 and 2) and undergoes repair or replacement before the disbond reaches the deeper steps. UT (although superior and comprehensive in comparison) might not be required, and simple (low effort) thermography might be sufficient. Additionally, discontinuities have never been identified on the IML in the history of the F/A-18. Unfortunately, the exact dimensions of the CF-188 IWSLJ are confidential and could not be used. However, the IWSLJ ultrasonic testing Calibration Block serves as a reference sample because it is an actual sectional cut of the IWSLJ.

Figure 47 shows the IWSLJ ultrasonic testing Calibration Block with dimensions 35 cm x 10 cm x 1.3 cm. The Calibration Block has lines along the width of the sample indicating step one, step two, and the outer edge of the ninth step. The Calibration Block also has drilled out 12.7 mm flat bottom holes (FBH) on the rear face to simulate disbond and delamination areas for ultrasonic testing. The front or calibration face of the block has lettering from A to E. Letters B to E have pairs and are differentiated with an encompassing red or black circle. Note that letters A and E are intentionally only in black circles; the Calibration Block was received with this feature. For the purposes of UT, the letters encircled in red denote a disbond or delaminated area, while the black encircling denotes a good bond or region without defect. The lettering of Figure 47 represents the following: Point A, over the titanium (or step zero without CFRP), is used for the titanium UT calibration; the Bs are located over step one and represent the UT calibration point for disbond areas; the Cs are over step two and are also used for disbond areas; and the Ds & Es are forward and aft of the ninth step and represent the UT calibration point for a delaminated area.

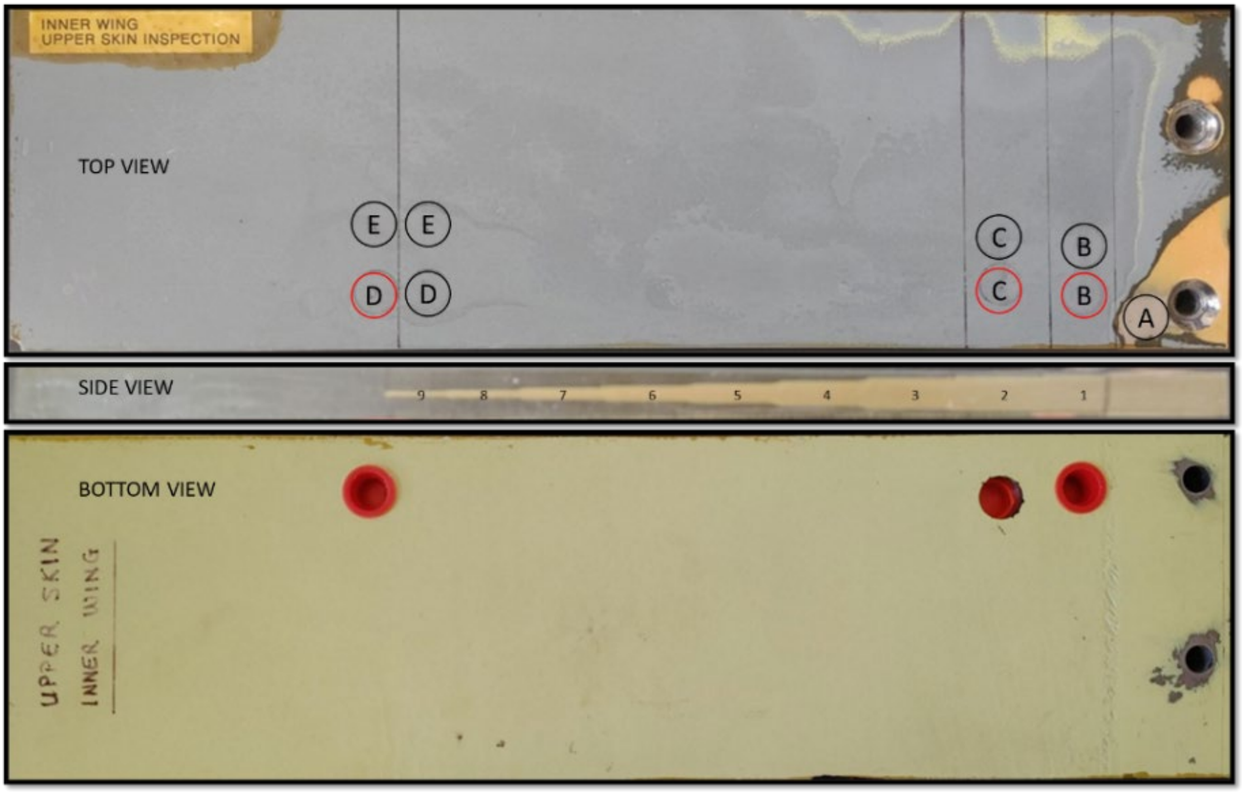

Figure 47: IWSLJ Ultrasonic Testing Calibration Block.

The Calibration Block cross-sectional view (or side view) exposes the nine steps of the inner wing stepped lap joint as shown in Figure 47. The dimensions of the steps and CFRP thicknesses are critical for defining the material conditions for the experimental objective. Note that the titanium steps (or splice plate) are not parallel to the CFRP surface; the titanium splice plate has an observable one-degree slope as it tapers from step one to nine. However, the effects of the slope were negligible in all inspection methods used in this thesis. Hence, the titanium alloy and CFRP surfaces are considered parallel for the purposes of this thesis. The thicknesses of the titanium alloy steps and CFRP in the IWSLJ Ultrasonic Testing Calibration Block are shown in Table 11.

Table 11: Titanium and CFRP thickness of the IWSLJ Ultrasonic Testing Calibration Block. An instrument error ± 0.01 mm can be applied.

Step No.	CFRP thickness (from one symmetrical side)		Titanium thickness		Total thickness	
	mm	inch	mm	inch	mm	inch
1	0.5	0.020	11	0.433	12	0.472
2	1	0.039	10.7	0.421	12.7	0.500
3	2	0.079	9	0.354	13	0.512
4	3	0.118	7.5	0.295	13.5	0.531
5	4	0.157	6	0.236	14	0.551
6	5	0.197	5	0.197	15	0.591
7	6	0.236	3.5	0.138	15.5	0.610
8	7	0.276	2	0.079	16	0.630
9	7.5	0.295	1	0.039	16	0.630

6.1.2 Manufactured Specimens

The following is a detailed description of the specimens used in the experimental evaluation. It should be noted that mould release and thermal tape are used to simulate a kissing bond and disbond area (respectively) within the specimen. Additionally, FBHs are used to simulate a disbond in conventional ultrasonic testing. FBHs are not the best representation for a disbond area in thermography. A FBH is a prominent defect that would be normally detected by thermography. However, it is still a relevant feature in thermography because it acts as an observable landmark feature for dimensioning and accuracy across all methods. For the purpose of this experimental work, all specimens are composed of Grade-5 titanium Ti-6Al-4V and VTC401 Prepreg unidirectional CFRP as detailed in Table 12. Note that the CFRP plies are together, and then, bonded to the titanium alloy. Also, the CFRP are an unsymmetrical lay-up of [0/09]. The unsymmetrical lay-up of the plies led to warping and great numbers of delamination.

Table 12: Titanium and CFRP thickness for each manufactured specimen. An instrument error ± 0.01 mm can be applied. Additionally, the CFRP thicknesses for Bonded Panels 1 - 4 are the global averages ± the variation.

Test Specimen ID	Number of Plies	General Lay-up Orientation	Surface Treatment	CFRP Thickness		Titanium Thickness		Most Similar IWSLJ Step
				mm	inch	mm	inch	
Bonded Panel 1	4	[0/90]	600 Grit Sandpaper + Acetone	1.14	0.045	2.54	0.100	2
Bonded Panel 2	13	[0/90]	600 Grit Sandpaper + Acetone	3.56	0.140	2.54	0.100	4
Bonded Panel 3	26	[0/90]	600 Grit Sandpaper + Acetone	7.65	0.301	2.54	0.100	9
Bonded Panel 4	2 4 6	[0/90]	600 Grit Sandpaper + Acetone	0.5 1.5 2.0	0.020 0.059 0.079	4.70 3.56 2.54	0.185 0.140 0.100	1 2 3
Sample No.1 [52]	14	[0/90]	Varied	2.1	0.083	6.35	0.250	3

6.1.2.1 Bonded Panels 1 – 3

Bonded Panels 1 - 3 were designed to both simulate disbond areas and evaluate the effect of depth of penetration with regards to thermography. The flat titanium Ti-6Al-4V plate was 152.4 mm in length (6 inches), 152.4 mm in width (6 inches), and 2.54 mm (0.100 inches) in thickness. The titanium plate also has distinguishing notches or indentations on the corners for proper orientation during evaluation. The titanium plates were first cleaned with Neodisher LaboClea A8™ and grit blasted with silica. The Neodisher LaboClea A8™ removes foreign object debris and other contaminants from the surface of the titanium. Also, the grit blasting smoothens the titanium surface – removing stress risers and surface contaminants. Therefore, both Neodisher LaboClea A8™ and grit blasting improve bonding strength. The number of plies or layers of CFRP, the surface treatment, and the varying thickness for each specimen is captured in Table 12. The layup was cured, and then, the surface was treated with sanding and acetone. Thereafter, the cured CFRP was bonded to the titanium alloy. The layup orientation was in the 0˚ and 90˚ direction with the 90˚ply on the outside for Bonded Panel 1 and 3. Of note, Bonded Panel 1 has a length of 146.1 mm (5.75 inches) and a width of 142.9 mm (5.625 inches), whereas Bonded Panels 2 and 3 were 152.4 mm in length (6 inches), and 152.4 mm in width (6 inches). The film adhesive used was FM 300K by Cytec, the same adhesive used for the CF-188. A top and cross-sectional view of the panel can be seen in Figures 48 and 49.

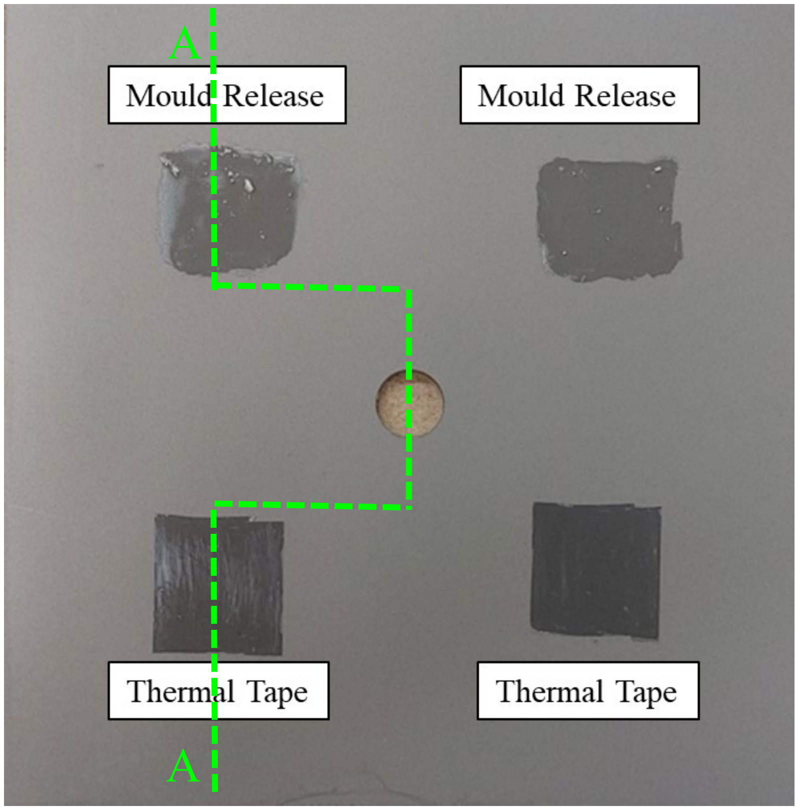

Figure 48: Example of Bonded Panel 1 – 3 showing titanium plate with thermal tape inserts and mould release gel. The neon A-A represents the sectional cut for Figure 49.

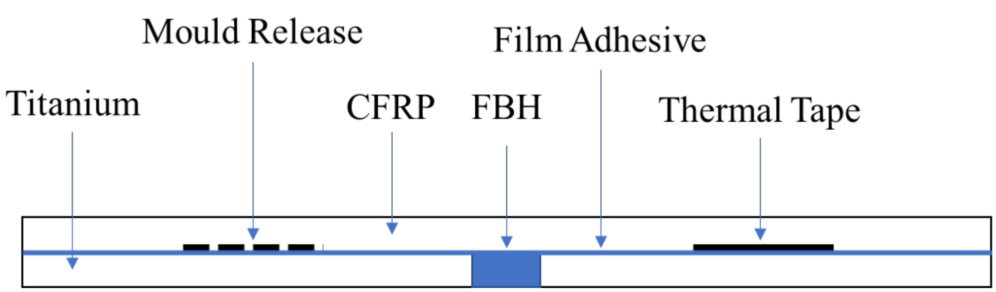

Figure 49: Cross sectional (A-A) view of Bonded Panels 1 - 3.

6.1.2.2 Bonded Panel 4

Bonded Panel 4 has machined steps with the intent of studying the first three steps closely. The number of plies or layers of CFRP, the orientation of the CFRP layers, the surface treatment, and the varying thickness for each specimen is captured in Table 12. Figure 50 shows the layout of the disbond area inserts. Note that the film adhesive used was FM 73M by Cytec rather than

FM 300K. FM 73M is an adhesive with superior mechanical properties to FM 73M and the use of this different adhesive did not affect the overall experimental work because the artificial defects were still achieved.

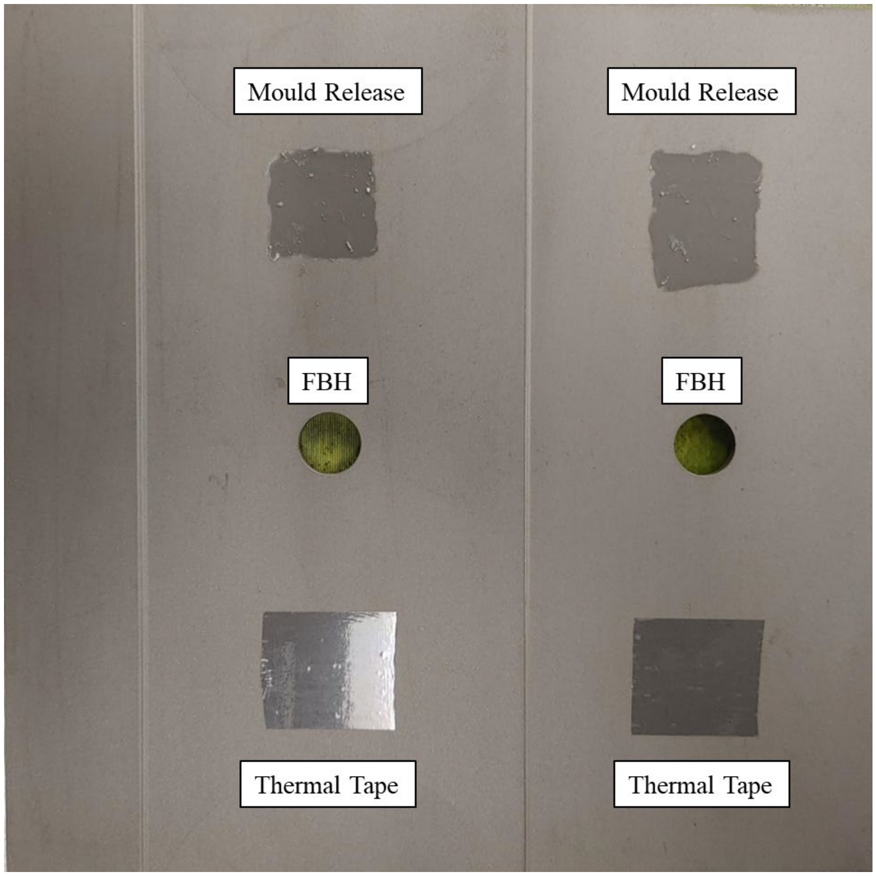

Figure 50: Example of Bonded Panel 4 showing titanium plate with thermal tape inserts and mould release gel.

6.1.2.3 Sample No. 1

Sample No. 1, shown in Figures 51 and 52, was manufactured and labeled by Capt. Myriam Rochon [52]. The intent of Sample No. 1 was to simulate kissing bonds for ultrasonic testing through various inserts and surface treatments. However, Sample No. 1 proved to be useful for thermography as well. The specifics of the manufacturing process for Sample No.1 are contained within Capt. Myriam Rochon's Thesis [52]. The flat titanium Ti-6Al-4V plate was 177.8 mm in length (7 inches), 177.8 mm in width (7 inches), and 3.18 mm (0.125 inches) in thickness [52]. The titanium plate also has distinguishing notches or indentations on the corners for proper orientation during evaluation. There are 14 plies or layers of CFRP with a layup orientation of 0˚ and 90˚. Table 13 summarizes the details of the simulated disbond areas in Sample No. 1.

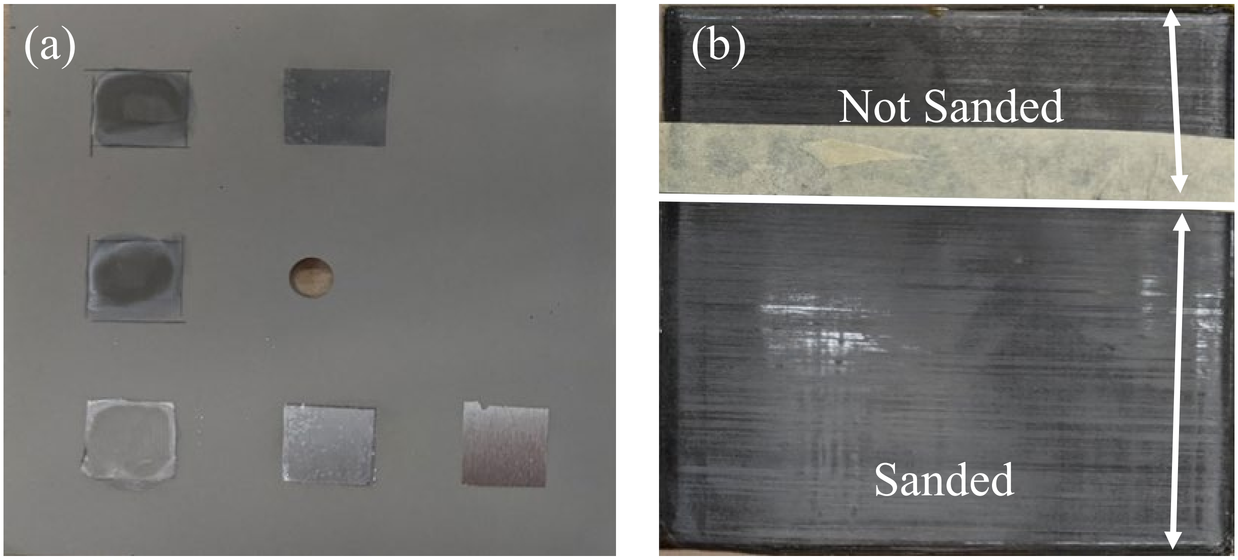

Figure 51: The (a) titanium and (b) CFRP for Sample No.1 with displayed surface treatment for bonding adapted from [52].

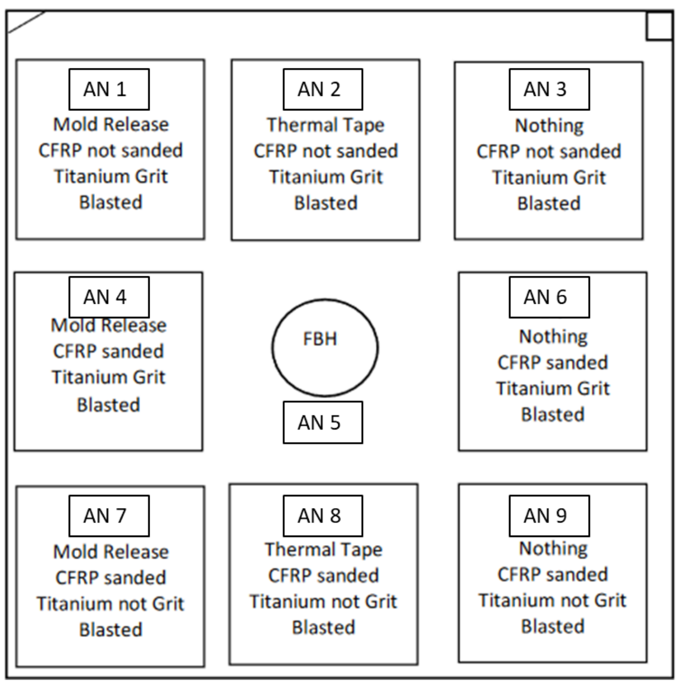

Figure 52: Disbond area mapping of the disbonds created by the surface treatment of titanium and CFRP [52].

Prepreg CFRP, PROPreg 14002-D, was used in the manufacturing process. The CFRP was also 177.8 mm in length (7 inches), 177.8 mm in width (7 inches), and 2.1 mm (0.083 inches) in thickness [52]. A 177.8 mm x 177.8 mm film of 3M™ Scotch-Weld™ Structural Adhesive Film AF 163-2 served as the bonding adhesive to the Ti-6Al-4V and CFRP.

Table 13: Detailed outline of Sample No. 1's disbond area mapping as illustrated in Figure 52.

Sample No. 1 Area Number	Surface Treatment	Insert(s) for Artificial defects	Target Effect for Study
1	CFRP not sanded Titanium sand blasted	Mould Release	Disbond Area (Kissing Bond)
2	CFRP not sanded Titanium sand blasted	Thermal Tape	Disbond Area (Traditional UT Disbond)
3	CFRP not sanded Titanium sand blasted	No Insert	Kissing bond due to Surface Treatment
4	CFRP sanded with 600 Grit Sandpaper Titanium sand blasted	Mould Release	Disbond Area (Kissing Bond)
5	CFRP sanded with 600 Grit Sandpaper Titanium sand blasted	FBH	Disbond Area (Traditional UT Disbond)
6	CFRP sanded with 600 Grit Sandpaper Titanium sand blasted	No Insert	Kissing bond due to Surface Treatment
7	CFRP sanded with 600 Grit Sandpaper Titanium not sand blasted	Mould Release	Disbond Area (Kissing Bond)
8	CFRP sanded with 600 Grit Sandpaper Titanium not sand blasted	Thermal Tape	Disbond Area (Traditional UT Disbond)
9	CFRP sanded with 600 Grit Sandpaper Titanium not sand blasted	No Insert	Kissing bond due to Surface Treatment

In Figure 52 and Table 13, a variety of inserts and surface treatment were used to simulate disbond areas in the Bonded structure. In the centre of the titanium plate, there is an FBH, which is traditionally used as a calibration method for disbond areas in ultrasonic testing. The FBH is 0.5 inches (12.7 mm) in diameter and matches the FBHs in the IWSLJ Ultrasonics Calibration Block. The FBH was straight through the titanium alloy, and hence, the depth of the FBH was the same as the thickness of the titanium alloy. Thermal tape and mould release wax (Grignard™ Mould Magic™) were also used to create the disbond areas because they are both resistant to the heat generated in the lamination process. The cure temperature for laminations is 120 degrees Celsius, whereas the melting point of the mould release is 260 degrees Celsius, and the thermal tape is 220 – 260 degrees. In order to promote better bonding in areas of the CFRP, the surface of the CFRP was sanded with 600 grit sandpaper. The titanium plates were first cleaned with Neodisher LaboClea A8™. In Figure 51, the titanium plate was grit blasted with silica with the exception of the bottom three disbond designated areas [52].

6.1.3 Manufacturing Process – CFRP and Ti Bonding

The manufacturing of a test specimen started with the CFRP composite face sheet panel. Using an industrial roll of unidirectional pre-impregnated carbon fibre, the required size and orientation of each ply was determined and cut to the same dimensions as the titanium plate. Each ply was stacked one on top of another and pressed under vacuumed pressure to ensure that there were no air pockets between plies. Air pockets and other foreign objects can lead to delamination, disbond areas and cracks. Hence, it is critical to mitigate or eliminate the potential for air pockets and foreign object defects or discontinuities. Once the plies were stacked and compressed, the stack was placed between two layers of release film to prepare for curing. The curing process involved placing the stack into a custom-built oven that allowed for a vacuum pressure to be applied to the stack. Figure 53 shows one of the custom-built ovens with a heat resistant silicone membrane for a top cover, and a one-inch-thick aluminum plate heated by coils adhered to the underside of the aluminum plate. The vacuum pressure was generated by a suction pump that applied 29 inchHg (14 psi) during the curing process at 120 degrees Celsius. Once the composite was cured, the next step was to prepare both the titanium and composite for secondary bonding.

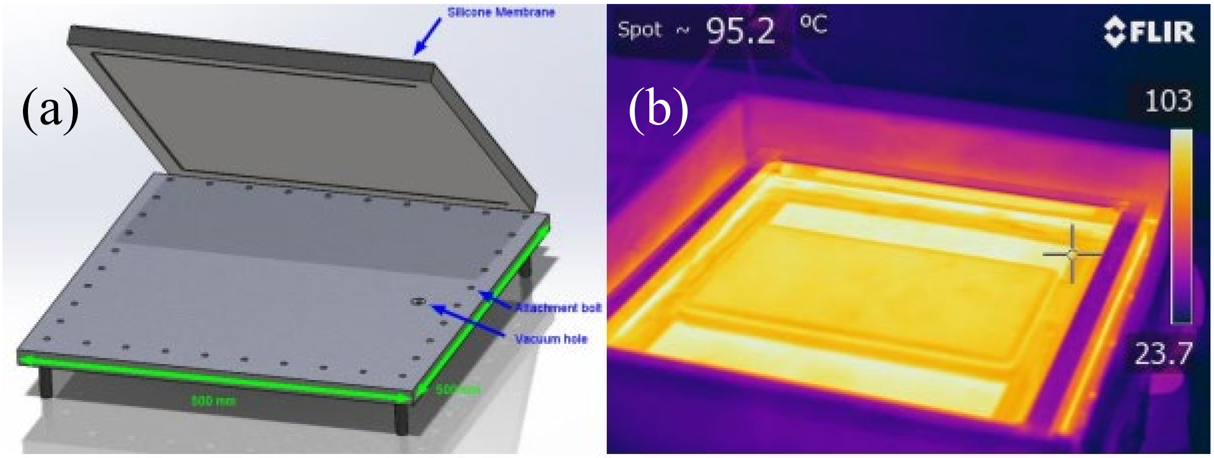

Figure 53: (a) A 3D image of the custom-built oven illustrating the silicone membrane top cover, attachment bolt, and vacuum hole. (b) A thermal image of the custom-built oven in operation with the silicone membrane under vacuum pressure covering the stack [31.

To prepare the titanium for secondary bonding, the titanium plates were first cleaned with Neodisher LaboClea A8™, and then grit blasted with silica [52]. In order to promote better bonding in areas of the CFRP, the surface of the CFRP was sanded with 600 grit sandpaper. Disbond areas were created with a combination of the following: Thermal Tape, Gringnard™ Mould Magic mould release wax, and surface treatment. The location and composition of the disbond areas were dependant on the specimen design. Finally, the Ti-6Al-4V, CFRP, adhesive, and disbond material were assembled and bonded in the custom-built oven under vacuum press. The bonding process, used to bond the titanium and composite, was the same process used to cure the composite face sheets.

6.2 Pulsed Thermography Testing

6.2.1 Pulsed Thermography Apparatus

Tanner Rellinger [31] designed and manufactured a pulsed thermography apparatus for his Master's thesis at the Royal Military College of Canada. The apparatus, as well as the complimentary MATLAB and Arduino code, were used in support of the objectives in this thesis. Additionally, a FLIR T620 thermal camera was used for imaging and the FLIR ResearchIR software was used for image processing. As shown in Figure 54, the pulsed thermography apparatus consisted of a mounting plate, an electrical box for the Arduino hardware, a camera mount, and two 500-Watt halogen bulbs underneath the mounting plate. The halogen bulbs had parabolic reflectors to provide uniform heating across the sample. The legs and cross beams of the apparatus were made of carbon fibre. During operation the sample was placed at the base of the apparatus directly underneath the halogen bulbs.

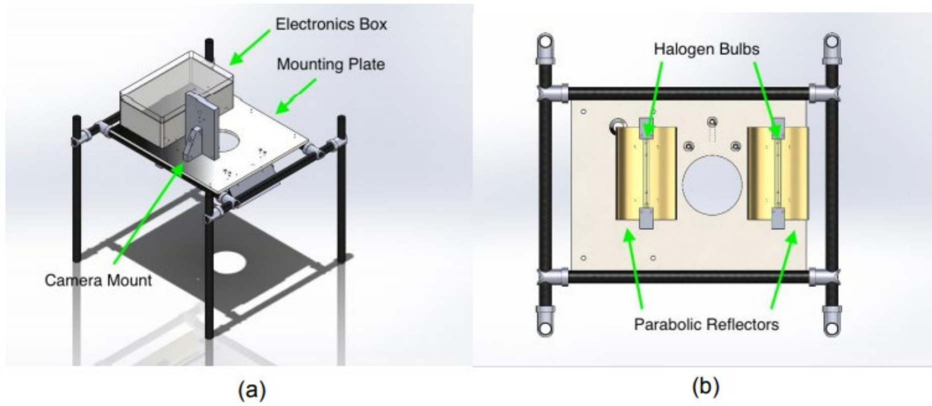

Figure 54: IR thermography apparatus created by Tanner Rellinger at RMC. (a) Shows the location of the electronic box, mounting plate, and camera mount. (b) The underside of the mounting plate, which identifies the location of the halogen bulbs and parabolic reflector. Image used from [31] with the author's permission.

6.2.2 Pulsed Heating

To produce the optimal thermogram (infrared image) and reduce the potential for false positives, the following was accomplished. First, to reduce the risk of a false positive on a thermogram, uniform surface heating was required. This is accomplished by properly positioning the halogen bulbs, while simultaneously flashing under the control of Arduino and MATLAB coding. Additionally, the specimens were positioned directly at the centre of the two bulbs at a distance of approximately 33 cm. Second, a heating time of 2 – 4 seconds was used in order to produce an optimal thermogram. Too much heating (or heating for a long duration of time) would lead to a saturated thermogram and too little heating may not have allowed the disbond areas to be visible on the thermogram. Third, the bare surface of the CFRP was glossy and reflective. This was problematic because heat from environmental sources could reflect off the surface of the sample and lead to a false positive on the thermogram as shown in Figure 55. Hence, the sample was covered with a black rubber coating to prevent reflections. Note that a glossy finish on CFRP is generally not a problem for composite material with regards to thermography. Some composites have a glossy surface finish, but still have an emissivity above 0.8 and thus a black rubber coating is not required. However, the black rubber coating increases the emissivity to approximately 0.97 and thus promotes better heat transfer. The heating operation consisted of positioning the sample at the base of the apparatus centered under the halogen bulbs. The Arduino hardware and code (via

MATLAB) controlled by the FLIR ResearchIR software, acquired multiple thermograms in sequential frames.

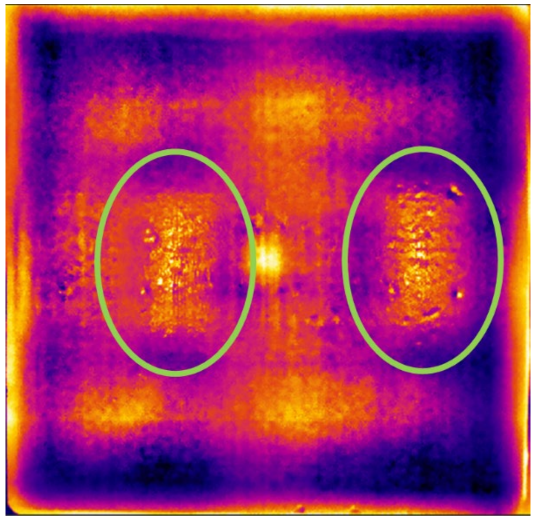

Figure 55: Thermographic image or thermogram, showing false positives outlined in green due to reflections from the halogen bulbs.

6.2.3 Infrared Imaging

The FLIR T620 thermal camera is capable of measuring temperatures between -40 to 650˚C [53]. It has a sensitivity of 0.04˚C, a sensor resolution of 640 x 480 pixels, and a spectral range of 7.5 – 14 µm [53]. Additionally, it has maximum full frame rate of 30 Hz. The camera is also capable of taking a single thermogram or a sequence of thermograms at a desired frequency [53]. The imaging process or operation consists of the following steps:

1. Ensure that the camera is connected to the FLIR ResearchIR software on a computer in real-time. Additionally, open MATLAB and the complimentary Arduino code for the heating process.
2. Manually focus the camera on a distinct object within camera view for the sharpest possible image.
3. For the purposes of this thesis, a sequence of thermograms at a frame rate of 30 Hz was used to most accurately evaluate the dimensions of the disbond area.
4. Finally, run the image capture on the software for the sequence of thermograms. Simultaneously, run the MATLAB program, activating the halogen bulbs and the heating process.

The FLIR ResearchIR software has many post imaging processing features. There is the option of selecting different Palettes to further highlight defects or objects of interest. Additionally, the software allows manipulation within a Region of Interest (ROI).

6.3 Induction Thermography Testing

6.3.1 Induction Thermography Apparatus

A commercial induction heating system, the Ambrell® *EASYHEAT* 2.4 kW Induction Heating System, was used for the induction thermography experimental investigation. The *EASYHEAT* 2.4 kW induction heating system is compact, water cooled, and equipped with a movable work head with freedom of movement of 3 m (10 feet) from the power source as shown in Figure 56. The circulating water cools the induction coil and complimenting components with a flow rate of 1.2 kg/min, meaning that heat is mainly generated by the induction heating process and there is negligible heat transfer to the test specimen by radiation. Additionally, the induction heating unit can operate across a frequency range of 150-400 kHz and can achieve a maximum coil current output of 300-400 Amps. Almost the entirety of the frequency range was used during experimentation. Furthermore, all Ambrell® induction heating systems are built with an RLC electrical circuit, and they automatically adjust to the resonance frequency of the test specimen. The induction heating unit can operate in a fixed or scanning configuration. Throughout the investigation, the work head was mounted to a rail type scanning motion system, which allowed for stationary and scanning data acquisition. The coil on the work head was typically 2.5 cm above the test specimen and the camera was generally about 20 cm above the test specimen. A stationary setup provided uneven heating and was prone to over-saturation of heat. Hence, it was not used as often as the scanning setup (63).

Figure 56: Ambrell® EASYHEAT 2.4 kW Induction Heating System.

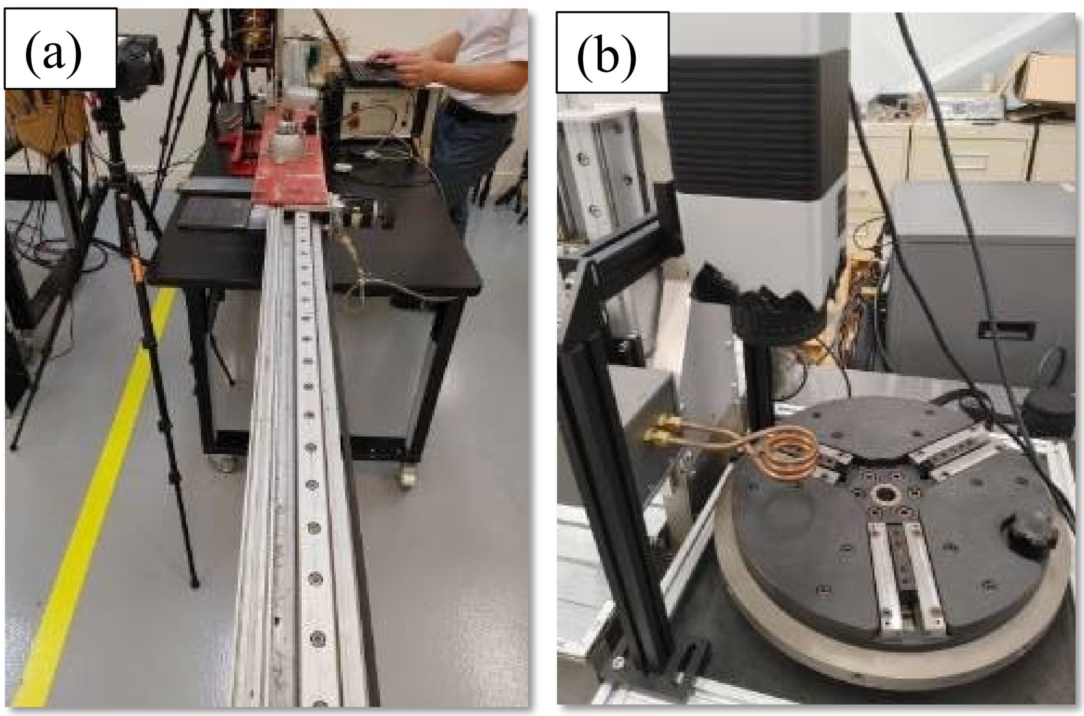

Figure 57: Ambrell® EASYHEAT 2.4 kW Induction Heating System. (a) Scanning setup. (b) Stationary setup.

6.3.2 Procedural Considerations

Induction thermography has many considerations including coil geometry, skin depth, specimen material, specimen geometry, electromagnetic effects, etc. Hence, a considerable amount of care is required to get viable results. The infrared camera and induction work head were carefully mounted perpendicular to the test specimen. The perpendicular mounting configuration prevented uncertainty in measurements due to a slant range. To promote electromagetic coupling, the induction coil was only 6.35 mm from the specimen surface. To best increase thermal contrast between the discontinuity and the unaffected region, the test specimens were coupled with a large aluminum block (Figure 58) and a fan was used to blow air across the surface of the test specimen. This promoted additional conduction and convection in the unaffected region of the test specimen, while the induction heating process highlighted the boundaries of the discontinuities with concentrated heat. Additionally, it also reduced edge effects. In order to conduct induction thermography, the ideal parameters (heating time, lift-off, coil geometry, etc) were first established as in Section 7.1. Once the ideal experimental parameters were determined, the induction heating process was carried out on the specimen. Thereafter, the IR camera could be used to image the specimen.

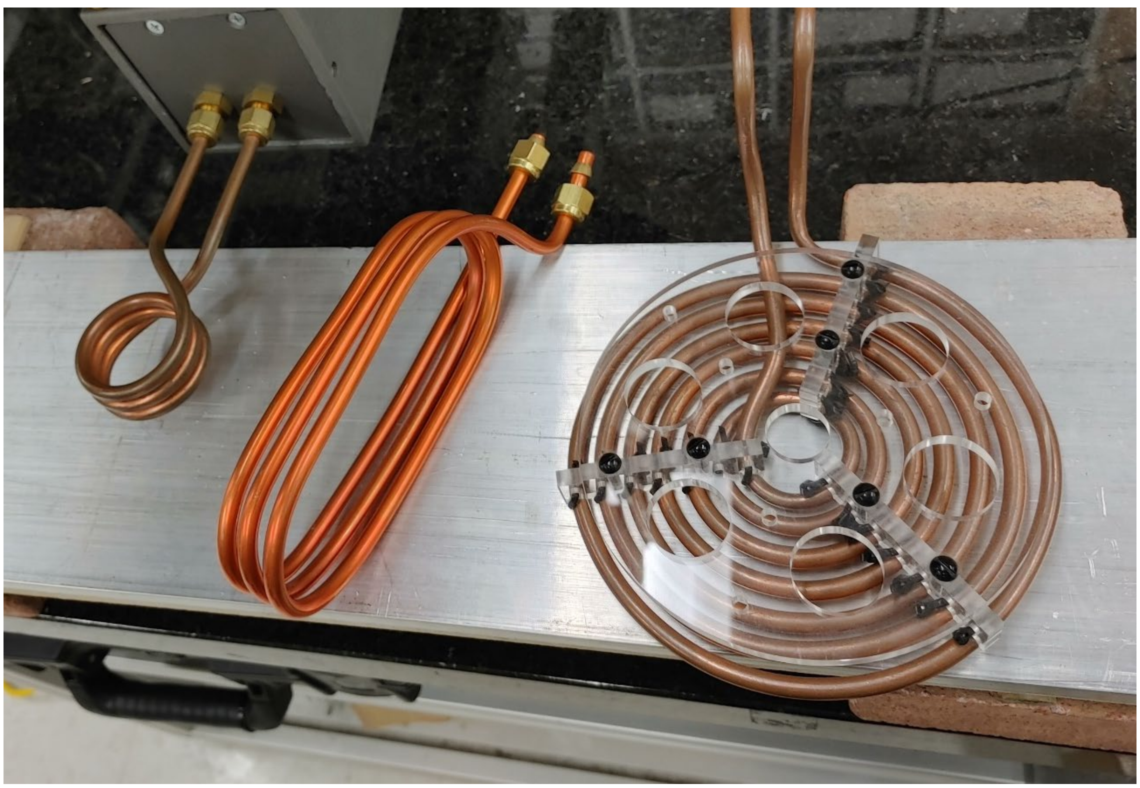

Figure 58: Some of the coils used for induction heating placed on top of a large aluminum block.

6.3.3 Infrared Imaging

Similar to the pulsed thermography, the same FLIR T620 thermal camera captured all thermograms and was mounted to a scanning motion apparatus. The first three steps of the induction thermography imaging process are exactly the same as the pulsed thermography steps previously mentioned. Induction thermography has the following differences in the imaging process in comparison to flash thermography:

1. Turn on the Ambrell® *EASYHEAT* 2.4 kW Induction Heating System and set the desired current using the control box. In a scanning operation, turn on the scanning motion apparatus and set the desired motion speed.
2. Finally, simultaneously, run the Ambrell® *EASYHEAT* 2.4 kW Induction Heating System, scanning motion apparatus, FLIR Research IR and the MATLAB program to capture a sequence of thermograms.

The FLIR ResearchIR software was used for post processing and analysis.

6.4 Infrared Thermography Image Processing

Image processing is significant and involves interpreting thermograms, because critical information may be unnoticed given the quality of the thermogram and conditions of the imaging process. Hence, there are many different operations to enhance the quality of the image and extract the target features within the thermogram. This section outlines some important observations with regards to image processing.

6.4.1 Pre-Processing

Thermogram pre-processing are the preliminary steps taken to augment or improve the quality of the images prior to using them for analysis. There are some important considerations to take into account. Namely, the following list of observations:

1. **Bad pixels** are defective pixels of erroneous value and are classified into two categories: Dead pixel and Hot Pixels. Dead pixels are pixels that are permanently turned off due to a contamination or a defective detector. Hot Pixels register values in excess of the surrounding pixels. Although there are many ways to correct for bad pixels, the simplest way is to isolate the bad pixel and eclipse its value with the average value of surrounding good pixels. Therefore, the bad pixel would be replaced with a good pixel.
2. **Fixed pattern noise** is used to describe a specific noise pattern that is inherent to the imaging sensors. Although not typically noticeable, fixed pattern noise can lead to false positives. One way of correcting for fixed pattern noise is to isolate the noise by imaging a black body and subtracting the isolated noise from the subject thermogram.

3. **Noise filtering** is a general pre-processing practice by which unwanted noise is removed from the desired thermogram (i.e., non-uniform heating, edge effect, electromagnetic noise due to the induction system, etc.). There are many different types of filters for the different types of noise. For random noise, temporal averaging can be used or spatial filtering such as a box filter, a gaussian filter, a butterfly filter, a median filter, or a harmonic filter can be used.
4. **Vignetting** is an optical irregularity, which results in the centre of the thermogram appearing lighter than the edges. It is caused by malfunctioning elements in the body of the lens or the barrel of the camera that blocking light around the edges. Increasing the F-number or ratio of the focal length to the diameter of the lens can compensate for vignetting.

6.4.2 Post-Processing

The FLIR ResearchIR interface software has several Automatic Gain Control (AGC) algorithms and other tools (different palettes, ROI isolation method, etc.) that can be used to enhance the thermogram in post-processing. Of the many different AGC algorithms, the Advanced Plateau Equalization (APE) was heavily used to significantly enhance the contrast between the discontinuity and the surrounding unaffected environment. The APE algorithm achieves high contrast by constraining noise at an upper limit, clipping the background values at a lower limit, and interpolating (stretching) the intensity values between the limits.

6.5 Ultrasonic Testing

QETE's TecScan ARMANDA system and TecView 2 software were used to perform an automated ultrasonic C-Scan inspection on Sample No.1. The rubber coating used on the CFRP surface during the IR thermography testing was removed to allow for better coupling between the ARMANDA probe and the test sample. The couplant for this ultrasonic testing was water. Given the material similarities between the test sample and the CF-188 IWSLJ, the sample was inspected in accordance with the CF-188 IWSLJ RCAF NDE technique 188-355-U established by QETE [6]. As per the RCAF NDE technique 188-355-U, a scan was first performed on the 188-355-U CFRP-Ti reference coupon to both validate the equipment setup and provide a reference calibration

[6]. Additionally, the reference scan provided the following applicable characteristics (Appendix B):

- *The effective sound transmission into the sample confirmed by assessing the Neg Peak amplitude of the UT signal at the specific near-surface CFRP-Ti bondline (OML bondline on the CF188 IWSLJ Ref Coupon);*
- *Phase shift of UT signal from OML (or near surface) CFRP-Ti FBH's, which simulates near surface CFRP-Ti disbonds; and*
- *CFRP skin-ply delamination.*

A scan was then performed on the subject sample. Of note, the backwall response or IML of the titanium layer in the sample was appropriately gated in the TecView 2 software due to the consistent nominal thickness of the titanium and CFRP layers. This allowed for an examination of expected disbond areas on the Ti layer backwall response.

CHAPTER 7 – RESULTS

In order to achieve the objective of this thesis, four distinct experimental studies were conducted using Induction Thermography, Pulsed Thermography, and Ultrasonic Testing. Namely, those studies consist of: (1) a parametric evaluation to obtain the ideal parameters for induction thermography; (2) the ability of the three methods to detect and dimension the discontinuities; (3) the effects of defect depth on detection; and (4) the sensitivity of detection. Only induction thermography was used for Study 1. Studies 2 – 4 used all three methods. The sensitivity detection in Study 4 differs from Study 2 in that Study 4 covers different surface treatments that may lead to disbond areas. This chapter will provide a detailed overview of the four studies and the associated results. Lastly, each study will be separated into the following sections: an introduction, goal, how the goal was achieved, results, and conclusion.

7.1 Parametric Investigation for Induction Thermography (Study 1)

7.1.1 Introduction

This study focused on parametric evaluation to obtain the ideal parameters for induction thermography. Specifically, coil selection and induction heating parameters were determined as a net result of the study. The study considered the lift-off distance, the rate of heating, coil geometry, and coil orientation. An experimental test matrix with consideration for the exact outline of the experimental testing was captured in Appendix C, Induction Thermography Test Plan. Appendix C served as an overarching guideline for all four studies. It was not followed exactly due to experimental time constraints. This study is important because there are literally thousands of possible adjustments/considerations (see Figure 59) in induction thermography and a poor or lacking parametric study may lead to undesirable effects.

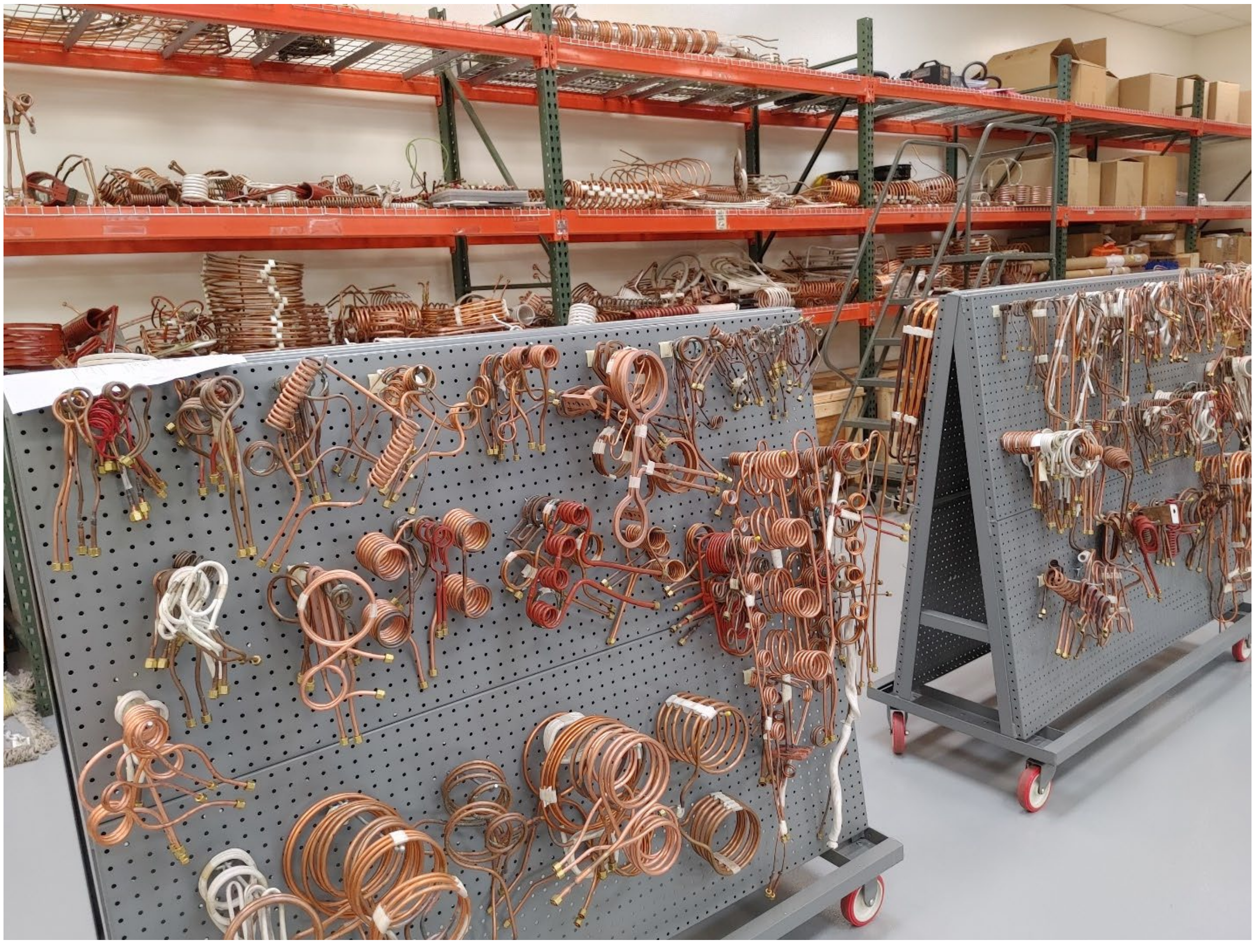

Figure 59: An image showcasing thousands of different induction coils at Ambrell Corporations in Rochester, New York, United States of America.

These considerations and their significance are also captured within the details of Table 14. The Ambrell® *EASYHEAT* Induction Heating System automatically sensed the presence of the test specimen and adjusted its frequency to match the resonance frequency of the test specimen and coil system. The automatic adjustments within the RLC circuit were achieved as capacitor reactance tried to match inductance reactance. The frequency would automatically increase slightly if the coil was further away from the specimen and decrease as the coil was brought closer to the specimen. Frequency is inversely proportional to inductance and capacitance. Therefore, there was less inductance with the coil further away (resulting in increased frequency) and more inductance as the coil was brought closer (resulting in decreased frequency). This trend was due to electromagnetic coupling within an RLC circuit (further explained in Section 6.3.1 and with Equations (48) and (49)). Hence, frequency could not be experimentally manipulated.

Table 14: Bayerl et al. [6] – parameters influencing induction thermography efficiency.

Parameter	Effect on Heating	Remarks
Coil Geometry	Dependent on magnetic flux density.	Coil geometries should be designed to fit the heating problem or component being heated. While flat components may require pancake coils, shaft components may benefit from helical coils.
Magnetic Flux Concentration	Application usually leads to higher heating rates.	Risk of inhomogeneous heating due to locally higher magnetic flux. There are heating applications that benefit from a more concentrated magnetic flux. For these applications, a device called a concentrator may be used with the induction system. The concentrator focuses more energy into a specified area. The heat is less general and more focused. However, concentrators are expensive to make and have a short lifespan.
Coupling Effect	The smaller the coupling distance (lift off) the higher is the heating effect.	Homogeneous heating sometimes requires a less efficient coupling distance (danger of local overheating).
Frequency	A high frequency is generally better for the fast heating of composites.	Very high values limit penetration, also dependent on size for specimen, high-frequency generators are less efficient. Generally, higher frequency is more effective for coupling to near surface material and low frequency is more effective for larger components.
Inductor Current	A high current leads to more power in the system and thus a faster heating rate.	Risk of local overheating (micro-level).

7.1.2 Experimental Goal

Coil parameters were determined by first experimentally evaluating the trends resulting from lift-off distance, the rate of heating, coil geometry and coil orientation. Ultimately, the following parameters were established from the results of the trends: lift off distance (separation distance from the surface of the specimen to the bottom plane of the coil) was determined to be **6.35 mm (0.25 inch) for the best coupling and rate of induction heating**; a current setting of **75 – 100 A provided a reasonable rate of induction heating**; **the induction heating process should be conducted within a 2 - 10 seconds range; a pancake coil design was marginally satisfactory for stationary even heating; and a reasonable speed for the scanning process was determined to be 1.5 cm/s.** These experimentally determined parameters are discussed further in the following sub-sections.

7.1.3 Lift-Off Distance Trends

7.1.3.1 Induction Heating and Lift-Off Distance

In order to determine a reasonable lift-off distance that provided relatively high electromagnetic coupling and an efficient rate of induction heating, the time required to increase the temperature by 5 ˚C was determined for lift-off distances between 6.35 mm (0.25 inch) and 25.4 mm (1 inch). The temperature was increased from room temperature of the panel. Thermography does not require more than 10 ˚C of temperature different for defect detection. Given that no more than 10 ˚C of temperature difference was required, 5 ˚C was selected based on being a reasonable bound for this evaluation. The experimental setup consisted of a helical coil with three tubular turns because it is a common coil that was readily available. Bonded Panel 2 (13 plies of [0/90] CFRP and 2.54 mm Titanium alloy) was used for this evaluation and the induction system current was increased in increments of 25 A from 25 to 125 A. Note that power was not controlled and was a function of the input current. The temperature of the surface of the panel was automatically measured with a FLIR IR camera. Finally, the data collected was analyzed and graphically presented to observe the targeted trend.

In Figure 60, the time required to increase temperature by 5 ˚C was plotted as a function of lift-off distance to illustrate the rate of induction heating. The graphs resulting from 75 A and 100 A are shown in Figure 60. The data from the 25 A, 50 A, and 125 A sampling point was determined to be unsatisfactory because of either an insufficient rate of induction heating or too high a rate of induction heating. This evaluation was critical in determining a reasonable lift-off distance that provided relatively high electromagnetic coupling and efficient rate of induction heating. Lift-off distance and current was also important for controlling the induction process. Specifically, if the rate of heating was too high, it became difficult to run the experiment because the panels would become saturated before there was time to collect usable data. Tables 15 and 16 provide more details.

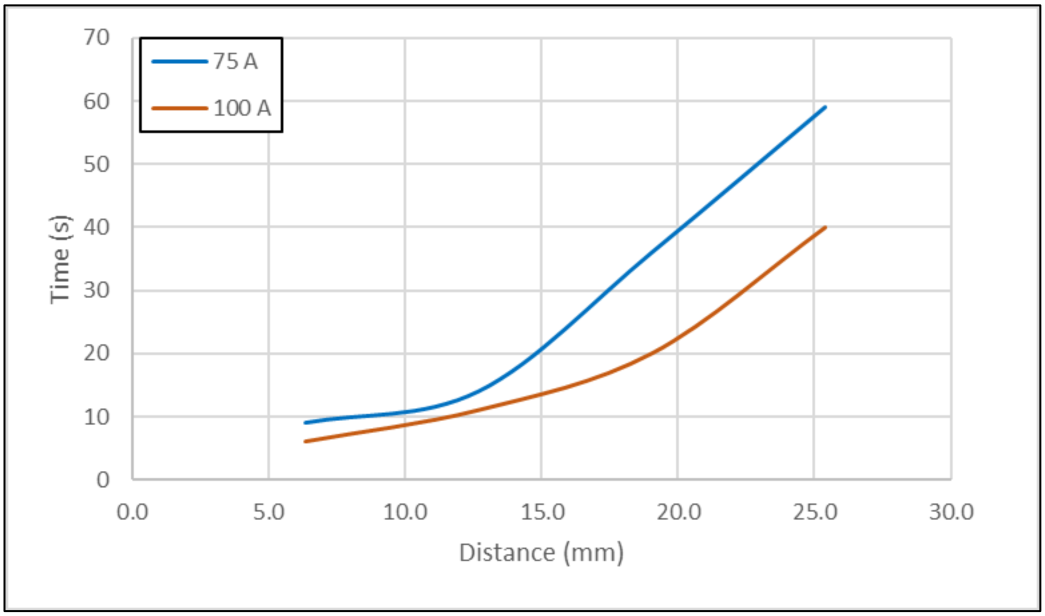

Figure 60: Time required to increase the temperature by 5 ˚C as a function of lift-off distance on Bonded Panel 2, 13 plies [0/90] CFRP. Current set to 74.9 A and 100.1 A.

Table 15: Time required to increase the temperature by 5 ˚C as a function of lift-off distance with Ambrell® control box set to 74.9 A. Note that "--" denotes a misplaced recording, but is not of significance to the final result.

Distance [mm]	Time [s]	Frequency [kHz]	Power [W]
6.35	9	297	323
12.7	14	290	294
19.1	36	287	287
25.4	59	--	284

Table 16: Time required to increase the temperature by 5 ˚C as a function of lift-off distance with Ambrell® control box set to 100.1 A. Note that "--" denotes a misplaced recording, but is not of significance to the final result.

Distance [mm]	Time [s]	Frequency [kHz]	Power [W]
6.35	6	295	546
12.7	11	287	491
19.1	20	--	463
25.4	40	--	458

From the data in Figure 60, it was determined that **6.35 mm allowed the best coupling and rate of induction heating** for the purposes of the investigation. Induction heating is not a precision process compared to processes seen in ECT or UT. Hence, the qualifier for this assessment was the most practical or reasonable distance, which allowed quickest heating where viable data could be collected. Note that lower distances than 6.35 mm were trialled, but the rate of heat was too great to control and gather useful data. Additionally, distances closer than 6.35 mm were not practical for study because it was difficult to maintain separation distance from the coil and specimens. The specimens were not perfectly flat or consistently parallel/squared to the coil, and often, the coil made contact with the specimen at distances such as 3.2 mm during scanning. There was more flexibility with uneven surfaces with 6.35 mm of separation distance. Additionally, as the lift-off distance was increased, the rate of induction heating decreased. The data also showed that an increase in current resulted in an increase in the rate of induction heating. Finally, at a fixed current with the lift-off distance increasing, the power decreased, and the frequency increased as the Ambrell induction system tried to maintain resonance. This agreed with the theory presented in Equations (45) to (49) because there is an inverse relationship between frequency and inductance. Flux is cancelled by the current induced in the specimen, and therefore, inductance is less at smaller lift off distances and frequency must increase. Also, with less inductance, less capacitance is required to balance the inductance and there is less overall impedance for the induction system. Hence, less power is required, and the induction system automatically reduces the coil power. According to Equation (49), frequency will increase as inductance decreases in a resonance RLC series circuit. Lastly, frequency dictates how deep the electromagnetic field penetrates the material (skin depth), and with greater frequency, there is reduced skin depth according to Equation (29).

7.1.3.2 Change in Temperature and Lift-Off Distance

Similarly, the same experiment was performed again with attention to the temperature. Hence, to determine a reasonable lift-off distance that provided relatively high electromagnetic coupling and an efficient rate of induction heating, the maximum change in temperature after 10 seconds of heating was also determined as a function of lift-off distance between 6.35 mm and 25.4 mm. Ideally, the temperature should not change more than 10 ˚C. The data required from induction thermography could be obtained with a temperature difference of less than 10 ˚C. Hence, 10 ˚C was a reasonable bound for the purpose of this study. The same three turn helical coil (shown in Figure 57 (b)) was used. The induction system current was fixed at 100.1 A, 74.9 A, and 50 A. Figure 61 shows graphs of the change in temperature after 10 seconds of heating versus the lift off distance. These results are also summarized in Tables 17 to 19.

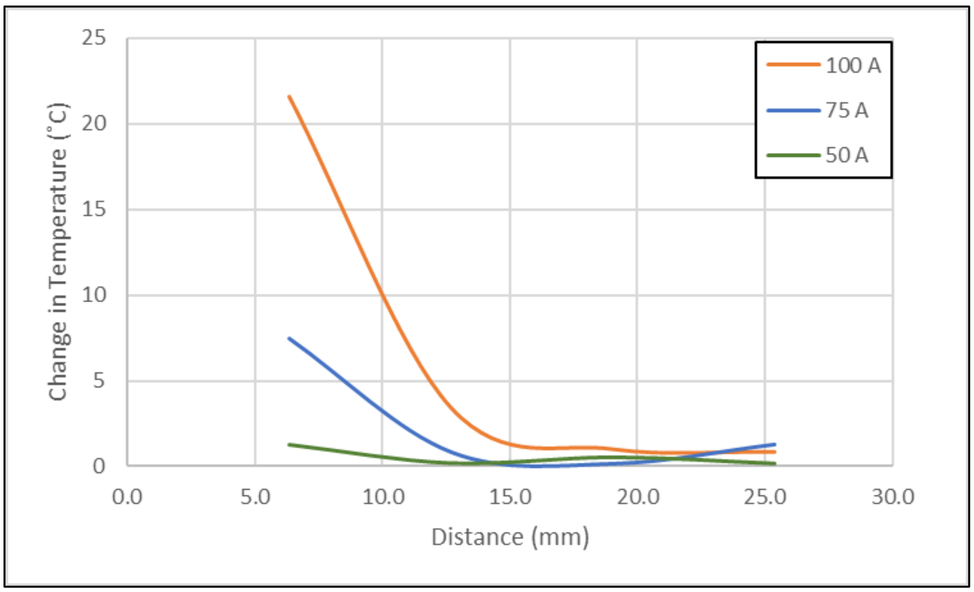

Figure 61: Change in temperature as a function of lift-off distance on Bonded Panel 2, 13 plies [0/90] CFRP. Current set to 100.1 A, 74.9 A, and 50 A.

Table 17: Temperature increase after 10 seconds of heating for different lift off distances with Ambrell® control box set to 100.1 A. Note that "--" denotes a misplaced recording, but is not of significance to the final result.

Distance [mm]	Δ Temperature [s]	Frequency [kHz]	Power [W]
6.35	22	295	546
12.7	3.4	287	491
19.1	1.0	--	463
25.4	0.9	--	458

Table 18: Temperature increase after 10 seconds of heating for different lift off distances with Ambrell® control box set to 74.9 A. Note that "--" denotes a misplaced recording, but is not of significance to the final result.

Distance [mm]	Δ Temperature [s]	Frequency [kHz]	Power [W]
6.35	7.4	297	323
12.7	0.9	290	294
19.1	0.2	287	287
25.4	1.3	--	284

Table 19: Temperature increase after 10 seconds of heating for different lift off distances with Ambrell® control box set to 50 A. Note that "--" denotes a misplaced recording, but is not of significance to the final result.

Distance [mm]	Δ Temperature [s]	Frequency [kHz]	Power [W]
6.35	1.3	304	146
12.7	0.2	296	121
19.1	0.5	293	132
25.4	0.2	--	119

From the data shown in Figure 60 and 61, it was confirmed that **6.35 mm allowed the best coupling and rate of induction heating** for the purposes of this thesis. Additionally, an induction system current between **75 – 100 A provided a reasonable rate of induction heating**. As the lift-off distance was increased, the temperature of the specimen generally decreased. In Figure 61 at 50 A of current, there were some unstable readings due to the increasing separation distance at 50 A of system input current. This was attributed to the magnetic field strength decreasing to a point where the resonance condition could not be maintained. The data also showed that an increase in current resulted in an increase in temperature.

7.1.3.3 Change in Temperature and Lift-Off Distance (Ti-6Al-4V and CFRP)

The temperature changes for Ti-6Al-4V and CFRP in isolation were also compared following 2 seconds of heating. Two seconds was selected because it is a reasonable amount of time for induction heating. For this experiment, 152.4 mm x 152.4 mm x 2.54 mm the titanium (Ti-6Al-4V) was examined independently from six plies of [0/90] CFRP (152.4 mm x 152.4 mm x 2 mm). Furthermore, this evaluation is significant to develop an understanding of the induction heating process of each material separately. For the experimental setup, a current was determined when both materials could show an increase of temperature of 10 ˚C in 2 seconds. Therefore, an induction system current of 50 A was determined for the CFRP, and a current of 60 A was determined for the titanium. A pancake coil (6.35 mm square tube, 5 turns, 12.7 mm inside diameter, 88.9 mm outside diameter) was used. The change from the helical coil to the pancake coil was negligible in this experiment because only the trends of the two materials were examined.

Figure 62 shows that both materials exhibited the expected trend with the CFRP having a higher change in temperature than the titanium. This was expected because titanium has more mass per unit volume to heat, and in this instance, a larger heat capacity. Table 20 shows the details of the results.

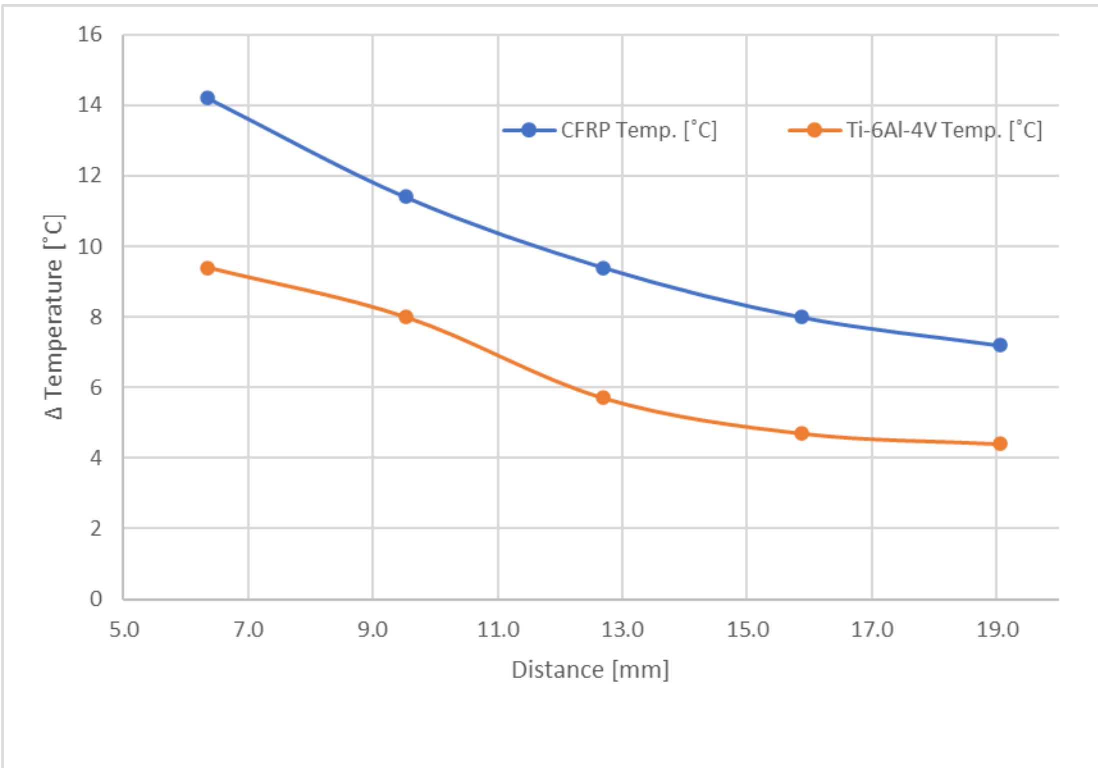

Figure 62: Change in temperature after 2 seconds of heating as a function of lift-off distance on Titanium Ti-6Al-4V and 6 plies [0/90] of CFRP. Ambrell® control box was set to 60 A and 50 A for Ti-6Al-4V and CFRP, respectfully.

Table 20: Trends in temperature, power, and frequency as a function of distance.

Distance [mm]	CFRP			Titanium Ti-6Al-4V		
	ΔTemp. [C]	Power [W]	Freq. [kHz]	ΔTemp. [C]	Power [W]	Freq. [kHz]
6.35	14	72	293	9	54	348
9.53	11	44	294	8	43	329
12.7	9	40	295	6	41	320
15.9	8	35	296	5	40	313
19.1	7	28	296	4	34	309

7.1.4 Heating Rate Trend

7.1.4.1 Change in Temperature and Time

In order to avoid overheating and thermal saturation for the infrared camera, the change in temperature over time was graphed for the Ti-6Al-4V and CFRP independently. Induction system currents of 50 A and 60 A were selected for the CFRP and titanium, respectively, to increase temperature by 10 ˚C at 6.35 mm lift-off distance. The same pancake coil was used.

In Figure 63, both materials exhibit an expected trend of increased temperature with increased time. The CFRP has a higher rate of change in temperature as a function of time. Once again, this is expected because titanium has more mass per unit volume which increases the heat capacity. The difference in heating rate is 2.3 ˚C per second, which was determined from linear lines of best fit shown in Figure 63.

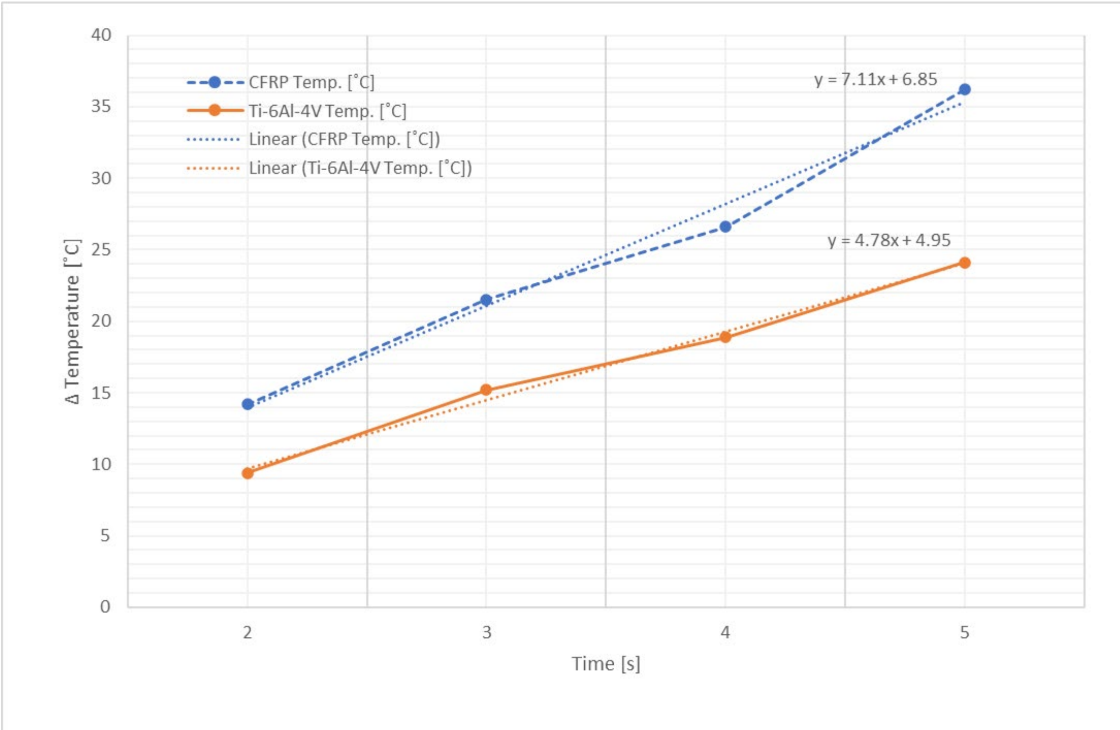

Figure 63: Change in temperature as a function of time for titanium Ti-6Al-4V and 6 plies [0/90] of CFRP. Ambrell® control box was set to 60 A and 50 A, respectfully.

7.1.4.2 Change in Temperature and Time (Bonded Panel)

To avoid overheating and thermal saturation for the infrared camera, the temperature was plotted against time for a Bonded panel. For the experimental set-up, a helical coil with three tubular turns and Bonded Panel 2 were used for this evaluation. The induction system current was increased in increments of 25 A from 25 to 125 A. The data from the 25 A, 50 A, and 125 A sampling point were determined to be unsatisfactory because of either an insufficient rate of induction heating or a high rate of induction heating. Note that power was not controlled and was a function of the input current. The temperature of the surface of the panel was automatically measured with a FLIR IR camera. Figure 64 shows the change in temperature as a function of time on Bonded Panel 2. The legend shows the lift off distances of 6.35 mm (0.25 inch), 12.7 mm (0.5 inch), 19.1 mm (0.75 inch), and 25.4 mm (1 inch). Each graph in Figure 64 corresponds to the current settings of 100.1 A, 74.9 A, and 50 A, respectively.

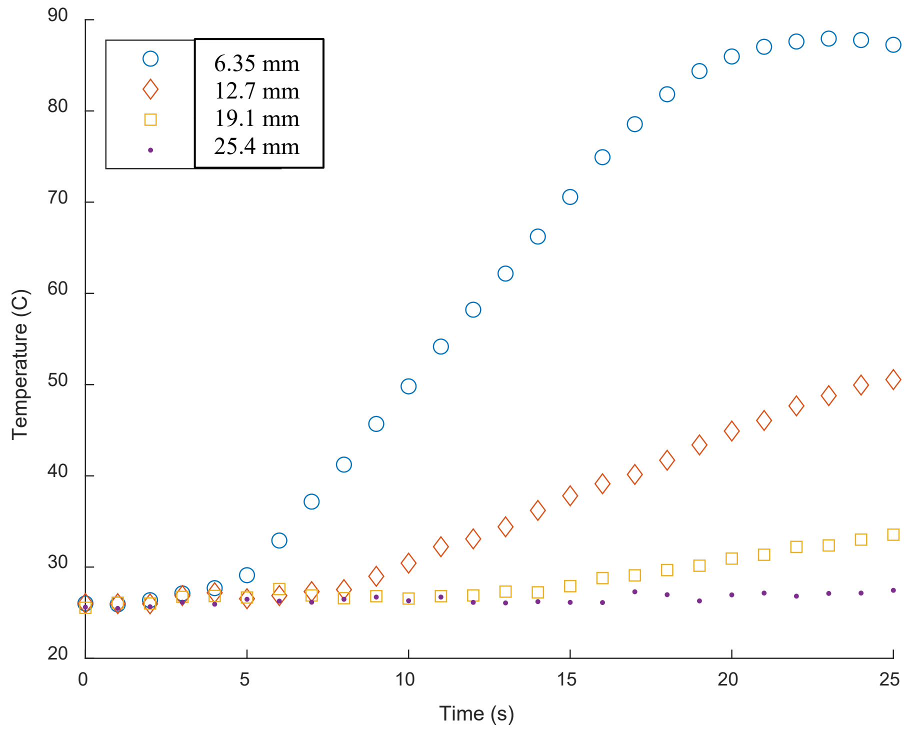
6.35 mm
12.7 mm
19.1 mm
25.4 mm
Temperature (C)
Time (s)
(a)

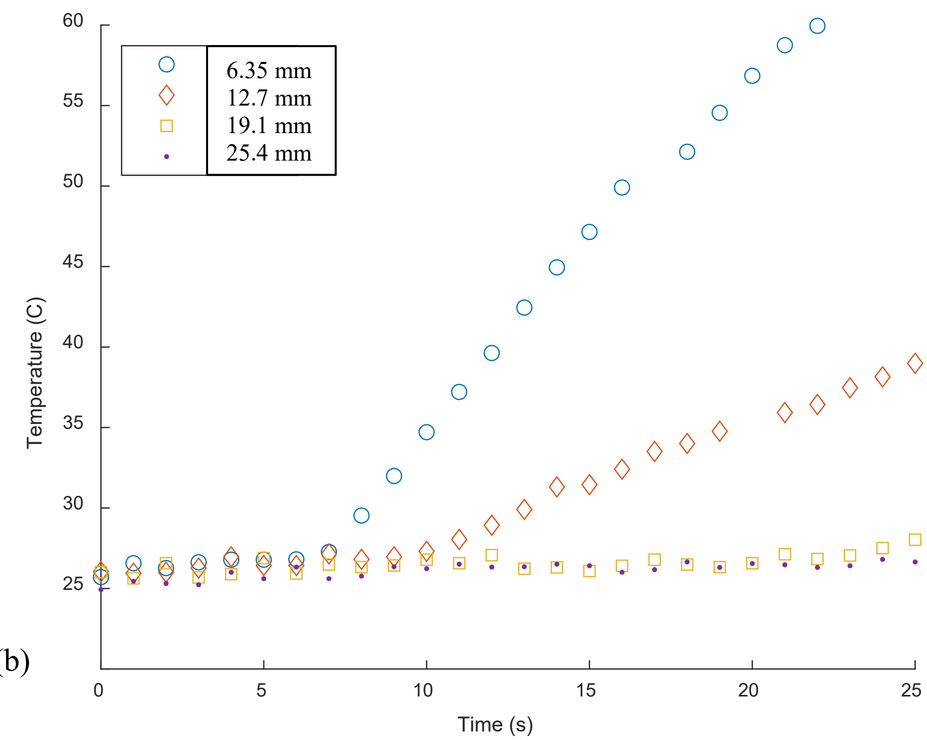
6.35 mm
12.7 mm
19.1 mm
25.4 mm
Temperature (C)
Time (s)
(b)

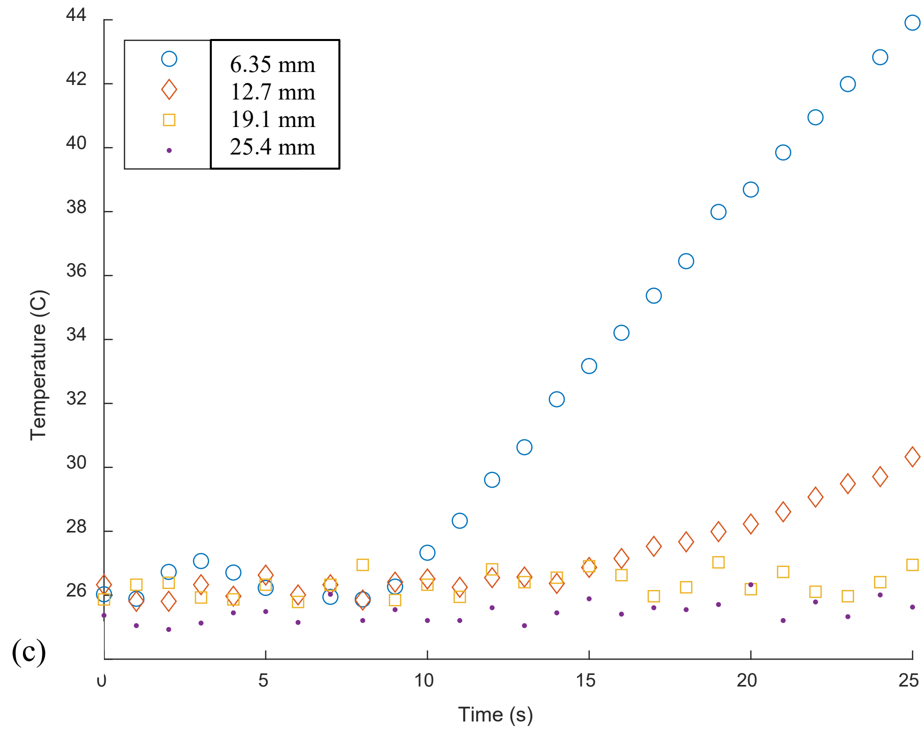

Figure 64: Change in temperature as a function of time on Bonded Panel 2, 13 plies [0/90] of CFRP. (a) 100.1 A, (b) 74.9 A, and (c) 50 A. The legend contains the lift off distances.

In Figure 64, (a) the Ambrell® control box is set to 100.1 A with a resultant resonance frequency of 287-295 kHz, (b) the Ambrell® control box is set to 74.9 A with a resultant resonance frequency of 287-297 kHz, and (c) the Ambrell® control box is set to 50 A with a resultant resonance frequency of 291-304 kHz.

Figure 64 shows that a **reasonable time for induction heating evaluation was determined to be within 10 seconds.** At 100.1 A and 74.9 A, there was a temperature rise of 24 ˚C and 8 ˚C (respectively) within 10 seconds. Given that the reasonable temperature limit was 10 ˚C with 74.9 – 100.1 A of current, 10 seconds was more than enough time to achieve sufficient induction heating. Beyond 10 seconds, there was too much heating, which would result in thermal saturation. Figure 64 also showed that a distance of 6.35 mm produced a quick rise in heat; this is desirable to run the experiments efficiently since it reduces experiment run times.

7.1.5 Heating Rate and Scanning Speed

A scanning speed was established to provide a relatively high electromagnetic coupling and efficient induction heating. Scanning in this thesis was defined as the application of induction heating as the induction coil travels in a linear direction and parallel to the specimen. This experiment was performed by measuring the rapid change in temperature resulting from scanning speeds between 0.5 cm/s and 2.5 cm/s. The lift-off distance was set at 6.35 mm. Scanning speed was important for uniform heating, better thermal contrast, reduced probability of overheating, and rapidly inspecting a large specimen. Stationary induction heating often led to overheating, uneven heating, and more time spent during inspection. Hence, scanning speed was examined. The experimental set-up consisted of Bonded Panel 2 and the induction system current was set at 60.5 A. The scanning speed was increased from 0.5 cm/s to 2.5 cm/s in increments of 0.5 cm/s.

Figure 65 shows that the change in temperature as a result of induction heating decreased with an increasing scanning speed. This was due to decreasing time for induction heating at a point in the scanning process. Furthermore, it was determined that **a reasonable speed for the scanning process was 1.5 cm/s.** There was too much heat for visible contrast (between the defect and unaffected region) at 0.5 cm/s, and unsatisfactory (not enough) heating at 2.5 cm/s. Interestingly enough, the frequency automatically decreased as the speed increased. When the coil is in linear motion, induced eddy currents were less effective at canceling flux generated by the coil, because the eddy currents did not have time to be fully be established before the induction coil had moved on. Hence, resonant frequency decreased.

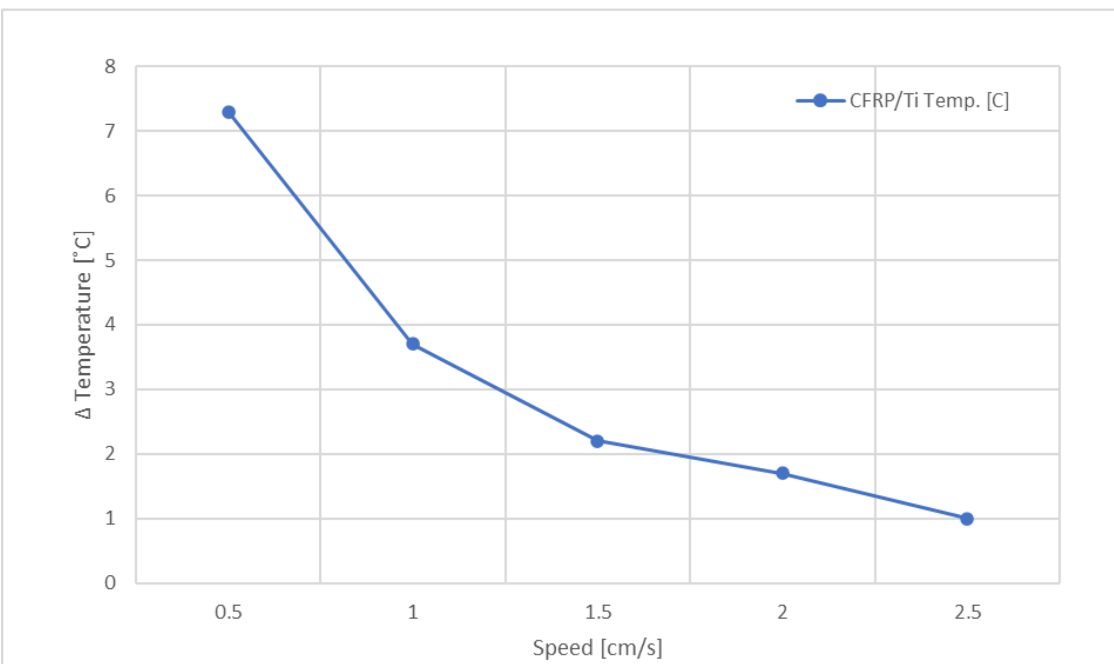

Figure 65: Change in temperature as a function of scanning speed on Bonded Panel 2, 13 plies [0/90] of CFRP. (Top Left) Ambrell® control box set to 60.5 A with a resultant resonance frequency of 287-300 kHz.

7.1.6 Coil Geometry and Orientation Trend

The purpose of this experiment was to evaluate the capability of the coils to produce even heating. This was determined by comparing a helical, a channel and two pancake coils. These off-the-shelf coils were selected because they are the most common coils used in induction heating [54]. Rightfully so, because these are the most efficient coils for heating [54]. Only the helical coil was tested perpendicular and parallel to the surface of the specimen. Furthermore, this investigation served as a qualitative assessment of coil geometry and orientation.

In terms of coil geometry, an important criterion for experimentation was even heating. Even heating was important to ensure that all discontinuities were highlighted with increased temperature and a reduced probability of false positives. In Figure 66, the surface temperature profile as a function of being heated with a helical coil is shown. The horizontal plane of 800 by 1200 units represents the dimensions of the (image) plane, and the contour bars shows the temperature in ˚C. Note that Figure 66 was the only 3D image to be re-constructed in MATLAB and only served to provide an understanding of the heat distribution. The induction heating was determined to be uneven (temperature difference of 50 ˚C between different locations in the panel) and the highest heat concentration was under the circular profile of the helical induction coil. This is due to high magnetic flux density in that region. Although helical coils are the most common and efficient coils [54], the heating pattern of the coil (placed perpendicular to the specimen) was ineffective at producing the required induction heating.

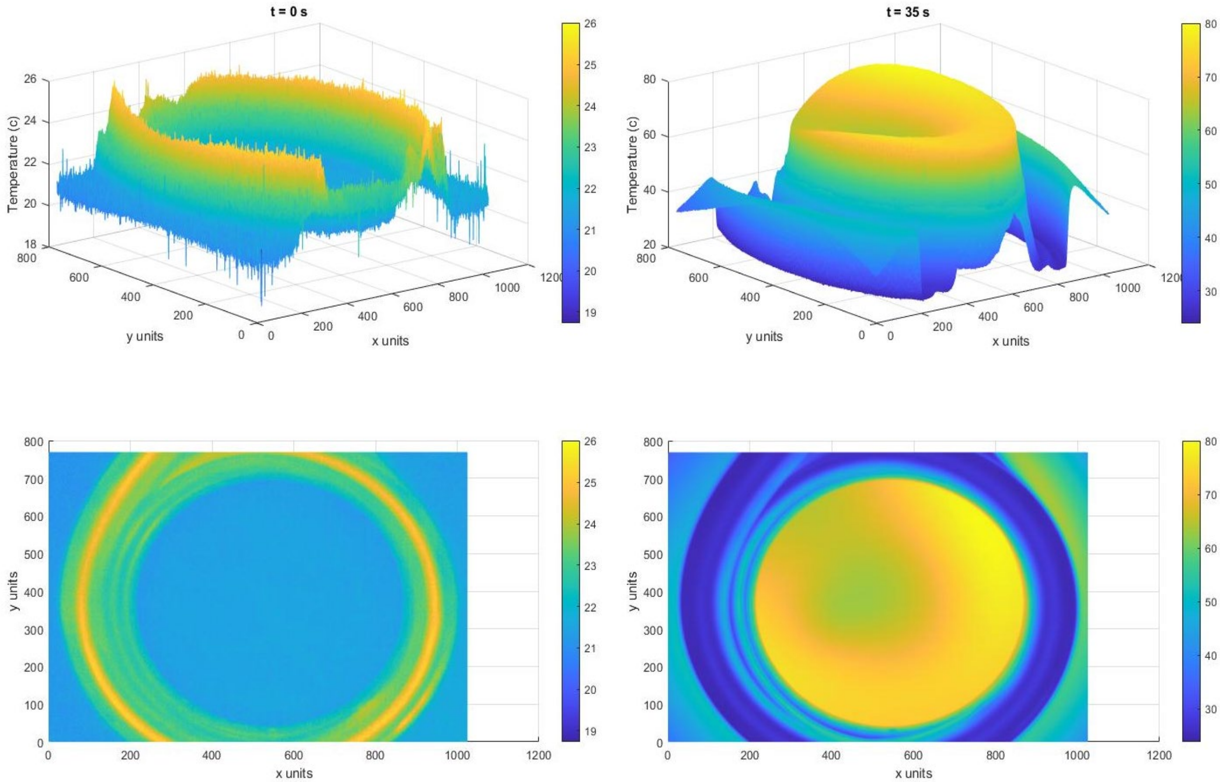

Figure 66: A 3D MATLAB re-construction image of stationary induction heating with the data collected by the IR camera. A helical coil (50.8 mm ID, 6.35 mm square tube, 3.175 mm gap) at lift-off distance 6.35 mm and 100.1 A of system current.

A **channel coil** was evaluated for even heating of the specimen, and similar to the helical coil, it was found to be unsatisfactory for stationary even heating. Figure 67 shows the channel coil and the resulting heating pattern. The areas of higher heat concentration (in yellow) are shown as being directly beneath the coil and not evenly distributed along the image. Also, Figures 67 to 69, the yellow represents a temperature of approximately 31 ˚C and purple represents a temperature of 21 ˚C.

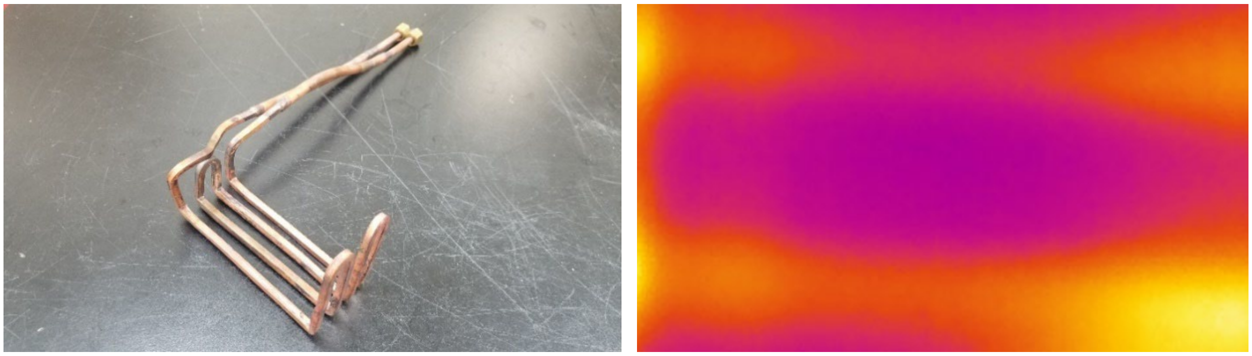

Figure 67: Channel coil (6.35 mm square tube, 9.5 mm gap, 127 mm wide) and resulting thermal heat pattern.

The **pancake coils** were also evaluated for even heating because they were thought to be the best candidate for even heating of a surface. Figure 68 shows the double pancake coil and the resulting heating pattern. Although there was less heating in the centre of the coil, the heating pattern **was marginally satisfactory for stationary even heating.** Marginally satisfactory is defined as portions of the test specimen not being actively heated. Once again, areas of higher heat concentration are in yellow, and areas of lower heat are in purple.

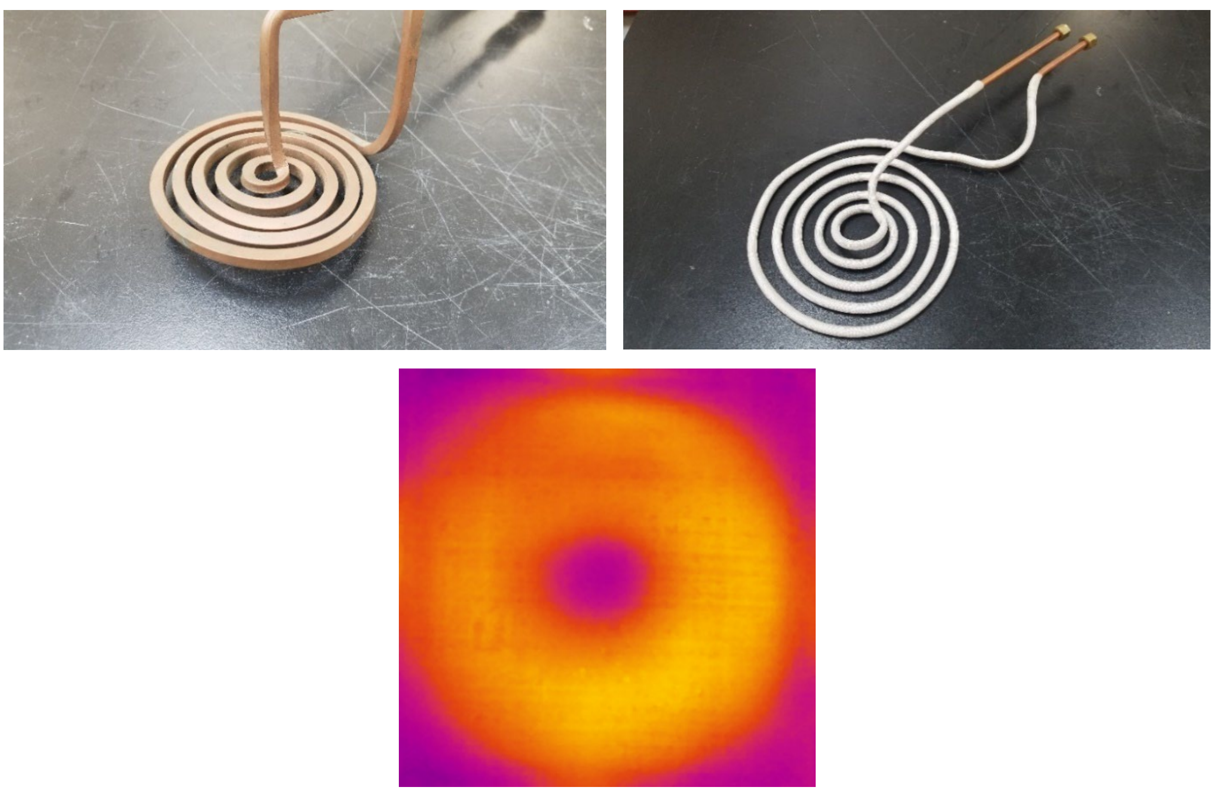

Figure 68: Image of a large pancake coil (right), a small pancake coil (left), and the resulting generic thermal heat pattern. Small pancake coil – 6.35 mm square tube, 5 turns, 12.7 mm ID, 88.9 mm OD. Large pancake coil – 38.1 mm ID, 165.1 mm OD, 5 turns, 6.35 mm tubing, fiberglass sleeve finish.

There was a final attempt for better stationary even heating. A double pancake coil was evaluated for even heating because it was viewed as an optimized version of a standard pancake coil. The double pancake coil would provide heating to the centre of the coil. However, similar to the previous coils, it was unsatisfactory for stationary even heating. Figure 69 shows the double pancake coil and the resulting heating pattern. Areas of higher heat concentration are in yellow, and areas of lower heat are in dark purple. Overall, the standard pancake coil provided the most uniform heating of all the coils in the stationary testing.

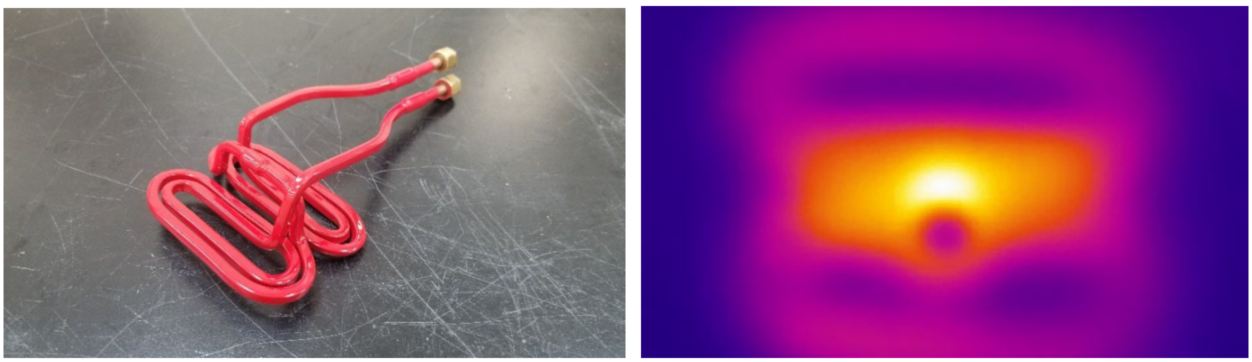

Figure 69: Double Oval Pancake coil (11 mm x 70 mm ID, 95 mm wide x 76 mm long (outer dimensions), 1.6 mm gaps between turns, 6.35 mm square tube) and resulting temperature gradient or thermal heat pattern.

7.1.7 Conclusion

This study focused on parametric evaluation to obtain the optimum parameters for induction heating with consideration of the lift-off distance, the rate of heating, the coil geometry, and the coil orientation. It was determined that a lift-off distance of **6.35 mm allowed the best coupling and rate of induction heating, 75 – 100 A provided a reasonable rate of induction heating**, **induction heating should be conducted within a 2 - 10 seconds range, a pancake coil was marginally satisfactory for stationary even heating, and a reasonable speed for the scanning process was 1.5 cm/s.** Note that stationary heating was not used beyond Study 1 because of unsatisfactory (uneven) heating conditions. In the scanning operation, all coils provided satisfactory heating. However, with the knowledge of the parametric study, a custom coil (6.35 mm circular tube, 3 turns, 28.6 mm width, 152.4 mm length) shown in Figure 70 was designed and built for scanning. It was a cross between a channel coil and a helical coil in a parallel orientation. The cross of these coils leveraged between the area coverage of the channel coil and the efficient uniform heating of the helical. The main advantage was the coil's ability to cover all potential discontinuities during scanning operations, to be covered in the next section.

Figure 70: A custom designed induction coil for scanning operations.

7.2 Detection And Dimensioning of Discontinuities (Study 2)

The purpose of this study was to determine whether the artificial discontinuities could be detected and dimensioned. Although the experimental investigation focused on infrared pulsed and induction thermography, ultrasonic testing was incorporated as a means of comparison. The induction heating experimental parameters for this study consisted of the coil shown in Figure 70, 6.35 mm of lift-off distance, and a current setting from 75 – 100 A. Additionally to increase thermal contrast between the disbond area and the surrounding area, the specimens were coupled to a large bar of aluminium for increased thermal conduction and a fan was used to blow cool air across the surface of the specimen for increased convection.

Table 21 highlights the detection and dimensioning results of this study. The table identifies the test specimen, the artificial defect being examined, the depth of the defect, the detection of the defect, the dimensions of the defect prior to lamination, and the measurements from the three methods. Table 21 has both the x and y component of the measurements, but since the disbond areas are either squared or can be defined with a single dimension (i.e. the FBH by its diameter), only one value for measurement is shown. In cases where both the x and y measurement are distinct or different, both the x and y value for measurement are shown. Of note, the induction thermography data was collected from a scanning operation. Additionally, there was no detectable evidence of an artificial disbond area caused by the mould release in Bonded Panels 1 to 3; this is most-likely due to the mould release fusing or blending into the adhesive during the curing process, or it is truly an undetectable kissing bond. Hence, the mould release data for those panels was discarded. Furthermore, the greyed-out area in Table 21 represents undetectable results. Lastly, the whited-out areas with a nil result denote results that were detected but could not be accurately dimensioned due to noise or overlapping discontinuities. The overall detection rate for this study was 53% for UT, 40% for PT, and 20% for IT.

For the thermography in this study, the primary post processing was Advanced Plateau Equalization (APE). It significantly enhanced the contrast between an artificial defect and the surrounding unaffected environment. Additionally, the thermograms were taken at the time of maximum contrast to obtain the greatest dissimilarity between the artificial defect and the surrounding unaffected environment. Section 7.5.1 explains the method for measuring the size of the defects from the thermograms.

Table 21: The results from the detection and dimensioning study.

Test Specimen ID	Artificial Defects	Depth		Detection			Pre-Lamination		Ultrasonic Testing		Pulsed Thermography		Induction Thermography	
		mm	inch	UT	PT	IT	mm	inch	mm	inch	mm	inch	mm	inch
Bonded Panel 1	FBH	1.14	0.045	N	Y	Y	12.7	0.50			14.73	0.58	13.97	0.55
	MR - Upper LH	1.14	0.045	N	N	N	25.4	1.00						
	MR - Upper RH	1.14	0.045	N	N	N	25.4	1.00						
	TT - Lower LH	1.14	0.045	N	N	N	25.4	1.00						
	TT - Lower RH	1.14	0.045	N	N	N	25.4	1.00						
Bonded Panel 2	FBH	3.56	0.140	Y	Y	Y	12.7	0.50	12.70	0.50	21.59	0.85	15.75	0.62
	MR - Upper LH	3.56	0.140	N	N	N	25.4	1.00						
	MR - Upper RH	3.56	0.140	N	N	N	25.4	1.00						
	TT - Lower LH	3.56	0.140	Y	N	N	25.4	1.00	25.40	1.00				
	TT - Lower RH	3.56	0.140	Y	N	N	25.4	1.00	25.40	1.00				
Bonded Panel 3	FBH	7.65	0.301	Y	N	N	12.7	0.50	10.16	0.40				
	MR - Upper LH	7.65	0.301	N	N	N	25.4	1.00						
	MR - Upper RH	7.65	0.301	N	N	N	25.4	1.00						
	TT - Lower LH	7.65	0.301	N	N	N	25.4	1.00						
	TT - Lower RH	7.65	0.301	N	N	N	25.4	1.00						
Bonded Panel 4	FBH 1	1.50	0.056	Y	Y	Y	12.7	0.50	13.97	0.55	15.75	0.62	13.71	0.54
											16.51	0.65		
	MR 1	1.50	0.056	N	Y	N	25.4	1.00			20.83	0.82		
	TT 1	1.50	0.056	Y	Y	N	25.4	1.00	25.4	1.00				
	FBH 2	2.00	0.079	Y	Y	Y	12.7	0.50	12.95	0.51	13.97	0.55	13.21	0.52
	MR2	2.00	0.079	N	N	N	25.4	1.00						
	TT 2	2.00	0.079	Y	N	N	25.4	1.00	25.4	1.00				

Table Notes:

FBH is an abbreviation for Flat Bottomed Hole
MR is an abbreviation for Mould Release
TT is an abbreviation for Thermal Tape

LH is an abbreviation for Left Hand
RH is an abbreviation for Right Hand
Y is an abbreviation for Yes
N is an abbreviation for No
UT is an abbreviation for Ultrasonic Testing
PT is an abbreviation for Pulsed Thermography
IT is an abbreviation for Induction Thermography

7.2.1 Specimen Breakdown

The following is a detailed analysis and corresponding discussion with regards to each test specimen captured in Table 21. The intent of the following analysis and discussion is to highlight the salient observations of the study.

7.2.1.1 Bonded Panel 1

Bonded Panel 1 and the other specimens were constructed with five artificial discontinuities. Thermal tape inserts, mould release gel, and a FBH were used to create artificial discontinuities. In Figure 71, Bonded Panel 1 had a significant number of delaminated areas due to poor inter-ply bonding during the manufacturing process. This particular condition improved the study, because it was a challenge for the ARMANDA AUT inspection system (the current system used to inspect the IWSLJ). In terms of detection, only pulsed (flash) and induction thermography were able to detect the FBH and no other artificial defect. In Figure 71, the FBH was indicated with a contrasting circle in the centre of the image. All inspection methods were also able to capture various amounts of the delaminated areas, although it was not an intended performance measure. Furthermore, it is entirely possible that delaminated areas were hiding the deliberate defects.

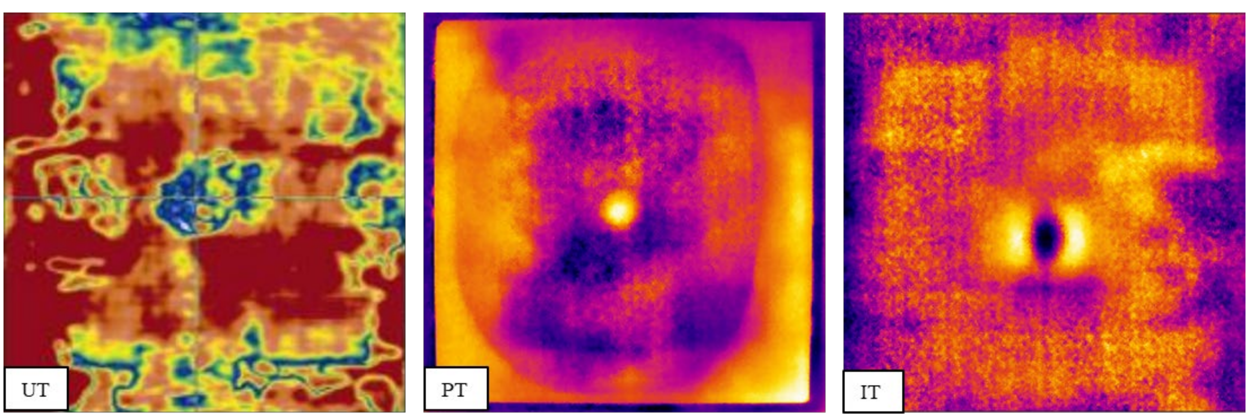

Figure 71: Bonded Panel 1 (CF/E-Ti) with the application of Ultrasonic Testing, Pulsed Thermography, and Induction Thermography.

In terms of dimensioning, there was a significant amount of noise for the UT inspection, which resulted in a failure to gather any useful information. Although the FBH was clearly visible, a diameter of 25.4 mm (twice the actual size of the hole) was measured from the contours that resembled the FBH. However, UT experts considered the FBH impossible to define due to the inability of finding the FBH in the large amount of noise. PT gave a diameter of 14.73 mm with 16% error (Appendix D and E). Likewise, IT gave a diameter of 13.97 mm with 10% error. Interestingly, IT performed the best in term of dimensioning the FBH. This is due to two aspects: (1) Induction thermography as an inspection method is not as sensitive to defect information overload as ultrasonic testing; and (2) induction thermography has the advantage of volumetric heating with the skin effect – meaning that heating can occur directly on the titanium, which reduces lateral heat diffusion. The effect is also the explanation for why the FBH is cooler than the surrounding titanium.

7.2.1.2 Bonded Panel 2

In Figure 72, Bonded Panel 2 also had several delaminated areas. In terms of detection, all inspection methods were able to detect the FBH. The UT inspection method was able detect the thermal tape as well. All inspection methods investigated here were also able to capture various amounts of delaminated area, although it was not an intended performance measure.

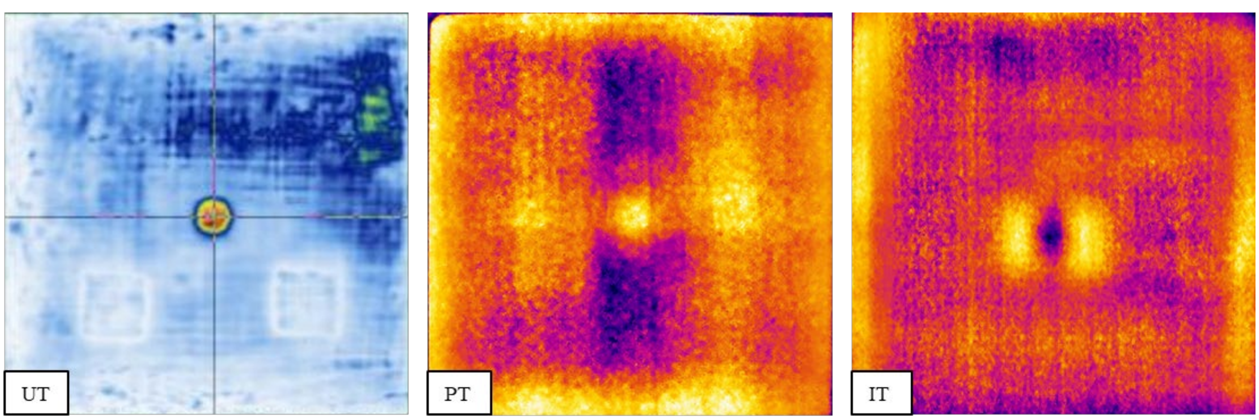

Figure 72: Bonded Panel 2 (CF/E-Ti) with the application of Ultrasonic Testing, Pulsed Thermography, and Induction Thermography.

In terms of dimensioning, there was a significant amount of noise for the UT inspection, which resulted in a reduction of data quality. However, there was a 0% error rate for the UT inspection method for the FBH and thermal tape inserts because the outline of the disbond areas matched the actual dimensions of the artificial defects. PT gave a diameter of 21.59 mm with 70% error for the FBH. Likewise, IT gave a diameter of 15.75 mm with 24% error for the FBH. UT proved to be the superior method. The induction thermography dimension was more accurate than the pulsed thermography, because of volumetric heating and the reduction in lateral heat diffusion.

7.2.1.3 Bonded Panel 3

In Figure 73, Bonded Panel 3 proved to be difficult to inspect because of a number of delaminated areas in the CFRP and the depth of the artificial discontinuities. The red patches at the top of the UT image were determined to be delaminated areas. In terms of detection, the UT inspection method was the only method capable of detecting an artificial disbond area; it was able to detect the FBH, the barely visible circle at the centre of the UT image. The pulsed thermography image, seen in Figure 73, has an area of slightly higher temperature in the centre of the sample. That area is the thermal reflection of the IR camera, and therefore, was not considered as a disbond area. The heating pattern in the induction thermography image is the heating pattern for CFRP in a [0/90] orientation. Note that the heating pattern for the IWSLJ has a [0/45/90] orientation type pattern as shown in Study 3.

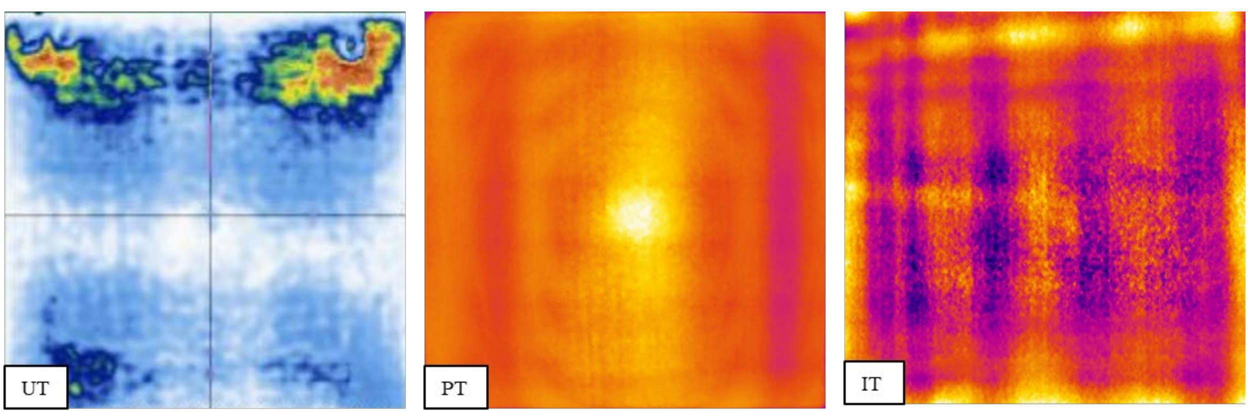

Figure 73: Bonded Panel 3 (CF/E-Ti) with the application of Ultrasonic Testing, Pulsed Thermography, and Induction Thermography.

In terms of dimensioning, there was once again a significant amount of noise for the UT inspection, which resulted in a reduction of data quality. However, the FBH was measured to be 10.16 mm with -20% error by the UT inspection method. This dimension saw a reduced size because the FBH was barely visible. Again, UT proved to be the superior method. In comparing the images of Bonded Panel 3 in Figure 73, the UT image looked to be farther away (more physical distance) than the other images. This perception was directly linked to how the image was captured and does not reflect different dimensions with regards to the panel. Also, the fibre pattern was only prominent in the induction thermography image because induction heating occurs along the length of the fibres.

7.2.1.4 Bonded Panel 4

In Figure 74, in terms of detection, the UT inspection method was able to detect the FBHs and thermal tape inserts. Pulsed thermography method was able to detect the FBHs and one mould release defect. Finally, induction thermography was only able to detect the FBHs. In terms of dimensioning, it was interesting to note that induction thermography was just as accurate as UT at 97% and more accurate than flash thermography's 83% accuracy. This was due to electromagnetic skin depth and volumetric heating that occurs in induction thermography.

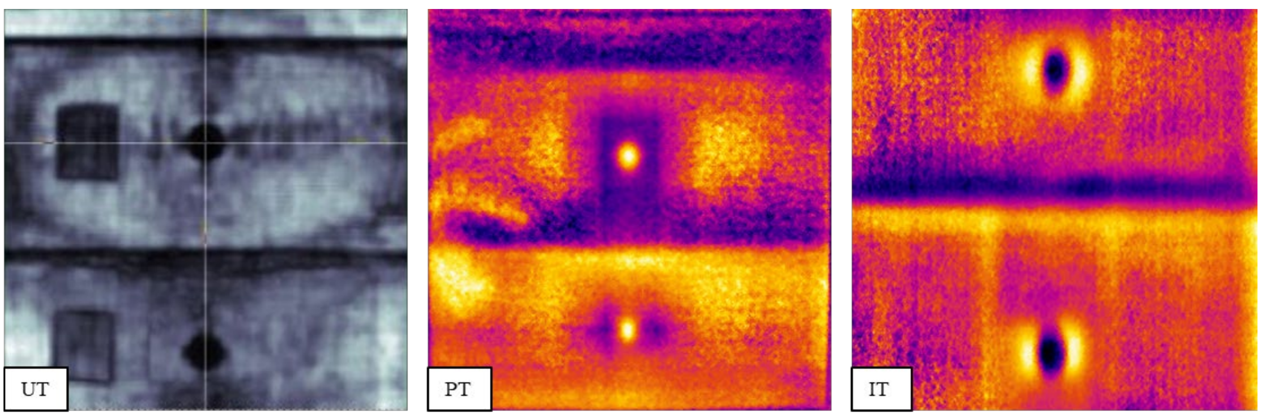

Figure 74: Bonded Panel 4 (CF/E-Ti) with the application of Ultrasonic Testing, Pulsed Thermography, and Induction Thermography.

7.3 Detecting Discontinuities at Different Depths (Study 3)

The detection of discontinuities at different inspection depth was significant because the IWSLJ has nine steps at different depths at which disbond areas can occur. However, the first two steps are the most significant because they have the highest likelihood for disbond areas. Bonded Panel's 1 to 4 and Sample No. 1 best simulate steps 1 to 4 and 9. Figure 75 showed that all inspection methods were able to detect the FBHs on simulated Steps 1 to 4 and only ultrasonic testing was able to detect the FBH at simulated Step 9. Table 22 showed that additional testing at depth was done on the IWSLJ Calibration Block with both thermography methods. The results agreed with the observation that both pulsed and induction thermography have a capacity for detection up to the fourth step. However, only UT was able to show all 9 steps.

Table 22 from *Netzelman et al.* [4] explains why both induction and pulsed thermography are limited to the fourth step. It results from the thermal penetration depth (the depth achieved by the thermal energy). In Table 23, the skin depth and the thermal penetration are of the same order, but thermal penetration is smaller. Hence, thermal penetration is the limiting factor for not observing heat at depth. For CFRP, the skin depth and the thermal penetration are significantly different. The thermal penetration in the CFRP is the overwhelming limiting factor for not observing heat at depth. In the case of this thesis, the CFRP is on top of the titanium, and therefore, the thermal penetration presents a major limiting factor to not observing heat at depth (or beyond the fourth step to be exact). With induction heating, heating is most likely occurring beyond the fourth step. However, the thermally insulating properties of the CFRP is most likely preventing heat from penetrating through to the IR camera, although an induction system of significant high power could probably generate enough heat to pass through the CFRP. Regardless, thermography could potentially be used for inspecting the first 2 steps.

Table 22: Penetration depth testing on the IWSLJ Calibration Block.

Test Specimen ID	Artificial Defects	Depth		Detection		
		mm	inch	UT	PT	IT
IWSLJ	Step 1	0.5	0.020	Y	Y	Y
	Step 2	1.0	0.039	Y	Y	Y
	Step 3	2.0	0.079	Y	Y	Y
	Step 4	3.0	0.118	Y	Y	Y
	Step 5	4.0	0.157	Y	N	N
	Step 6	5.0	0.197	Y	N	N
	Step 7	6.0	0.236	Y	N	N
	Step 8	7.0	0.276	Y	N	N
	Step 9	7.5	0.295	Y	N	N

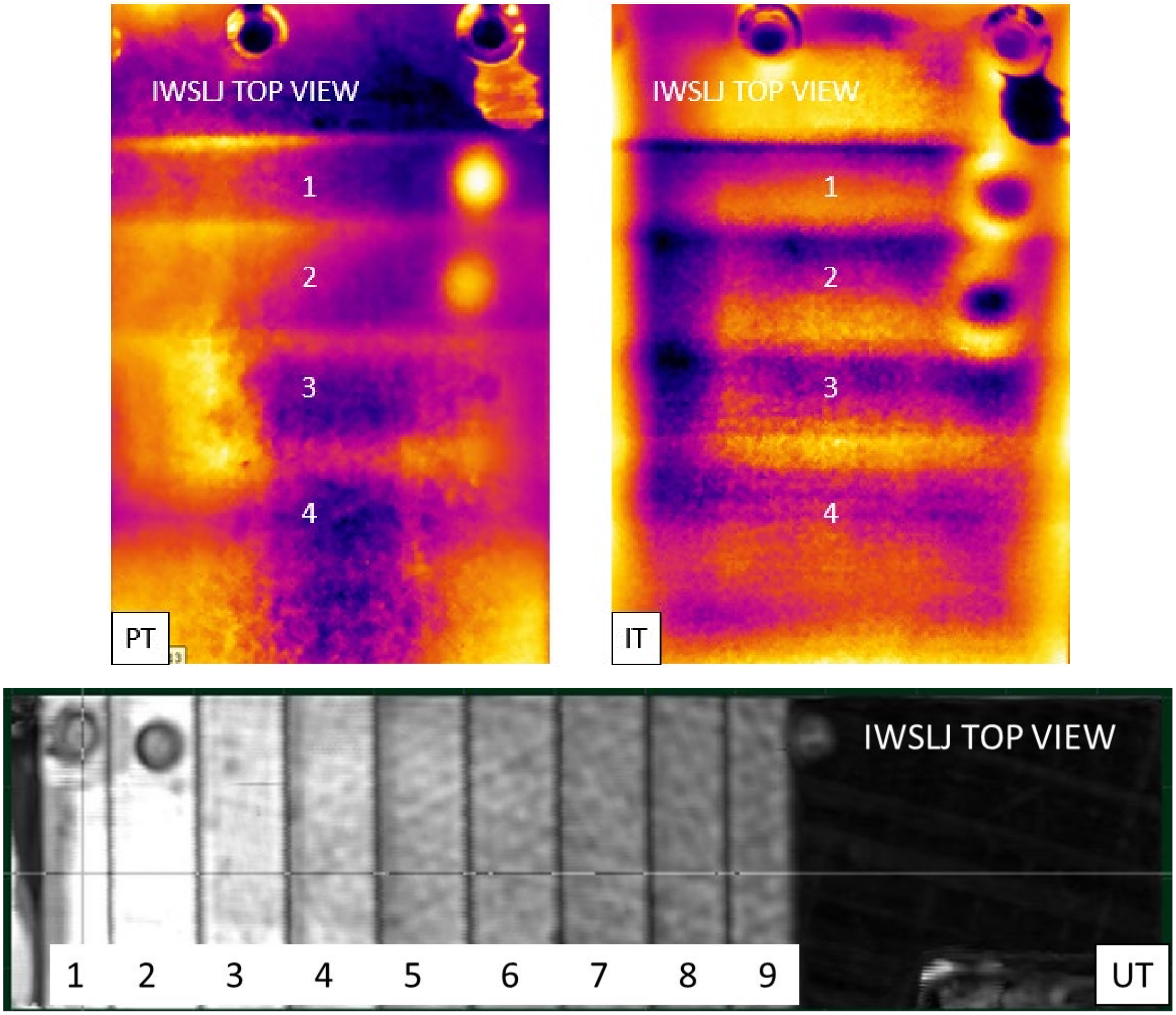

Figure 75: Top view of IWSLJ ultrasonic testing Calibration Block under pulsed thermography, induction thermography, and ultrasonic testing.

Table 23: IWSLJ material highlighting skin depth versus thermal penetration [4].

	Electrical Conductivity in 10^6 S/m	Relative Magnetic Permeability	Thermal Diffusivity in 10^{-6} m^2/s	Electromagnetic Skin Depth in mm (100 kHz)	Thermal Penetration Depth in mm (t=0.1 s)
Titanium 6AL-4V	0.58	1	6.59	2.09	1.62
Carbon Fibre Reinforced Polymer	0.001	1	3.65	50	1.21

7.4 Detection Sensitivity (Study 4)

This study was an evaluation of each method's ability to detect and dimension specific artificial discontinuities over a variety of different surface treatments. Sample No. 1 proved to be the ideal test specimen for this study because of the large variety of defects simulated. Table 24 presents the manufacturing details of Sample No.1 in terms of surface treatment and artificial defect inserts used. Additionally, Table 24 shows the results of this study. In summary, both the ultrasonic testing and the pulsed thermography were able to detect all artificial discontinuities as shown in Figure 76. Meaning that both simulated traditional UT and kissing disbond areas were detectable. Induction thermography was only able to detect and define the FBH. Furthermore, ultrasonic testing and pulsed thermography were only able to define the thermal tape inserts and the FBH. For this study, ultrasonic testing provided the most details in terms of detection sensitivity. Of note, the boundaries of the mould release gel insert were not well-defined. Hence, the boundaries could not be dimensioned.

Table 24: Summary of results for detection sensitivity testing for Sample No.1.

Test Specimen ID	Artificial Defects	Depth		Detection			Pre-Lamination		Ultrasonic Testing		Pulsed Thermography		Induction Thermography	
		mm	inch	UT	PT	IT	mm	inch	mm	inch	mm	inch	mm	inch
Sample No. 1	AN 1	2.10	0.083	Y	Y	N								
							29.97	1.18	30.48	1.20	26.42	1.04		
	AN 2	2.10	0.083	Y	Y	N	25.91	1.02	26.67	1.05	18.54	0.73		
	AN 3	2.10	0.083	Y	Y	N								
	AN 4	2.10	0.083	Y	Y	N								
	AN 5	2.10	0.083	Y	Y	Y	12.70	0.50	12.70	0.50	14.22	0.56	13.46	0.53
	AN 6	2.10	0.083	Y	Y	N								
							27.94	1.10	36.83	1.45	39.37	1.55		
	AN 7	2.10	0.083	Y	Y	N	27.94	1.10	33.02	1.30	41.15	1.62		
	AN 8	2.10	0.083	Y	Y	N								
	AN 9	2.10	0.083	Y	Y	N								

Note: AN is an abbreviation for Area Number

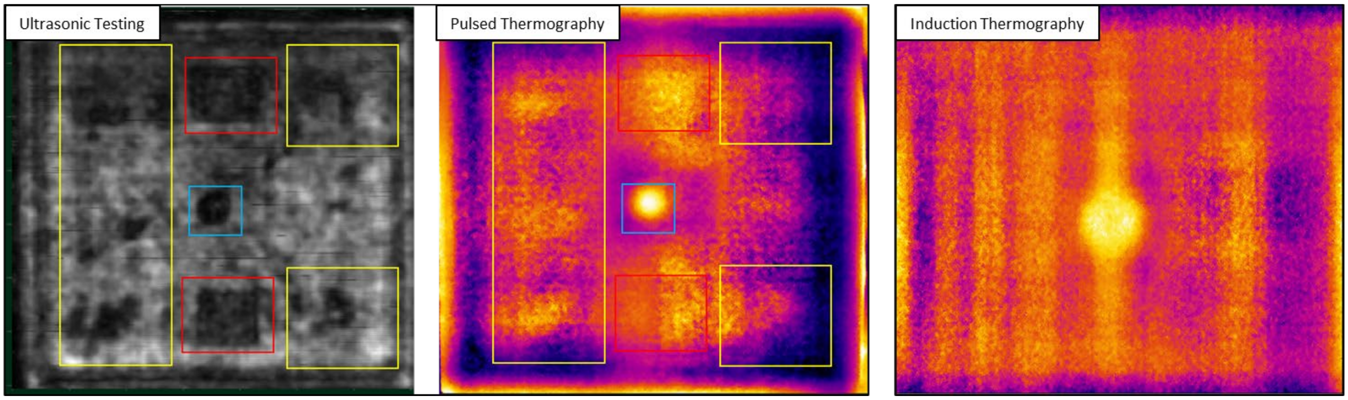

Figure 76: Sample No.1 (CF/E-Ti) with the application of Ultrasonic Testing (left), Pulsed Thermography (middle), and Induction Thermography (right). The thermal tape inserts are outlined in red. The FBH is outlined in blue. The mould release wax and evidence of other embedded flaws are outlined in yellow.

For an in-depth interpretation of the ultrasonic testing results, reference Appendix B, D, E, and F. For an initial report from Ambrell Corporation® regarding induction heating of Titanium and CFRP, reference Appendix G. For the Ambrell Corporation® EASYHEAT Induction system specifications, reference Appendix H.

7.4.1 Error Analysis

An error analysis was performed on the dimensions of the defect measured from the ultrasonic testing, pulsed thermography, and induction thermography on the test specimens. Error was defined as the percent difference between the size of the defect measured from the images and the actual dimensions of the defects. The details of the error analysis are captured within Table 25. In general, the ultrasonic testing presented very little error in most cases. Additionally, induction thermography proved to be more accurate with dimensions than pulsed thermography. Pulsed thermography was able to detect more discontinuities than induction thermography.

Table 25: Error for ultrasonic testing, pulsed thermography, and induction thermography.

Test Specimen ID	Artificial Defects	Error Analysis		
		UT	PT	IT
Bonded Panel 1	FBH		16%	10%
	MR - Upper LH			
	MR - Upper RH			
	TT - Lower LH			
	TT - Lower RH			
Bonded Panel 2	FBH	0%	70%	24%
	MR - Upper LH			
	MR - Upper RH			
	TT - Lower LH	0%		
	TT - Lower RH	0%		
Bonded Panel 3	FBH	-20%		
	MR - Upper LH			
	MR - Upper RH			
	TT - Lower LH			
	TT - Lower RH			
Bonded Panel 4	FBH 1	10%	24%	8%
	MR 1		-35%	
			-18%	
	TT 1	0%		
	FBH 2	2%	10%	4%
	MR2			
	TT 2	0%		
Sample No. 1	AN 1			
	AN 2	2%	-14%	
		3%	-27%	
	AN 3			
	AN 4			
	AN 5	0%	12%	6%
	AN 6			
	AN 7	32%	41%	
		18%	47%	
	AN 8			
	AN 9			

The *Wysocka-Fotek's* [55] method to be described below was used to determine the dimensions of all defects captured with thermography at maximum contrast. The method was used because a direct measurement may not fully capture all pixels related to the defect. Additionally, thermal energy also dissipates laterally during heat diffusion; this phenomenon makes the defect appear larger than the actual measurement. The *Wysocka-Fotek's* [55] method accounts for lateral heat diffusion and captures the entirety of all pixels indicative of a defect area. In a 2D thermographic image, a defect area has a Gaussian temperature profile or shape with the highest/lowest temperatures at the center of the defect as shown in Figure 77.

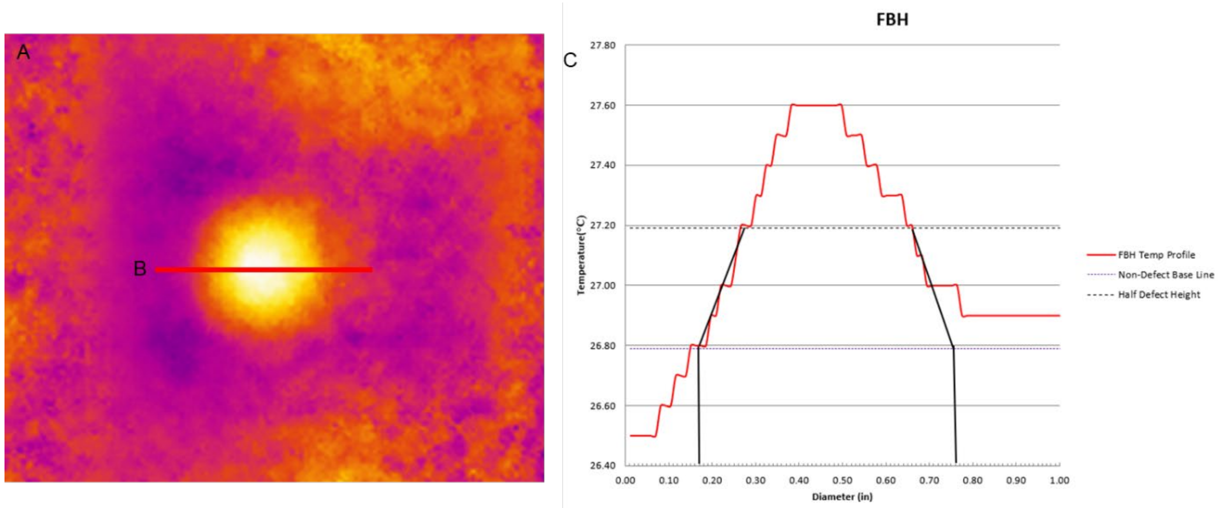

Figure 77: (A) Thermographic image of the Flat Bottom Hole (FBH). (B) Temperature profile line segment within the FLIR ResearchIR software. (C) Graphical representation of the FBH Gaussian temperature profile.

The Gaussian temperature profile forms the basis of the *Wysocka-Fotek's* [55] method as depicted in Figure 77 (C). To determine the length of a disbond area with the *Wysocka-Fotek's* [55] method in Figure 78, the following steps were taken [55]:

1. In the FLIR ResearchIR software, draw an overlapping temperature profile line across the defect or disbond area of interest in the thermographic image;
2. From the Gaussian temperature profile produced, determine the average surface temperature of the non-defect region and plot this temperature (as a base line) across the Gaussian temperature profile (a);
3. At the half height of the defect in the Gaussian temperature profile, plot a tangent line that intersects with the base line on both sides of the Gaussian distribution curve (b); and
4. The defect length is measured between the two intersections on both sides of the Gaussian distribution curve.

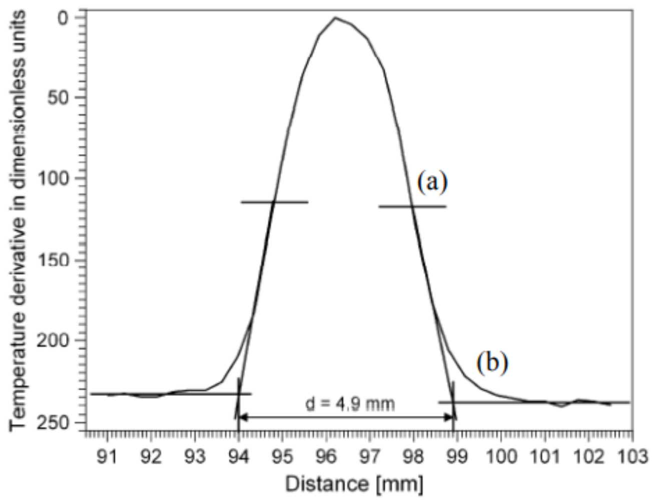

Figure 78: Wysocka-Fotek's method to determine the length of disbond areas [55]. For the y-axis, note that temperature, not temperature derivation, was used in this thesis.

The *Wysocka-Fotek's* method gave an accurate estimation of the disbond area length and width, especially so for induction thermography. Even with a highly defined defect with exceptional thermal contrast, the *Wysocka-Fotek's* method would not be able to render the exact dimensions. This is inherent in the method given the following reasons:

1. The method relies on an accurate estimation of the average surface temperature to set a baseline. Seldomly is the surface temperature perfectly uniform and the sample material(s) absolutely free of minor defects (small voids, impurities, delaminations, etc). Hence, there will always be error in the average surface temperature baseline. Furthermore, the higher the sensitivity required, the more error incurred in establishing the baseline. This is the case when the temperature profile of the defect is close to the temperature profile of the unaffected surrounding area on the specimen; and
2. The method also heavily depends on the accurate placement of the tangent line shown in Figure 78. The task becomes more difficult with more erratic Gaussian temperature profiles.

The Full Width Half Maximum (FWHM) thermographic measurement technique was explored to gain higher accuracy and less error in dimensioning the discontinuities. Similar to the *Wysocka-Fotek's* method, the FWHM method also measures from the half maximum value (Figure 79). However, the FWHM method draws two vertical lines starting from the half maximum temperature value directly down to the baseline temperature value as shown in Figure 79. Finally, the width of the defect is bounded by the two lines.

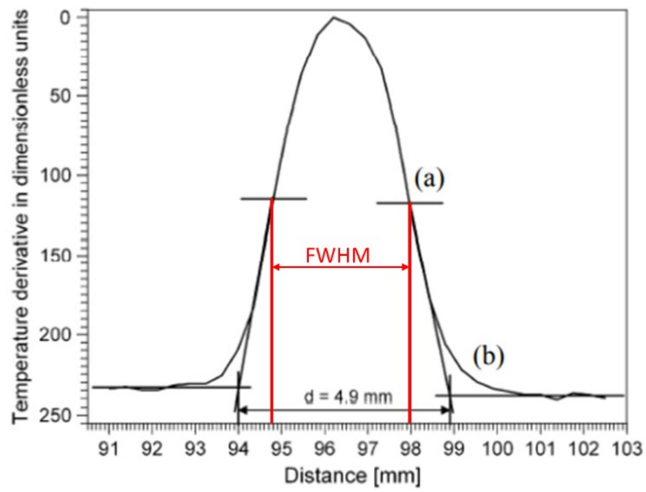

Figure 79: Full Width Half Maximum method (highlighted in red) to determine the length of disbond areas [55].

The FWHM method was discarded due to high percent error of approximately -60% in defect measurements. The error was likely due to the lateral heat dispersion affecting the FWHM measurement.

CHAPTER 8 – DISCUSSION

The IWSLJ serves as the primary structural member transferring loads between the wing and fuselage. Although the IWSLJ is designed to prolong aircraft life by evenly distributing shear stress along its steps, disbond areas have the potential to lead to a wing-fuselage separation. The IWSLJ is vulnerable at the MCI due to prolonged exposure to high temperatures, moisture ingress, and fatigue. Consequently, disbond areas may form due to adhesive internal failure or the adhesive and surrounding material may experience an adherent failure. Steps 1 and 2 are most vulnerable to disbond areas, which have the potential to quickly grow to Step 5. Presently, there is no research of the rate of disbond growth or the critical size of the disbond area for the IWSLJ. Although UT has proven to be highly successful in detecting disbond areas in the IWSLJ, the testing is complex, lengthy, and requires expensive equipment [6]. Furthermore, if disbond areas are detected early (in the form of kissing bonds for the first two steps) by thermography, UT should not be required. This is why thermography was worth investigating; however, some interesting challenges were discovered.

This chapter aims to discuss the results by comparing all methods used in the studies and outline limitations of thermography. Finally, closing remarks will state whether thermography should be considered for inspecting of the IWSLJ.

8.1 Summary – Comparison Analysis

Table 26 contains a summary and comparison of the results obtained throughout this thesis. It is important to have a clear comparison in order to assess whether thermography is a potential inspection method for the IWSLJ. The rate of detection for artificial disbond defects was investigated and UT, using the ARMANDA system, had the highest detection rate. CFRP proved to be the limiting factor for the detection rate of all three methods. For UT, CFRP is normally highly attenuating, and in the case of the panels created, the detection rate was worsened by signal scatter from unintended defects (delaminated areas, voids, resin rich, resin starved, etc.). CFRP was challenging for thermography because it was thermally insulating and had many delaminations. Induction thermography had a lower detection rate than pulsed thermography due to a lack of contrast caused by heat generation at the same skin depth. Uniform heating, over heating, and heat diffusion time were also limiting factors against induction heating. It was difficult to achieve even heating with induction due to localized heating (increasing the odds of over heating) and electromagnetic effects such as the edge effect. Furthermore, flash thermography allowed for more time for heat to diffuse, which allowed heat in the unaffected regions of the specimen to disperse, while keeping a higher temperature at the defect.

Ultrasonic testing was also superior in the accuracy of defect dimensions and for depth of penetration. The dimensional error in thermography was due to the lateral dispersion of heat. The limited penetration depth in thermography can be attributed to the thermal insulation properties of CFRP. The insulating properties of the CFRP prevented the heat from going beyond the fifth step. Although not significant, it should be mentioned that the overall cost for the flash thermography experimental setup was approximately \$25 k, the induction system experimental setup was approximately \$45 k, and the TecScan© ARMANDA system was approximately \$300 k. Induction thermography was significantly more efficient in terms of power usage. As low as 7 W for induction thermography in comparison to 1000 W for flash thermography.

It is clear that the ARMANDA system is the superior inspection system, but it comes at a cost. The setup and inspection time for the ARMANDA system is lengthy. The setup is also complicated and laborious. This is because the ARMANDA system is difficult to properly calibrate, complicated to operate, and a high level of UT expertise is required to process the large quantity of inspection data. Also, there are many parts to the inspection system. Few members in all of the DND and the CAF are authorized to carry out inspections with the ARMANDA system. It is also one of a kind, and not "off the shelf." Lastly, although slower and more tedious, conventional handheld pulsed echo UT is capable of similar results as the ARMANDA system at a fraction of the cost [52], but without the C-Scan capability. Nevertheless, it can detect and dimension kissing bonds. The advantages and disadvantages can be seen in Table 26.

Table 26: A summary and comparison of the UT, Flash Thermography, and Induction Thermography results gathered throughout this thesis.

	Ultrasonic Testing, ARMANDA	**Pulsed (Flash) Thermography**	**Induction Thermography**
Detection	53% Detection Rate	40% Detection Rate	20% Detection Rate
Dimension	~3% Error	~29% Error	~10% Error
Depth	All 9 Steps	Steps 1 - 4	Steps 1 - 4
Sensitivity	All Disbond Areas + FBH	All Disbond Areas + FBH	Only FBH
Inspection Time	45 min	~3 min	~2 min
Ranking for Min Setup Time	3	1	2
Cost	~$300k	~$25k	~$45k
Advantage	All inspection data recorded Data can be presented in A, B, and C Scan Post analysis of data available The entire IWSLJ can be inspected IML disbond areas are detectable for steps 1 – 4 Great for detection, dimension, depth, and sensitivity Repeatable	Good sensitivity and reasonable defect detection Quick to setup and easy to use Results are easier to interpret Uniform heating Low financial cost	Fast and relatively accurate Covers a large surface area Results are easier to interpret Efficient heating
Disadvantage	Lengthy inspection time and setup time More financial cost Advanced UT training required Complicated equipment	Lateral heat dispersion leads to high error in dimensions Low depth of penetration	Low sensitivity and detection rate Uneven heating in stationary study

Desirable	Less Desirable	Least Desirable

8.2 Other Sources of Error and Challenges

There were a variety of other sources of error observed during this study. The other sources of potential error were identified after consulting with experts [31] and would only be confirmed with destructive testing. With reference to Figure 80, the ultrasonic image clearly shows all artificial defects as well as other unintended defects as sources of error. This image serves as a complimentary reference to the IR thermographic image. The dark blue to black region of the IR thermal image (A) is a region of slightly lower temperatures. This region (A) was unintendedly created during the manufacturing process of the CFRP; The dark blue to black region (A) is **slightly thinner** than the rest of the CFRP – creating a slightly uneven temperature distribution. Region (B) was determined to be an example of an unintended defect in the CFRP (**an interlamination void and/or delamination and/or a resin rich/starved area**). This conclusion was derived from a strong agreement with the same observations noted by *Rellinger* [31]. Region (C) was determined to be a great example of a **bonding problem**. In Region (C), the CFRP was sanded and the titanium did not receive a surface treatment. This led to a bonding/adhesion problem that was observed on both images. These three example regions highlighted other sources of error in the experimentation process. Of note, heat saturation was another source of error. During lengthy use of the thermography apparatus, details in the thermograms were blurred with elevated temperatures due to prolonged operation.

8.2.1 Defect Types

Three inserts were used to simulate conventional UT disbond areas and kissing bonds. Namely, a FBH (conventional disbond), thermal tape (kissing bond), and mould release (kissing bond). In terms of ultrasonic testing, the FBH and the thermal tape results presented as a conventional disbond area. The mould release and surface treatment results presented as a kissing bond. All were realistic types of disbond areas and can be expected to appear as defects on the IWSLJ. This was supported by UT experts at QETE who were fortunate enough to study a few IWSLJ with different types of disbond areas.

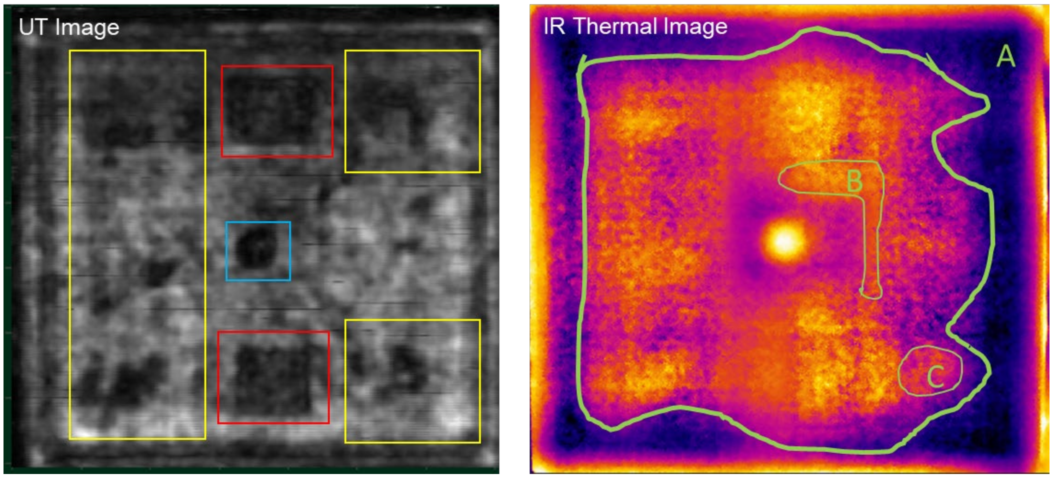

Figure 80: Defect mapping highlighting deliberate defects on the UT image and unintended defects on the thermal image in Sample No.1.

8.2.2 Thermal Saturation

Thermal saturation is localized over heating cause by a high current leading to more power in the system and thus a faster local heating. This a common problem with induction heating because of the efficiency of the heating process; A relatively small amount of power is required to generate adequate heat. Thermal saturation causes the discontinuity on the thermogram to appear blurry or faint. As shown in Figure 81, the two 12.7 mm holes of the IWSLJ are barely visible due to thermal saturation. There are a number of ways to correct for thermal saturation. The most common to adjust time, distance, and power.

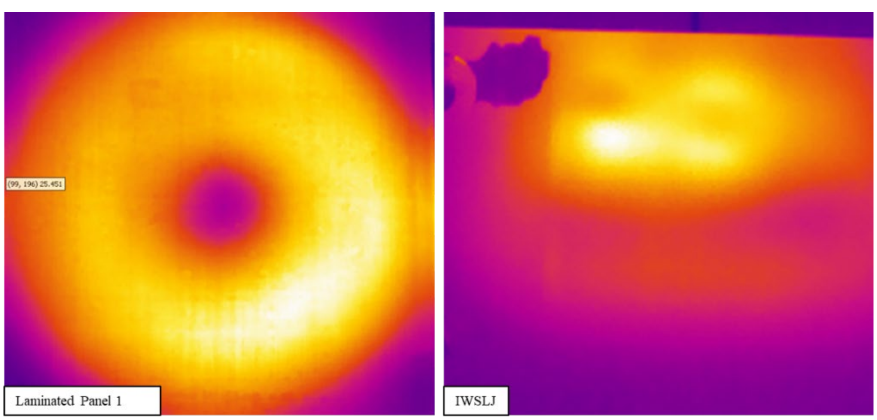

Figure 81: Thermal saturation with induction heating due to overheating of the test specimen.

8.2.3 Edge Effect

Edge effect is the change of the electrical path and magnetic flux at the edges of a test specimen due to the differences in current density. There is a tendency for eddy current to build up at the edge of the test specimen resulting in a high concentration of heat as shown in Figure 82. Edge effect was unavoidable during induction heating because of the size of the test specimen. However, it did not significantly affect the outcome of the results. The easiest means of addressing edge effect is leveraging on the expertise of trained thermography technicians and using advanced data processing techniques.

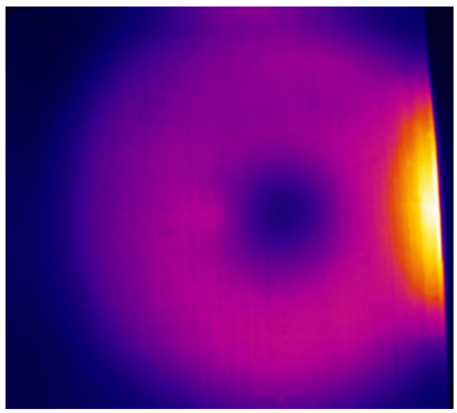

Figure 82: Thermal saturation along the edge of the test specimen due to edge effect.

8.2.4 Cancellation Effect

Figure 83 showed that cancellation effect occurs as a result of opposite sides of the coil being too close to each other. The opposing magnetic fields generated by the alternating current flowing through the coil cancel each other out. In the case displayed in Figure 83, there is a region of no heating because of insufficient inductance as a result of the cancellation effect. The cancellation effect can be corrected by altering the shape of the coil to include more space between the opposing sides of the inductor.

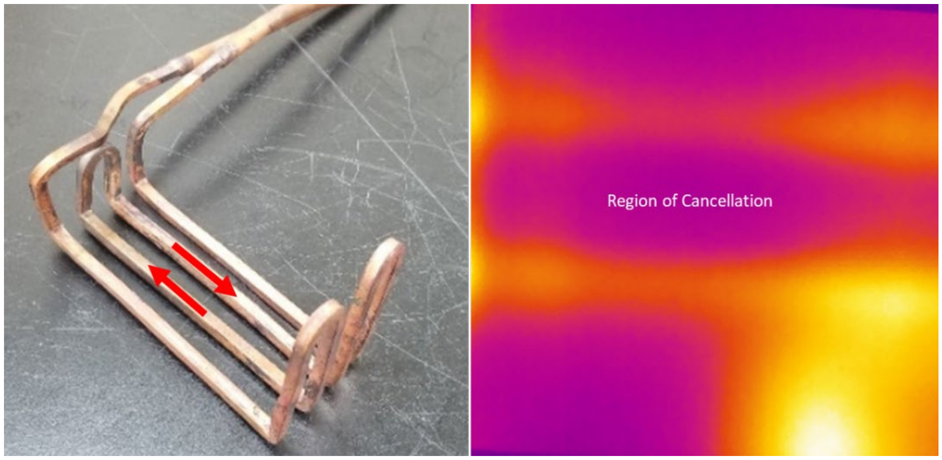

Figure 83: Cancellation effect observed with the channel coil. The red arrows show the opposing flow on alternating current.

8.2.5 CFRP Heating Pattern

In Figure 84, one of the disadvantages of conducting induction thermography on CFRP is that heat concentrates at fibre junctions. This results in a distinct heating pattern based on the fibre ply orientation. It also causes localized regions of elevated heat that may be interpreted as a discontinuity. Since the electrical thermal diffusivity of titanium is almost twice that of CFRP, the titanium's thermal signature was more prominent than the CFRP's. Hence, the CFRP heating pattern did not present a problem for signal interpretation.

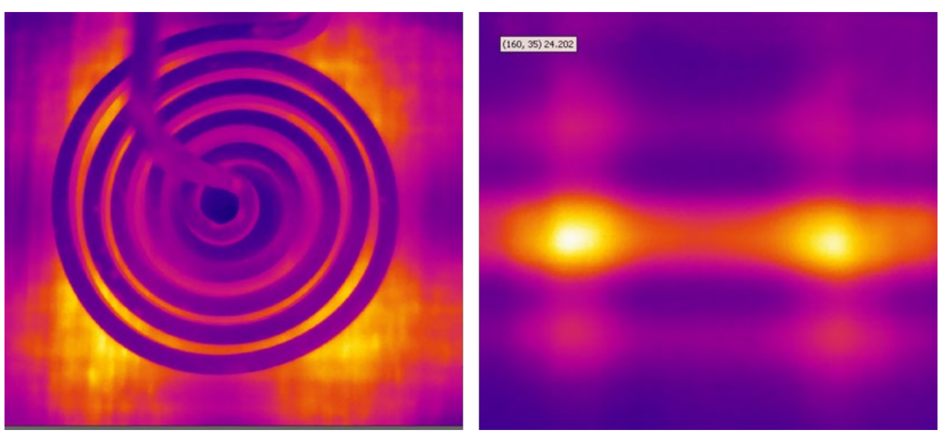

Figure 84: CFRP heating pattern from induction heating.

8.3 Conclusion

All infrared thermography results were compared against ultrasonic testing (UT) results, and it was determined that ultrasonic testing was the superior NDT method for inspection of the IWSLJ. However, thermography (induction and pulse) cannot be used to inspect the entirety of the IWSLJ and should not be used to as a standalone inspection method. If thermography was used as a standalone method, there would be a potential of missing defects in the material. Of note, pulse thermography was unable to detect the artificial inserts (thermal tape and mould release) in Bonded Panel 1 because of the numerous delaminated areas. Furthermore, pulsed thermography was unable to detect the same inserts in Bonded Panels 2 and 3 due to the depth of the defects.

Overall, infrared thermography (specifically flash thermography) can be used as a potential inspection method for the CF-188 IWSLJ – specifically for the first two steps of the IWSLJ and in concert with ultrasonic testing. In order to capture more information from different perspectives, it would be ideal to use both inspection methods.

CHAPTER 9 – CONCLUSIONS AND FUTURE WORK

This thesis aimed to determine whether infrared pulsed (flash) and induction thermography could be a possible inspection method for the CF/E-Ti IWSLJ through an experimental investigation. The resulting conclusions were captured in the studies as detailed:

- Study 1 – A parametric study was performed to determine the optimal parameters for induction heating of the CF/E-Ti test specimen. Numerical analysis through FEM was used to determined that a usable frequency range was 240 – 375 kHz, the number of turns required for the coil, and that the pancake coil was the ideal coil for steady-state stationary testing. Furthermore, the pancake coil offered the most uniform heating. The experimental evaluation determined that a lift-off distance of 6.35 mm allowed the best electromagnetic coupling, 75 – 100 A was reasonable for induction heating, only 2 - 10 seconds of heating was required, a pancake coil was marginally satisfactory for stationary even heating, and a reasonable speed for the scanning process was 1.5 cm/s. Finally, the parametric study also resulted in a custom coil for induction scanning;
- Study 2 – A defect detection and dimensioning was conducted to characterize disbond areas within the CF/E-Ti test specimens. Flash thermography was able to detect more defects than the induction thermography with a detection rate of 40% versus 20%. However, induction thermography was able to achieve higher accuracy in measurement due to volumetric heating at skin depth. The overall error for flash thermography was 29% and the error for induction thermography was 10%;
- Study 3 – A penetration depth study was performed to identify the penetration limit of flash and induction thermography with respect to the IWSLJ. The penetration limit for both methods was determined to be the fourth step (3 mm) a result of the insulation and heat distribution properties of the CRFP. Given these results, thermography cannot be used for the entirety of the IWSLJ (all nine steps) with the Ambrell® *EASYHEAT* 2.4 kW Induction Heating System or act as a standalone inspection method for the IWSLJ. However, it was determined that thermography (specifically flash thermography) could be used alongside ultrasonic testing to examine the first two steps (the most critical steps) of the IWSLJ;
- Study 4 – A detection sensitivity study was conducted to assess the level of discriminating detail obtained by each inspection method. Varying artificial disbond defects were

embedded within Sample No. 1 at a depth comparable to the third step of the IWSLJ (2 mm). It was determined that both ultrasonic testing and pulsed thermography were able to detect all artificial defects. Meaning that both simulated traditional UT and kissing disbond areas were detectable. Induction thermography was only able to detect and define the FBH, which is not a good representation of a disbond area. At best, a FBH could represent a very aggressive disbond simulation for thermography.

In future endeavors, the same work should be performed on a full size IWSLJ with known disbond areas from natural causes. A full size IWSLJ would change aspects of induction thermography such as conduction and convection. It would be a larger heat-sink that may improve the contrast between the disbond area and surrounding unaffected region. Furthermore, an induction system of low frequency and higher power may be able to overcome the induction properties of the CFRP and penetrate to the ninth step. Also, a probability of detection study should be conducted to assess the performance of thermography. Finally, *Tanner Rellinger's* [31] vision of having a MATLAB code automatically identify, discriminate, and measure regions of interest should be explored to mitigate an inspector's subjective interpretations.

Furthermore, more advanced thermographic data processing such as Pulse Phase Thermography, Principal Component Analysis, and Derivative Processing should be explored. Pulse Phase Thermography is a well-established algorithm used for processing thermographic data in frequency domain with the aim to extract information about the defect size and depth and applies a Discrete Fourier Transform to thermal images obtained following flash heating of the front surface of a specimen. The output is represented by a function of the phase in terms of frequency. Principal Component Analysis is a statistical tool used for identification of specific patterns in data sets and analyzing data sets in a way which enables depicting similarities and differences of specific patterns occurring in the data using statistical modes acquired by decomposing data to singular values. Finally, Derivative Processing or Thermography Signal Reconstruction Processing fits experimental log-log plot thermogram with a logarithmic polynomial of degree where the temperature increases as a function of time for each pixel of the thermography. It reduces an image's noise, while increasing its temporal and spatial resolution.

REFERENCES

[1] Krause, T., PH587 Class Notes, 15 September 2020.,

[2] A. Edwards, “Characterization of the Effects of Water and Disbond on Ultrasonic Signals in Honeycomb Composite Structures.” Department of Physics, Royal Military College of Canada, Kingston, Ontario, Canada, Sep. 2010.

[3] I. M. Z. Abidin and M. Z. Umar, “Advantages and applications of eddy current thermography testing for comprehensive and reliable defect assessment,” p. 10.

[4] U. Netzelmann, G. Walle, S. Lugin, A. Ehlen, S. Bessert, and B. Valeske, “Induction thermography: principle, applications and first steps towards standardization,” presented at the Quantitative InfraRed Thermography Asia 2015, 2015. doi: 10.21611/qirt.2015.0152.

[5] J. Hayes-Griss, J. Wang, A. Litchfield, and A. Charles, “Numerical Analyses of F/A-18 Wing Root Step Lap Joints – Part 2: Assessment of Disbond Progression Behaviour.” Aerospace Division, Department of Defence Science and Technology Group. Australian Government, Apr. 2018.

[6] S. Savage, “CF188 IWSLJ (Inner Wing Stepped Lap Joint) Automated Ultrasonic Inspection 188-355-U.” QETE NDE, Jul. 05, 2019.

[7] X. Maldague, P. O. Moore, and American Society for Nondestructive Testing, Eds., *Infrared and thermal testing*, 3rd ed. Columbus, OH: American Society for Nondestructive Testing, 2001.

[8] “Comparison of Pulse Thermography (PT) and Step Heating (SH) Thermography in Non-Destructive Testing of Unidirectional GFRP Composites - ProQuest.” https://www.proquest.com/openview/a33aa0e8b68d454d66e2649853a67d75/1?pq-origsite=gscholar&cbl=2026485 (accessed Dec. 20, 2021).

[9] U. Netzelmann and J. Guo, “Induction thermography on CFRP and the role of anisotropy,” presented at the 2018 Quantitative InfraRed Thermography, 2018. doi: 10.21611/qirt.2018.063.

[10] M. Genest and G. Li, “Inspection of Aircraft Engine Components Using Induction Thermography,” in *2018 IEEE Canadian Conference on Electrical & Computer Engineering (CCECE)*, Quebec City, QC, May 2018, pp. 1–4. doi: 10.1109/CCECE.2018.8447832.

[11] M. Genest, G. Li, M. Genest, and G. Li, “INDUCTION THERMOGRAPHY OF STEEL COUPONS WITH CRACK,” p. 4.

[12] S. Yarlagadda, H. J. Kim, J. W. Gillespie, N. B. Shevchenko, and B. K. Fink, “A Study on the Induction Heating of Conductive Fiber Reinforced Composites,” *J. Compos. Mater.*, vol. 36, no. 4, pp. 401–421, Feb. 2002, doi: 10.1177/0021998302036004171.

[13] T. Bayerl, M. Duhovic, P. Mitschang, and D. Bhattacharyya, “The heating of polymer composites by electromagnetic induction – A review,” *Compos. Part Appl. Sci. Manuf.*, vol. 57, pp. 27–40, Feb. 2014, doi: 10.1016/j.compositesa.2013.10.024.

[14] J. Vrana *et al.*, “MECHANISMS AND MODELS FOR CRACK DETECTION WITH INDUCTION THERMOGRAPHY,” in *AIP Conference Proceedings*, Golden (Colorado), 2008, vol. 975, pp. 475–482. doi: 10.1063/1.2902698.

[15] T. Petzold, “Modelling, analysis and simulation of multifrequency induction hardening,” Epubli, Berlin, 2014.

[16] A. Bermúdez, D. Gómez, M. C. Muñiz, P. Salgado, and R. Vázquez, "Numerical simulation of a thermo-electromagneto-hydrodynamic problem in an induction heating furnace," *Appl. Numer. Math.*, vol. 59, no. 9, pp. 2082–2104, Sep. 2009, doi: 10.1016/j.apnum.2008.12.005.
[17] "McDonnell Douglas F/A-18 Hornet," *Wikipedia*. Aug. 18, 2021. Accessed: Aug. 21, 2021. [Online]. Available: https://en.wikipedia.org/w/index.php?title=McDonnell_Douglas_F/A-18_Hornet&oldid=1039394851
[18] W. Seneviratne, J. Tomblin, and M. Kittur, "Durability and residual strength of adhesively-bonded composite joints," in *Fatigue and Fracture of Adhesively-Bonded Composite Joints*, Elsevier, 2015, pp. 289–320. doi: 10.1016/B978-0-85709-806-1.00010-0.
[19] M. Li, M. Huang, Y. Chen, P. Gong, and X. Yang, "Effects of processing parameters on kerf characteristics and surface integrity following abrasive waterjet slotting of Ti6Al4V/CFRP stacks," *J. Manuf. Process.*, vol. 42, pp. 82–95, Jun. 2019, doi: 10.1016/j.jmapro.2019.04.024.
[20] X. Li, X. Zhang, H. Zhang, J. Yang, A. B. Nia, and G. B. Chai, "Mechanical behaviors of Ti/CFRP/Ti laminates with different surface treatments of titanium sheets," *Compos. Struct.*, vol. 163, pp. 21–31, Mar. 2017, doi: 10.1016/j.compstruct.2016.12.033.
[21] "Ti-6al-4v - an overview | ScienceDirect Topics." https://www.sciencedirect.com/topics/engineering/ti-6al-4v (accessed Nov. 29, 2020).
[22] W. D. Callister and D. G. Rethwisch, *Materials science and engineering: an introduction*, 9th edition. Hoboken, NJ: Wiley, 2014.
[23] "Titanium - Element information, properties and uses | Periodic Table." https://www.rsc.org/periodic-table/element/22/titanium (accessed Nov. 29, 2020).
[24] R. Pederson, "Microstructure and phase transformation of Ti-6Al-4V," p. 62.
[25] inc Jeppesen Sanderson, *A & P technician airframe textbook.* Englewood, Colo.: Jeppesen Sanderson Inc., 2003.
[26] "titanium processing | Technology, Methods, & Facts," *Encyclopedia Britannica*. https://www.britannica.com/technology/titanium-processing (accessed Nov. 30, 2020).
[27] M. E. Kazemi, L. Shanmugam, L. Yang, and J. Yang, "A review on the hybrid titanium composite laminates (HTCLs) with focuses on surface treatments, fabrications, and mechanical properties," *Compos. Part Appl. Sci. Manuf.*, vol. 128, p. 105679, Jan. 2020, doi: 10.1016/j.compositesa.2019.105679.
[28] "Abrasive Blasting & Liquid Honing - Placentia, CA - Industrial Metal Finishing." https://www.indmetfin.com/abrasive-blasting-liquid-honing.html (accessed Dec. 01, 2020).
[29] "PCA250-2M06_TDS.pdf." Accessed: Nov. 29, 2020. [Online]. Available: https://www.pccomposites.com/wp-content/uploads/2015/07/PCA250-2M06_TDS.pdf
[30] U. Farooq, P. Myler, and B. K. Kandola, "Prediction of Barely Visible Impact Damage in Composite Panels Subjected to Blunt Nose Impact," p. 17.
[31] T. Rellinger, 'Detection of Low-Velocity Impact Damage in Carbon Fiber Sandwich Panels using Infrared Thermography.' Department of Mechanical and Aerospace Engineering, RMC. January 2019.

[32] "Autoclave Molding - an overview | ScienceDirect Topics." https://www.sciencedirect.com/topics/materials-science/autoclave-molding (accessed Dec. 01, 2020).
[33] "ASM Material Data Sheet." http://asm.matweb.com/search/SpecificMaterial.asp?bassnum=MTP641 (accessed Nov. 29, 2020).
[34] "Mechanical Properties of Carbon Fibre Composite Materials." http://www.performance-composites.com/carbonfibre/mechanicalproperties_2.asp (accessed Dec. 01, 2020).
[35] "Paper-1598.pdf." Accessed: Dec. 02, 2020. [Online]. Available: http://www.iccm-central.org/Proceedings/ICCM13proceedings/SITE/PAPERS/Paper-1598.pdf
[36] M. I. Hussain, Z. Mohd Zain, and K. Tee Lei, "Root Causes Analysis of Disbonds and Unidentifiable Ultrasonic Indications on Composite Materials." Applied Mechanics and Materials, Dec. 2013.
[37] A. Haeger *et al.*, "Non-destructive Detection of Drilling-induced Delamination in CFRP and its Effect on Mechanical Properties," *Procedia Eng.*, vol. 149, pp. 130–142, 2016, doi: 10.1016/j.proeng.2016.06.647.
[38] Richardson, M. O., & Wisheart, M. J. (1996)., "Review of low-velocity impact properties of composite materials. Composites Part A.".
[39] P. Galvez, J. Abenojar, and M. A. Martinez, "Effect of moisture and temperature on the thermal and mechanical properties of a ductile epoxy adhesive for use in steel structures reinforced with CFRP," *Compos. Part B Eng.*, vol. 176, p. 107194, Nov. 2019, doi: 10.1016/j.compositesb.2019.107194.
[40] N. E. Dowling, K. Siva Prasad, and R. Narayanasamy, *Mechanical behavior of materials: engineering methods for deformation, fracture, and fatigue*, 4. ed., Internat. ed. Boston, Mass.: Pearson, 2013.
[41] M. Vollmer and K.-P. Möllmann, *Infrared thermal imaging: fundamentals, research and applications*, Second edition. Weinheim, Germany: Wiley-VCH Verlag GmbH & Co. KGaA, 2018.
[42] "How Infrared Cameras Work." https://www.fluke.com/en-ca/learn/blog/thermal-imaging/how-infrared-cameras-work (accessed Apr. 03, 2021).
[43] D. J. Griffiths, *Introduction to electrodynamics*, 3rd ed. Upper Saddle River, N.J: Prentice Hall, 1999.
[44] H. C. Ohanian, "On the approach to electro- and magneto-static equilibrium," *Am. J. Phys.*, vol. 51, no. 11, pp. 1020–1022, Nov. 1983, doi: 10.1119/1.13364.
[45] "Skin Depth." https://pulsedpower.net/Applets/Electromagnetics/SkinDepth/skindepth.html (accessed Jun. 27, 2022).
[46] "Series RLC Circuit and RLC Series Circuit Analysis," *Basic Electronics Tutorials*, Jun. 25, 2013. https://www.electronics-tutorials.ws/accircuits/series-circuit.html (accessed Apr. 09, 2022).
[47] "COMSOL Multiphysics Reference Manual," p. 1742.
[48] F. Ciampa, P. Mahmoodi, F. Pinto, and M. Meo, "Recent Advances in Active Infrared Thermography for Non-Destructive Testing of Aerospace Components," *Sensors*, vol. 18, no. 2, p. 609, Feb. 2018, doi: 10.3390/s18020609.
[49] D. E. Bray, *Nondestructive Evaluation: A Tool in Design, Manufacturing and Service*, 1st ed. CRC Press, 2014. doi: 10.1201/9781315272993.

[50] "2.3 Wave Propagation | Olympus IMS." https://www.olympus-ims.com/en/ndt-tutorials/flaw-detection/wave-propagation/ (accessed Jun. 27, 2022).
[51] A. K. Edwards, S. Savage, P. L. Hungler, and T. W. Krause, "Examination of F/A-18 honeycomb composite rudders for disbond due to water using through-transmission ultrasonics," *Ultrasound*, vol. 66, no. 2, pp. 36–44, Jul. 2011, doi: 10.5755/j01.u.66.2.529.
[52] M. Rochon, "Detectability of Disbonds in Titanium & Carbon Fibre Material Composite —The Case of the CF-188 Inner Wing Stepped Lap Joint." Department of Chemical Engineering, RMC. September 21
[53] "Support for FLIR T620 - Discontinued | FLIR Systems." https://www.flir.ca/products/t620/ (accessed Apr. 28, 2021).
[54] A. Corporation, "Induction Heating Coil Design & Fabrication | PDF Brochure." https://www.ambrell.com/induction-heating-work-coils-brochure (accessed Jul. 16, 2022).
[55] O. Wysocka-Fotek, M. Maj, and W. Oliferuk, "Use of Pulsed IR Thermography for Determination of Size and Depth of Subsurface Defect Taking into Account The Shape of Its Cross-Section Area," *Arch. Metall. Mater.*, vol. 60, Jun. 2015, doi: 10.1515/amm-2015-0181.

Appendix A – Consideration to Other NDT Techniques

Visual inspection or testing, as shown in Figure 1, is a basic non-destructive evaluation method in which a test object (or workpiece) is observed through direct means by the human eye or indirectly with an optical instrument. A qualified technician with the related industrial experience or inspector would examine the test object for discontinuities (defects) against conformance specifications. For a competent evaluation, the test object must be clean, adequately illuminated, and visually inspected [1]. Additionally, the manufacturing process, historical records, and failure characteristics should be known to the inspector. Although the results are often qualitative, visual inspections are ideal for scrutinizing a variety of surface defects. However, since disbond areas and other defects associated with CF-188 IWSLJ failure are primarily subsurface, a visual inspection would be an inappropriate method.

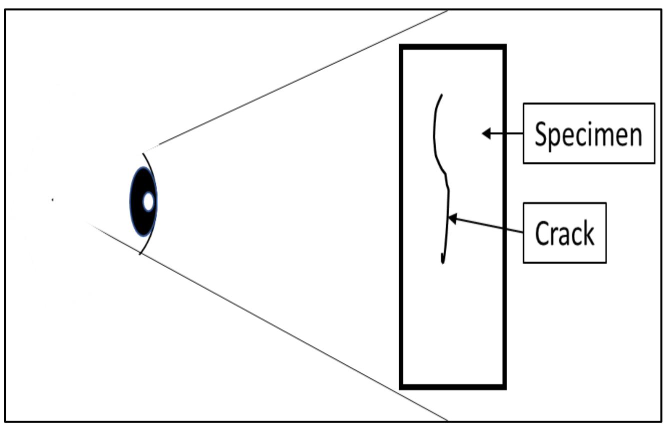

Figure 1: Visual Inspection.

Liquid penetrant testing is a similarly inappropriate method for scrutinizing disbond areas. PT is ideal for discontinuities openly exposed to the surface of a nonporous test object and is heavily used in industrial settings as a rapid (and cost effective) means of inspection [1]. PT employs the use of a petroleum or water based liquid dye penetrant, which seeps into open surface discontinuities via means of capillary action as shown in Figure 2. Discontinuities (including cracks, laps, pits, pores, and seams) become visually apparent with the application of white developer to the test object surface. Penetrant is drawn out of the surface cracks by capillary action using a developer. The results are semi-qualitative.

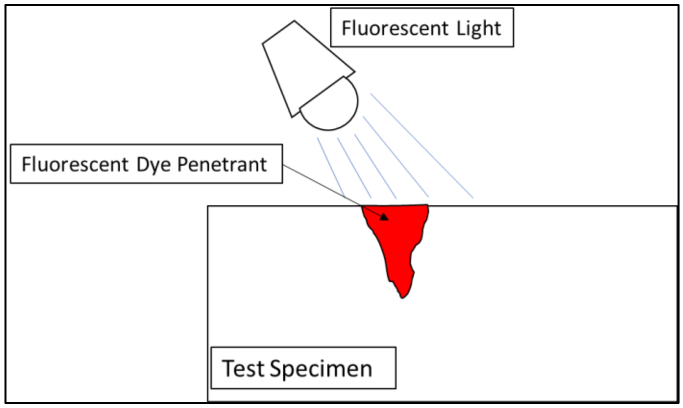

Figure 2: Liquid penetrant testing.

Radiographic testing is a generic term for penetrating radiation and its respective differential absorption. Radiographic testing can be either particulate or electromagnetic radiation. Material density and variations in thickness results in varying penetrating radiation absorption rates. Specialized detectors receive the unabsorbed radiation passing through the test material and generate a two-dimensional image on radiation sensitive film or computed sensor technology as shown in Figure 3. Radiographic testing is an expensive inspection involving complex equipment. Additionally, the penetrating radiation presents a special safety hazard and the method may not work for disbond areas in CF/E-Ti FML as disbonds without matrix cracking do not lead to change in material density nor thickness changes. For this reason, radiographic testing would not be an ideal inspection method for disbond areas.

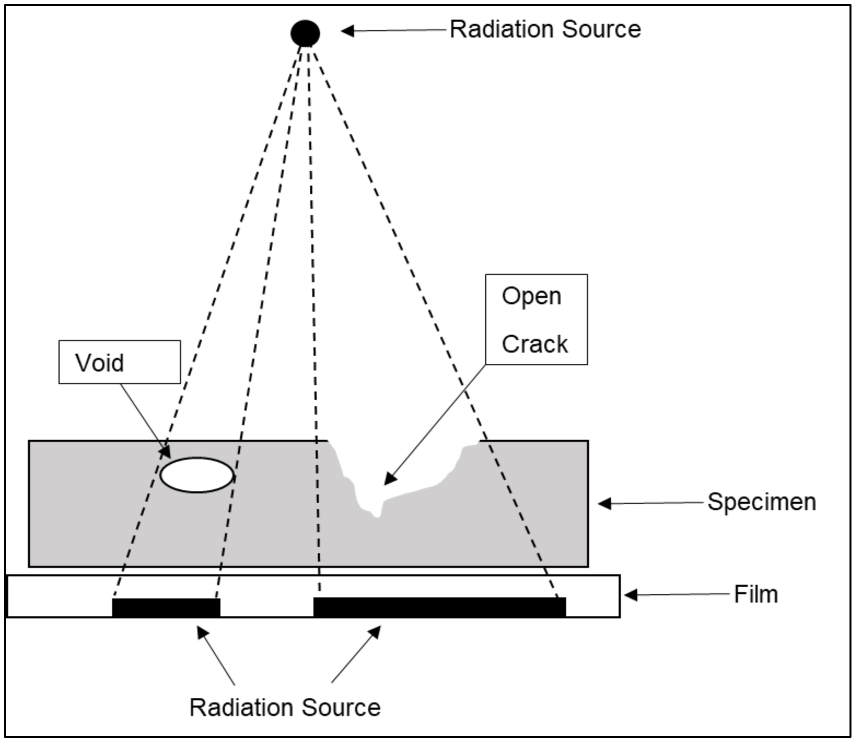

Figure 3: Radiographic inspection.

Eddy current testing stems from the principles of electromagnetic induction. ET involves Faradays Law, high frequency alternating current flows through an inductor or coil, which creates a varying magnetic field or primary field around the coil (Figure 4). The magnetic field then induces eddy currents in a conductive test object. Contrariwise, the eddy currents within the test object material produces a secondary magnetic field, which acts to cancel the primary magnetic field according to Lenz's Law. Eddy currents can be affected by many different material characteristics (permeability, conductivity, geometry, and thickness). Targeted discontinuities such as cracks increase the resistance to the flow of eddy currents and the current path resistance translates to a voltage deflection on instrumentation. Eddy current testing may not be a viable method for finding disbond areas in CF/E-Ti FML due to the planar (unidirectional) orientation of the CFRP, and the depth of the disbond area.

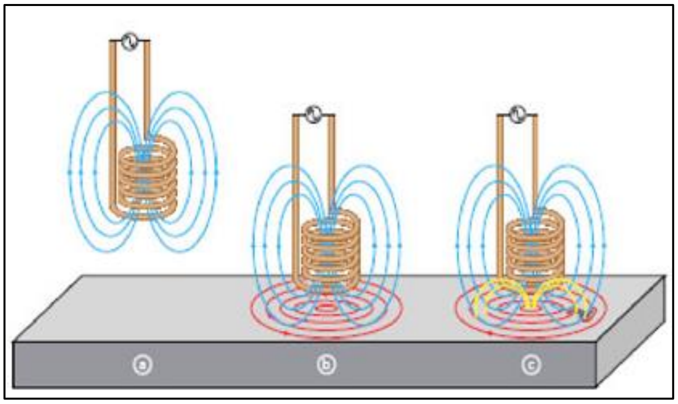

Figure 4: Eddy current inspection. (a) an alternating current flowing through a coil generates a magnetic field. (b) Eddy current forms as the coil is place close to a conductive material according to Lenz's Law. (c) a defect disturbs the magnetic coupling and the defect signal registers as coil impedance variation *[2]*.

Other inspection methods, such as **magnetic particle inspection or tap testing**, would either not be successful in locating disbond areas or would only provide qualitative results. **Ultrasonic Testing and Thermography** will be discussed in the theory chapter of this thesis. However, the following are drawbacks to ultrasonic testing as the premier inspection method for disbond areas in FML. Presently, complex electronic equipment is involved, it is often expensive for the relatively small area inspected, and high operator expertise is required to interpret the inspection results [3]. IR thermography is ideal because it is reliable, fast, efficient, cost effective, and has the potential of covering a large area.

[1] X. Maldague, P. O. Moore, and American Society for Nondestructive Testing, Eds., *Infrared and thermal testing*, 3rd ed. Columbus, OH: American Society for Nondestructive Testing, 2001.

[2] "Introduction to Eddy Current Testing | Olympus IMS." https://www.olympus-ims.com/en/eddycurrenttesting/ (accessed Apr. 21, 2022).

[3] "Canadian Institute for Non-destructive Evaluation," *CINDE*. https://www.cinde.ca/ (accessed Apr. 10, 2021).

Appendix B – QETE Report I

RMC CFRP-Ti Coupon – QETE ARMANDA AUT C-Scan Inspection

An automated ultrasonic C-Scan inspection was performed by QETE on a CFRP-Ti coupon from RMC Kingston, using the TecScan ARMANDA and TecView 2 software. The coupon contained various embedded flaw inserts, including a FBH (flat-bottom hole) simulating loss of bond between the CFRP and Ti, various surface preparations, Mould-Release conditions and Tape inserts. The coupon had a rubber coating on the CFRP surface that was used to remove reflectivity during previous thermographic inspection of the coupon.

Due to time constraints and similarities between RMC's coupon and the CF188 IWSLJ structural materials, the coupon was inspected using a similar setup to that used to inspect the CF188 IWSLJ (Inner Wing Stepped Lap Joint), per RCAF technique 188-355-U developed by QETE. Prior to scanning the RMC coupon, the equipment and setup was validated by performing a routine reference scan of technique 188-355-U CFRP-Ti Ref coupon. The Ref scan provides a means of asserting the following characteristics, which are directly applicable to the RMC CFRP-Ti coupon:

- effective sound transmission into the part
    - confirmed by assessing the Neg Peak amplitude of the UT signal at the specific near-surface CFRP-Ti bondline (OML bondline on the CF188 IWSLJ Ref Coupon)
- phase shift of UT signal from OML (or near surface) CFRP-Ti FBH's, which simulate near surface CFRP-Ti disbonds
- CFRP skin-ply delaminations

Because RMC's coupon consisted of a CFRP bonded to a single layer of Ti, both of which have consistent nominal thicknesses, it was possible to specifically gate the backwall response of the Ti layer. This provided a means of assessing the effect of the various inserts and FBH on the expected Ti layer backwall response.

Results – 5MHz C-Scan

The first C-Scan was performed on RMC's coupon in the as-is condition, i.e. with the rubber coating still present on the coupon's CFRP surface. The frequency used to inspect the coupon was the same as that used to inspect the CF188 IWSLJ (5MHz transducer). The following observations were made:

- The tape inserts were somewhat visible (Fig 1 – red outlines)
- The FBH was visible, but not as clearly defined as would be expected (Fig 1 – yellow outline)
- Other embedded flaws difficult to discern, not only on the C-Scan image but also on the B-Scan images (Fig 1 – blue outlines)
- In general, the UT waveform signal response observed on the A-Scan appeared to be affected by the rubber coating: it was highly attenuated, and displayed wider time-base characteristics as what is normally observed for CFRP-Ti structures.
    - Because of this, it was decided to remove the rubber coating and to replace the transducer with one rated at 10MHz, in hopes of increasing the fidelity of the inspection and detectability of the embedded flaws

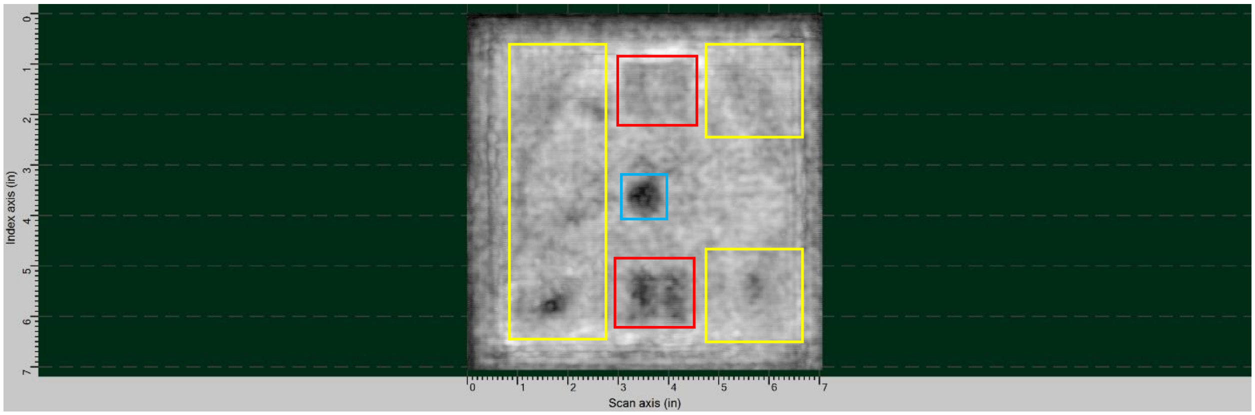

Fig 1 – 5MHz C-Scan image of RMC Kingston's CFRP-Ti coupon, showing evidence of tape inserts (red outlines) FBH (blue outline) and very low contrast for the remaining embedded flaw inserts (yellow outlines). Note that the "0" coordinates on the Index and Scan axis correspond to the "chipped" corner of the coupon.

Results – 10MHz C-Scan

A second C-Scan was performed at 10 MHz (Fig 2), with the following observations:

- Tape inserts show higher contrast and definition than 5MHz scan, both on the C-Scan image and the B-Scan images (Fig 3 – red outlines, Fig 3 – white arrows)
- The FBH is clearly better defined (Fig 4)
- Other embedded flaws have become visible on the C-Scan image and also reveal some characteristics on the B-Scan images (Fig 5 – white arrows)
    - Note that all other embedded flaws were clearly noticeable on the C-Scan and B-Scan images

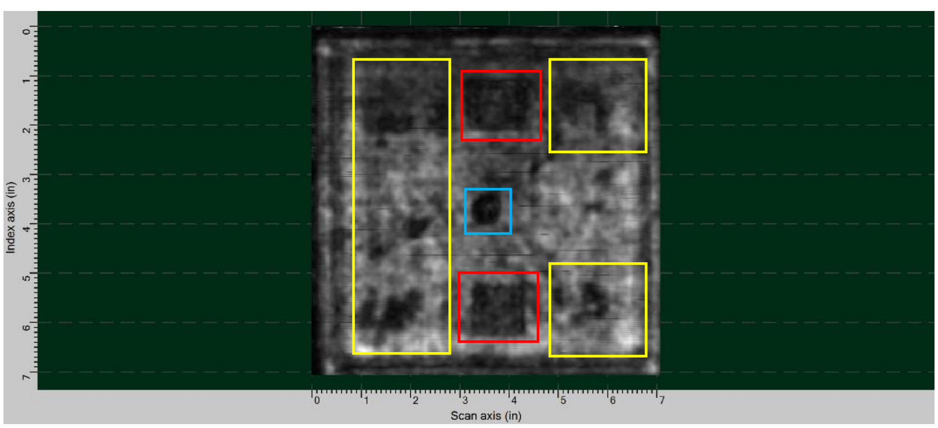

Fig 2 – 10Mhz C-Scan image of RMC Kingston's CFRP-Ti coupon, showing evidence of tape inserts (red outlines) FBH (blue outline) and evidence of various other embedded flaws in the coupon. The FBH is also better defined by the 10MHz C-Scan. Note that the "0" coordinates on the Index and Scan axis correspond to the "chipped" corner of the coupon.

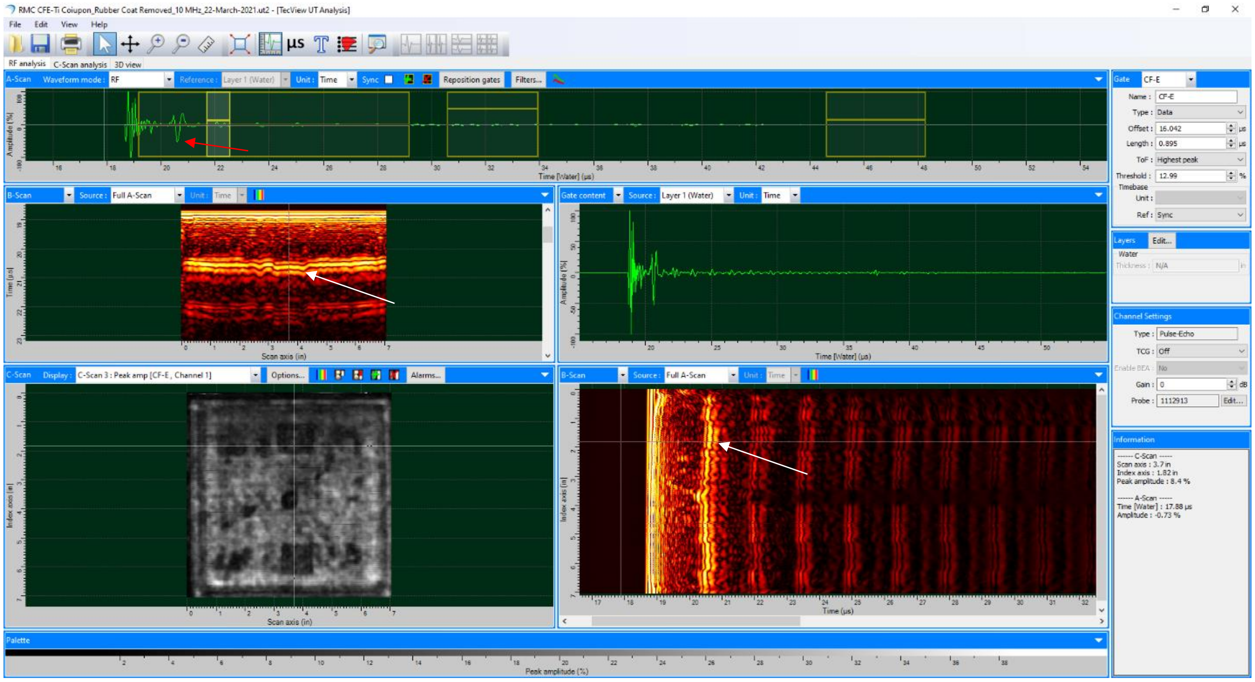

Fig 3 – 10Mhz C-Scan image of RMC Kingston's CFRP-Ti coupon, highlighting the effect of the embedded tape on the signal response from the CFRP-Ti bondline (white arrows on Scan & Index B-Scan images), whereby a slight shift in time corresponds to the additional tape layer material. Note the predominantly Neg Peak amplitude signal indicating coupling or bonding between the CFRP & Ti layers.

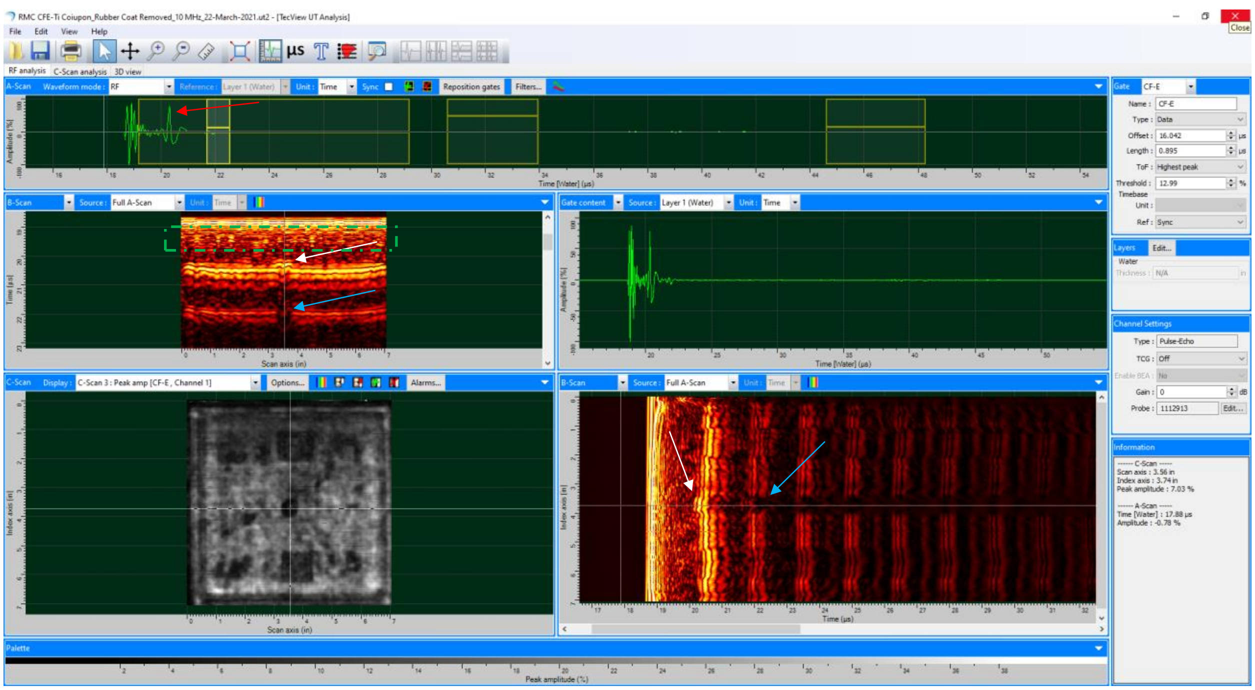

Fig 4 – 10Mhz C-Scan image of RMC Kingston's CFRP-Ti coupon, highlighting the effect of the FBH on the signal response from the CFRP-Ti bondline (white arrows on Scan & Index B-Scan images), whereby a slight shift in time to the left corresponds to the reflection of the UT signal at the FBH, and complete loss of backwall from the titanium backwall (blue arrows). Note the predominantly Pos Peak amplitude signal indicating loss no titanium present, which is consistent with disbonds between the CFRP & Ti layers. Also note the reflectors throughout the CFRP layers, indicating potential inter-ply resin and/or bonding issues (green dash outline).

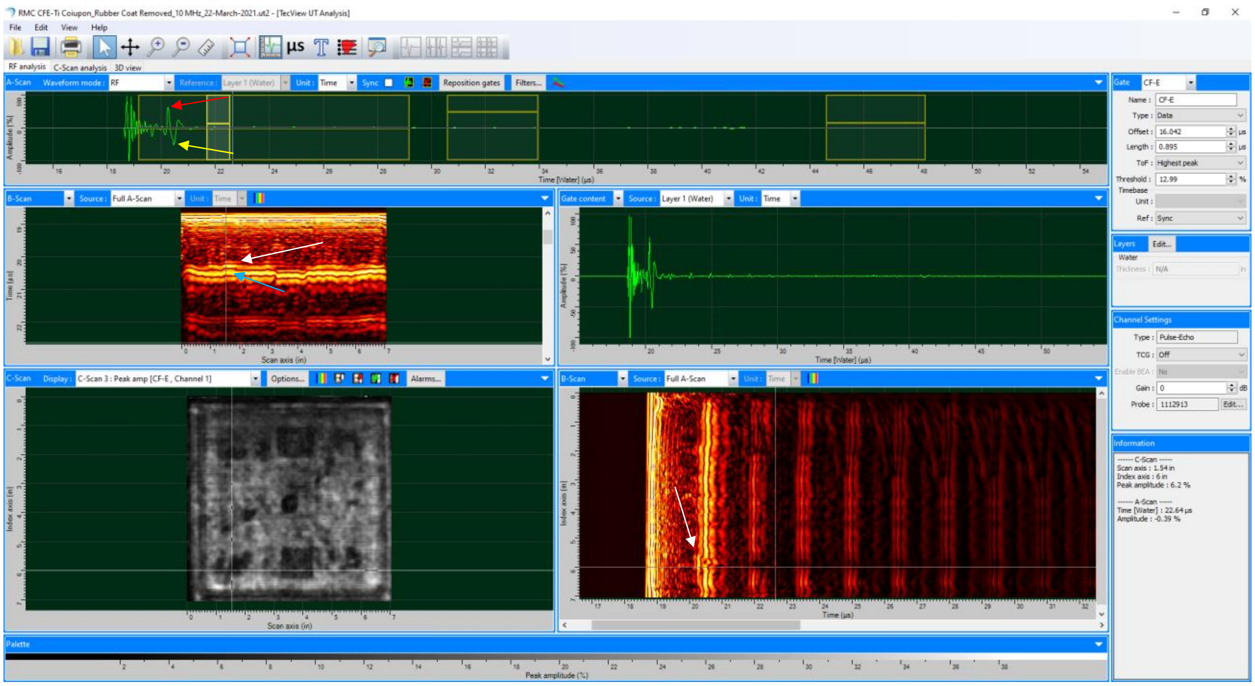

Fig 5 – 10Mhz C-Scan image of RMC Kingston's CFRP-Ti coupon, highlighting the effect of the Mould-release gel on the signal response from the CFRP-Ti bondline (white arrows on Scan & Index B-Scan images), whereby a good increase in Pos Peak amplitude is observed (red arrow on A-Scan), on a portion of the embedded flaw. However, the CFRP-Ti bondline appears to be intact as indicated by the presence of the normal CFRP-Ti reflection on the B-Scan Images (blue arrows), and the presence of the normal (albeit ever so slightly) lower Neg Peak amplitude signal typical of a good CFRP-Ti bondline.

Conclusion

With the TecScan ARMANDA AUT C-Scan inspection system, the inspection of the RMC Kingston CFRP-Ti coupon at a frequency of 10MHz revealed predictable detectability of the CFRP-Ti FBH, and showed great success at detecting the tape inserts. Given the short time allowed to inspect the coupon, the ARMANDA system showed great potential at detecting what effects that various surface preparations, mould-release gel and tape inserts had on the corresponding AUT C-Scan UT signal response.

Additional testing of the coupon could help optimize the inspection setup, which could potentially yield better detectability of embedded flaws by yielding higher contrast and definition of those flaws.

Prepared by: Steven Savage
Manager, QETE NDE Lab
Steven.Savage@forces.gc.ca
819-939-9375 / 613-462-3936

Appendix C – Induction Thermography Test Plan

TEST PLAN

FOR

INDUCTION THERMOGRAPHY

Version	Change Date	By	Description
Version Number	Date of Change	Change agent	Change(s) made

Table of Contents

Introduction

Technological advancements in Infrared (IR) thermography and IR camera capabilities have rendered the method as reliable, fast, efficient, and cost effective, significantly so with complex high-performance advanced materials [3]. Thermography has a reputation of being a qualitative assessment tool due to lack of specific information that may be acquired such as a specific defect location and dimensions of the damage. However, technological advancements and research have demonstrated their effectiveness in fully quantifying defects. Given advancements in IR thermography, the Canadian General Standards Board (CGSB) is establishing the method for Canada through standards and requirements for certification. With the industrial focus on cost savings, quality, and mass production, IR thermography is capable of being automated, affecting a greater inspection area in minimal time, and producing high quality defect characterization or dimensioning [3] [4]. Additionally, IR thermography can be applied to ferrous and non-ferrous material, detect sub-surface hidden defects, reliably discriminate between true and false defects, and remains less expensive than ultrasonic and radiographic testing.

Scope

In Scope

Carbon Fibre Reinforced Polymer (CFRP) and Titanium (Ti-6Al-4V) will be tested with the use of induction thermography for discontinuities.

Quality Objective

The objective of the testing is to accomplish the following:

Part I – Establishing ideal parameters (Time, Lift-Off, Coil Geometry, etc.) for induction thermography

1. Titanium (Ti-6Al-4V) heating with consideration to time, coil orientation, and lift-off/coil-material separation distance;

2. CFRP heating with consideration to time, coil orientation, and lift-off/coil-material separation distance; and

3. CFRP and Ti-6Al-4V laminate heating with consideration to time, coil orientation, and lift-off/coil-material separation distance.

Part II – Characterizing disbond areas (size and location) in fibre-metal laminate with induction thermography

4. Stationary Test. Performing induction thermography on CFRP and Ti-6Al-4V laminate with consideration to discontinuities in the test sample; and

5. Scanning Test. Performing induction thermography on CFRP and Ti-6Al-4V laminate with consideration to discontinuities in the test sample.

Roles and Responsibilities

Roles and responsibilities of team members

- Ambrell Corporation will provide an induction heating system and the subject matter expertise as well as the test facility.

- Test Manager will direct and moderate the testing with the guidance of Ambrell Corporation staff.

Test Methodology

Overview

The test methodology selected for this project will be determined by Ambrell Corporation and the Test Manager at the Ambrell Corporation Laboratory.

Test Environment

The following environmental/atmospheric conditions will be recorded prior to the commencement of testing.

ENVIRONMENTAL/ATMOSPHERIC CONDITIONS		
Observer/Testing Staff	Name:	Name:
	Name:	Name:
Location and Elevation	Location:	Elevation:
Date	Start:	End:
Time	Start:	End:
Humidity	Measured:	Relative:
Temperature	Atmospheric:	Room:
Pressure		
Wind/Airflow Rate		

Test Levels

Test Levels are derived from the quality objective. Namely, the following.

Part I – Establishing ideal parameters (Time, Lift-Off, Coil Geometry, etc) for induction thermography

1. Titanium (Ti-6Al-4V) heating with consideration to time, coil orientation, and lift-off/coil-material separation distance;

Time Consideration			
Testing Conditions			
Current [Amp]	**Voltage [V]**	**Power [Watts]**	**Frequency [Hz]**
Time [sec]	Heat Generation [degC]		
1			
2			
…			

Lift-Off Consideration			
Testing Conditions			
Current [Amp]	**Voltage [V]**	**Power [Watts]**	**Frequency [Hz]**
Distance [mm]	Heat Generation [degC]	Fixed Time [sec]	
1		10	
2		10	
…		…	

Coil Type and Orientation Consideration			
Testing Conditions			
Current [Amp]	**Voltage [V]**	**Power [Watts]**	**Frequency [Hz]**
Time [sec]	Coil Orientation [deg]	Heat Generation [degC]	
1			
2			
…			

Please note that IR imaging data will be recorded with use of the FLIR IR Software.

2. CFRP heating with consideration to time, coil orientation, and lift-off/coil-material separation distance; and

Time Consideration			
Testing Conditions			
Current [Amp]	**Voltage [V]**	**Power [Watts]**	**Frequency [Hz]**
Time [sec]	Heat Generation [degC]		
1			
2			
…			

Lift-Off Consideration			
Testing Conditions			
Current [Amp]	**Voltage [V]**	**Power [Watts]**	**Frequency [Hz]**
Distance [mm]	Heat Generation [degC]	Fixed Time [sec]	
1		10	
2		10	
…		…	

Coil Type and Orientation Consideration			
Testing Conditions			
Current [Amp]	**Voltage [V]**	**Power [Watts]**	**Frequency [Hz]**
Time [sec]	Coil Orientation [deg]	Heat Generation [degC]	
1			
2			
…			

Please note that IR imaging data will be recorded with use of the FLIR IR Software.

3. CFRP and Ti-6Al-4V laminate heating with consideration to time, coil orientation, and lift-off/coil-material separation distance.

Time Consideration			
Testing Conditions			
Current [Amp]	**Voltage [V]**	**Power [Watts]**	**Frequency [Hz]**
Time [sec]	Heat Generation [degC]		
1			
2			
…			

Lift-Off Consideration			
Testing Conditions			
Current [Amp]	**Voltage [V]**	**Power [Watts]**	**Frequency [Hz]**
Distance [mm]	Heat Generation [degC]	Fixed Time [sec]	
1		10	
2		10	
…		…	

Coil Type and Orientation Consideration			
Testing Conditions			
Current [Amp]	**Voltage [V]**	**Power [Watts]**	**Frequency [Hz]**
Time [sec]	Coil Orientation [deg]	Heat Generation [degC]	
1			
2			
…			

Please note that IR imaging data will be recorded with use of the FLIR IR Software.

Part II – Characterizing disbond areas (size and location) in fibre-metal laminate with induction thermography

4. Stationary Test. Performing induction thermography on CFRP and Ti-6Al-4V laminate with consideration to discontinuities in the test sample; and

Stationary Induction Thermography			
Testing Conditions			
Current [Amp]	**Voltage [V]**	**Power [Watts]**	**Frequency [Hz]**
LiftOff Distance [mm]	Heat Generation [degC]	Fixed Time [sec]	Coil Type
…	…	…	…

Please note that IR imaging data will be recorded with use of the FLIR IR Software.

5. Scanning Test. Performing induction thermography on CFRP and Ti-6Al-4V laminate with consideration to discontinuities in the test sample.

Scanning Induction Thermography			
Testing Conditions			
Current [Amp]	**Voltage [V]**	**Power [Watts]**	**Frequency [Hz]**
LiftOff Distance [mm]	Heat Generation [degC]	Fixed Time [sec]	Coil Type
…	…	…	…

Please note that IR imaging data will be recorded with use of the FLIR IR Software.

Test Completeness

The following are the criterias that will deem the testing complete:

- 100% test coverage; and/or
- The test staff is satisfied with the results given condition; and/or
- The laboratory time limit was reach; and/or
- The betterment of results cannot by furthered.

Test Deliverables

The following are the delivarables: the Test Plan, data gained from recording software, and any other documents resulting from the testing.

Resource Needs

Testing Equipment

The following is the equipment list required for the testing:

- 1 x RMC Computer
- 1 x RMC FLIR IR Camera
- 1 x Ambrell Induction System with respective Coil(s)
- 1 x Scanning Apparatus
- Connecting Cables
- Test Samples or Coupons

Other equipment may be used for testing.

Appendix D – QETE Report II

RMC CFRP-Ti Samples – QETE ARMANDA AUT C-Scan Inspection

Introduction

Automated ultrasonic C-Scan inspections were performed by QETE on four (4) CFRP-Ti (CF/E-Ti) samples provided by Capt Keith George, NDT PG student at RMC Kingston, in support to NDT PG thesis subject analysis. The inspections were performed using the TecScan ARMANDA automated X-Y scanner system with TecView 2 software. The four samples inspected comprised of the following:

- Sample 1: thin-skin CF/E-Ti bonded sample, approx.35g
- Sample 2: slightly thicker-skin CF/E-Ti bonded sample, approx. 130g
- Sample 3: thickest-skin CF/E-Ti sample, approx.. 280g
- Sample 4: 3-step CF/E-Ti stepped sample

All samples were manufactured with thermal tape inserts, FBH's (flat-bottom holes) and mould release gel. Sample 4 contained the embedded flaws on steps 2 & 3.

The inspection of the four samples was conducted using RCAF NDT Technique 188-355-U, developed by QETE specifically for the inspection of the CF188 Inner Wing Stepped Lap Joint (IWSLJ). The settings used to inspect the four samples were the same as those used for the first RMC CF/E-Ti inspected in March 2021. These settings were primarily the same as used for the CF188 IWSLJ inspection, with the exception that the transducer was substituted with a 10MHz one to optimize the results on the March 2021 RMC Kingston sample.

Results and Discussion

The initial scan results using the 10MHz frequency transducer produced excessively noisy scans. The samples generated significant noise from the CF/E plies which affected the quality of the ultrasound signals generated at the CF/E-Ti bond-line. As such, the 10MHz transducer was replaced with a 5MHz transducer, which yielded better slightly better scan data. Even at 5MHz, significant changes to the acquisition settings/parameters (in the TecView Inspection module) had to be made in order to optimize the quality of the scan data.

Nonetheless, as can be seen in the images below, some samples did not produce usable C-Scan data. This was especially the case for sample #3, whereby significant noise was present and appeared to be caused by the CF/E skin plies. Sample 1, which exhibited poor data quality at 10MHz, will be re-scanned at 5MHz, the results of which will be provided in an updated version of this report. Additionally, none of the samples provided exhibited detectable evidence of the mould release gel. Perhaps the gel fuses with the adhesive during the curing process, making its detection by ultrasonics difficult to potentially impossible.

It would be worth considering sectioning some of these samples to better understand the bonding between the CF/E skin plies and that of the CF/E-Ti bond-line. There is some interest from QETE Composite Engineer, Mr. Rob Hoffman, and QETE NDE Lab, to further investigate these samples at a later time. This would strengthen QETE's understanding of CF/E-Ti bonded samples and the effect of CF/E skin-ply bonding variability has on AUT C-Scan data quality and interpretation.

Sample 1: Sample needs to be re-scanned at 5MHz frequency and revised settings. Will provide sample 1 findings in updated report.

Sample 2

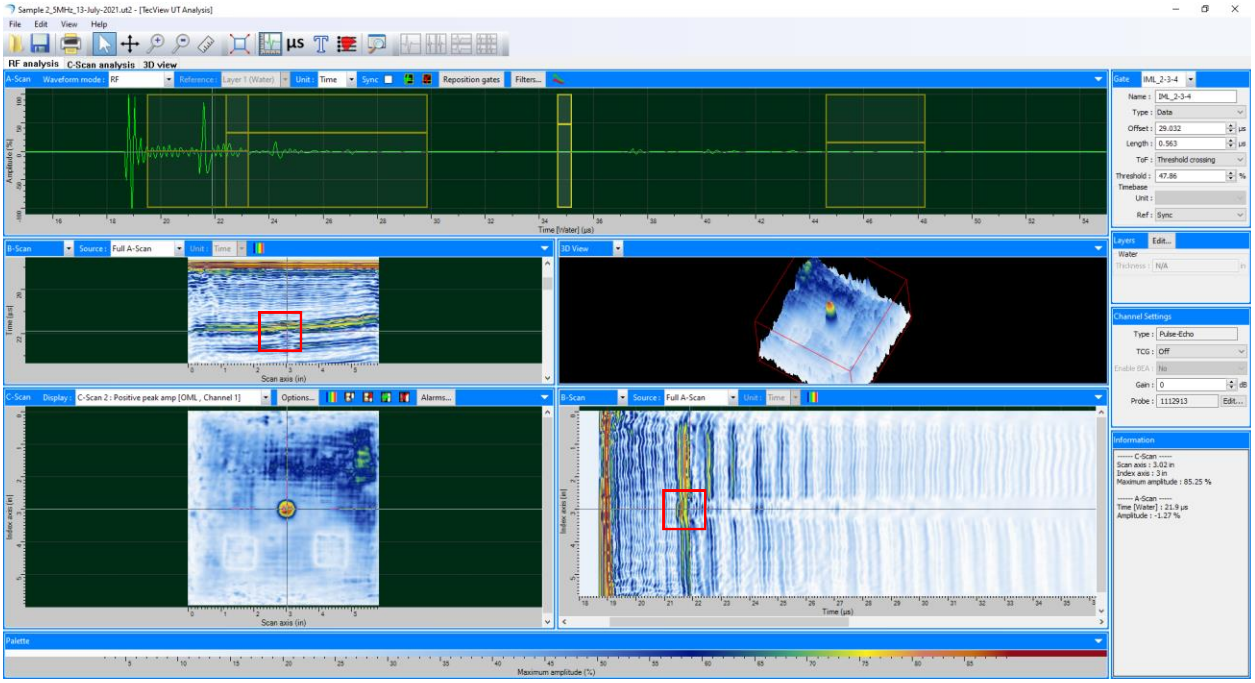

Fig 1 - Screen capture of sample 2 showing FBH at CF/E-Ti bond-line

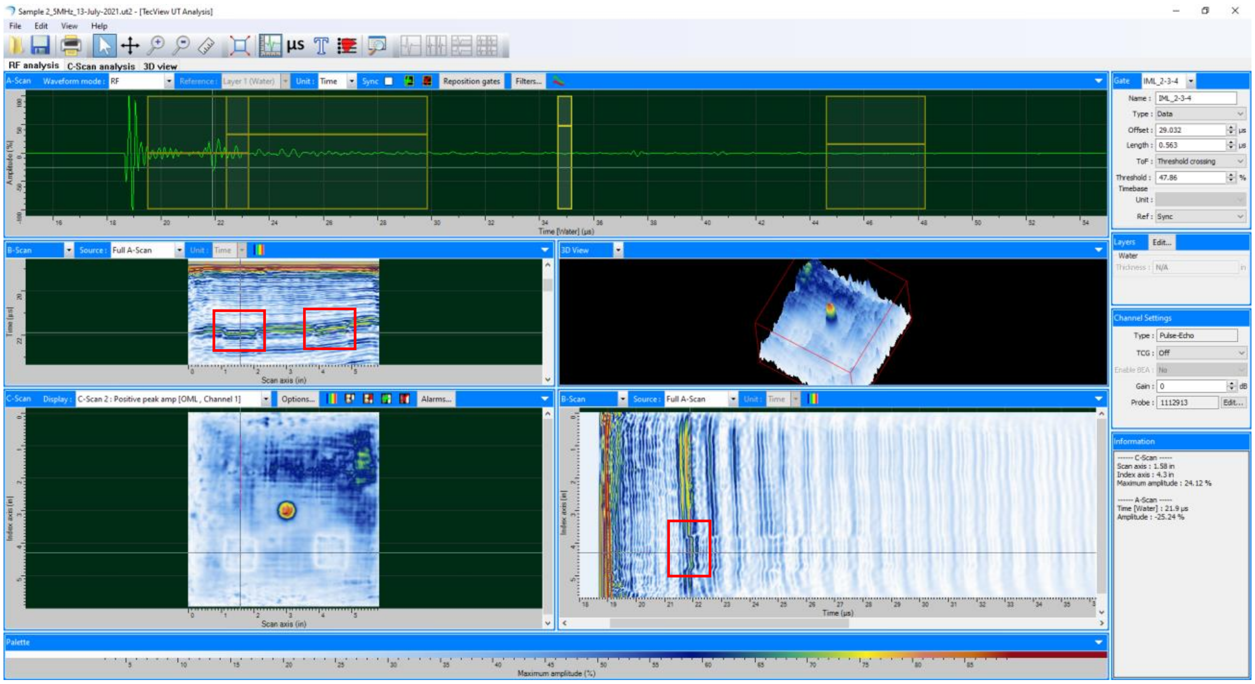

Fig 2 - Screen capture of sample 2 showing effect of thermal tape on CF/E-Ti bond-line

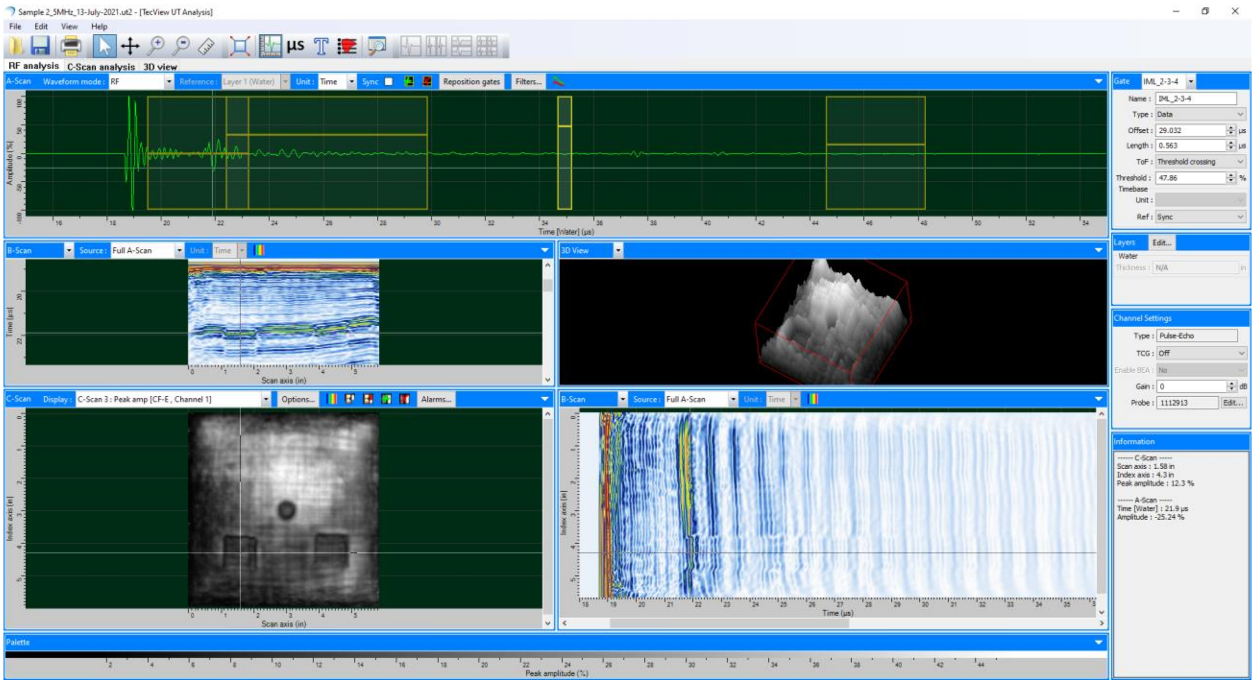

Fig 3 - Screen capture of sample 2 showing effect of thermal tape on CF/E-Ti bond-line, using scan data from a different data gate (slightly later time capture of the data)

Sample 3

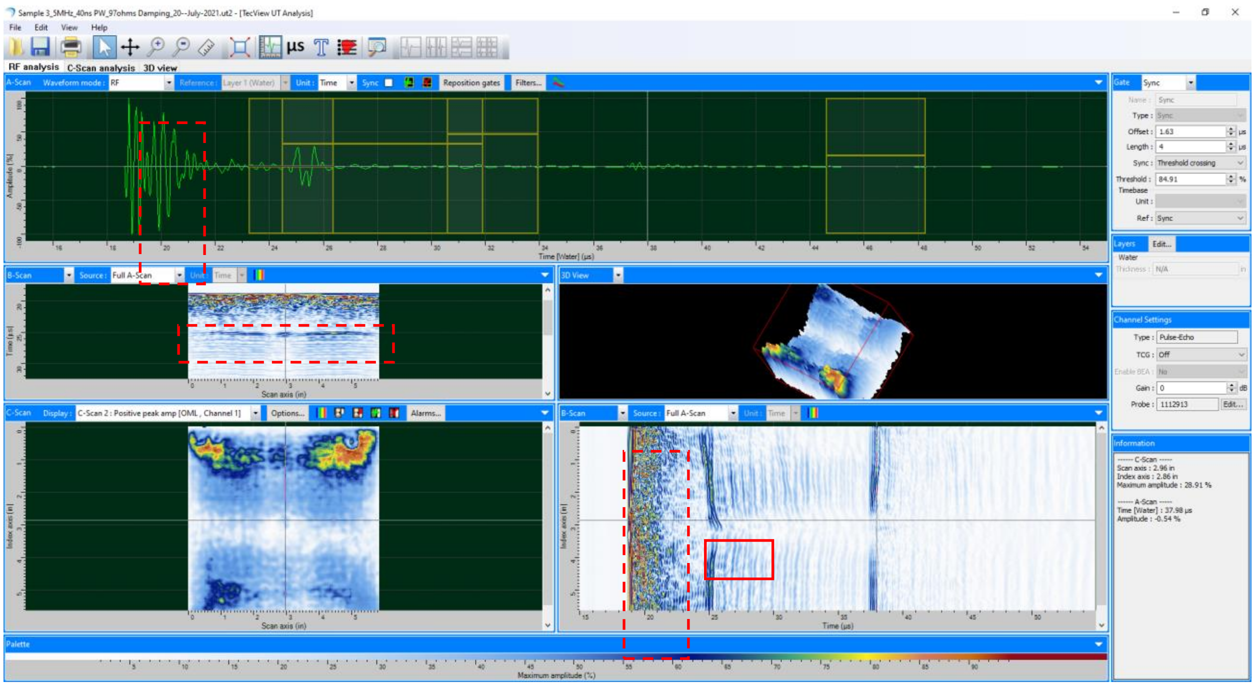

Fig 4 - Screen capture of sample 3 showing effect of FBH at CF/E-Ti bond-line (red outline, B-Scan image). Sample 3 generated significant noise from the CF/E skin plies (red-dash outlines), producing low-quality scan data.

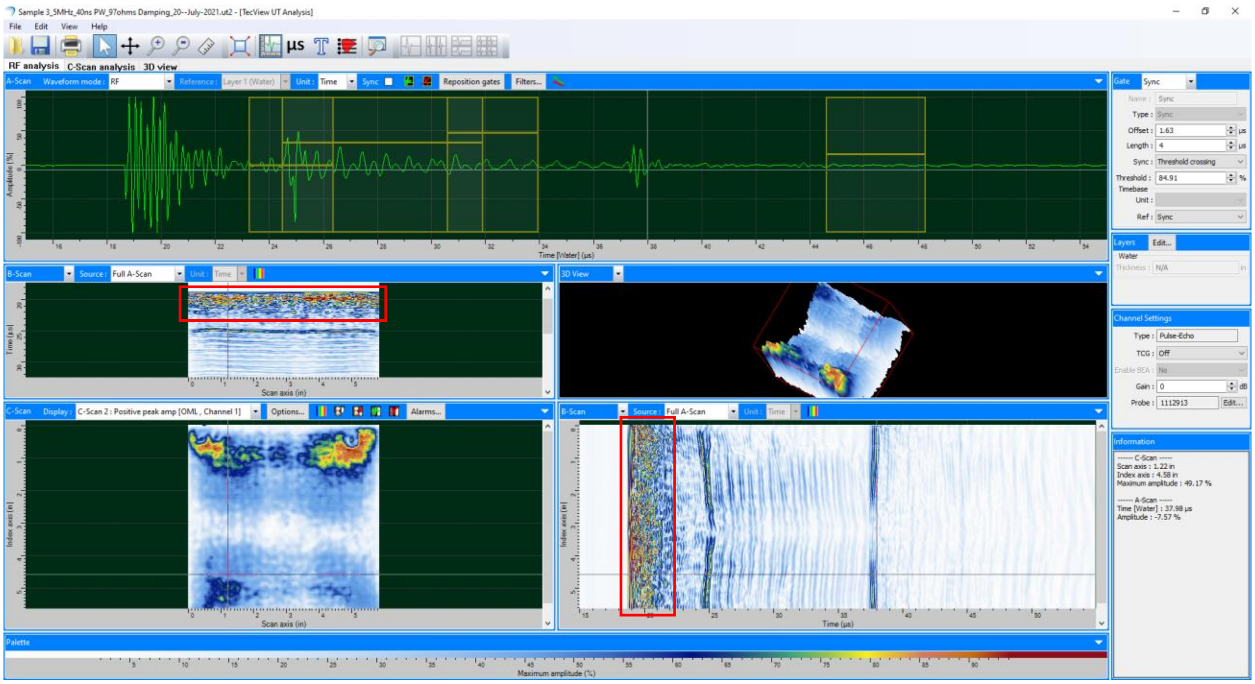

Fig 5 - Screen capture of sample 3 with cursor placed on area containing thermal tape. As evidenced by the C-Scan image, there was no usable information from this scan, likely because of the excessive noise generated by the CF/E skin plies (red outlines – B-Scan images).

Sample 4

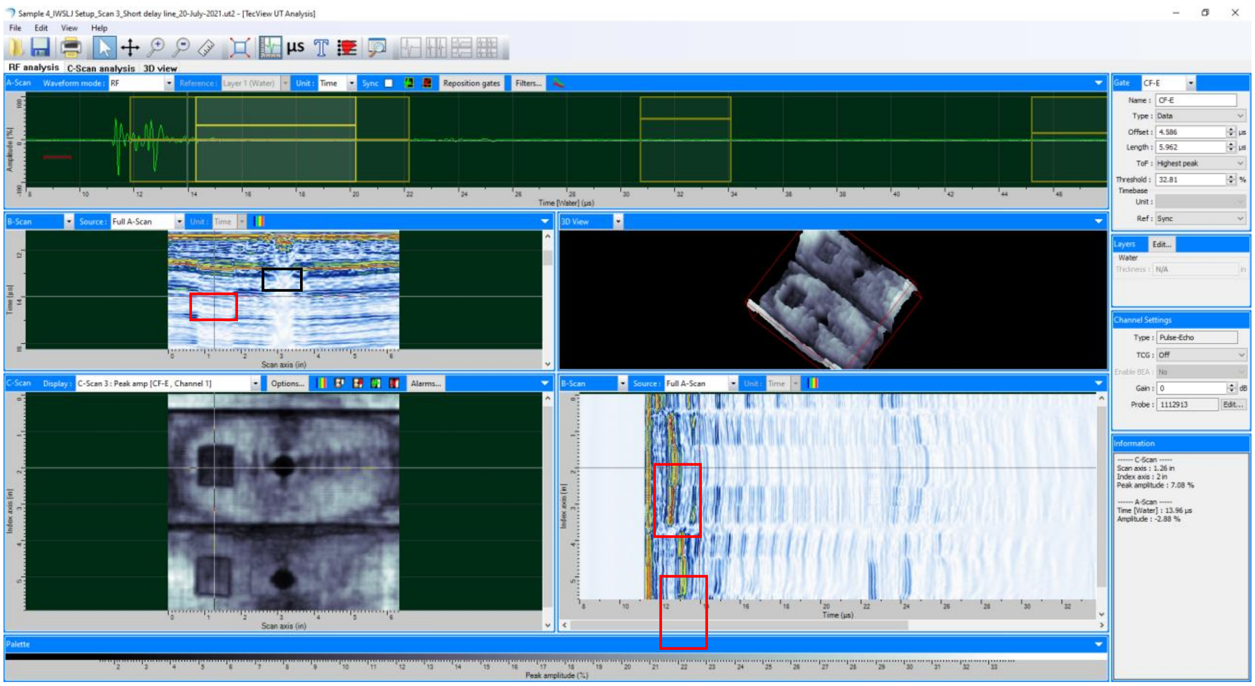

Fig 6 - Screen capture of sample 4 showing effect of thermal tape on "Step 2" C/E-Ti bond-line on (red outline, B-Scan images). Note the FBH response, which shows the FBH occurring early in the CF/E-Ti skin plies, which would indicate a delamination rather than a CF/E-Ti disbond (black outline).

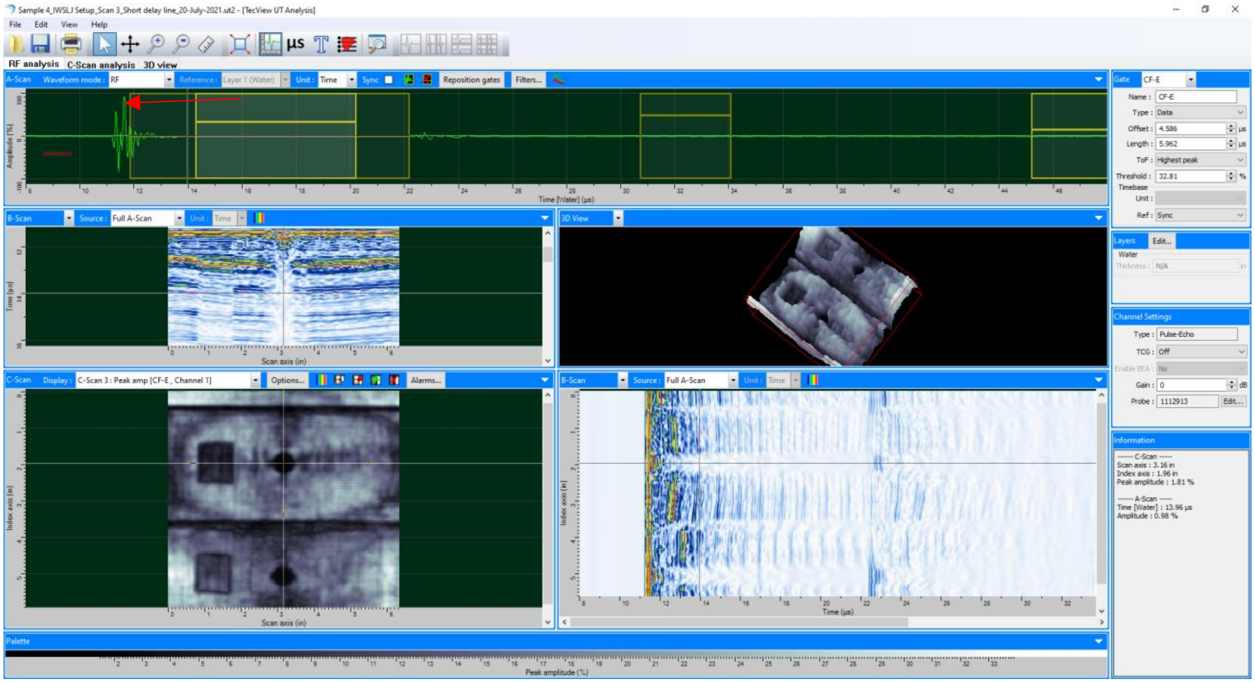

(a)

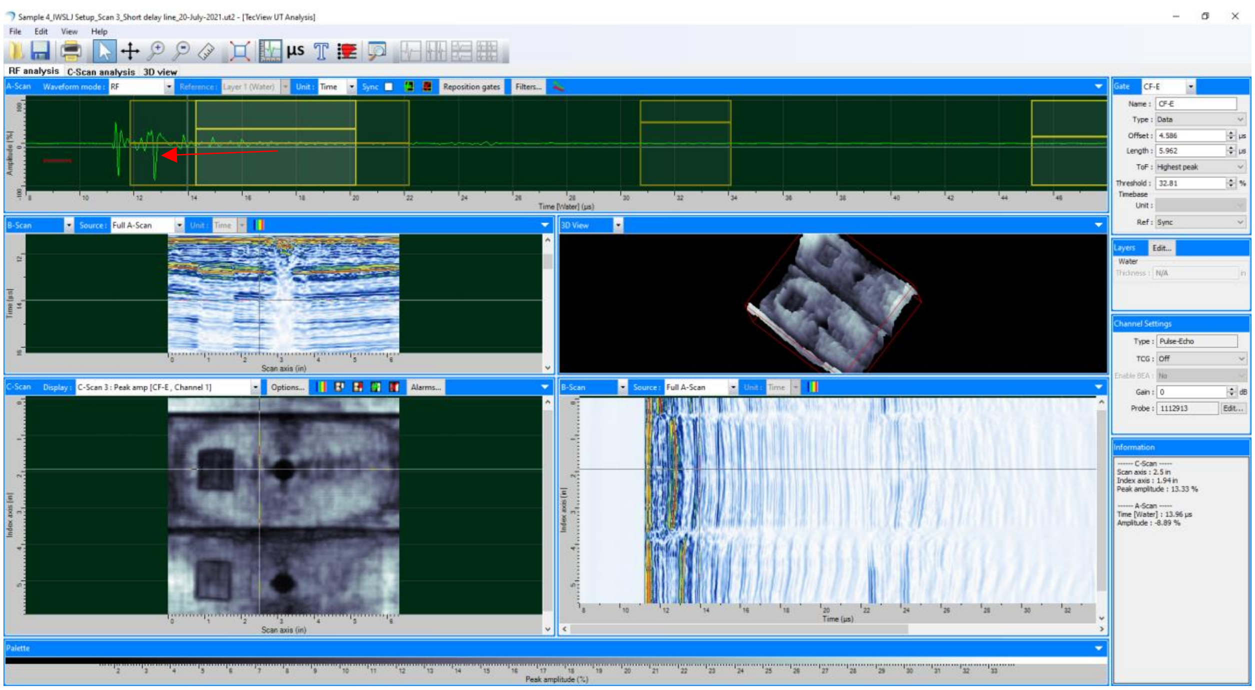

(b)

Fig 7 - Screen capture of sample 4 showing FBH response, which clearly shows the indication is occurring “early” in time, as indicated by the red arrow on the A-Scan window of capture (a). Capture (b) shows the CF/E-Ti bond-line response appears later in time compared to the FBH, further indicating the FBH to be a CF/E skin-ply delamination (red arrow on A-Scan window).

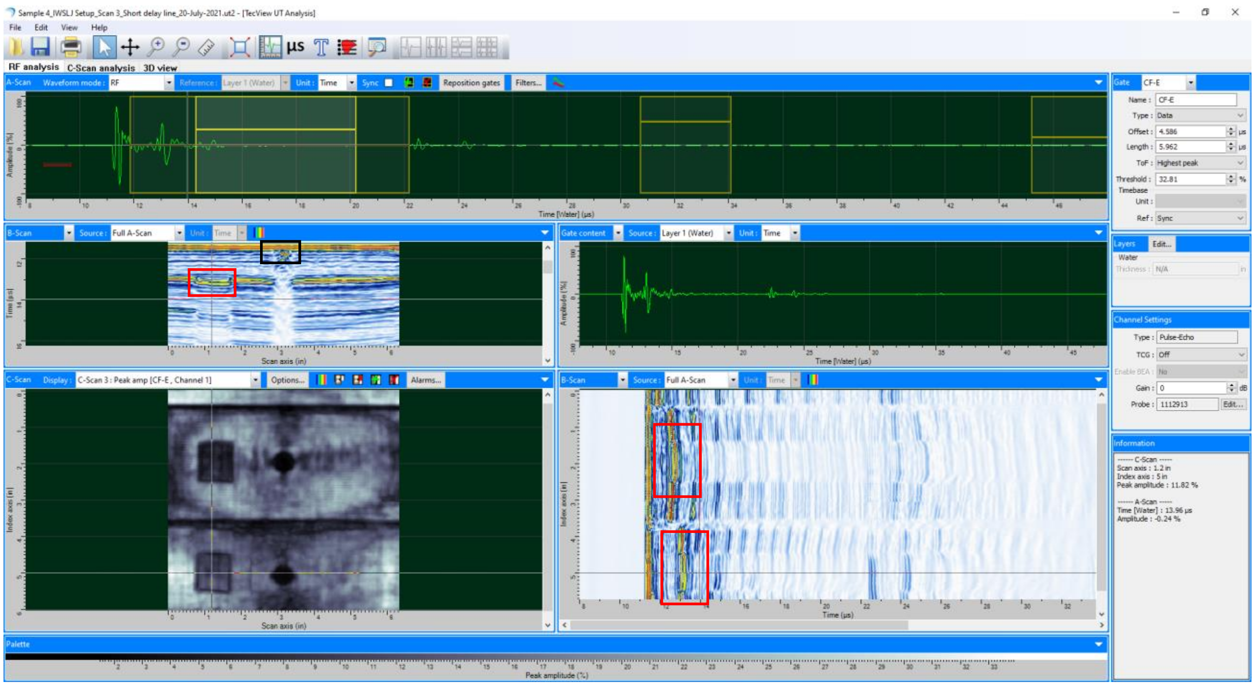

Fig 8 - Screen capture of sample 4 showing effect of thermal tape on "Step 2" C/E-Ti bond-line on (red outline, B-Scan images). Note the FBH response, which shows the FBH occurring early in the CF/E-Ti skin plies, which would indicate a delamination rather than a CF/E-Ti disbond (black outline). The response from the thermal tape and FBH on step 3 are consistent with the response from these embedded flaws on step 2.

Prepared by: Steven Savage
Manager, QETE NDE Lab
Steven.Savage@forces.gc.ca
819-939-9375 / 613-462-3936

Appendix E – QETE Report III

RMC CFRP-Ti Samples – QETE ARMANDA AUT C-Scan Inspection

Introduction

Automated ultrasonic C-Scan inspections were performed by QETE on four (4) CFRP-Ti (CF/E-Ti) samples provided by Capt Keith George, NDT PG student at RMC Kingston, in support to NDT PG thesis subject analysis. The inspections were performed using the TecScan ARMANDA automated X-Y scanner system with TecView 2 software. The four samples inspected comprised of the following:

- Sample 1: thin-skin CF/E-Ti bonded sample, approx.35g
- Sample 2: slightly thicker-skin CF/E-Ti bonded sample, approx. 130g
- Sample 3: thickest-skin CF/E-Ti sample, approx. 280g
- Sample 4: 3-step CF/E-Ti stepped sample

All samples were manufactured with thermal tape inserts, FBH's (flat-bottom holes) and mould release gel. Sample 4 contained the embedded flaws on steps 2 & 3.

The inspection of the four samples was conducted using RCAF NDT Technique 188-355-U, developed by QETE specifically for the inspection of the CF188 Inner Wing Stepped Lap Joint (IWSLJ). The settings used to inspect the four samples were the same as those used for the first RMC CF/E-Ti inspected in March 2021. These settings were primarily the same as used for the CF188 IWSLJ inspection, with the exception that the transducer was substituted with a 10MHz one to optimize the results on the March 2021 RMC Kingston sample.

Results and Discussion

The initial scan results using the 10MHz frequency transducer produced excessively noisy scans. The samples generated significant noise from the CF/E plies which affected the quality of the ultrasound signals generated by the CF/E-Ti bond-line. As such, the 10MHz transducer was replaced with a 5MHz transducer, which yielded slightly better scan data. Even at 5MHz, significant changes to the acquisition settings/parameters (in the TecView Inspection module) had to be made in order to optimize the quality of the scan data.

As shown in the images below, some samples did not produce usable C-Scan data. This was the case for samples #1 and #3, whereby significant noise was present and appeared to be caused by poor and inconsistent inter-ply bonding within the CF/E skin. Additionally, none of the samples exhibited detectable evidence of the mould release gel. Perhaps the gel fuses with the adhesive during the curing process, making its detection by ultrasonics difficult to potentially impossible.

It would be worth considering sectioning some of these samples to better understand the bonding between the CF/E skin plies and that of the CF/E-Ti bond-line. There is some interest from QETE Composite Engineer, Mr. Rob Hoffman, and QETE NDE Lab, to further investigate these samples at a later time. This would strengthen QETE's understanding of CF/E-Ti bonded samples and the effect of CF/E skin-ply bonding variability has on AUT C-Scan data quality and interpretation.

Sample 1:

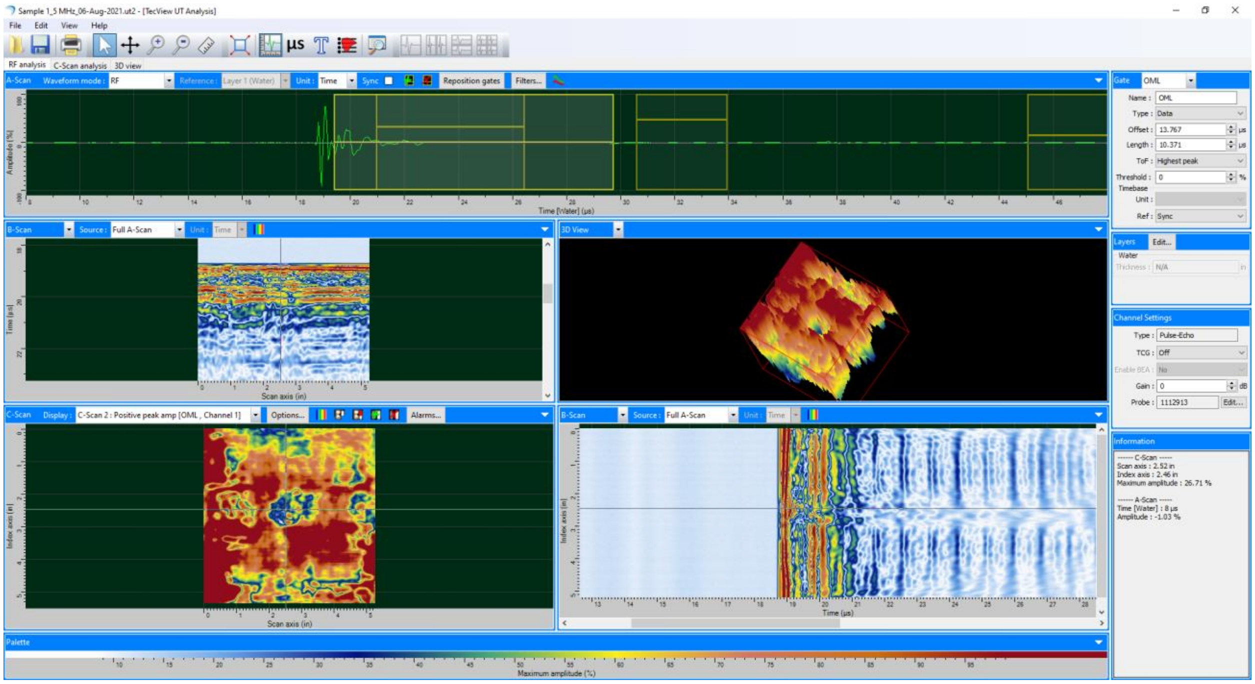

Fig 1 - Screen capture of sample 1 at 5MHz scan frequency. The Pos (positive) Peak C-Scan image fails to show any useful information relating to the embedded flaws between the CF/E and Titanium. Most notably, with the cursor placed on the area containing the CF/E-Ti FBH, it is not possible to define the FBH as in samples 2 & 4. The A-Scan signal response should be similar to that of sample 2, albeit with the FBH UT echo signal shifted slightly left toward the interface echo (due to the thinner CF/E skin).

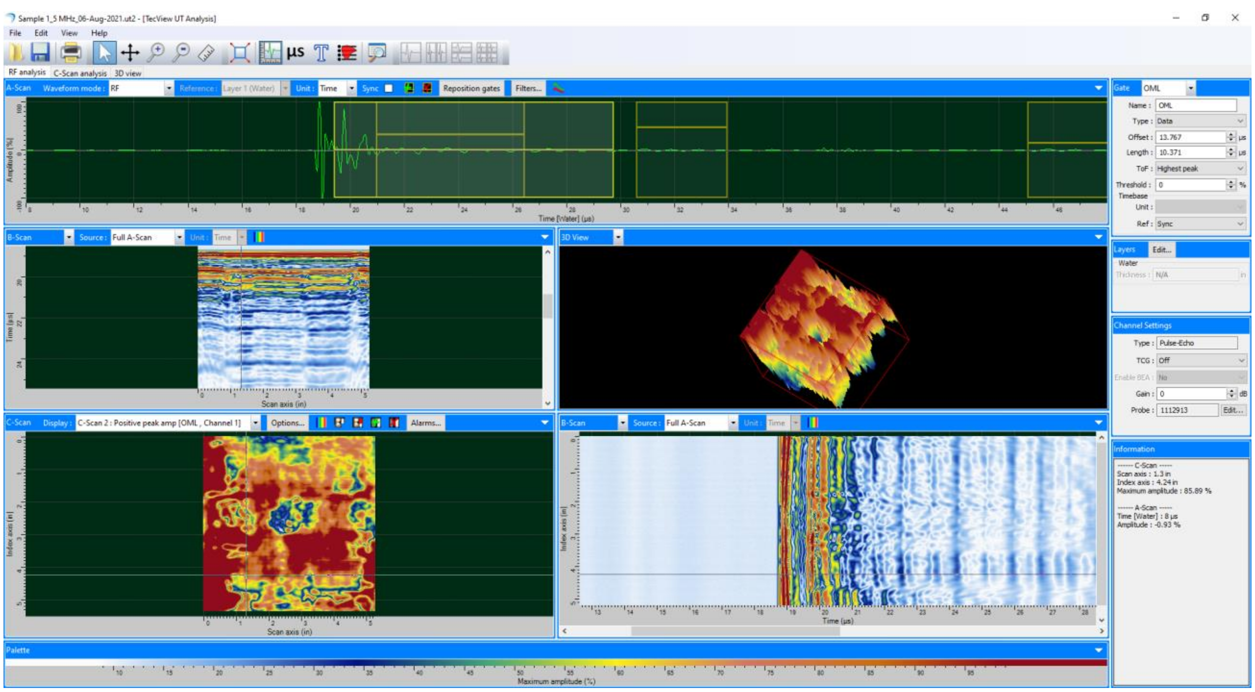

Fig 2 - Screen capture of sample 1 at 5MHz scan frequency, with the cursor placed on one of the Thermal Tape inserts between the CF/E skin and Titanium. As with Fig 1 of Sample 1, the Scan data quality was unable to display any useful information. Most notably, the C-Scan image is unable to clearly define the Thermal Tape insert (when compared to sample 2). While the B-Scan data does show some anomaly in the UT echo repetitions, it is extremely difficult to make any sound judgment or interpretation as to the cause of the echo repetitions.

Sample 2

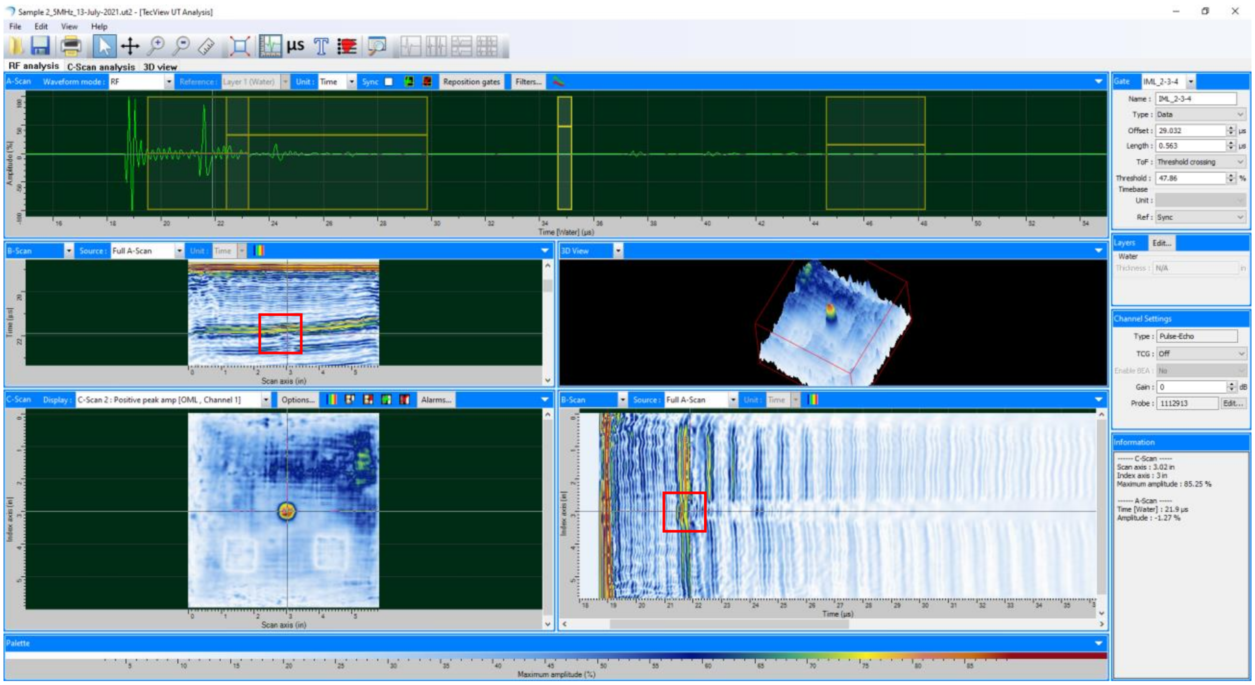

Fig 3 - Screen capture of sample 2 showing FBH at CF/E-Ti bond-line

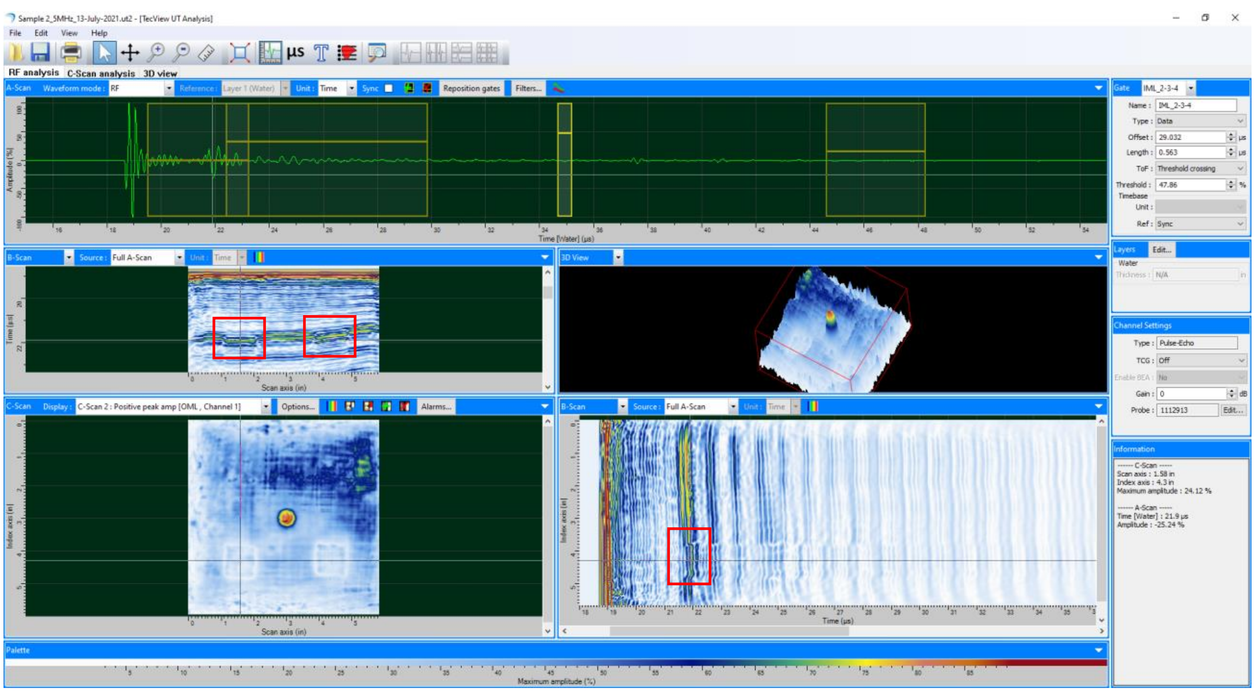

Fig 4 - Screen capture of sample 2 showing effect of thermal tape on CF/E-Ti bond-line

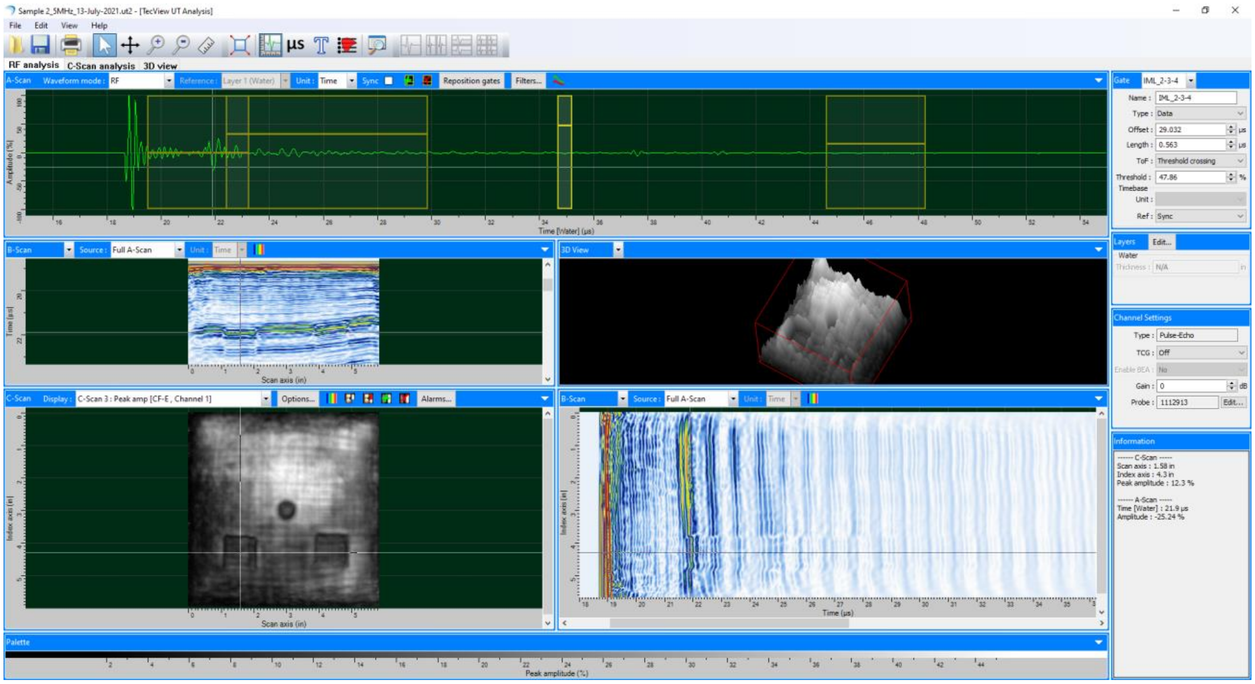

Fig 5 - Screen capture of sample 2 showing effect of thermal tape on CF/E-Ti bond-line, using scan data from a different data gate (slightly later time capture of the data)

Sample 3

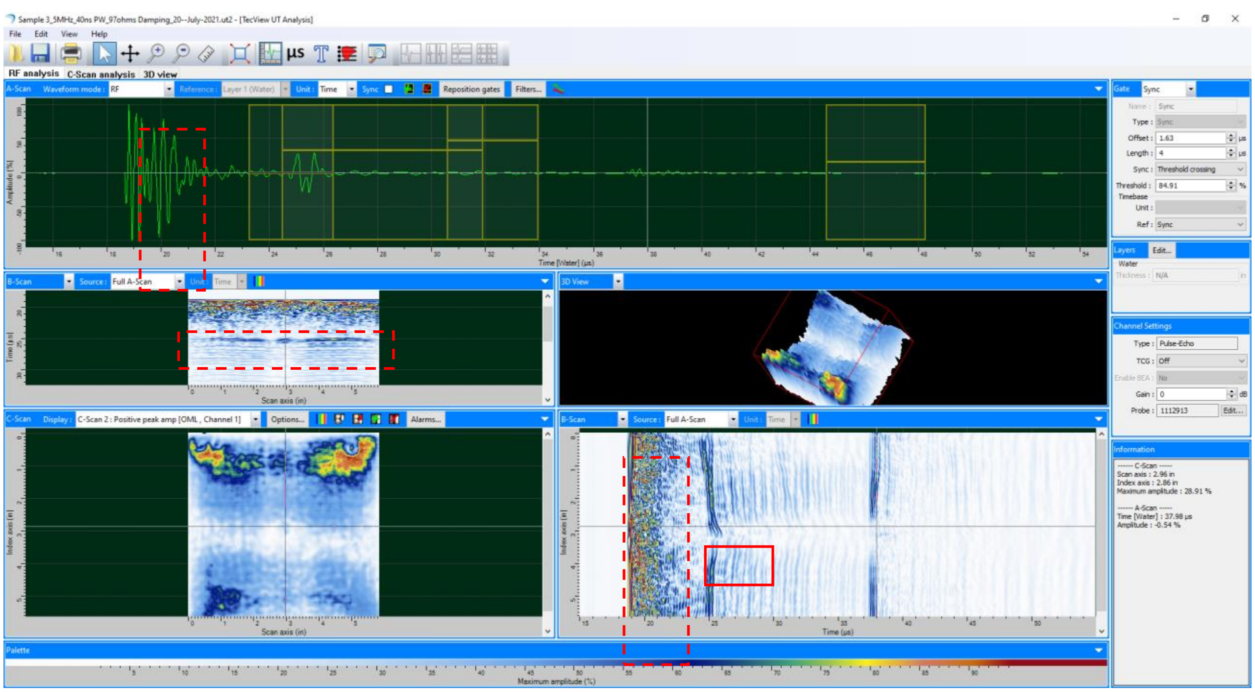

Fig 6 - Screen capture of sample 3 showing effect of FBH at CF/E-Ti bond-line (red outline, B-Scan image). Sample 3 generated significant noise from the CF/E skin plies (red-dash outlines), producing low-quality scan data.

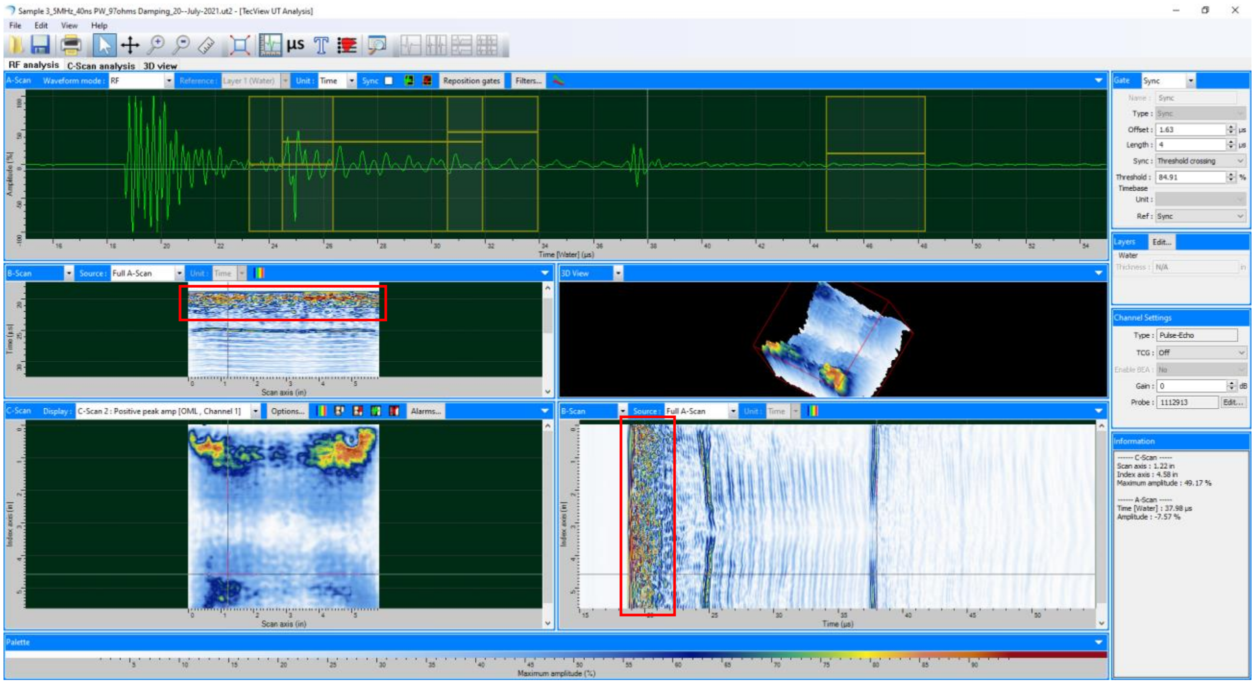

Fig 7 - Screen capture of sample 3 with cursor placed on area containing thermal tape. As evidenced by the C-Scan image, there was no usable information from this scan, likely because of the excessive noise generated by the CF/E skin plies (red outlines – B-Scan images).

Sample 4

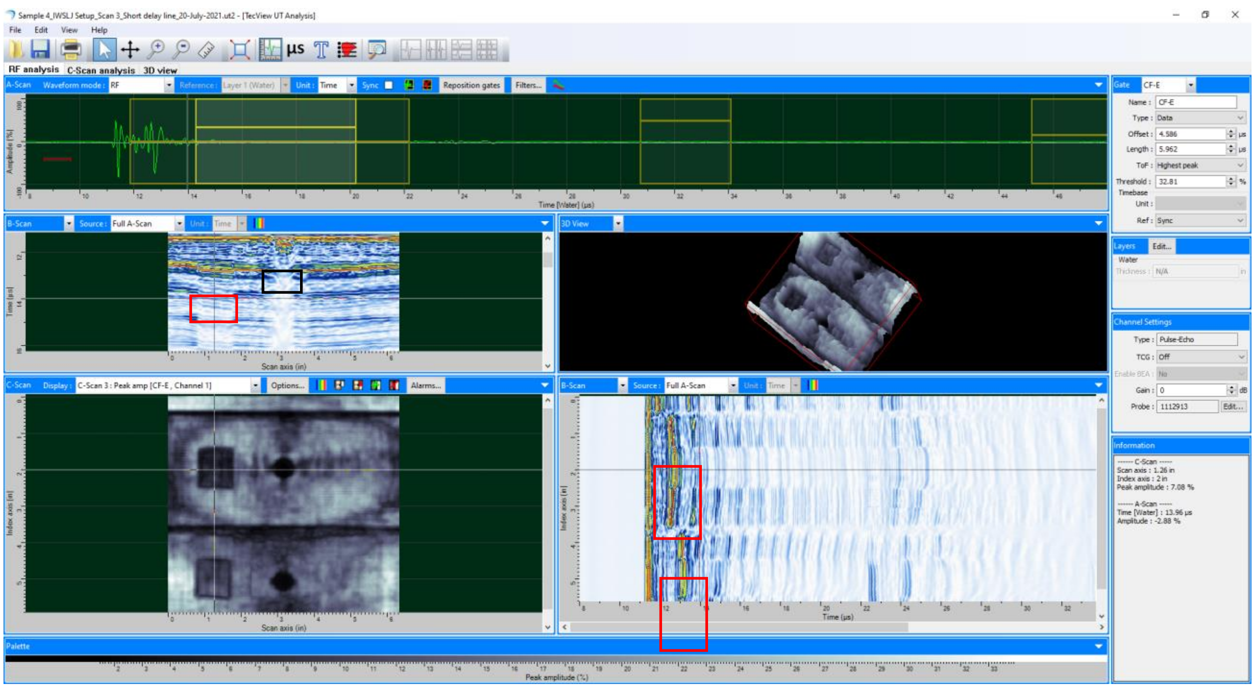

Fig 8 - Screen capture of sample 4 showing effect of thermal tape on “Step 2” C/E-Ti bond-line on (red outline, B-Scan images). Note the FBH response, which shows the FBH occurring early in the CF/E-Ti skin plies, which would indicate a delamination rather than a CF/E-Ti disbond (black outline).

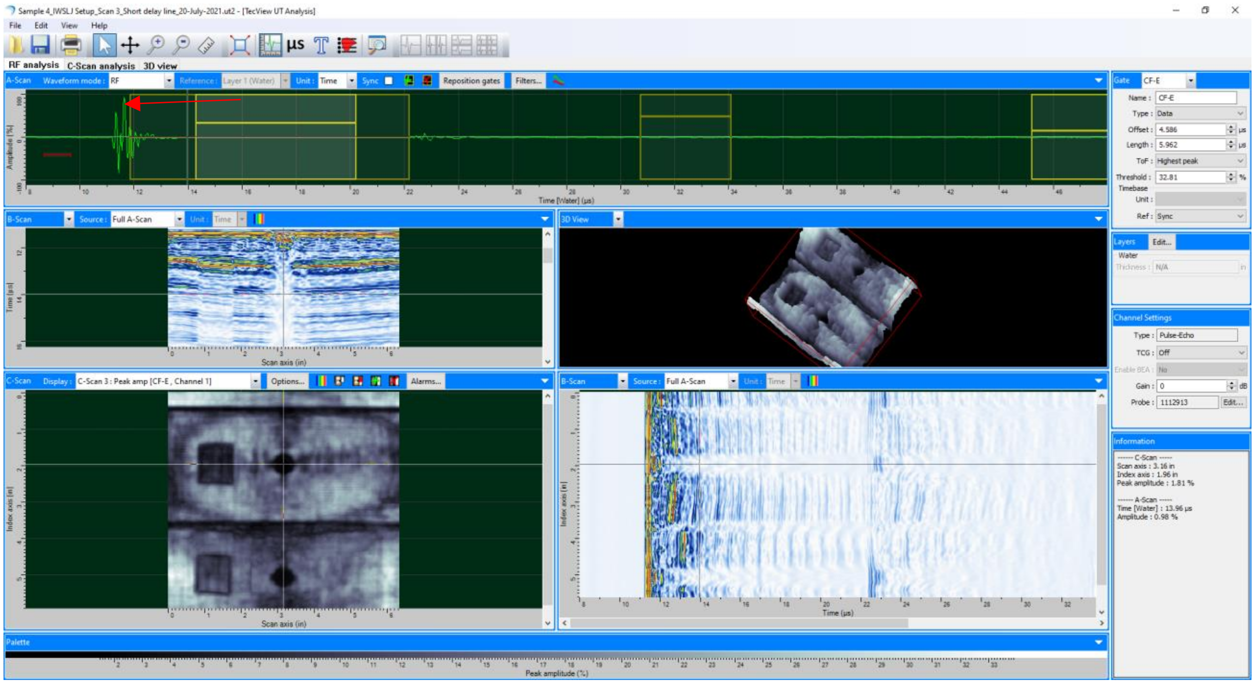

(a)

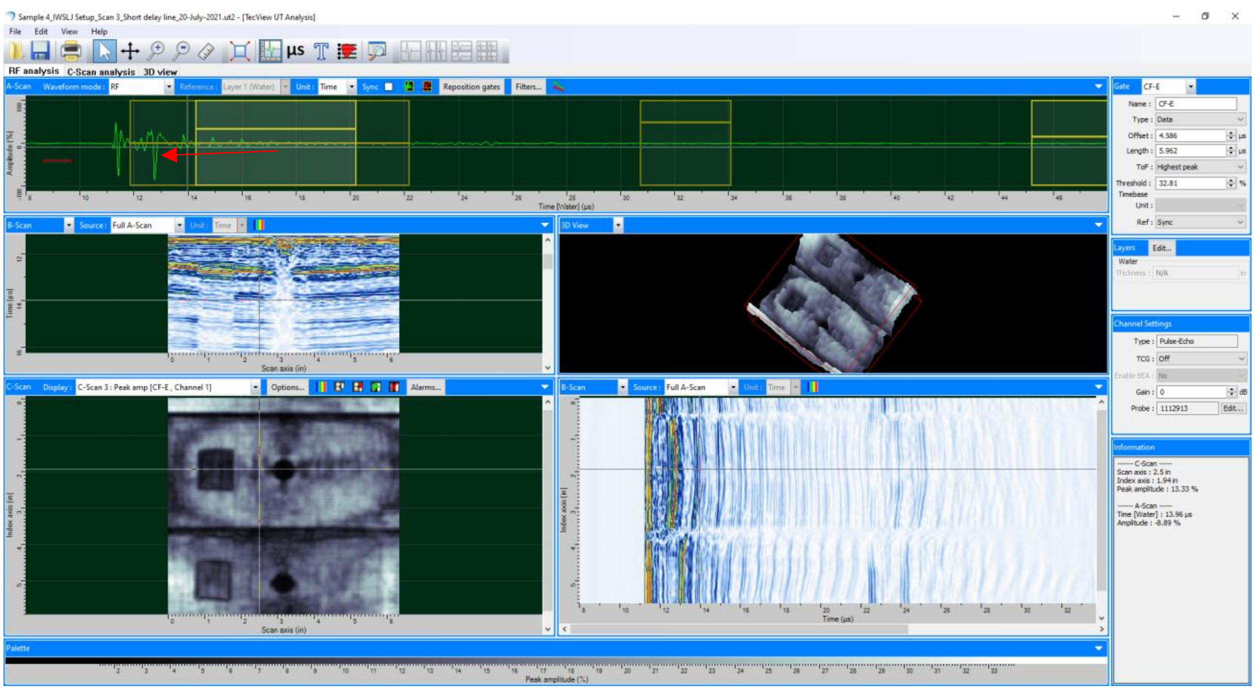

(b)

Fig 9 - Screen capture of sample 4 showing FBH response, which clearly shows the indication is occurring "early" in time, as indicated by the red arrow on the A-Scan window of capture (a). Capture (b) shows the CF/E-Ti bond-line response appears later in time compared to the FBH, further indicating the FBH to be a CF/E skin-ply delamination (red arrow on A-Scan window).

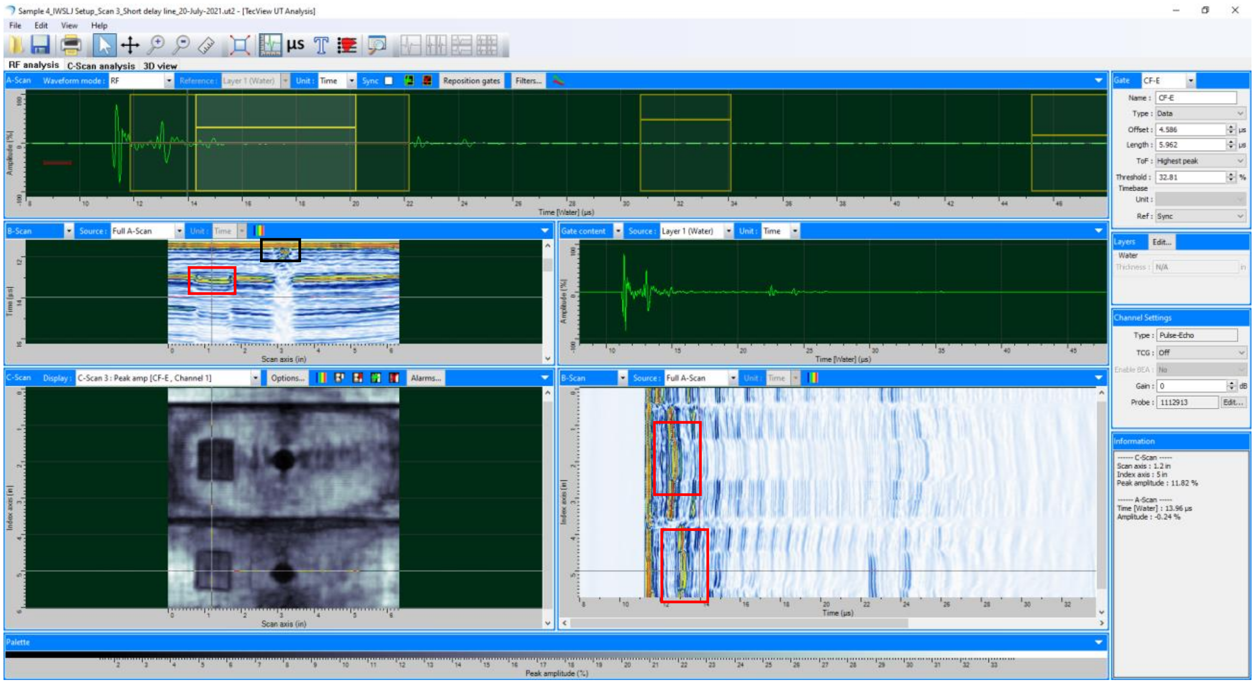

Fig 10 - Screen capture of sample 4 showing effect of thermal tape on “Step 2” C/E-Ti bond-line on (red outline, B-Scan images). Note the FBH response, which shows the FBH occurring early in the CF/E-Ti skin plies, which would indicate a delamination rather than a CF/E-Ti disbond (black outline). The response from the thermal tape and FBH on step 3 are consistent with the response from these embedded flaws on step 2.

Prepared by: Steven Savage
Manager, QETE NDE Lab
Steven.Savage@forces.gc.ca
819-939-9375 / 613-462-3936

Appendix F – QETE Report IV

25-May-2022

Specialized AUT C-Scan Testing of CF188 IWSLJ CFRP-Ti Sample

Task

1. In support to NDT-PG Thesis by Capt Keith George, QETE was tasked to conduct specialized NDE in the form of AUT C-Scan (automated ultrasonic C-Scan) testing on a CF188 IWSLJ (Inner Wing Stepped Lap Joint) CFRP-Ti (carbon fiber resin polymer to titanium) sample.

Sample Description

2. The sample is an extracted section of a CF188 Inner Wing Upper Skin Plank, with FBH's (flat bottom holes) located at the OML (outer mold line) of steps 1 and 2, as well as just outboard of step 9. Note that step 1 of the CFRP-Ti bonded joint is the inboard-most step.

Test Methodology

3. AUT C-Scan testing of the IWSLJ sample was performed using the TecScan ARMANDA (automated robotic manipulator arm for non-destructive assessment) inspection system. The inspection was standardized using RCAF NDT Technique 188-355U, which was developed by QETE for the sole purpose of inspecting the RCAF's CF188 Inner Wings under C-13-K91-000/NS-045. The inspection was performed using a scan resolution of 0.020" x 0.020" Scan / Index increment.

Test Results

4. AUT C-Scan testing of the IWSLJ sample revealed OML disbond indications at Steps 1 and 2, and a CFRP skin-ply delamination just outboard step 9. All of these indications are consistent with the locations of the embedded FBH's. The indications were measured using the TecView Analysis measuring tool, with the following results:

a. Step 1 FBH: approx. 0.500" x 0.4852"
b. Step 2 FBH: approx. 0.474" x 0.440"
c. CFRP FBH: approx. 0.500" x 0.500"

Discussion

5. AUT C-Scan testing of the IWSLJ sample revealed identical ultrasonic signal responses as those obtained with RCAF NDT Technique 188-355-U reference coupon and F/A-18 Inner Wings Root Splice Plate Stepped Lap Joint disbonds and CFRP skin ply delaminations. Testing of the coupon was consistent with CF188 IWSLJ fleet inspections currently being conducted by QETE under C-13-K91-000/NS-045. Screenshots of the C-Scan images are shown in Figs 1 to 4.

6. This was expected as the sample derives from a real CF188 Inner Wing Upper Skin Plank and contains FBH's similar to those embedded on 188-355-U reference coupon, with the exception that the latter contains FBH's on all steps (1-9) of the OML and IML bondlines, as well as CFRP laminate FBH's in the CFRP solid laminate portion of the coupon at 25%, 50% and 75% depth.

C-Scan Screenshot – Neg Peak Amplitude Mapping of OML Bondline – Step 1 Defect-Free Area

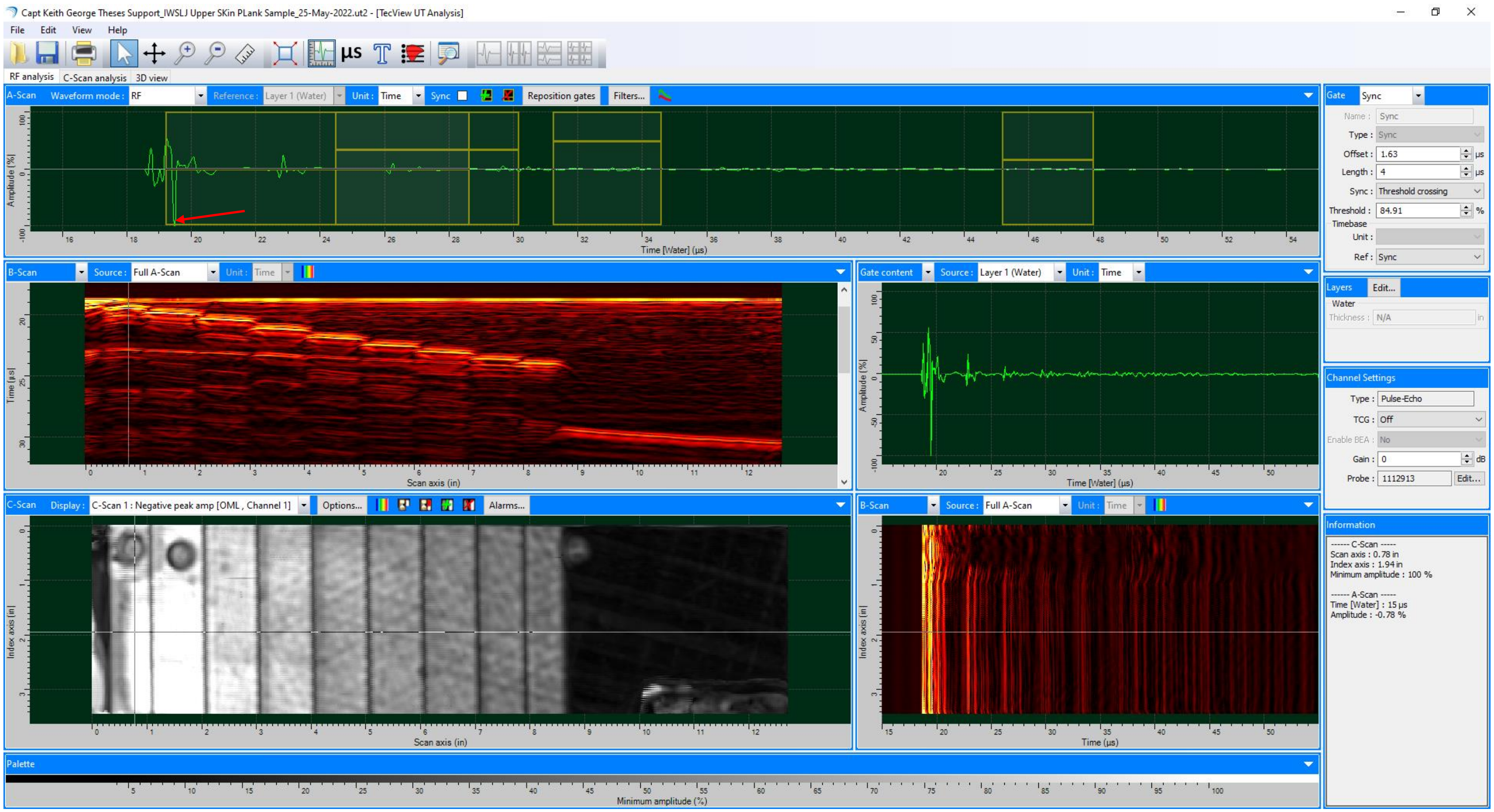

Fig 1 – Screenshot of IWSLJ Neg Peak Amplitude mapping of OML bondline, with the cursor placed on Step 1 defect-free area. The Neg Peak Amp C-Scan image is used to assess ultrasound transmitted into the titanium portion of the CFRP-Ti bonded joint. A good OML bondline produces a predominantly Neg Peak UT signal on the A-Scan display (as shown by the red arrow). On this screenshot, the cursor has been placed on a non-defect area of Step 1, indicating a good bond. This UT signal will move further to the right on the A-Scan display as the cursor is moved over steps 2 through 9 respectively.

C-Scan Screenshot – Pos Peak Amplitude Mapping of OML Bondline – Step 1 FBH

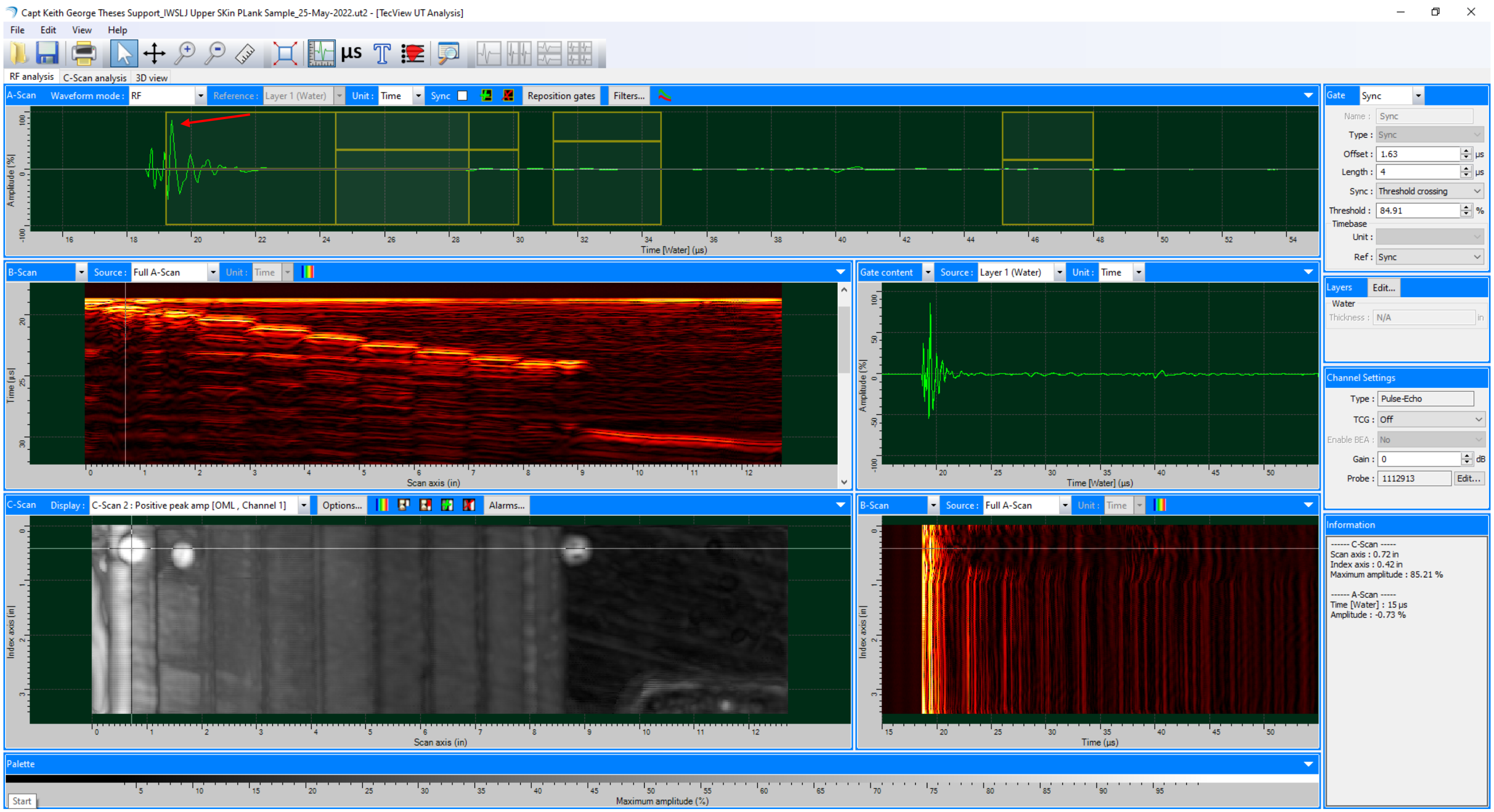

Fig 2 – Screenshot of IWSLJ Pos Peak Amplitude mapping of OML bondline, with the cursor placed on Step 1 FBH. The Pos Peak Amp C-Scan image is used to display flaws which occur at the OML bondline, which produce strong Pos Peak UT signals (red arrow on A-Scan display window). On this screenshot the cursor has been placed on the FBH located on Step 1. Note the UT signal change from Neg Peak to Pos Peak amplitude, as compared to Fig 1, where the cursor is placed on a bonded area of Step 1.

C-Scan Screenshot – Pos Peak Amplitude Mapping of OML Bondline – Step 2 FBH

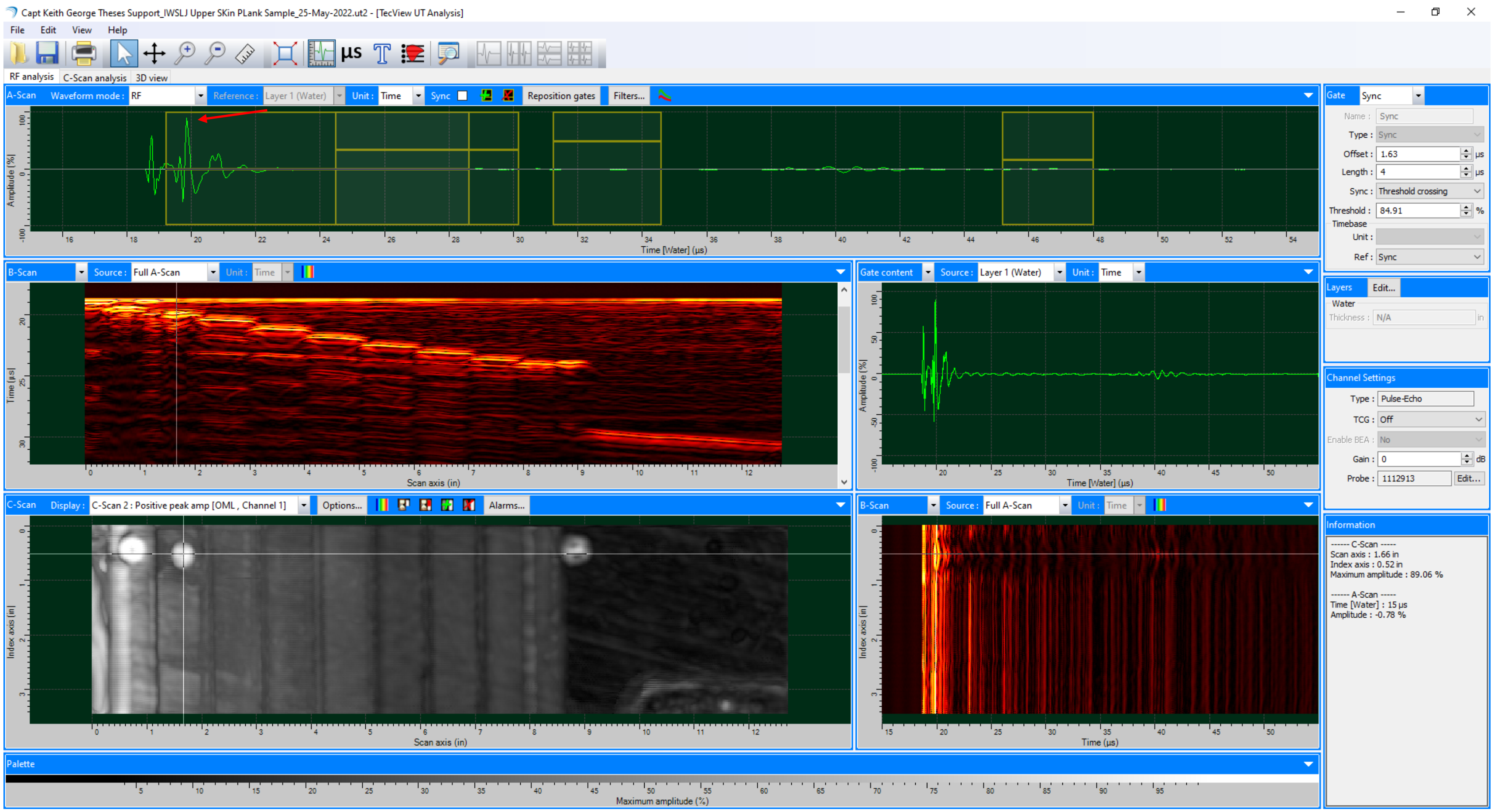

Fig 3 – Screenshot of IWSLJ Pos Peak Amplitude mapping of OML bondline, with the cursor placed on Step 2 FBH. The Pos Peak Amp C-Scan image is used to display flaws that occur at the OML bondline, which produce correspondingly strong Pos Peak UT signals (red arrow on A-Scan display window). Notre the A-Scan window, which shows the UT signal shifting slightly to the right, which corresponds to the slightly thicker CFRP skin at Step 2.

C-Scan Screenshot –Peak Amplitude Mapping of CFRP laminate Skin – Defect-Free Area

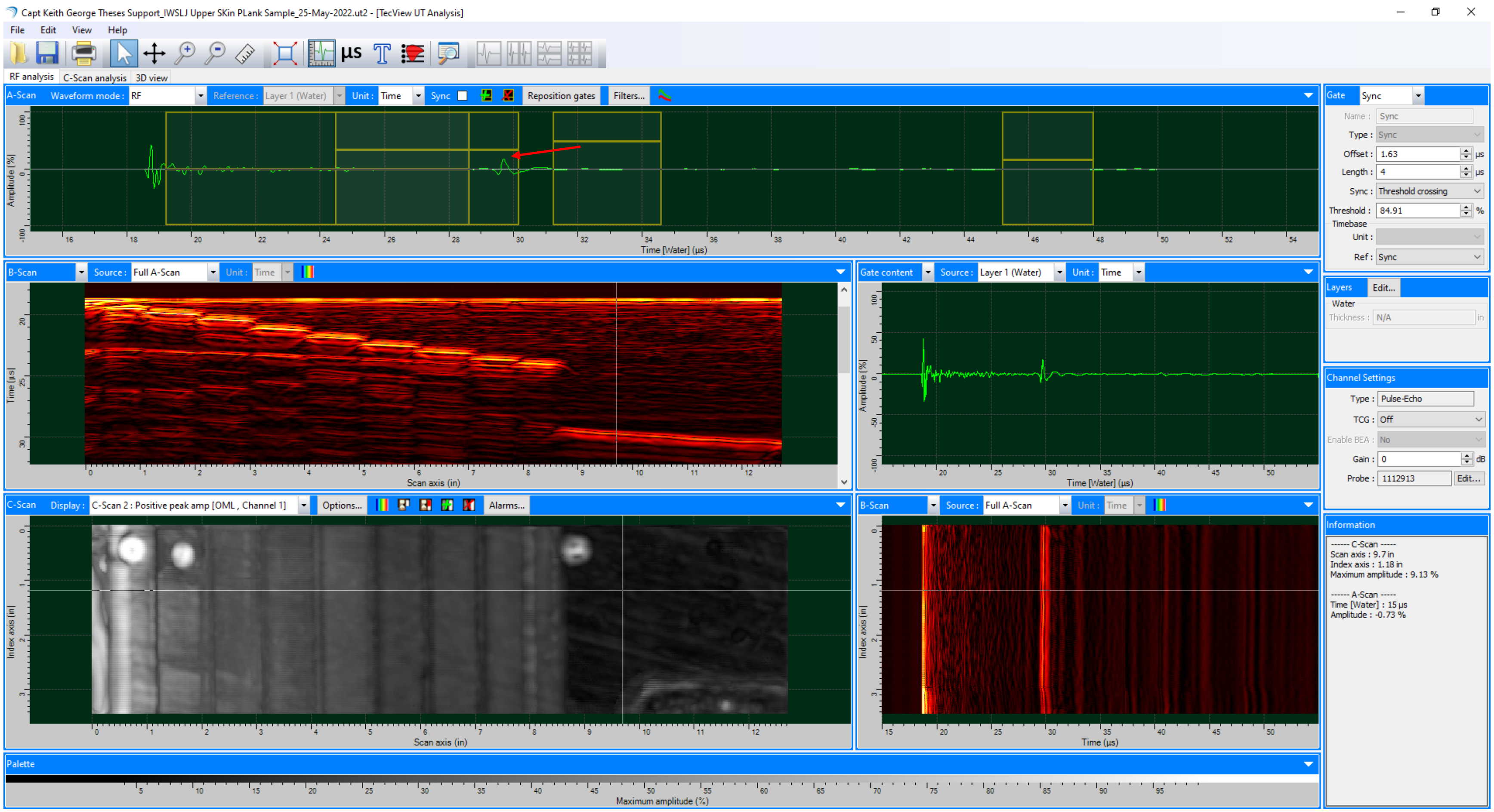

Fig 4 - Screenshot of IWSLJ Peak Amplitude mapping of CFRP Laminate Skin, with the cursor placed on a defect-free area of the CFRP. The corresponding UT signal is generally a Pos Peak UT signal, as shown by the red arrow.

C-Scan Screenshot –Peak Amplitude Mapping of CFRP laminate Skin – CFRP FBH

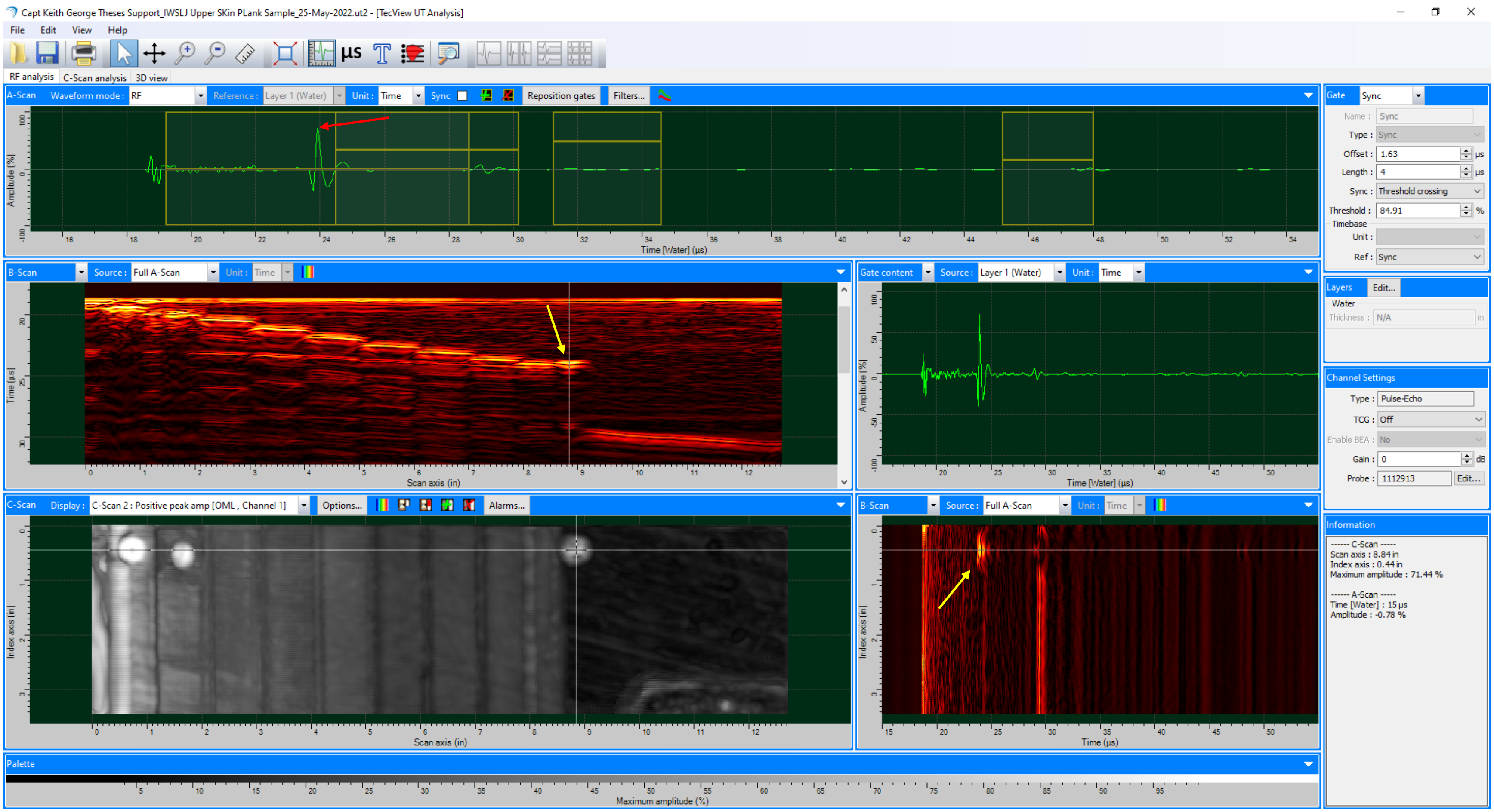

Fig 5 - Screenshot of IWSLJ Peak Amplitude mapping of CFRP Laminate Skin, with the cursor placed on a the CFRP FBH, located just outboard of Step 9. Note the stronger Pos Peak signal displayed on the A-Scan window (red arrow), and corresponding reflector on the B-Scan windows (yellow arrows).

Appendix G – Ambrell Corporation® Report

Summary of Ambrell Applications Laboratory Testing

Objective: Heat carbon fiber/titanium plate by at least 10˚C for an induction thermography application.

Equipment: Ambrell EasyHeat™ 0112, 1.2 kW, 150-400 kHz solid state induction power supply, equipped with a remote work head containing a single 0.33 μF capacitor.

Frequency: 300 kHz

Material: Carbon fiber & titanium.

Temperature: Temperature rise of at least 10˚C.

Testing: A custom-designed, 3” wide, single position, multi-turn pancake coil was built to generate the required heating for the application. Initial tests were conducted to optimize the power delivered to the part. The induction coil is pictured in *Figure 1* below.

Figure 1: Induction coil used in the experiment.

1655 Lyell Ave, Rochester, NY 14606 USA • Tel: +1 585 889 9000 • Fax: +1 585 889 4030
www.ambrell.com

The sample was then placed over the induction coil, carbon fiber side down, with an air gap of about 3/16” between the sample and coil. This is shown in *Figure 2* below.

Figure 2: Sample located over the induction coil.

Induction heat was then turned on and the sample was heated from room temperature past 40°C within 5 seconds. The IR thermal image of this is shown in *Figure 3* below.

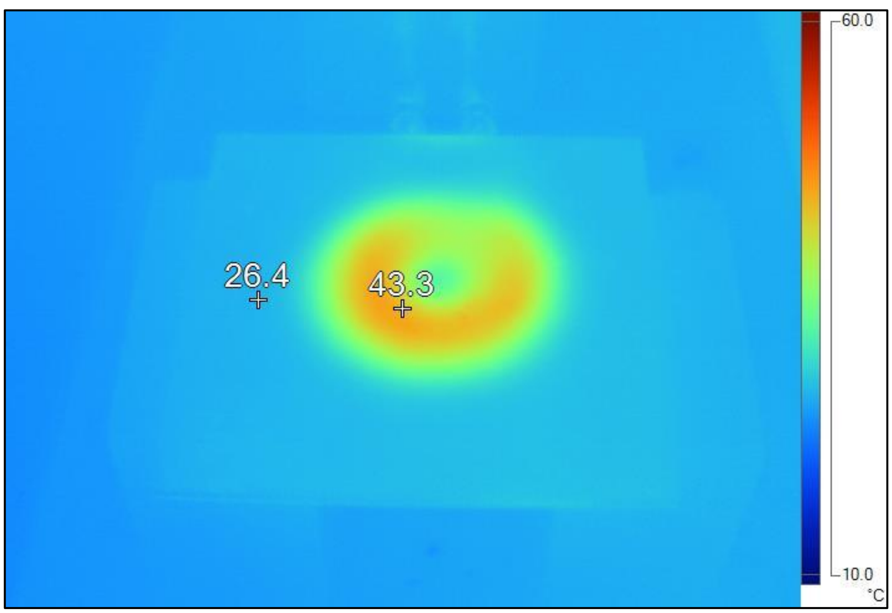

Figure 3: IR thermal image of the sample being heated.

Conclusion: Laboratory testing has confirmed the feasibility of the heating process for heating the customer samples at least 10˚C using the Ambrell EasyHeat™ 0112, 1.2 kW, 150-400 kHz induction power supply. Some process development may still be needed at the customer site once the induction system is delivered to account for the unique fixture/ handling techniques used.

Ambrell is pleased to provide the facilities and efforts of its applications laboratory and engineers to produce this report on a complimentary basis.

The information contained in this report is based on calculations and laboratory findings gathered under Ambrell laboratory conditions. Ambrell does not assume any liability or obligation for the results obtained. We cordially invite you to discuss these results with our technical staff at your convenience.

Respectfully submitted,

Ilmar Begishev
Ambrell Applications Laboratory

Appendix H – Ambrell Corporation® EASYHEAT Induction System Specifications

EASYHEAT® 1.2 to 2.4 kW Induction Heating Systems

Ambrell®
INDUCTION HEATING SOLUTIONS
an inTEST Company

The compact EASYHEAT induction heating systems are a reliable solution for heating parts with a quick, clean source of heat. With a movable work head that can be located up to 3m (10') from the power supply, it is ideal for repeatable, non-contact heating of parts.

Equipped to operate over a broad frequency range (150-400 kHz), EASYHEAT is ideal for heating parts of many geometries and compositions with precise power control within 25 W resolution.

Avoid time-consuming changeovers with agile tuning for single-cycle and continuous heating operations. One system can supply deep, bulk heating for brazing and soldering for more shallow, concentrated heating for case-hardening for smaller parts. Flameless, non-contact induction heating minimizes energy waste by focusing energy only on the part and zone to be heated. Select and monitor power levels from the front panel LCD and sealed touch pad. Remote power control is available for employing contact inputs, analog inputs or optional serial data port. Easily control the length of the heating cycle with a built-in programmable digital timer.

EASYHEAT is a water-cooled system, requiring connection to a heat exchanger or other mechanism for dissipating heat.

Versatile

- Efficient heating of many geometries
- Repeatable, reliable heating with agile frequency tuning
- Movable workhead; up to 3m (10')
- Remote serial operation or logging (optional)
- Five language display suite (EN, FR, IT, DE, ES)
- Field-calibration capable

Easy-to-Use

- Self-adjusting for accurate, repeatable results
- View set-point, output, frequency and timer
- Built-in timer, stop-watch
- Push-button RF power control

Compact and Light

- Smallest feature-rich 2.4 kW model

EASYHEAT features a front panel programmable controller allowing you to define up to four different heating profiles, each with up to five time/power steps.

OPTIONS AND ACCESSORIES

- Heat exchanger or chiller
- Optical pyrometer (closed-loop temperature control)
- External controller (plc)
- Extended work head cable lengths
- Footswitch
- Serial data interface
- Pendant station
- Start-up assistance

Experience the Excellence.™

SPECIFICATION	0112	0224	UNITS
RF Terminal Power	1.2	2.4	kW
AC Line Power	1.6	3.3	kVA
AC Line Protection	15	15	A
Frequency	150-400		kHz
RF Coil Current	300-400		A max
AC Line Voltage	117 or 220	220	Vac ± 10%, 1Ø
Front Panel Display	2 line x 16 character LCD; displays frequency, power, setpoint, timer and fault descriptions		
Display Language Suite[1]	Five language display suite (EN, FR, IT, DE, ES)		
Serial Communications	Via RS485 terminal mode		Optional
Timer	Built in; 10ms to 10,000 seconds		
Heating Controller	4 programmable profiles, 5 steps per profile		
RF Rise Time	<5		ms
Tune Time	<5		ms
Compliance	CE Marked, 220 models only		
Max Ambient Temp	45 (115)		C° (F°)
Unit Weight	10.4 (23)		kg (lb)
Dimensions	Rack 483 x 400 x 133 (19 x 15.7 x 5.3)		WxDxH mm (in)
	Bench 436 x 398 x 129 (17.2 x 15.7 x 5.1)		
WATER COOLING (Sys[2])			
Flow	1.5 (0.4)	2.8 (0.75)	l/m (g/m)
Max Input Pressure	5.6 (80)		Bar (lb/in^2)
Pressure Differential	2.8 - 5.5 (40-80)		Bar (lb/in^2)
Max Water Temp	35 (95)		C° (F°)

1) Factory set 2) System includes workhead

Two Application Specific Work Heads

LEFT	RIGHT	UNITS
102 x 267 x 102 (4 x 10.5 x 4)	102 x 204 x 102 (4 x 8 x 4)	mm (in)
4 (8.8)	3 (6.6)	kg (lb)

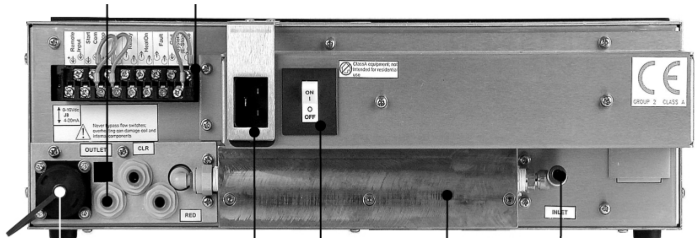

Visit our extensive library of Application Notes at: www.ambrell.com

Ambrell
INDUCTION HEATING SOLUTIONS
an inTEST Company

www.ambrell.com

ISO 9001:2015 CERTIFIED

Ambrell Corporation
United States
Tel: +1 585 889 9000
Fax: +1 585 889 4030
sales@ambrell.com

Ambrell B.V.
The Netherlands
Tel: +31 880 150 100
Fax: +31 546 788 154
sales-eu@ambrell.com

Ambrell, Ltd.
United Kingdom
Tel: +44 1242 514042
Fax: +44 1242 224146
sales-uk@ambrell.com